Supersonic organic Rankine cycle radial-inflow turbines for onboard thermal energy harvesting

Preliminary design guidelines and detailed design of a laboratory test rig for experimental validation

Majer, M.

DOI
10.4233/uuid:32c9d5f4-b1f9-49f4-8a6f-3fec274a5e8e

Publication date
2025

Document Version
Final published version

Citation (APA)
Majer, M. (2025). *Supersonic organic Rankine cycle radial-inflow turbines for onboard thermal energy harvesting: Preliminary design guidelines and detailed design of a laboratory test rig for experimental validation*. [Dissertation (TU Delft), Delft University of Technology]. Delft University of Technology. https://doi.org/10.4233/uuid:32c9d5f4-b1f9-49f4-8a6f-3fec274a5e8e

Important note
To cite this publication, please use the final published version (if applicable).
Please check the document version above.

Supersonic organic Rankine cycle radial-inflow turbines for onboard thermal energy harvesting

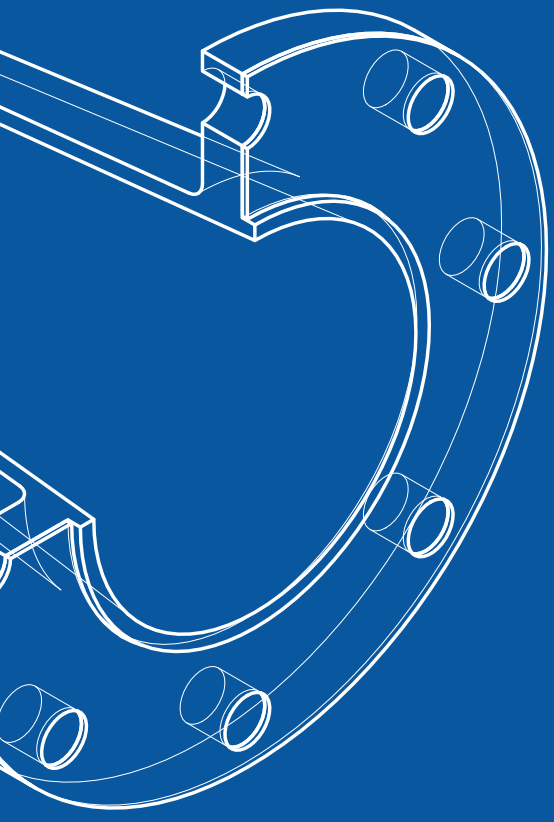

Preliminary design guidelines and detailed design of a laboratory test rig for experimental validation

Matteo Majer

SUPERSONIC ORGANIC RANKINE CYCLE RADIAL–INFLOW TURBINES FOR ONBOARD THERMAL ENERGY HARVESTING

PRELIMINARY DESIGN GUIDELINES AND DETAILED DESIGN OF A LABORATORY TEST RIG FOR EXPERIMENTAL VALIDATION

SUPERSONIC ORGANIC RANKINE CYCLE RADIAL–INFLOW TURBINES FOR ONBOARD THERMAL ENERGY HARVESTING

PRELIMINARY DESIGN GUIDELINES AND DETAILED DESIGN OF A LABORATORY TEST RIG FOR EXPERIMENTAL VALIDATION

Dissertation

for the purpose of obtaining the degree of doctor

at Delft University of Technology,

by the authority of the Rector Magnificus prof. ir. T.H.J.J. van der Hagen,

chair of the Board for Doctorates,

to be defended publicly on Friday 19 September 2025 at 10:00 o'clock.

by

Matteo MAJER

Master of Science in Mechanical Engineering, Politecnico di Milano, Italy
born in Milan, Italy

This dissertation has been approved by the promotors.

Composition of the doctoral committee:

Rector Magnificus	Chairperson
Prof. dr. ing. P. Colonna di Paliano	Delft University of Technology, *promotor*
Dr. M. Pini	Delft University of Technology, *promotor*
Dr. C.M. De Servi,	Delft University of Technology, *copromotor*
Independent members:	
Prof. dr. R. Pecnik	Delft University of Technology
Prof. Dr. -Ing. J. Seume	Leibniz University Hannover, Germany
Dr. A. Spinelli	Politecnico di Milano, Italy
Dr. O. Pryor	Southwest Research Institute, United States
Prof. dr. M. Kotsonis,	Delft University of Technology, *reserve member*

The research presented in this dissertation has been performed at the Flight Performance and Propulsion Section, Department of Flow Physics and Technology, Faculty of Aerospace Engineering. This work is part of the research project "Airborne Thermal Energy Harvesting for Aircraft" (ARENA), funded by the Dutch Technology Foundation TTW, Applied Science Division of NWO, the Technology Program of the Ministry of Economic Affairs, and by Aeronamic B.V. (Grant No. 17906).

Printed by: Ridderprint B.V.

Front & Back: Illustration by Matteo Majer and cover design by Titti Benedetti.

ISBN 978-94-6518-102-8

An electronic version of this dissertation is available at
http://repository.tudelft.nl/.

Contents

List of Figures . . . . . **viii**

List of Tables . . . . . **xv**

Summary . . . . . **xvii**

Samenvatting . . . . . **xix**

Nomenclature **1**

1 Introduction **9**
1.1 Context and background 10
1.1.1 Thermal energy harvesting from propulsive engines 11
1.1.2 Propulsion technology for climate neutral aviation 12
1.1.3 Combined-cycle engines 14
1.2 Organic Rankine cycle supersonic turbines 16
1.2.1 Design guidelines for radial-inflow turbines 17
1.2.2 Experimental research facilities 18
1.3 Scope of the research 18
1.4 Thesis outline 20

2 Design guidelines for high-pressure ratio supersonic radial-inflow turbines of organic Rankine cycle systems **27**
2.1 Introduction 28
2.2 Theoretical framework 29
2.2.1 Generalized scaling law for RITs 29
2.2.2 Nonideal compressible fluid dynamics effects on losses in turbines 30
2.3 Turbine design methodology 31
2.3.1 Calculation of turbine efficiency 36
2.3.2 Loss accounting 36
2.3.3 Model verification 41
2.4 Results 44
2.4.1 Influence of the working fluid and $\bar{\gamma}_{Pv}$ on stage efficiency 45
2.4.2 Loss breakdown analysis 50
2.4.3 Influence of the meridional velocity ratio on efficiency 53
2.5 Design guidelines 55

2.6 Conclusion & outlook . . . 56

3 Preliminary design of the ORCHID turbogenerator: a novel prototype for experimental research on RITs for high-temperature ORC systems . . . 63
3.1 Introduction . . . 64
3.2 Fluid dynamic performance assessment . . . 67
3.3 Preliminary mechanical design . . . 74
3.3.1 Conceptual rotor layout . . . 75
3.3.2 Bearings . . . 76
3.3.3 Seals . . . 79
3.3.4 Initial turbine layout . . . 82
3.3.5 Impeller wheel design . . . 83
3.4 Structural analysis of the impeller . . . 84
3.4.1 Estimation of the mechanical loads . . . 84
3.4.2 Finite elements mechanical analysis . . . 88
3.5 Thermal analysis of the assembly . . . 91
3.5.1 Estimation of the bearings power losses . . . 91
3.5.2 Estimation of the cooling load using finite elements analysis . . . 93
3.6 Rotordynamic analysis . . . 97
3.6.1 Modeling of the rotordynamic coefficients . . . 97
3.6.2 Analysis of the lateral vibrations . . . 108
3.7 Conclusion & outlook . . . 113

4 Detailed design and realization of the ORCHID turbine test bed . . . 123
4.1 Introduction . . . 124
4.2 The ORCHID . . . 125
4.3 Turbine test bed . . . 128
4.3.1 Design requirements . . . 128
4.3.2 Test bed layout . . . 129
4.3.3 Turbogenerator layout . . . 134
4.3.4 Electric generator integration . . . 144
4.4 Instrumentation . . . 146
4.4.1 Uncertainty quantification . . . 147
4.5 Conclusion & outlook . . . 153

5 Final remarks and outlook . . . 157
5.1 Original contributions . . . 158
5.2 Main conclusions . . . 159
5.3 Limitations and recommendations for future work . . . 165
5.4 Outlook and future research directions . . . 167

Appendices . . . 175
A Emissions . . . 175
B Aircraft energy balance . . . 176
C Combined cycles . . . 177
D Coefficients of the Baines loss model for radial-inflow turbine impellers . . . 178

E Stage sizing routine in *TurboSim* . . . 179
F Geometrical scaling parameters used in *TurboSim* . . . 180
G ORCHID turbine test section auxiliary components . . . 181
H Application of the linear complementarity problem to compute the pressure of cavitating liquid fluid-films . . . 182

Appendix . . . **175**

Acknowledgements . . . **187**

About the Author . . . **189**

List of Publications . . . **191**

List of Figures

1.1 Photograph of the high-temperature low capacity ORC turbogenerator rotor commercialized by a Dutch company. The purely radial expander wheel is visible on the left end of the generator shaft, and one half of the disassembled stator ring rests on the table top. Courtesy of Triogen [11]. 11

1.2 Trend of effective fuel consumption (EFC) and fuel consumption per seat certified between 1958 and 1994. Note that engines can be operational for 10 to 20 years from the entering-into-service date, hence engines certified in the 1990s were likely to be still operational between 2005 and 2015. Figure adapted from [26]. 13

1.3 Process flow diagram of a CC-TS engine, courtesy of Krempus [38]. 15

1.4 Process flow diagram of a CC-TF engine, courtesy of Krempus [38]. 16

2.1 Shock loss (left) and mixing loss at increasing cascade downstream Mach number (right) as a function of the generalized isentropic pressure-volume exponent $\bar{\gamma}_{Pv}$. The loss coefficients are normalized by the one of air in ideal gas conditions ($\bar{\gamma}_{Pv} = 1.4$). Loss is computed assuming $VR_{\text{sh}} = 1.2$. 32

2.2 Meridional view of a radial-inflow turbine stage with all the relevant dimensions indicated. 32

2.3 Workflow diagram of the turbine preliminary design method. 33

2.4 On the left y-axis: entropy change obtained by solving the RH governing equations (solid lines) as a function of the pre-shock Mach number M_{A} assuming i) a constant shock angle $\epsilon = 45°$, and ii) a varying shock angle as a function of M_{A} (Equation 2.30). On the right y-axis: shock angle ϵ as a function of M_{A} (dashed line). 39

2.5 Variation of the tangential velocity ratio as given by Equation 2.33 for two values of k (solid lines) and comparison with CFD results (×). 40

2.6 Loss breakdown obtained from calculation with *TurboSim* (ROM) and CFD. 44

2.7 Total-static efficiency of RITs as a function of $\bar{\gamma}_{Pv}$ for working fluids of different molecular complexity MC. $SP = 0.025$ m, while $VR = 6$, 20 and 80 from top to bottom. ψ_{is} is equal to 0.7, 1.0 and 1.3 from left to right, and $\phi_{2,\text{is}}$ was fixed to 0.4. The gray bands indicate a ±1% uncertainty interval around the arithmetic average. 46

2.8 Total-total (◯) and total-static (△) efficiency as a function of the load coefficient ψ_{is}, for different values of VR and for a fixed value of the flow coefficient $\phi_{2,is} = 0.4$. The markers indicate the average value of efficiency among the cases listed in Table 2.5, while the colored bands show the min-max variation of the efficiency for $\tilde{\gamma}_{Pv}$ that varies between 0.78 and 1.15. . 47

2.9 Total-total (◯) and total-static (△) efficiency as a function of the load coefficient ψ_{is}, for different values of $\phi_{2,is}$ and for a fixed value of the expansion ratio $VR = 20$. The colored markers indicate the average value of efficiency among the cases listed in Table 2.5, while the colored bands show the min-max variation of the efficiency for $\tilde{\gamma}_{Pv}$ that varies between 0.78 and 1.15. The black dots display the values of the maxima at different values of $\phi_{2,is}$ estimated by fitting the data with a 2nd order polynomial, shown with the dashed line. The black dashed curves are 2nd order polynomials fitting the optimal combinations of ψ_{is} and $\phi_{2,is}$. 48

2.10 Reduced $P-T$ diagram for MM showing γ_{Pv} contours and three paradigmatic expansions at $VR = 20$, and starting from the inlet conditions listed in Table 2.5, namely MMi (□), MMni1 (◯), and MMni2 (△). 49

2.11 Meridional flow path of the optimal designs A, B and C of Figure 2.9. The axial and radial coordinates are non-dimensionalized by the tip radius of case B. 50

2.12 Impeller absolute flow angles (α) and relative flow angles (β) for the A, B and C cases. 51

2.13 Stage (stator + impeller) loss breakdown for optimum designs A, B and C shown in Figure 2.9. The optimal work coefficients are, respectively, 1.15, 1.3 and 1.4. Results obtained for $VR = 20$. 51

2.14 Absolute Mach number at the outlet of the stator (◯) and relative Mach number at the outlet of the impeller (□) as a function of the load coefficient ψ_{is}, for the LMC, MMi, MMni1 and MMni2 cases listed in Table 2.5 at fixed $VR = 20$, $SP = 0.025$ m, and $\phi_{2,is} = 0.4$. 52

2.15 Cumulative stator (◯) and impeller (□) loss as a function of the load coefficient ψ_{is}, for the LMC, MMi, MMni1 and MMni2 cases listed in Table 2.5 at fixed $VR = 20$, $SP = 0.025$ m, and $\phi_{2,is} = 0.4$. 52

2.16 Loss breakdown in the stator (a) and the impeller (b) for the LMC and MMni2 cases listed in Table 2.5. $\psi_{is} = 1.35$, $\phi_{2,is} = 0.4$ and $VR = 20$. 53

2.17 Design maps showing the contours of total-total (a, b, c) and total-static (d, e, f) efficiency of turbines operating at $VR = 49.7$, and for increasing values of μ. The fluid is siloxane MM. The red markers in (b) and (e) highlights the design point and efficiency of the ORCHID turbine. 54

2.18 Optimal ψ (×) and ϕ_2 (△) as a function of VR, and corresponding maximum η_{tt} and η_{ts} as a function of VR. The blue markers indicate the duty coefficients that maximize η_{tt} and the red ones those that maximize η_{ts}. The results were obtained for the LMC, MMi, MMni1 and MMni2 cases listed in Table 2.5. 56

3.1 Simplified schematic of the ORCHID turbine stage flow path, including the cavity behind the impeller disk. The numbers correspond to the main sections along the streamwise direction of the machine. Solid lines indicate physical boundaries, short-dash lines indicate the leading and trailing edge sections of the stator vanes and impeller blades, and the diffuser outlet boundary. The long-dash line indicates the rotational axis, and the letters "h" and "s" indicate the impeller hub and shroud contours. Finally, the arrows indicate the direction of the flow, and the fill colors illustrate qualitatively the the flow temperature (red = hot, orange = warm, blue = cool). 66
3.2 Isentropic (or ideal) turbine expansion processes (A, B, C, D) in the reduced temperature-entropy diagram of siloxane MM. The reduced temperature and entropy are defined as $T_r = T/T_{cr}$ and $s_r = s/s_{cr}$, where the subscript cr refers to the vapor liquid critical point. The red dashed line indicates the critical isobar. The outlet static pressure of 0.44 bar is assumed the same for all the expansion processes. 67
3.3 ORCHID turbine off-design performance results. The line colors in the four figures correspond to the different rotational speeds considered, which were only reported in the legend of Figure 3.3a for brevity. In Figure 3.3a and 3.3b the circular markers indicate stator outlet conditions, whereas the triangular ones indicate the rotor inlet conditions. 69
3.4 Loss accumulated at 1) stator trailing edge, 2) impeller leading edge, and 3) impeller trailing edge. The isentropic static temperature at each section j, i.e., $T_{j,is}$, and the entropy difference (with respect to the reference entropy at the inlet 0' of the stage) Δs_{j-0} were computed by mass flow averaging the quantities at each section of interest. 71
3.5 Mach number contours at midspan (i.e., 50 % of local blade height) with superimposed flow streamlines (in white) for three operating points of the ORCHID turbine. The plot shows the absolute Mach number in the stationary domain (stator) and the relative Mach number in the rotary domain (impeller). 72
3.6 Normalized entropy contours at midspan (i.e., 50 % of local blade height) for three operating points of the ORCHID turbine. 73
3.7 Two stage e-compressor CS15. Image courtesy of *Aeronamic* [7]. 74
3.8 Rotorshaft configurations. 75
3.9 Assembly of a 125 kW RIT for low-temperature ORC industrial applications. Image courtesy of Yuksek & Mirmobin [8]. 76
3.10 Turbogenerator powertrain assembly of a 250 kW AXT for low-temperature ORC industrial applications. Image courtesy of Di Bella [10]. 76
3.11 Overview of different bearing types. (a) Passive and active magnetic journal bearings, (b) gas lubricated and gas-foil journal bearings, (c) liquid lubricated journal bearing. 78
3.12 Cross-sectional view of the REB cartridge chosen to support the ORCHID turbine rotor. Dimensions are in mm. 80
3.13 Lip seal representation taken from [34]. 81

3.14 ORCHID turbine cross-section, showing the main components and details of the oil delivery system. Red lines indicate the rotating parts. Details K and L are viewed from a cross-section rotated 90° with respect to J-J section. Components: shaft (A); bearings cartridge (B); turbine wheel (C); coupling flange (D); lock-nut (E); stainless steel thin-disk (F); contact lip seal on the impeller side (G); contact lip seal on the coupling side (H); non-contact gas seal (J). 82
3.15 Cross-section of the impeller blisk. 83
3.16 Impeller side (b) and front (c) view of the manufactured blisk in aluminum (the nose cone was not machined for simplicity). 84
3.17 ORCHID turbine gross torque at varying inlet pressure and rotational speed. 85
3.18 Free body diagram reporting the forces that contribute to the impeller net axial thrust F_{ax}. F_{bf} is the force exerted by the flow in the cavity behind the impeller disk on its backface, F_s is the shroud pressure force, and F_{out} is the reaction force to the outlet flow axial momentum. The main dimensions necessary for the computation of F_{bf} are indicated, namely $R_{LS,i}$ the labyrinth seal inner radius, R_{sh} the shaft outer radius, and R_1 the impeller disk outer radius. 86
3.19 Net axial thrust acting on the ORCHID turbine impeller for the operating conditions of Table 3.3. The quantity was plotted against the corrected mass flow rate $\dot{m}_{corr}$, allowing to generalize the fitting to different inlet conditions. The dashed curves represent a numerical fitting of the data. 87
3.20 Grid independence study for the 316L blisk. a) Plots of the stress, and b) plots of the directional deformations. 89
3.21 Von Mises stress contours for the 316L blisk. 90
3.22 Bearing power loss against shaft rotational speed on the horizontal axis, and the corrected mass flow rate on the vertical one. The white isolines indicate the power loss of row L in percentage. The three red markers indicate three operating conditions, specifically the on-design point ◯, the highest inlet pressure and temperature point △, and a low temperature and high pressure operating condition ×. 93
3.23 Frictional torques for bearing row L, on the left two plots, and R, on the right two plots. The solid lines indicate the speed dependent frictional torque M_0, while the dashed lines depict the load dependent torque M_1. . 94
3.24 Geometrical domain used for the steady-state thermal FEA of the ORCHID turbine. 95
3.25 Grid sensitivity analysis for the estimation of the ORCHID turbine thermal load to be dumped by the lubricant. 96
3.26 Cross sectional view of the tetrahedral mesh used to estimate the thermal load $\dot{Q}_{tot}$. 96
3.27 Cut-off of the rolling element bearing cartridge. 97
3.28 SFD pressure profile at midplane for $e_r = 0.25$ calculated with Equation 3.17. 99
3.29 SFD stiffness and damping direct coefficients at 100 krpm as a function of the relative rotor eccentricity (e_s/g) and of the relative orbit radius (e_r). . . 100

3.30 SFD dynamic coefficient range for several values of orbit radius and eccentricity. The gray shaded bands are used to account for the variation of coefficients with relative static eccentricities between 0 and 90 %, while the colored bands refer to the variation of rotordynamic coefficients with increasing relative orbit radii between 5 and 85 % assuming a centered rotor. The dashed back lines indicate the average value. 101

3.31 Geometry of the PGS showing the main dimensions in mm. 103

3.32 Computational domain used for the CFD flow simulations of the PGS. The employed boundary conditions are also indicated. The flow through the geometry of the gap between the shaft outer surface and the PGS inner surface is modeled. 103

3.33 Leakage massflow rate through the PGS as a function of the radial clearance. Comparison between CFD results (×) against predictions with the Egli equation (solid line). 105

3.34 Stiffness (left) and damping (right) coefficients computed with CFD simulations. Dotted lines are linear fits used as input for the rotordynamic analysis. 106

3.35 Cross-coupled stiffness coefficient k_{xy} (y-axis) computed using the Wachel method of API 617 (solid lines), the modified Wachel formula for siloxane MM (dashed lines) and the numerical correlation of Moore & Ransom (dotted lines) as a function of the stage inlet total pressure (x-axis) for three rotational speeds, namely 80, 98, and 120 krpm. 107

3.36 Schematic representation of the rotordynamic model showing the mass distribution of the rotor discretized using disks. The locations where the most important rotordynamic coefficients have been applied as lumped parameters are shown by means of yellow arrowheads. These include the REB stiffness, the SFD damping, the PGS stiffness and damping and the impeller FSI stiffness. The residual unbalance computed as per ISO 1940-1:2003 [64] standard is indicated by the red dot, while the coupling disk and the impeller blades lumped masses are indicated by the blue dots. x- and y- axes allow to evaluate the dimensions in mm of the rotor. 108

3.37 Campbell diagram of the ORCHID turbine rotor. The solid lines indicate the damped natural frequencies associated to each vibration mode up to 5000 Hz. Dotted oblique lines represent synchronous and super-synchronous excitation frequencies with respect to the shaft speed. Black dots represent critical speed crossings, occurring if the excitation frequency matches the damped natural frequency of any of the modes. Only intersections involving the 1X and 2X shaft excitations are considered for this preliminary analysis. 110

3.38 Mode shapes at the critical speeds reported in Table 3.14. The solid blue line represents the shaft center line, while the red line indicates the cartridge outer ring center line. Orbits described by the two center lines are represented in grey. 111

3.39 On the left, Campbell diagram of the rotor system as a function of shaft speed. The colored bands indicate the impact of a varying bearing stiffness in an interval ±30% of the nominal value given by Hertz contact theory. On the right, system natural frequencies as a function of the bearing stiffness at the nominal speed of 100 krpm. 112
3.40 System natural frequencies (left) and stability map (right) as a function of the multiplying coefficient η of stiffness cross-terms at $n = 100$ krpm. The colored bands indicate the impact of a varying bearing stiffness in an interval ±30% of the nominal value given by Hertz contact theory. 112

4.1 P&ID diagram of the ORCHID setup, figure courtesy of [1]. 126
4.2 CAD drawing of the balance of plant of the ORCHID setup, figure courtesy of [1] and adapted for the current use. 127
4.3 P&ID of the ORCHID turbine test bed. The P&ID diagram was realized by Paul Straatman and refashioned by the author of this dissertation for illustrative purposes. 130
4.4 Side and front views of the emergency sliding gate valves with piston actuator (VE102A/B) [5], and its main dimensions (for standard pipes DN50). The valve positioner is not shown. 132
4.5 Side and front cross-section views of the control sliding gate valve with diaphragm actuator (V101) [4], and its main dimensions (for standard pipes DN50). The valve positioner reported here is different than the intended one. The layout of V103 is identical to the one represented in this figure, however with larger dimensions. 133
4.6 Single pass liquid-liquid plate heat exchanger, image courtesy of [7]. . . . 134
4.7 ORCHID turbine complete powertrain. The indicated dimensions are in mm. 135
4.8 Cross-sectional view of the coupling mechanism. 136
4.9 Coupling flange. 136
4.10 Coupling shaft. 136
4.11 One quarter cross-section of the ORCHID turbine assembly. 137
4.12 Cross-section of the ORCHID turbine rotor assembly. 138
4.13 Cross-sectional view of the rolling element bearings cartridge by [3]. Dimensions are in mm. 139
4.14 Dynamic viscosity of ISO VG32 and Siloxane MM as a function of temperature. The viscosity of MM was obtained via the dedicated REFPROP [8] fluid library. 139
4.15 Power loss in the bearings (a) and maximum lubricant temperature at the outlet of the bearing housing (b) considering a lubricant feed rate of 1 L min^{-1}, at an initial temperature of 50 °C. 140
4.16 Direct damping coefficient for centered squeeze-film damper ($e_s = 0$) computed using Equation 4.2. (a) ORCHID turbine initial design with ISO VG 32 oil, and (b) ORCHID detailed design with liquid MM as lubricant. The lubricant feed rates have been fixed equal to 1 L min^{-1}, and an inlet temperature of 50 °C was considered for both cases. 141

4.17 Top: plot of the blade root section in the blade-to-blade plane for the initial and the final impeller geometry. Bottom: blade thickness distribution along the meridional direction. 142
4.18 Cross-sectional view of the Von-Mises stress contours in the initial impeller wheel design (a) and the final design (b). The contours of (a) were rescaled to the minimum and maximum values of (b), to facilitate the comparison of the stress fields. 143
4.19 View of the DC converter module with main dimensions (mm), and working curve characteristic (Vdc vs. A). 145
4.20 Schematic of the SCADA system for control and acquisition. More details about this system can be found in [1], Section 5.5. Compared to the SCADA system of the ORCHID reported in [1], signals directed to and arriving from the turbine test bed are handled by a separate NI cRIO 9149 card. The card communicates with the ORCHID I/O controller via Ethernet cable, whereas the instruments and sensors are interfaced to the NI 9149 card via fieldbus. A high voltage line brings the power converted by the generator to the DC-AC converter (SM15K), which is then routed to the HTT heater. 145
4.21 ORCHID turbine efficiency as a function of the reduced mass flow rate and at different rotational speeds. The markers are the average values of the efficiency at each operating point. The darker bands indicate the propagated uncertainty calculated assuming the actual uncertainty of the A/D signal conversion for NI9208 card 1. The lighter bands indicate the propagated uncertainty calculated assuming the uncertainty of the A/D signal conversion for NI9208 specified by the manufacturer. 152
4.22 ORCHID turbine power as a function of the reduced mass flow rate and at different rotational speeds. The markers are the average values of the efficiency at each operating point. The darker bands indicate the standard uncertainty calculated as per the second term on the right hand side of Equation 4.7. The darker bands indicate the propagated uncertainty calculated assuming the actual uncertainty of the A/D signal conversion for NI9208 card 1, while the lighter bands by assuming the A/D signal conversion uncertainty specified by the manufacturer. 153

1 Appendix: Sankey diagram of a modern aircraft showing the breakdown of the input fuel LHV. 176
2 Appendix: Iterative routine implemented in *TurboSim* for sizing a RIT stage. 179

List of Tables

2.1 Entropy change across a normal shock in a flow through a planar nozzle calculated with an inviscid 2D CFD model and comparison with the solution of the RH equations. In both cases, the pre-shock conditions are $P_A = 2.93\ bar$ and $M_A = 1.84$ and the fluid is Siloxane MM. 39

2.2 Boundary conditions and fluid models used in the uRANS simulations. The thermodynamic conditions of the MM fluid have been computed using a look-up table (LUT) method. The LUT has been generated using the multi-parameter equation of state (MEoS) [33] implemented by Huber *et al.* [17]. 42

2.3 Turbine performance prediction obtained with the ROM, CFD and experiments. The experimental data are available for the T100 only. 43

2.4 Fluids used to generate the data displayed in Figure 2.7 and their main characteristics. 46

2.5 Boundary conditions for the turbine operating with the LMC and the HMC (siloxane MM) fluid. MMi denotes siloxane MM in ideal gas conditions, while MMni1 and MMni2 refer to MM conditions in the nonideal thermodynamic regime. 47

3.1 Main design variables and geometrical constraints for the design of the ORCHID turbine stage by De Servi *et al.* [1]. 65

3.2 Main geometrical characteristics and calculated performance of the ORCHID turbine stage by De Servi *et al.* [1]. 66

3.3 Operating points selected for the off-design performance assessment of the ORCHID turbine. 68

3.4 Summary of ORC turbogenerator units and their main characteristics. . . 77

3.5 Data of the REB cartridge. Static and dynamic load capacities are intended for a single bearing row. 80

3.6 Absolute value of the force components in the axial force balance at OP7, computed with the hybrid method [37] and with CFD. 88

3.7 Properties of 316L and Ti64 at ambient temperature from Ansys® Mechanical [38] material database. 88

3.8 Results of the finite element simulations on the blisk assuming different materials. 91

3.9 Coefficients and geometrical parameters used for the calculation of the frictional torque M defined as per Equation 3.14. 92

3.10 Comparison of dynamic coefficients for different seal types. LS: Labyrinth Seal, FPDS: Fully-partitioned Pocket Damper Seal, and HS: Honeycomb Seal. 102
3.11 Boundary conditions for gas seal CFD simulations. 104
3.12 Comparison of seal dynamic coefficients calculated with CFD and with a simplified model. 106
3.13 Constant direct stiffness and damping coefficients used in the rotordynamics calculation. The stiffness was computed using Hertz contact theory and the value reported is the average throughout the range of rotational speed investigated. It was assumed $k_{yy}^{REB} = k_{xx}^{REB}$ and $c_{yy}^{REB} = c_{xx}^{REB}$. 109
3.14 Critical speed and damping ratio of several modes crossing the 1X and 2X shaft excitation frequency. 110

4.1 Inertia about the rotation axis of the components of the powertrain. The values of the inertia of different components were computed using a CAD modeling software, considering the properties of the materials of each component. The turbine rotor rotor inertia was computed considering an assembly consisting of the impeller, the turbine shaft, the lock nut, the piston rings, and the inner raceway of the bearings. The value of inertia for the generator rotor was provided by the manufacturer. 131
4.2 Plate heat exchanger HX301 specifications and design point characteristics provided by the manufacturer [7]. 134
4.3 Data of the rolling element bearings cartridge. Static and dynamic load capacities are intended for a single bearing row. 139
4.4 Results of the FEA of the modified impeller wheel, and of the stator-rotor CFD analysis including the final impeller blade design. The stator model was not changed compared to that of Chapter 3. 142
4.5 List of instruments and their specifications used for control and monitoring of the ORCHID turbine. 146
4.6 Accuracy and standard uncertainty of the instruments in Table 4.5. The temperature T is measured in °C, while the mass flow rate $\dot{m}$ is measured in $kg\,h^{-1}$. 148
4.7 Correlation coefficients used in the uncertainty propagation model. The coefficients were computed with Pearson's formula using data obtained from the off-design CFD simulations of the ORCHID turbine documented in Section 3.2. 151

1 Appendix: Values of the turbine design parameters and loss coefficients used in Chapter 2. 180
2 Appendix: List of the auxiliary components selected to operate the ORCHID turbine test section, and related information. 181

SUMMARY

The ongoing environmental crisis has accelerated the development of radical new technologies that aim at decreasing, and possibly eliminate in the future, the carbon footprint across the industrial spectrum. Reuse and waste management are at the forefront of this transformation and enable prolonging the life-cycle of valuable raw materials, reducing the energy consumption of industrial processes, and abating the emissions related to operation of prime movers for commercial transportation and freights. Organic Rankine cycle (ORC) power systems for the conversion of thermal energy into electricity, at temperatures ranging from ≈ 120 °C to > 500 °C and with a power capacity from few to tens MW, are commercially available and employed to obtain CO_2-free electricity from geothermal reservoirs, industrial waste heat, the exhaust of gas turbines and stationary internal combustion engines, and the combustion of biomass. However, the market potential of high-temperature and high efficiency ORC systems with power output up to several hundreds kW is arguably very large. Suitable working fluids for these cycles are made of complex molecules, and therefore the speed of sound of the expanding organic vapor is of the order of tens m/s and the flow within a single-stage radial-inflow turbine – which is often selected as an optimal compromise between operating costs, which are related to its efficiency, and investment costs, which are instead more intimately linked to its size and complexity – is bound to be highly supersonic. Its design is thus challenging not only from the fluid dynamic point of view, but also because of many other aspects related to high rotational speed, sealing and bearings technology, and rotordynamics. These high-speed machines are the ideal expander type for low-capacity systems in which $T_{source} \leq 550$ °C, such as long-haul trucks (≈ 10-30 kW), shipping vessels (≈ 100-500 kW), and aircraft (≈ 100-500 kW).

This dissertation documents work performed as part of the ARENA project, whose objective is the estimation of aircraft performance including combined-cycle propulsion systems making use of organic Rankine cycle for onboard thermal energy recovery. The first objective of this dissertation is to advance the current knowledge regarding the optimal design of supersonic radial-inflow turbines for such applications. The second goal is to design a prototype turbogenerator and integrate it within a test bed for the ORCHID, whose main purpose is the generation of data for verification and validation of supersonic RITs, and in the future to serve as an open test case for advanced R&D on propulsion and power technologies. The first main contribution of this work to the research field of high-temperature ORC turbines is the formulation of novel preliminary design guidelines for radial-inflow turbines, obtained with *TurboSim*, a preliminary design code written in *Python* which was extended to analyze the impact of critical turbine design parameters on losses and efficiency. The results were used to formulate best practices for selecting stage duty coefficients that maximize expander efficiency, including the effect of the volumetric flow ratio and of the isentropic pressure-volume exponent to

account for the impact of nonideal thermodynamic effects on expander performance, which was not accounted for in previous tools. The tool was used within the ARENA project to perform the preliminary design, and estimate the efficiency and weight, of RIT for combined-cycle turboshaft and turbofan engines for novel hybrid-electric aircraft. The second main contribution is the design and realization of a test facility for supersonic radial-inflow ORC turbines, whose detailed design process to select the turbogenerator layout, its main components, and the specifications of the assembly and its individual parts are developed and applied in this dissertation. The test bed, featuring a supersonic RIT for high-temperature ORC systems of low power capacity ($\approx$ 10 kW), will enable measurements of the fluid dynamic efficiency of high-pressure ratio RITs, and the assessment of the impact of design choices (e.g., vane count, impeller blade shape, tip clearance) on turbine performance. The results of the experimental campaigns could also provide knowledge applicable to other types of radial turbines and supersonic turbomachinery, such as turbines for rocket engines and expanders to drive fuel cell turbocompressors. Research on oil-free gas bearings and seals is also possible and highly relevant, and the powertrain assembly which couples the turbine to a high-speed electric machine for braking power will facilitate research and development of next-generation high-speed electric generators—a critical technology for more electric and all-electric aircraft.

SAMENVATTING

De aanhoudende klimaatproblematiek heeft de ontwikkeling van radicaal nieuwe technologieën versneld, die gericht zijn op het verkleinen en mogelijk in de toekomst elimineren van de ecologische voetafdruk in de hele industriële sector. Hergebruik en afvalbeheer staan centraal in deze transformatie en maken het mogelijk de levenscyclus van waardevolle grondstoffen te verlengen, het energieverbruik van industriële processen te verminderen en de uitstoot die vrijkomt bij primaire aandrijfsystemen in commercieel transport en vrachtvervoer te beperken. De omzetting van thermische energie in elektriciteit bij temperaturen variërend van ongeveer 120 °C tot meer dan 500 °C, met een vermogenscapaciteit van enkele tot tientallen megawatt, is commercieel beschikbaar via energiesystemen op basis van de organische Rankine-cyclus (ORC). Deze systemen worden ingezet voor de opwekking van CO_2-vrije elektriciteit uit geothermische bronnen, industriële restwarmte, uitlaatgassen van gasturbines en stationaire verbrandingsmotoren, evenals uit de verbranding van biomassa. Het marktpotentieel van ORC-systemen met een vermogen tot enkele honderden kilowatt, opererend met hoge temperaturen en hoge efficiëntie, is naar verwachting zeer groot. Geschikte werkvloeistoffen voor deze cycli bestaan uit complexe moleculen, waardoor de geluidssnelheid van de expanderende organische damp in de orde van tientallen meters per seconde ligt. De stroming in een eentraps radiale instroomturbine (RIT) — die vaak wordt gekozen als een optimaal compromis tussen operationele kosten (gerelateerd aan het rendement) en investeringskosten (die voornamelijk afhangen van de grootte en complexiteit) — is daardoor sterk supersonisch. Het ontwerp van dergelijke turbines is dus niet alleen een uitdaging vanuit vloeistofdynamisch oogpunt, maar ook vanwege andere aspecten, zoals de hoge rotatiesnelheid, afdichting- en lagertechnologie, en rotordynamica. Deze hogesnelheidsmachines zijn het ideale type expansiemachine voor systemen met laag vermogen, waarbij $T_{\text{source}} \leq 550$ °C, zoals langeafstandsvrachtwagens (≈10-30kW), schepen (≈100-500kW) en vliegtuigen (≈100-500kW).

Dit proefschrift documenteert het werk dat is uitgevoerd als onderdeel van het ARENA project, waarvan het doel is om de prestaties van vliegtuigen te schatten die gebruik maken van gecombineerde cyclus-aandrijfsystemen met behulp van de organische Rankine-cyclus voor de terugwinning van thermische energie aan boord. Het eerste doel van dit proefschrift is het bevorderen van de huidige kennis over het optimale ontwerp van supersonische radiale instroomturbines voor dergelijke toepassingen. Het tweede doel is het ontwerpen van een prototype turbogenerator en deze te integreren in een nieuwe testopstelling binnen de ORCHID. Het belangrijkste doel van deze testopstelling is om data te genereren voor de verificatie en validatie van supersonische RIT's, en in de toekomst te dienen als een testopstelling voor geavanceerd onderzoek naar voortstuwing- en energietechnologieën. De eerste belangrijke bijdrage van dit werk aan het onderzoeksveld van hogetemperatuur-ORC-turbines is de formulering van nieuwe richtlijnen

voor het voorlopige ontwerp van radiale instroomturbines. Deze richtlijnen zijn verkregen met TurboSim, een voorlopig ontwerpprogramma geschreven in Python, dat verder is ontwikkeld om de impact van essentiële turbine-ontwerpparameters op verliezen en efficiëntie te analyseren. De resultaten zijn gebruikt om richtlijnen op te stellen voor het selecteren van trapbelastingcoëfficiënten die de efficiëntie van de turbine maximaliseren. Hierbij is rekening gehouden met de invloed van de volumestroomverhouding en de isentropische druk-volume-exponent om de impact van niet-ideale thermodynamische effecten op de prestaties van de turbine te modelleren, wat in eerdere tools niet werd meegenomen. De tool werd binnen het ARENA-project gebruikt voor het voorlopige ontwerp en de schatting van de efficiëntie en het gewicht van RIT's voor gecombineerde cyclus turboshaft- en turbofanmotoren voor nieuwe hybride-elektrische vliegtuigen. De tweede belangrijke bijdrage is het ontwerp en de realisatie van een testfaciliteit voor supersonische radiale instroom ORC-turbines. In dit proefschrift wordt het gedetailleerde ontwerpproces beschreven voor de selectie van de turbogeneratorconfiguratie, de hoofdcomponenten en de specificaties van de assemblage en de afzonderlijke onderdelen van deze testfaciliteit. De testopstelling, met een supersonische RIT voor hogetemperatuur-ORC-systemen met een laag vermogen (≈10kW), maakt het mogelijk om metingen uit te voeren van de vloeistofdynamische efficiëntie van RIT's met een hoge drukverhouding en om de impact van ontwerpkeuzes (zoals het aantal schoepen, de vorm van de waaierbladen en de tipspeling) op de turbineprestaties te beoordelen. Onderzoek naar olievrije gaslagers en afdichtingen is eveneens mogelijk en uiterst relevant. Daarnaast zal de aandrijflijnassemblage, die de turbine koppelt aan een elektrische machine voor remvermogen, het onderzoek en de ontwikkeling van de volgende generatie hogesnelheidsgeneratoren faciliteren—een cruciale technologie voor meer elektrische en volledig elektrische vliegtuigen.

NOMENCLATURE

Roman Symbols

$\ddot{\boldsymbol{x}}$	Second time derivative of $\boldsymbol{x}$ [m/s^2]
$\dot{\boldsymbol{x}}$	First time derivative of $\boldsymbol{x}$ [m/s]
$\boldsymbol{x}$	Vector of spatial coordinates [m]
$\dot{m}$	Mass flow rate [kg/s]
$\dot{Q}$	Thermal power [kW]
$\dot{W}$	Power [W]
$\dot{x}$	Horizontal displacement rate in Cartesian coordinate system [m/s]
$\vec{G}$	Array of geometrical scaling parameters [–]
A	Area [m^2]
a	Accuracy [varies]
b	Blade height or span [m]
B_c	Fluid dependent coefficient in the Wachel formula (MW / 10) [–]
c	Blade chord [m] or Damping coefficient [N·s/m]
c_{eff}	Effective damping coefficient ($c - k/\omega$) [N·s/m]
C_D	Dissipation coefficient [–]
C_r	Radial tip leakage parameter [–]
C_x	Axial tip leakage parameter [–]
$C_{P_b,\text{eff}}$	Effective base pressure coefficient [–]
D	Diameter [m]
D_H	Hydraulic diameter [m]
D_s	Specific diameter [–]
E	Energy [J] or Energy factor in loss model [–] or Young's modulus [GPa]
e	Rotor orbit radius [m]
e_r	Relative rotor orbit radius (e/g) [–]
e_s	Static rotor eccentricity [m]

F	Force [N]
g	Cascade pitch [m] or SFD / PGS radial clearance [μm]
H	Shape factor in boundary layer model [–]
h	Specific enthalpy [J/kg] or Lubricant film thickness [m] or Damping ratio [-]
I_z	Polar inertia about the rotation axis [kg/mm^2]
k	Empirical constant in friction coefficient [–] or Stiffness coefficient [N/m] or Coverage factor [–]
K_p	Empirical coefficient for impeller passage loss model [–]
K_r	Radial discharge coefficient for impeller tip leakage loss model [–]
K_x	Axial discharge coefficient for impeller tip leakage loss model [–]
K_{xr}	Axial-radial discharge coefficient for impeller tip leakage loss model [–]
L	Length [m]
L_H	Hydraulic length [m]
LHV	Lower heating value [J/kg]
M	Mach number [–] or Torque [Nm]
MC	Molecular complexity [–]
MW	Molecular weight [kg/kmol]
N	Blade count [–]
n	Rotational speed [rpm or krpm]
P	Pressure [Pa]
P_b	Base pressure [Pa]
Q	Critical kinetic energy ratio in loss model [–]
R	Radius or radial direction in cylindrical coordinate system [m] or Gas constant [J/(kg·K)]
s	Specific entropy [J/(kg·K)]
SF	Safety factor [–]
SP	Size parameter [m]
T	Temperature [K]
t	Trailing edge thickness [m] or Time [s]
U	Peripheral speed [m/s]
u	Deformation [mm] or Uncertainty [varies]

V	Absolute velocity [m/s]
v	Specific volume [m^3/kg]
W	Relative velocity [m/s]
w	Euler work [J/kg]
x	Horizontal coordinate/displacement in Cartesian coordinate system [m]
y	Vertical coordinate/displacement in Cartesian coordinate system [m]
Z	Compressibility factor [–]
z	Axial coordinate/displacement in Cartesian and cylindrical coordinate system [m]

Greek Symbols

α	Absolute flow angle [deg]
$\bar{\gamma}_{Pv}$	Average isentropic pressure-volume exponent along expansion [–]
β	Relative flow angle [deg] of Fluid bulk modulus [Pa]
Δ	Variation (difference) in quantity magnitude [varies]
δ	Flow deviation [deg]
δ^*	Boundary layer displacement thickness [m]
$\dot{\omega}$	Angular acceleration [rad/s^2]
ϵ	Shock angle [deg]
ϵ_r	Radial tip gap [m]
ϵ_x	Axial tip gap [m]
η	Efficiency [–] or First LCP variable [kg/m^3]
γ	Ratio of specific heats (isentropic exponent for ideal gases) [–]
γ_{Pv}	Local isentropic pressure-volume exponent for dense gases [–]
μ	Impeller meridional velocity ratio (outlet/inlet) [–] or Dynamic viscosity [Pa·s]
ν	Impeller radius ratio (outlet/inlet) [–] or Kinematic viscosity [mm^2/s]
ω	Angular speed [rad/s] or Frequency [Hz]
ω_0	Natural frequency [Hz]
∂	Infinitesimal variation in quantity magnitude [varies]
ϕ	Flow coefficient [–]
ψ	Work coefficient [–]
ρ	Density [kg/m^3] or Cross-correlation factor [–]

σ	Slip factor [–] or Stress [MPa] or Standard deviation [varies]
σ_y	Yield strength of the material [MPa]
τ	Time step [s]
θ	Boundary layer momentum thickness [m] or Tangential direction in cylindrical coordinate system [rad]
ξ	Impeller cone angle [rad] or Second LCP variable [kg/m^3]
ζ	Loss coefficient [–]

Subscripts

θ	Tangential direction
x	x direction
y	y direction
z	z direction
0	Turbine inlet section
1	Stator outlet section
2	Impeller inlet section
3	Impeller outlet section
4	Diffuser outlet section
A	Pre-shock
ax	Axial
B	Post-shock
bf	Backface
cr	Critical
ew	Endwall
f	Fuel or fluid
g	Geometric
h	Hub
imp	Impeller
in	Inlet
is	Isentropic
leak	Leakage
m	Meridional or mid-span

mo	Mixedout
mx	Mixing
out	Outlet
pass	Passage
prof	Profile
r	Reduced or Radial
s	Shroud
sen	Sensor
sh	Shock or shaft
st	Stator
t	Total
ts	Total-static
tt	Total-total
turb	Turbine
vM	von Mises
w	Relative frame of reference

Superscripts

*	Normalized
R	Rotary domain
S	Stationary domain

Acronyms

hiTORC-RIT	High-temperature ORC radial-inflow turbine
TurboSim	Python-based preliminary turbine design tool
A/D	Analog/Digital
AC	Alternating Current
APU	Auxiliary Power Unit
ARENA	AiRborne thermal ENergy harvesting for Aircraft
BoP	Balance of Plant
CC	Combined Cycle
CC-TF	Combined-Cycle Turbofan

CC-TS	Combined-Cycle Turboshaft
CFD	Computational Fluid Dynamics
cRIO	compact RIO
DAQ	Data Acquisition
DC	Direct Current
DN	from French "Diametre Nominal"
ECU	Electronic Control Unit
EFC	Effective Fuel Consumption
EIS	Entry Into Service
EoS	Equation of State
FEA	Finite Element Analysis
FPDS	Fully Partitioned Damper Seal
FPT	Free Power Turbine
FS	Full Scale
FSI	Fluid Structure Interaction
GB	Gas Bearings
GFB	Gas Foil Bearings
GT	Gas Turbine
HEX	Heat Exchanger
HMC	High Molecularly Complex (fluid)
HPT	High Pressure Turbine
HS	Honeycomb Seal
HySIITE	Hydrogen Steam Injected Intercooled Turbine Engine
I/O	Input/Output
ICAO	International Civil Aviation Organization
LMC	Low Molecularly Complex (fluid)
LPT	Low Pressure Turbine
LS	Labyrinth Seal
LUT	Look-Up Table
MC	Molecular Complexity

MDM Octamethyltrisiloxane

MEoS Multiparameter Equation of State

MM Hexamethyldisiloxane (Siloxane MM)

MM Hexamethyldisiloxane

NI National Instruments

NICFD Non-Ideal Compressible Fluid Dynamics

OD Outer Diameter

OP Operating Point

ORCHID Organic Rankine Cycle Hybrid Integrated Device

P&ID Process and Instrumentation Diagram

PGS Pocket Gas Seal

PTFE Polytetrafluoroethylene

REB Rolling Element Bearings

RH Rankine–Hugoniot

RISE Revolutionary Innovation for Sustainable Engines

RIT Radial-Inflow Turbine

ROI Return on Investment

ROM Reduced Order Model

SAF Sustainable Aviation Fuel

SFD Squeeze Film Damper

SI Système International (International System of Units)

SST Shear Stress Transport

TFD Turbomachinery and Fluid Dynamics Institute

Ti64 Titanium alloy grade Ti6Al4V-T6

uRANS Unsteady RANS

WET Water-Enhanced Turbofan

WHR Waste Heat Recovery

1

INTRODUCTION

1

1.1. CONTEXT AND BACKGROUND

Organic Rankine cycle (ORC) power systems for the conversion of thermal energy into electricity, at temperatures ranging from ≈ 120 °C to > 500 °C and with a power capacity from few to tens MW, are commercially available and employed to obtain CO_2-free electricity from geothermal reservoirs, industrial waste heat, the exhaust of gas turbines and stationary internal combustion engines, and the combustion of biomass. The expander is most often a high-efficiency multistage axial turbine, which has reached technological maturity.

The commercial potential for smaller capacity ORC power plants is arguably very large, and ORC systems generating hundreds of kW of electricity and adopting either a radial-inflow turbine or a volumetric scroll expander have more recently been deployed. Turbines are an attractive technical solution, but even with the selection of a suitable working fluid, the isentropic efficiency of small turboexpanders is bound to be negatively affected by scaling effects. Economic and technical complexity constraints often drive the choice of a single-stage radial-inflow turbine.

Small-capacity ORC power plants available on the market feature relatively low thermal efficiency because volumetric machines cannot be designed for expansion ratios in excess of approximately 7. The limitation of the expansion ratio implies a relatively low value of the expander inlet temperature (≈ 150 – 170 °C). The comparatively low thermal efficiency of these systems often negatively affects their economic viability. As far as turbines are concerned, if supersonic flow is to be avoided, the expansion ratio is also limited to similar values. Conversely, for high expander inlet temperatures ranging from 200 °C to ≈ 350 °C, the expander is bound to be a supersonic turbine, whose fluid dynamic design is critical for achieving high conversion efficiencies. For a more extensive treatment of these aspects, see the review article of Colonna *et al.* [1].

Scarce public technical information is available on low-temperature and low-capacity commercial ORC power plants. In the recent past, a U.S. company [2] developed a system based on a hermetic assembly containing a radial-inflow turbine and permanent magnet generator on the same shaft supported by magnetic bearings [3]. The 125 kW unit was tested as a bottoming unit of a 31.6 MW marine vessel diesel generator recovering thermal energy from the 85 °C water of the cooling jackets. The working fluid was R245fa, the expander pressure ratio was small – about 3.6 at the design point – and the measured isentropic efficiency at the nominal rotational speed of 16.5 krpm was 89.1 %. Another U.S. company [4] developed a 250 kW fully sealed ORC turbogenerator unit [5] also featuring magnetic bearings and operating with R245fa as working fluid. The proposed application was the conversion of thermal energy from the condensing steam of many industrial processes, which is commonly at approximately 140 °C . The 3-stage axial impulse turbine ran at 20 krpm with a maximum pressure ratio of 7. The expander efficiency was not determined, but during the development tests the overall conversion efficiency of the ORC power plant was in excess of 12 % at the maximum turbine inlet pressure of 19.7 bar. Also several European companies from France [6], Germany [7], Spain [8], Italy [9] and Sweden [10] have commercialized low-temperature small-capacity ORC power plants, however no public detailed technical information is available.

1.1.1. THERMAL ENERGY HARVESTING FROM PROPULSIVE ENGINES

The market potential of high-temperature and high efficiency ORC systems with power output up to several hundreds kW is arguably very large. Financial viability would greatly improve compared to lower temperature systems because of the higher conversion efficiency, which in turn lowers the initial investment that is largely dependent on the cost of the heat transfer surfaces of the heat exchangers. Applications include waste heat recovery from engines (gas turbines, internal combustion engines, and in the future high-temperature fuel cells) both stationary and propulsive (automotive, naval, and in the future possibly aeronautical), and industrial waste heat recovery.

However, suitable working fluids for these cycles are made of complex molecules [1], therefore the speed of sound of the expanding organic vapor is of the order of tens m/s and the flow within a single-stage radial-inflow turbine is bound to be highly supersonic. Its design is thus challenging not only from the fluid dynamic point of view, but also because of many other aspects related to high rotational speed, sealing and bearings technology, and rotordynamics.

To the knowledge of the author, the only small-capacity high-temperature / high efficiency ORC power plant on the market is commercialized by a Dutch company [11]. The power capacity is approximately 150 kW and toluene was selected as the working fluid. The turbine, electrical generator and feed-pump are contained in a hermetically sealed assembly and liquid toluene is used to lubricate the bearings of the high-speed rotor, which is displayed in Figure 1.1.

Figure 1.1: Photograph of the high-temperature low capacity ORC turbogenerator rotor commercialized by a Dutch company. The purely radial expander wheel is visible on the left end of the generator shaft, and one half of the disassembled stator ring rests on the table top. Courtesy of Triogen [11].

The turbine configuration is rather unique, in that the flow direction is radial both at the inlet and at the outlet, and it is equipped with a radial-to-axial diffuser which, however, negatively affects fluid dynamic performance. The expander is designed to operate at 25.8 krpm, the nominal turbine inlet temperature is 317 °C, the inlet pressure is 32.1 bar, the design back pressure is 0.292 bar, leading to a highly supersonic flow in the stator

($M \approx 2.5$) and a pressure ratio of about 110 [12–15]. The overall system efficiency is not reported, but it can be deduced that it is approximately double that of low-temperature systems of the same capacity.

The concept of waste heat recovery from internal combustion engines of trucks with ORC systems is not new, and was investigated from a techno-economic point of view within both European [16, 17] and U.S. [18] publicly funded projects. However, the economic viability of such a system is strictly dependent on the return on investment (ROI) period, which for freight companies must be short (i.e., 3 to 5 years) to cope with rapid turnover rate of their trucks[1].

Considering the marine freight industry, a techno-economic study [19] found that the viability of thermal energy recuperation and re-use on large marine vessels is mostly dictated by the fuel price. The onboard waste heat recovery unit can therefore have a negative financial impact during periods when fuel prices drop significantly, and especially if one considers that most marine engine are fueled by cheap low grade fossil oils [20, 21] whose price is typically lower than that of higher grade fuels such as diesel and LNG.

In the commercial aviation and air freight industry, aircraft typically remain operational for at least 15 to 25 years, and jet fuel is approximately twice as expensive as heavy fuel oil used in ships [22]. These features could favor the adoption of ORC systems for heat recovery from engines and onboard thermal management in the more electric aircraft of the future, despite their technical and financial viability remain strongly dependent on the attainable fuel savings. The increased complexity of the power plant, as well as the added weight and drag penalty due to the additional components, can limit the benefits brought about by their integration into the propulsion system.

In the coming decades, aviation is expected to remain one of the most challenging transport sectors when it comes to achieving climate neutrality. In 2018, aviation was responsible for the generation of 2.4% of the entire CO_2 emissions worldwide [23]. Between 1960 and 2019, the amount of passengers traveling by air every year increased from 100 million to 4.56 billion, nearly as much as a 50-fold increase [24]. The International Civil Aviation Organization (ICAO) has estimated that air transport passengers demand will continue to grow at a rate of 6% annually [25], with a projected 3-fold increase in global emissions related to the commercial aviation sector by 2050 [23], should the environmental footprint of modern aviation not change drastically over the next few decades. For a brief overview of aviation emissions related to aircraft operation, see the Appendix A.

1.1.2. PROPULSION TECHNOLOGY FOR CLIMATE NEUTRAL AVIATION

Aircraft technology has already undergone much steady evolutionary improvements over its history. Figure 1.2 shows the historical trend of certified fuel consumption decrease for aircraft and gas turbine engines between the end of the 1950s and the 1990s. The aircraft effective fuel consumption per passenger seat (i.e., EFC seat) has plummeted

[1] It can be easily demonstrated that the break even time of long-haul trucks is ≤ 3 years.

beyond −70 % in less than 5 decades and much of this improvement is attributed to the increase in gas turbine efficiency, which alone accounts for −40 % of the EFC savings.

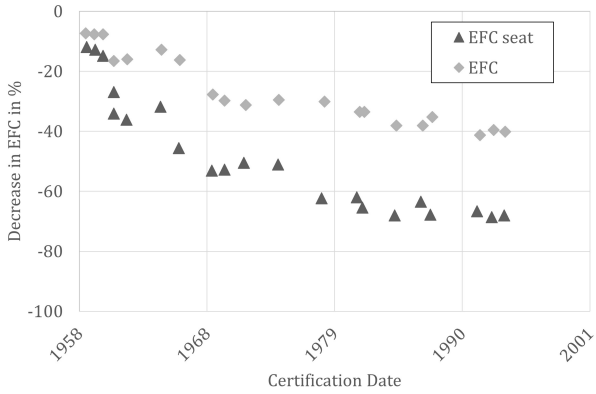

Figure 1.2: Trend of effective fuel consumption (EFC) and fuel consumption per seat certified between 1958 and 1994. Note that engines can be operational for 10 to 20 years from the entering-into-service date, hence engines certified in the 1990s were likely to be still operational between 2005 and 2015. Figure adapted from [26].

Technological developments, such as novel advanced materials, and aerodynamic and structural optimization, have led to ever higher gas turbine efficiency. State-of-the-art gas turbine systems reach efficiencies in excess of 40 % with a simple Joule-Brayton cycle configuration, which increases to more than 60 % if stationary combined-cycle power plants are considered [26].

Several R&D programs are ongoing worldwide with the aim of developing the next-generation of gas turbine-based propulsion systems. The Revolutionary Innovation for Sustainable Engines (RISE) is a CFM program[2] whose goal is to develop an highly efficient open rotor turbofan engine that can increase the propulsive efficiency by 20 % over modern day state-of-the-art. The RISE program reportedly aims to cut CO_2 emissions by 20 % if the engine runs on fossil fuels, but the engine could also be operated using sustainable aviation fuel (SAF) or hydrogen to meet the 2050 net-zero emissions target [27].

Next to RISE, Rolls Royce is developing the UltraFan engine concept as part of the Clean Aviation EU program [28]. The UltraFan is an ultra-high bypass ratio engine demonstrator that could reduce fuel burnt and CO_2 emissions by 25 %, NO_x by 40 % and noise emissions by 35 % compared to modern high-bypass turbofans [29]. These improvements are made possible by the largest fan ever developed for an aircraft, reaching 3.5 m of outer diameter, which is enabled by novel composite materials. The fan is powered by a high-speed low pressure turbine delivering 50 MW thanks to a newly developed planetary gearbox. Similar architectures are also being investigated by Pratt & Whitney [30] to roll out the next generation of their geared turbo fan engines.

[2] CFM is the industrial partnership between Safran and General Electric.

1.1.3. COMBINED-CYCLE ENGINES

The RISE and UltraFan engines are an evolution of modern high-bypass ratio turbofan engines and target increases in propulsive efficiency through larger and more powerful fans. The water-enhanced turbofan (WET) investigated by a consortium led by MTU Aeroengines and Pratt & Whitney, and including other aerospace companies such as Airbus and Collins Aerospace, and funded by a Clean Aviation research program [31], is an engine concept based on a combined-cycle (CC) configuration [32], in which part of the thermal energy-flow rate [J/s] carried by the exhaust of the gas turbine is converted into additional power. The water vapor contained in the combustion byproducts is condensed and collected, before being pressurized in the liquid state by a pump and evaporated using heat from the core exhaust flow. The superheated steam is then expanded in a steam turbine driving the LPT spool, and is then re-injected into the combustor with two benefits: i) lower NO_x are formed due to the reduction of adiabatic flame temperature, and ii) the flow expanding in the HPT and LPT turbines features higher specific heat due to the larger fraction of water in the flue gas, leading to higher specific work. The engine thermodynamic efficiency is thus higher as a result of thermal recuperation, and the turbomachinery can be made more compact due to the higher attainable specific work, leading to substantial weight reductions [33]. This system was initially estimated to yield 10 % lower CO_2 emissions, 90 % less NO_x emissions, and 50 % lower contrails formation compared to a modern turbofan engine [33], but recent developments have led MTU Aeroengines to discard the WET engine from their future strategy due to lower than expected efficiency savings [34].

A similar concept of CC-engine is being investigated by Pratt & Whitney, the so-called hydrogen steam injected intercooled turbine engine (HySIITE) [35]. According to limited public information[3], liquid hydrogen is superheated in an evaporator before it is injected into the combustor, using the thermal energy of the exhaust gas. In the process, the moisture in the exhaust gas is collected and successively superheated in a second heat exchanger, and the steam is partly fed to an intercooler upstream of the combustor to increase the thermodynamic efficiency of the system, and in part injected directly into the combustor to limit the production of NO_x. More details about this system have been recently published in a news article [36].

AIRBORNE THERMAL ENERGY HARVESTING WITH HIGH-TEMPERATURE ORC SYSTEMS

In 2020, the Propulsion and Power (P&P) research group of the Aerospace Engineering faculty of Delft University of Technology (TU Delft from hereon) initiated a research program on combined cycle engines. The ARENA[4] project is carried out by a consortium led by the P&P group, and composed of industrial players of the aviation sector such as Airbus, Safran, MTU and NASA, and second-tier component manufacturers like Aeronamic (turbomachines) and AKG (heat-exchangers). The project is financially supported by the Dutch Research Council (NWO[5]) with contributions from some of the companies and aims at studying innovative CC-engine concepts exploiting thermal recuperation

[3] The brief description of the concept was taken from https://aviationweek.com/special-topics/sustainability/pratt-outlines-hydrogen-steam-injection-engine-concept.

[4] ARENA: AiRborne thermal ENergy harvesting for Aircraft.

[5] https://www.nwo.nl/en/what-does-the-dutch-research-council-do

with high-temperature ORC systems. The main objective is pursued by means of systems and components studies, including the development of related modeling tools and their validation. Particular research efforts are devoted to the investigation of the heat exchangers (i.e., the evaporator and condenser) and the high-temperature radial turbine (*hiTORC-RIT*).

The performance of hybrid propulsive engines, consisting of a large-capacity gas turbine and a waste heat recovery ORC unit was investigated in the recent past. The Dragon is a fully turbo-electric aircraft concept first proposed by ONERA[6] [37]. Its propulsion system consists of a pair of two-spool turboshaft (TS) engines delivering electric power to arrays of electric propellers mounted under the wings. Part of the research within the ARENA project focused on the study of alternative solutions for the propulsion system of the Dragon aircraft.

In the research conducted by Krempus [38], two configurations of CC-engine were modeled. The first configuration that was studied was obtained by replacing the conventional TS-engine with a CC-TS engine. This investigation was also documented in Ref. [39]. Figure 1.3 shows the process flow diagram of this propulsion system, which includes an ORC unit for the thermal energy recovery from the primary engine. Its working fluid is cyclopentane. A ram air duct brings ambient air to cool the condensers, which are inclined to reduce the engine frontal area. The evaporator is placed in the exhaust of the free power turbine (FPT), which drives two 6 MW class generators. The ORC system of the optimized CC-TS power plant is suitable to recover ≈2 MW thermal power from the FPT exhaust, and has a net electric power output of 335 kW. The thermal efficiency of a single ORC unit is 17.2 %, its total mass around 260 kg, thus the power to mass ratio is 1.3 kW kg^{-1}. The radial turbine is a high-speed machine that generates 390 kW at the design rotational speed of 74.5 krpm. The total inlet fluid temperature of the turbine is 276 °C, whereas the cycle condensation temperature is ≈ 125 °. The Dragon aircraft powered by the two CC-TS engines achieves 1.5 % total mission fuel mass saving if compared to the baseline configuration. The heat exchangers impact negatively the propulsive efficiency of the engine, and are therefore the main cause preventing the CC-TS architecture from achieving substantially higher fuel savings.

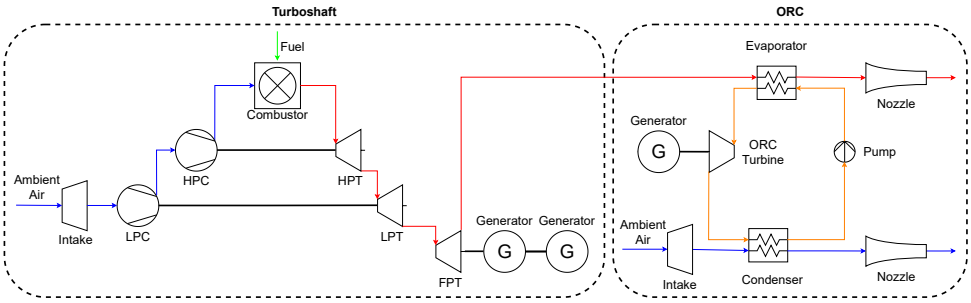

Figure 1.3: Process flow diagram of a CC-TS engine, courtesy of Krempus [38].

[6] ONERA is the French aerospace laboratory, see https://www.onera.fr/en.

Another advanced concept for the propulsion of the Dragon aircraft was investigated more recently [39], namely the combined-cycle turbofan (CC-TF): the engine also powers directly a fan. The design optimization was conducted by introducing an additional design variable for selecting the optimal ratio between the thrust produced by the electric propellers and the fan. The process flow diagram of the CC-TF is illustrated in Figure 1.4. Differently from the CC-TS power plant configuration, in the CC-TF, the LPT directly drives the electric generator. The ORC turbogenerator is a separate power unit to avoid direct coupling with the LPT generators, which would introduce a constraint on the ORC turbine rotational speed that should be accommodated by either increasing the turbine diameter or selecting a different working fluid. The optimized CC-TF design for the Dragon aircraft includes a 546 kg ORC unit for each CC-TF engine, generating 571 kW of additional power at cruise, corresponding to ≈ 21.5 % of the engine overall power. The turbine powering the ORC system features a rotational speed of 52 krpm and a total inlet fluid temperature of the turbine of 276 °C, thus the same as that of the CC-TS system. The total mission fuel mass required by this system is ≈4 % lower than that of the baseline configuration of the Dragon.

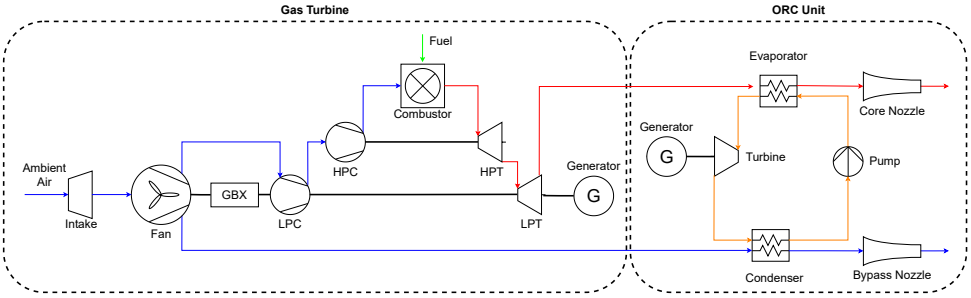

Figure 1.4: Process flow diagram of a CC-TF engine, courtesy of Krempus [38].

1.2. ORGANIC RANKINE CYCLE SUPERSONIC TURBINES

Airborne ORC systems are bound to be very different from those of stationary plants due to mass and volume constraints. Alongside the heat exchangers, the turbogenerator remains at the core of the technology as the overall energy conversion efficiency of the system depends to a large extent on the efficiency of the component. The thermodynamic design of the cycle, driven by the maximization of the conversion efficiency, often results in large pressure ratios and close to critical conditions at the inlet of the expander. As a consequence, even after a careful design, the flows within the expander can be highly supersonic – with Mach numbers beyond 2.5 –, while at least part of the expansion in the stator may occur in the nonideal thermodynamic region [40], i.e., where γ_{Pv}[7] $\neq \gamma$, thus where the ideal gas law is not rigorously applicable. These attributes are a well-known consequence of the use of high molecularly complex (HMC) fluids [42] in such systems, like siloxanes and hydrocarbons [1], and make finding the best turbine design a

[7] γ_{Pv} is one of three isentropic exponents governing dense gas dynamics, as initially theorized by Kouremenos & Kakatsios [41].

difficult task, often complicated by the lack of reliable data for validating the numerical tools and fine tuning the models. The large and under-exploited potential of thermal energy recovery using high-temperature ORC systems [43] has fostered the development of modeling and virtual prototyping techniques for *hiTORC-RIT*. The radial-inflow turbine is arguably the most suitable expander configuration as it yields the highest efficiency in a single stage arrangement, a well-known result of the historical work of Balje [44]. Work on mini-ORC systems for mobile and distributed power systems by Bahamonde *et al.* [45] showed that RITs can provide superior conversion efficiency as compared to three-stage axial turbines, i.e., the typical ORC expander, a mature technology thanks to decades of R&D in steam power, stationary waste heat recovery, and geothermal systems. The numerical study of De Servi *et al.* [46] confirms that *hiTORC-RIT* may attain comparatively high fluid dynamic efficiency ($\approx 80-85$ %), notwithstanding the shock-dominated flow occurring in the stator. Several works, see, e.g., the articles of [47–49], describe the relevant flow features occurring in these machines and document best practices for their optimal thermo-fluid dynamic design. However, as far as *hiTORC-RIT* are concerned, little information is available in the open literature regarding best practices for their optimal preliminary design.

1.2.1. DESIGN GUIDELINES FOR RADIAL-INFLOW TURBINES

Conventional preliminary design methods for RITs consist of design maps, i.e., diagrams displaying the attainable efficiency as a function of so-called duty coefficients, namely non-dimensional variables that have a direct influence on the performance of the expander, and allow one to decide upon the optimal shape of the flow path. Design maps for RITs have been initially proposed by Rodgers [50] and Chen & Baines [51], using empirical data about several gas turbine designs. These maps resemble the well-known Smith chart for axial turbines [52], and serve as a first rudimentary tool for the selection of the optimal geometrical configuration of the stage. However, as discussed, the preliminary design of ORC turbine stages encompasses additional aspects that are not accounted for by these rather elementary tools. As a result, the designer is required to account for the characteristics of the working fluid, which differ greatly between families of chemical compounds, and even between compounds belonging to the same family. Consequently, empirical design tools that were developed for turbines operating with working fluids that can be modeled as ideal gases are inaccurate not only for the prediction of the efficiency, but also for the determination of the set of optimal duty coefficients.

Seminal work on design guidelines for RITs of ORC systems was carried out by Perdichizzi & Lozza [53], which obtained expressions for the efficiency of turbines operating with working fluids of different molecular complexity. More recent studies [54–57] revolved around the fluid dynamic performance of stages operating with either low molecularly complex (LMC) and HMC working fluids, for low and high-temperature ORC systems. The researchers found that the optimal duty coefficients change as the stage expansion ratio increases, and the molecule complexity has negligible impact on maximum efficiency, and on the choice of the optimal duty coefficients. Giuffré & Pini [58] carried out a systematic study highlighting the influence of nonideal thermodynamic conditions on single-stage axial turbine performance, and their influence on the selection of the opti-

mal design parameters. Results showed that $\bar{\gamma}_{Pv}$, i.e., the average value of the isentropic pressure-volume exponent along the expansion [59], is a suitable similarity parameter to account for the impact of nonideal thermodynamic effects on stage efficiency. However, a similar study is yet to be carried out for radial-inflow turbines.

1.2.2. EXPERIMENTAL RESEARCH FACILITIES

Beyond design guidelines, the experimental assessment of radial-inflow ORC turbine performance is still largely undocumented in the literature, and, consequently, the validation of the numerical methods and tools used for their design is also missing. A few test benches for small-scale ORC turbines are or have been operational throughout Europe. A facility for testing a 10 kW axial-flow impulse turbine operating with ethanol as working fluid and featuring partial admission nozzles was designed and operated at the Turbomachinery and Fluid Dynamics Institute (TFD) of Leibniz University in Hannover [60]. The rotational velocity at the design point was 100 krpm, while the maximum stage pressure ratio of ≈ 50 was achieved with an admission degree of 0.5. The turbine and electric generator rotors were supported on custom high-precision ball bearings. More recently, a test facility resembling an ORC turbogenerator powered by the exhaust gases of a diesel engine and featuring a 12 kW supersonic RIT operating with octamethyltrisiloxane (siloxane MDM) as the working fluid has been commissioned at the Lappeenranta University of Technology [61]. The turbine stage was designed to rotate at 31.5 krpm, with a total-to-static pressure ratio of 112. The turbine, the main pump and the permanent magnet electric generator form a single assembly, similar to that described by [15]. The turbogenerator shaft is supported on hydrodynamic bearings lubricated with liquid siloxane MDM. A 2.3 kW radial-inflow turbogenerator system was designed, commissioned and is operated at the Laboratory of Applied Mechanical Design of the École Polytechnique Fédérale de Lausanne [62]. The nominal speed is 100 krpm, the working fluid is R245fa and the turbine features a rotor supported on custom designed gas-lubricated bearings, allowing for lower drag torque compared to liquid-lubricated bearings, and offering an efficient oil-free solution for low power capacity applications. Other laboratory facilities include those documented by [63–65], showcasing the increasing interest for small-scale ORC technology worldwide.

1.3. SCOPE OF THE RESEARCH

The research on supersonic high-temperature ORC radial-inflow turbines documented in this dissertation has been conducted following two major streams: on the one hand the development of predictive preliminary design tools and their application for the conception of design guidelines for system level studies, and on the other hand the design and realization of a unique turbine test bench for experimental research and validation of numerical models.

A preliminary design tool for RIT (i.e., *TurboSim*) was first developed in *Python* and verified using available data of existing radial turbines. *TurboSim* was then used to derive performance maps of *hiTORC-RIT* and investigate the impact of several design variables on efficiency. Finally, the obtained results were converted into design guidelines, i.e., simple models and rules to predict the efficiency and the set of duty coefficients to de-

termine the optimal stage configuration. The research was informed by the following overarching research questions:

A1 *Can TurboSim – a preliminary design tool for radial-inflow turbines – predict the efficiency of high-temperature ORC RITs?*

A1.1 *What loss mechanisms relevant to hiTORC-RIT should be modeled?*

A1.2 *What is the accuracy in predicting the efficiency compared to high-fidelity CFD methods?*

A2 *Can design guidelines for the selection of optimal duty coefficients, i.e., the work and flow coefficients, be formulated using the modeling framework implemented in TurboSim?*

A3 *Which scaling parameters are suitable to account for fluid complexity and nonideal thermodynamic effects on the efficiency?*

With the ultimate goal of validating numerical models and design guidelines, most of the research documented in this dissertation is about the conceptual and detailed design of a 10 kW turbogenerator test section that is about to be installed in the ORCHID, the organic Rankine cycle hybrid integrated device, a facility in operation at the TU Delft Aerospace Propulsion and Power (APP) laboratory. The ORCHID allows to perform fundamental studies on the expansion of dense organic vapors and applied studies on small high-temperature ORC turbines. This dissertation therefore documents the entire design and development process from the conception to a working prototype. The following research questions guided the design of the supersonic radial-inflow turbine unit for this test bed:

B1 *What rotor layout should be adopted for the design of a prototype laboratory turbine intended for experimental research on hiTORC-RIT?*

B1.1 *What components and features ensure (i) ease of access for maintenance, replacement, and updates of key components, and (ii) low mechanical losses and high reliability?*

B1.2 *What are the primary mechanical and thermal loads that need to be considered, how can they be accurately predicted, and what is their impact on the system's design?*

B2 *What is the rotordynamic response of the rotor supported on oil-lubricated rolling element bearings?*

B2.1 *What rotordynamic coefficients must be included in the mechanical model of the rotor?*

B2.2 *What modeling approaches are available to predict these coefficients, and can they provide accurate predictions of the values at both the design point and off-design conditions?*

B2.3 *What are the effects of these factors on the damped natural frequencies and the stability of the system?*

Alongside the turbine design, aspects related to its integration in a test section for the ORCHID were considered. The investigation encompassed several interconnected topics, such as the power management, the process control and monitoring, and the estimation of turbine performance. The outcome of the research allowed to answer the following research question:

B3 *What technical modifications and auxiliary systems are necessary to integrate the turbine into the ORCHID test section and ensure its proper functionality within the existing experimental facility?*

B4 *What sensors and instrumentation are necessary to measure the turbine power and its efficiency, and what is the expected accuracy of these measurements?*

1.4. THESIS OUTLINE

The dissertation is organized in four chapters.

Chapter 2 contains a thorough description of the preliminary design program for single stage radial turbines written in *Python*, called *TurboSim*.

Chapter 3 presents a detailed description of the preliminary design of the ORCHID turbine. In this chapter, the main assumptions and design choices are highlighted, and the initial assessment of the rotordynamic characteristics is presented. Furthermore, methods to estimate several quantities of relevance for the design of similar rotor systems have been implemented, documented and discussed.

Chapter 4 provides a description of the final prototype of the ORCHID turbogenerator, resulting from the collaboration with one of the industrial partners of the ARENA project. The chapter provides a detailed overview regarding the integration of the prototype turbine in the existing laboratory facilities, highlighting both mechanical and electrical aspects.

Finally, Chapter 5 provides a summary of the main conclusions drawn from this research, and an outlook on future directions.

BIBLIOGRAPHY

1. Colonna, P., Casati, E., Trapp, C., Mathijssen, T., Larjola, J., Turunen-Saaresti, T. & Uusitalo, A. Organic Rankine Cycle Power Systems: From the Concept to Current Technology, Applications, and an Outlook to the Future. *J. Eng. Gas Turb. Power* **137,** 100801–19. doi:10.1115/1.4029884 (2015).
2. *Calnetix Technologies* https://www.calnetix.com/.
3. Yuksek, E. L. & Mirmobin, P. Electricity Generation From Large Marine Vessel Engine Jacket Water Heat. *ASME 2015 9th International Conference on Energy Sustainability, ES 2015, collocated with the ASME 2015 Power Conference, the ASME 2015 13th International Conference on Fuel Cell Science, Engineering and Technology, and the ASME 2015 Nuclear Forum* **2.** doi:10.1115/es2015-49226 (2015).
4. *Concepts NREC* https://www.conceptsnrec.com/.
5. Di Bella, F. Gas turbine waste heat recovery using a 20,000 rpm sealless, turbine generator ORC system. *Symposium of the Industrial Application of Gas Turbines Committee* (2015).
6. *Enogia* https://enogia.com/.
7. *Orcan Energy* https://www.orcan-energy.com/.
8. *Rank* https://www.rank-%7BORC%7D.com/.
9. *Zuccato Energy* https://zuccatoenergy.com.
10. *Climeon* https://climeon.com/.
11. *Triogen* https://triogen.nl/.
12. Hoffren, J., Talonpoika, T., Larjola, J. & Siikonen, T. Numerical Simulation of Real-Gas Flow in a Supersonic Turbine Nozzle Ring. *Journal of Engineering for Gas Turbines and Power* **124,** 395–403 (2002).
13. Van Buijtenen, J. & Larjola, J. *Design and Validation of a New High Expansion Ratio Radial Turbine for ORC Application* in *Proceedings of the 5th Conference on Turbomachinery* (2003), 1–14.
14. Harinck, J., Turunen-Saaresti, T., Colonna, P., Rebay, S. & van Buijtenen, J. Computational study of a high-expansion ratio radial organic Rankine cycle turbine stator. *Journal of Engineering for Gas Turbines and Power* **132,** 1565–1636. doi:10.1115/1.3204505 (2010).
15. Harinck, J., Pasquale, D., Pecnik, R., Buijtenen, J. V. & Colonna, P. Performance improvement of a radial organic Rankine cycle turbine by means of automated computational fluid dynamic design. *Proceedings of the Institution of Mechanical Engineers, Part A: Journal of Power and Energy* **227,** 637–645. doi:10.1177/0957650913499565 (2013).

16. *Engine Waste Heat Recovery and Re-Use | European Commission* https://cordis.europa.eu/project/id/285103.

17. *Waste Heat Integrated Industrialised Trucks and Tractors Engine | European Commission* https://cordis.europa.eu/project/id/783959.

18. *2020 Vehicle Technologies Office AMR* EERE, Energy Efficiency and Renewable Energy, 2020. https://www.energy.gov/eere/vehicles/2020-vehicle-technologies-office-amr-presentations-program.

19. Olaniyi, E. O. & Prause, G. Investment Analysis of Waste Heat Recovery System Installations on Ships' Engines. *Journal of Marine Science and Engineering 2020* **8,** 811. doi:10.3390/jmse8100811 (2020).

20. *Amount of fuel consumed by ships worldwide by fuel type 2020 | Statista* https://www.statista.com/statistics/1266963/amount-of-fuel-consumed-by-ships-worldwide-by-fuel-type/.

21. *International prices of imported raw materials - Heavy fuel oil (North west Europe) 380 cst Cargo FOB - Prices in euros per ton - FOB - 3,5% of sulfur - Stopped series | Insee* https://www.insee.fr/en/statistiques/serie/010751333#Tableau.

22. *Fuel costs - weekly prices 2016-2022 | Statista* https://www.statista.com/statistics/526660/aviation-fuel-cost-comparison-across-regions/.

23. Overton, J. *The Growth in Greenhouse Gas Emissions from Commercial Aviation Part 1 of a Series on Airlines and Climate Change* Last accessed May 2, 2024. 2019. https://www.eesi.org/papers/view/fact-sheet-the-growth-in-greenhouse-gas-emissions-from-commercial-aviation.

24. ICAO. *Effects of Novel Coronavirus (COVID-19) on Civil Aviation: Economic Impact Analysis - Air Transport Bureau, International Civil Aviation Organization (ICAO), United Nations* Last accessed May 6, 2024. 2022. https://www.icao.int/sustainability/Documents/COVID-19/ICAO%20COVID-19%20Economic%20Impact_2023%2004%2027.pdf.

25. ICAO. *Presentation of 2021 Air Transport Statistical Results - Air Transport Bureau, International Civil Aviation Organization (ICAO), United Nations* Last accessed May 6, 2024. 2023. https://www.icao.int/annual-report-2021/Documents/20230320_Final_Table_en.pdf.

26. Mom, A. J. Introduction to gas turbines. *Modern Gas Turbine Systems: High Efficiency, Low Emission, Fuel Flexible Power Generation,* 3–20. doi:10.1533/9780857096067.1.3 (2013).

27. *RISE, Revolutionary Innovation for Sustainable Engines* https://www.cfmaeroengines.com/wp-content/uploads/2021/07/CFM_RISE_Whitepaper_Media.pdf.

28. *UltraFan (VHBR) Flight Test Demonstration* https://www.clean-aviation.eu/ultrafan-vhbr-flight-test-demonstration.

29. *UltraFan, The Ultimate Turbofan - Fact Sheet* https://www.rolls-royce.com/~/media/Files/R/Rolls-Royce/documents/innovation/ultrafan-fact-sheet.pdf.

30. Norris, G. *Pratt & Whitney Lays Out Next-Gen GTF Roadmap* Last accessed Jan 1, 2025. 2022. https://aviationweek.com/shownews/farnborough-airshow/pratt-whitney-lays-out-next-gen-gtf-roadmap.

31. *Sustainable Water-Injecting Turbofan Comprising Hybrid-electrics | SWITCH | Project | Fact sheet | HORIZON | CORDIS | European Commission* https://cordis.europa.eu/project/id/101102006.

32. Pouzolz, R., Schmitz, O. & Klingels, H. Evaluation of the Climate Impact Reduction Potential of the Water-Enhanced Turbofan (WET) Concept. *Aerospace* **8,** 59. doi:10.3390/aerospace8030059 (2021).

33. Kaiser, S., Schmitz, O., Ziegler, P. & Klingels, H. The Water-Enhanced Turbofan as Enabler for Climate-Neutral Aviation. *Applied Sciences* **12,** 12431. doi:10.3390/app122312431 (2022).

34. Norris, G. & Flottau, J. Tough choices. *Aviation week and space technology,* 16–17 (March 10 - 23 2025).

35. *Hydrogen Steam and Inter-Cooled Turbine Engine (HySITE)* https://arpa-e.energy.gov/technologies/projects/hydrogen-steam-and-inter-cooled-turbine-engine-hysite.

36. Norris, G. Pratt & Whitney unveils details of hydrogen-steam hybrid engine cycle. *Aviation week and space technology,* 34–35 (January 27 - February 9 2025).

37. Schmollgruber, P., Donjat, D., Ridel, M., Cafarelli, I., Atinault, O., François, C. & Paluch, B. Multidisciplinary design and performance of the onera hybrid electric distributed propulsion concept (Dragon). *AIAA Scitech 2020 Forum* **1, Part F,** 1–27. doi:10.2514/6.2020-0501 (2020).

38. Krempus, D. *Organic Rankine Cycle Waste Heat Recovery Systems for Aircraft Engines* PhD thesis (Delft University of Technology, 2025).

39. Krempus, D., Beltrame, F., Majer, M., Servi, C. M. D., Pini, M., Vos, R. & Colonna, P. Organic-Rankine-cycle Waste Heat Recovery System for the Turbofan Engines of a Partial-turboelectric Aircraft. *Journal of Propulsion and Power*. Submitted (2024).

40. Tosto, F. *Modeling and characterization of non-ideal compressible flows in unconventional turbines* PhD thesis (Delft University of Technology, 2023).

41. Kouremenos, D. A. & Kakatsios, X. K. The three isentropic exponents of dry steam. *Forschung im Ingenieurwesen* **51,** 117–122. doi:10.1007/bf02558416 (1985).

42. Guardone, A., Colonna, P., Pini, M. & Spinelli, A. Nonideal Compressible Fluid Dynamics of Dense Vapors and Supercritical Fluids. *Annual Review of Fluid Mechanics* **56,** 241–269. doi:10.1146/annurev-fluid-120720-033342 (2024).

43. Astolfi, M. *et al. Thermal Energy Harvesting: the Path to Tapping into a Large CO2-free European Power Source* White Paper. Version 1.0. Accessed via KCORC. 2022. https://kcorc.org/wp-content/uploads/2022/06/Thermal_Energy_Harvesting_-_the_Path_to_Tapping_into_a_Large_CO2-free_European_Power_Source.pdf.

44. Balje´, O. E. A Study on Design Criteria and Matching of Turbomachines: Part A—Similarity Relations and Design Criteria of Turbines. *Journal of Engineering for Power* **84,** 83–102. ISSN: 0022-0825. doi:10.1115/1.3673386 (1962).

45. Bahamonde, S., Pini, M., Servi, C. D., Rubino, A. & Colonna, P. Method for the Preliminary Fluid Dynamic Design of High-Temperature Mini-Organic Rankine Cycle Turbines. *Journal of Engineering for Gas Turbines and Power* **139.** doi:10.1115/1.4035841 (2017).

46. De Servi, C. M., Burigana, M., Pini, M. & Colonna, P. Design Method and Performance Prediction for Radial-Inflow Turbines of High-Temperature Mini-Organic Rankine Cycle Power Systems. *ASME. J. Eng. Gas Turbines Power* **141,** 091021. doi:10.1115/1.4043973 (2019).

47. Cappiello, A. & Tuccillo, R. Design Parameter Influence on Losses and Downstream Flow Field Uniformity in Supersonic ORC Radial-Inflow Turbine Stators. *Int. J. Turbomach. Propuls. Power* **6.** doi:10.3390/ijtpp6030038 (2021).

48. Cappiello, A. & Tuccillo, R. *Influence of Supersonic Nozzle Design Parameters on the Unsteady Stator-Rotor Interaction in Radial-Inflow Turbines for Organic Rankine Cycles* in *Turbo Expo: Power for Land, Sea, and Air* (2021). doi:10.1115/1.4054068.

49. Cappiello, A., Majer, M., Tuccillo, R. & Pini, M. *On the Influence of Stator-Rotor Radial Gap Size on the Fluid-Dynamic Performance of Mini-ORC Supersonic Turbines* in *Proceedings of the ASME Turbo Expo 2022: Turbomachinery Technical Conference and Exposition* **10B** (2022), V10BT35A015. doi:10.1115/gt2022-83309.

50. Rodgers, C. *Small High Pressure Ratio Turbines* Technical report TR-1987-01 (Sundstrand Turbomach, San Diego, CA, June 1987).

51. Chen, H. & Baines, N. C. The aerodynamic loading of radial and mixed-flow turbines. *International Journal of Mechanical Sciences* **36,** 63–79. doi:10.1016/0020-7403(94)90007-8 (1994).

52. Smith, S. F. A Simple Correlation of Turbine Efficiency. *The Aeronautical Journal* **69,** 467–470. doi:10.1017/S0001924000059108 (1965).

53. Perdichizzi, A. & Lozza, G. *Design Criteria and Efficiency Prediction for Radial Inflow Turbines* in *Proceedings of the ASME Turbo Expo: Power for Land, Sea, and Air* **1** (1987), V001T01A086. doi:10.1115/87-GT-231.

54. Mounier, V., Olmedo, L. E. & Schiffmann, J. Small scale radial inflow turbine performance and pre-design maps for Organic Rankine Cycles. *Energy* **143,** 1072–1084. doi:10.1016/j.energy.2017.11.002 (2018).

55. Da Lio, L. *Preliminary design of organic fluid turbines to predict the efficiency* PhD thesis (University of Padova, 2019).

56. Manfredi, M., Alberio, M., Astolfi, M. & Spinelli, A. *A Reduced-Order Model for the Preliminary Design of Small-Scale Radial Inflow Turbines* in *Turbo Expo: Power for Land, Sea, and Air* **4** (2021), V004T06A013. doi:10.1115/gt2021-59444.

57. Manfredi, M., Spinelli, A. & Astolfi, M. Definition of a general performance map for single stage radial inflow turbines and analysis of the impact of expander performance on the optimal ORC design in on-board waste heat recovery applications. *Applied Thermal Engineering* **224,** 119390. doi:10.1016/j.applthermaleng.2023.119390 (2023).

58. Giuffré, A. & Pini, M. Design Guidelines for Axial Turbines Operating With Non-Ideal Compressible Flows. *Journal of Engineering for Gas Turbines and Power* **143,** 011004. doi:10.1115/1.4049137 (2021).

59. Wheeler, A. P. S. & Ong, J. The Role of Dense Gas Dynamics on Organic Rankine Cycle Turbine Performance. *Journal of Engineering for Gas Turbines and Power* **135,** 102603. doi:10.1115/1.4024597 (2013).

60. Seume, J. R., Peters, M. & Kunte, H. Design and test of a 10 kW ORC supersonic turbine generator. *J. Phys.: Conf. Ser.* **821,** 012023. doi:10.1088/1742-6596/821/1/012023 (2017).

61. Uusitalo, A., Turunen-Saaresti, T., Honkatukia, J. & Dhanasegaran, R. Experimental study of small scale and high expansion ratio ORC for recovering high temperature waste heat. *Energy* **208,** 118321. doi:10.1016/j.energy.2020.118321 (2020).

62. Rosset, K., Pajot, O. & Schiffmann, J. Experimental Investigation of a Small-Scale Organic Rankine Cycle Turbo-Generator Supported on Gas-Lubricated Bearings. *ASME. J. Eng. Gas Turbines Power* **143,** 051015. doi:10.1115/1.4049988 (2021).

63. Klonowicz, P., Borsukiewicz-Gozdur, A., Hanausek, P., Kryłłowicz, W. & Brüggemann, D. Design and performance measurements of an organic vapour turbine. *Applied Thermal Engineering* **63,** 297–303. doi:10.1016/j.applthermaleng.2013.11.018 (2014).

64. Kang, S. H. Design and preliminary tests of ORC (organic Rankine cycle) with two-stage radial turbine. *Energy* **96,** 142–154. doi:10.1016/j.energy.2015.09.040 (2016).

65. Weiß, A. a. Experimental characterization and comparison of an axial and a cantilever micro-turbine for small-scale Organic Rankine Cycle. *Applied Thermal Engineering* **140,** 235–244. doi:10.1016/j.applthermaleng.2018.05.033 (2018).

2

Design guidelines for high-pressure ratio supersonic radial-inflow turbines of organic Rankine cycle systems

This chapter has been published in:

M. Majer, M. Pini, *Design guidelines for high-pressure ratio supersonic radial-inflow turbines of organic Rankine cycle systems*, Journal of the Global Power and Propulsion Society **8**, 1–28 (2025).

ABSTRACT
The radial-inflow turbine (RIT) is a widely adopted turbo-expander in power and propulsion systems of low-to-medium power capacity due to its high efficiency and compactness. Compared to conventional radial turbines for gas turbines and air cycle machines, the design of expanders for high-temperature organic Rankine cycle power systems involves additional challenges, as these machines operate with very high expansion or volumetric flow ratio and partly or entirely in the nonideal compressible fluid dynamic regime. This study examines the impact of the working fluid, of the volumetric flow ratio, and of the nonideal thermodynamic effects on the design guidelines for RIT. To this purpose, a reduced-order modeling framework for turbine fluid-dynamic design encompassing a loss model based on first principles is developed and verified against results from uRANS. Results highlighted that at the geometrical scale of interest the impact of the working fluid molecular complexity on the efficiency is marginal. Moreover, it is shown that the average isentropic pressure-volume exponent ($\bar{\gamma}_{Pv}$) can be used to predict the magnitude of nonideal thermodynamic effects on the stage efficiency, whose variation depends on the value of the volumetric flow ratio and of the work and flow coefficients. Design guidelines that can be used for preliminary turbine design in system-level calculations are presented in graphical form, and illustrate the relation between the optimal set of stage duty coefficients, i.e., the work and flow coefficients that maximize the efficiency, the stage efficiency, the volumetric flow ratio, and the similarity parameter $\bar{\gamma}_{Pv}$.

2.1. INTRODUCTION

The seminal work on design guidelines for RITs of ORC systems was carried out by Perdichizzi & Lozza [1], who investigated the fluid dynamic performance of stages operating at low and medium volumetric flow ratio (VR), up to $VR = 10$. The stator losses were predicted using the Craig and Cox correlation for axial turbines, adapted to radial vanes, while the impeller passage loss was computed using the models proposed by [2], including viscous drag on the blade profile and secondary flow loss due to tip leakage. The numerical results were found in good agreement with experimental data available for radial turbines. Two important findings were derived from the study: first, the volumetric flow ratio allows comparing the fluid dynamic performance of stages operating with different working fluids and expansion ratios (PR) using a single dimensionless parameter, $VR = PR^{\frac{1}{\gamma}}$, with γ the ideal gas specific heat ratio. Second, regardless the volumetric flow ratio, the maximum efficiency value is obtained for a value of the specific speed $N_s \simeq 0.1$, suggesting that the optimal value of the stage duty coefficients is not affected by VR.

The more recent work of Mounier *et al.* [3] documenting design guidelines for RITs of low-to-medium temperature ORC systems reported plots of the turbine efficiency as a function of N_s and the specific diameter (D_s). The study highlighted that the efficiency value becomes dependent on N_s and D_s as the pressure ratio PR exceeds 10. In addition, the optimal D_s value decreases appreciably as compressibility effects become more significant. The sensitivity of the calculated stage efficiency to the fluid molecular complexity was assessed on a limited range of working fluids, considering refrigerants of increas-

ing molecular complexity. Results showed negligible efficiency variations by varying the working fluid, corroborating that PR is an appropriate similarity parameter when comparing the fluid dynamic performance of turbines operating with fluids of similar molecular complexity, i.e., of the same class. In analogy to the study of Perdichizzi & Lozza [1], losses were modeled according to empirical correlations and contribution of the shock waves to losses was not accounted for.

Manfredi *et al.* [4] developed a mean-line design model for *hiTORC-RIT*, validating it against experimental data available for radial-inflow turbines operating at both on- and off-design conditions. A semi-empirical loss model was used to predict the turbine efficiency. Notably, the models of Glassman [2] and Baines [5] were adopted to compute the stator and impeller passage losses, while mixing losses were computed using first principles and a control volume approach, as recommended in other works [6–8]. The stator-impeller radial gap and the disk windage friction losses were estimated using the methods reported in Whitfield & Baines [9]. In a subsequent study, Manfredi *et al.* [10] concluded that the optimal choice of VR and of the size parameter (SP) is not dictated by the working fluid. Considering a wide range of fluid classes, from refrigerants through hydrocarbons to siloxanes, the authors found a deviation of about 0.5% in the optimal efficiency of stages designed for different working fluids.

Notwithstanding the recent works, a conclusive study presenting best design practices for *hiTORC-RIT* and clarifying the role of the fluid molecular complexity and of nonideal thermodynamic effects to loss and efficiency is not available. Such knowledge gap is filled in this study, in which design guidelines formulated in accordance to a suited scaling analysis are documented. To this purpose, a reduced-order model (ROM) for turbine preliminary design was developed and verified against results obtained with unsteady RANS (uRANS) simulations. The ROM implements semi-empirical loss correlations adapted to nonideal flows and a loss model for shock losses based on first principles. Results obtained with the ROM and corroborated via CFD simulations elucidate the impact of the volumetric flow ratio, of the working fluid, and that of nonideal thermodynamic effects on turbine efficiency and on the selection of duty coefficients for optimal stage design.

2.2. THEORETICAL FRAMEWORK

2.2.1. GENERALIZED SCALING LAW FOR RITS

The fluid dynamic efficiency of a radial turbine stage operating with a fluid in the ideal gas state can be expressed as

$$\eta = f\left(\psi, \phi, \mu, \alpha_{\text{out}}, PR, \gamma, Re, \boldsymbol{\sigma}\right), \tag{2.1}$$

where $\boldsymbol{\sigma}$ is the vector of the variables describing the geometrical characteristics of the stage, for instance the solidity or the trailing-edge to pitch ratio of both the stator and the impeller, and γ is the specific heat ratio of the fluid in the limit of dilute, i.e. perfect, gas. Equation 2.1 differs from that used to describe the fluid dynamic performance of axial turbomachine stages reported by, e.g., Giuffré & Pini [7], as for radial stages it is

common practice to fix the absolute flow angle α_{out} at the outlet of the impeller rather than the degree of reaction. Moreover, since in radial stages the meridional flow velocity across the impeller is usually non constant, the ratio of meridional flow velocities $\mu = V_{\text{m3}}/V_{\text{m2}}$ appears as an additional independent variable in Equation 2.1. According to Giuffré & Pini [7], the impact of the fluid and its thermodynamic conditions on the stage fluid dynamic performance is primarily dependent on two quantities: the density or volumetric flow ratio VR, which replaces the pressure ratio PR in Equation 2.1, and the isentropic pressure-volume exponent, γ_{Pv}, which is the exponent that generalizes the isentropic ideal gas relation Pv^{γ} for nonideal thermodynamic states and that provides the magnitude of nonideal compressible fluid dynamic (NICFD) effects [11, 12]. In the nonideal thermodynamic region, the value of γ_{Pv} depends on the fluid thermodynamic state, therefore an averaged value is needed to relate the effect of γ_{Pv} on the fluid dynamic performance of the stage. An average suited for expansion and compression processes in turbomachines is given by the following logarithmic relation [13]

$$\bar{\gamma}_{Pv} = \frac{\ln P_1/P_2}{\ln v_2/v_1}, \tag{2.2}$$

where P and v are the pressure and specific-volume at the beginning (1) and at the end (2) of the expansion process, and $\bar{\gamma}_{Pv}$ is the exponent which satisfies $Pv^{\bar{\gamma}_{Pv}} = K$. The density ratio can then be approximated as $VR = PR^{\frac{1}{\bar{\gamma}_{Pv}}}$. Both VR and $\bar{\gamma}_{Pv}$ are the parameters characterizing the fluid-dynamic performance of turbomachinery operating with the working fluid in thermodynamic states along the process partly or fully nonideal. Equation 2.1 can be consequently formulated as

$$\eta = f\left(\psi, \phi, \mu, \alpha_{\text{out}}, VR, \bar{\gamma}_{Pv}, Re, \boldsymbol{\sigma}\right). \tag{2.3}$$

Equation 2.3 is referred to as the generalized scaling law for design of radial-inflow turbines.

2.2.2. NONIDEAL COMPRESSIBLE FLUID DYNAMICS EFFECTS ON LOSSES IN TURBINES

While the effect of γ on the loss mechanisms and turbine stage efficiency has been adequately investigated [7, 8, 14, 15], studies documenting the influence of $\bar{\gamma}_{Pv}$ on losses are limited. Giuffré & Pini [7] found that, for VR values in the range of 3 to 5, axial turbine stages operating with working fluids in thermodynamic states for which $\bar{\gamma}_{Pv} > \gamma$ along the process are characterized by comparatively higher losses due to enhanced compressibility effects. On the contrary, lower losses characterize stages operating with complex fluid molecules in ideal gas conditions, for which $\bar{\gamma}_{Pv} = \gamma \rightarrow 1$. However, the magnitude of NICFD effects on losses remains dependent on the fluid and its thermodynamic states along the expansion process. Using a simple analytical model, Denton [16] demonstrated that the entropy generation across normal shock waves scales reasonably well with γ. By replacing γ with $\bar{\gamma}_{Pv}$, the model can be generalized to nonideal

compressible flows. The equation to compute the efficiency decrease occurring across a normal shock reads

$$\Delta\eta \approx \frac{\bar{\gamma}_{Pv}+1}{12\bar{\gamma}_{Pv}^2}\left(VR_{\text{sh}}^{\bar{\gamma}_{Pv}}-1\right)^2, \tag{2.4}$$

and shows that for a fixed VR_{sh} across the shock, the efficiency deficit is proportional to $\bar{\gamma}_{Pv}$, as shown in the left-hand side plot of Figure 2.1.

Recent investigations on flows of fluids of varying molecular complexity in transonic and supersonic blade rows [14] highlighted that the wake mixing process and the associated loss are largely affected by the γ value downstream of the trailing edge. If $\bar{\gamma}_{Pv}$ is introduced in place of γ, the relation can be extended to nonideal compressible flows and written in the form

$$\frac{\zeta_{\text{mo}}}{\zeta_{\text{mo}}^{\text{Air}}} = a\left(\bar{\gamma}_{Pv}\right)\cdot\left(M_{\text{out}}+0.25\right)+1, \tag{2.5}$$

in which M_{out} is the Mach number downstream of the cascade. The value of $a(\bar{\gamma}_{Pv})$ was computed by fitting of the data obtained from two-dimensional CFD simulations performed on turbine cascades operating with working fluids in ideal gas conditions, and with $\gamma \in (1.08, 1.67)$, yielding

$$a\left(\bar{\gamma}_{Pv}\right) = 0.1014\bar{\gamma}_{Pv}^3 - 0.2728\bar{\gamma}_{Pv}^2 - 0.122\bar{\gamma}_{Pv} + 0.4272.$$

The right plot of Figure 2.1 shows the trend of the mixing losses as a function of the average isentropic pressure volume exponent. Higher efficiency penalties due to wake-mixing occur in mixing processes of fluids made by complex molecules and in thermodynamic states of the fluid for which $\bar{\gamma}_{Pv} < \gamma$. Moreover, the higher the Mach number downstream of the cascade, the higher the loss for complex fluids in the nonideal thermodynamic regime.

The results shown thus far point out that any loss correlation developed for ideal gas flows should be adapted to compute losses and efficiency trends of radial turbines operating with working fluids in nonideal thermodynamic states by, at least, introducing suitable values of $\bar{\gamma}_{Pv}$ into the model.

2.3. TURBINE DESIGN METHODOLOGY

The turbomachinery design program *TurboSim* developed in this work is a reduced-order model based on a quasi-3D calculation method of the flow passing through a radial-inflow turbine stage, composed by a stator and an impeller. The flow quantities and the main machine dimensions are evaluated at *four* sections in the stream-wise direction along the flow path, i.e., at the inlet and outlet of each blade row, as depicted in Figure 2.2. However, as opposed to a conventional lumped parameters approach, the flow quantities at each section are also calculated at an arbitrary number of locations

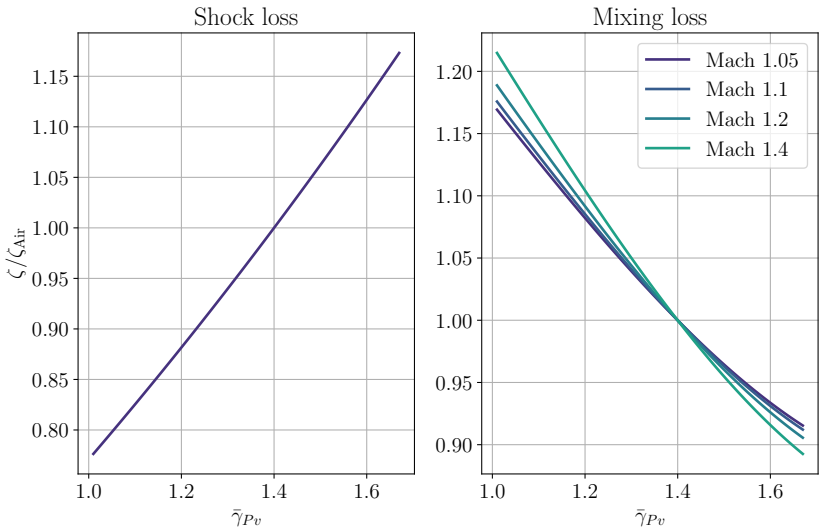

Figure 2.1: Shock loss (left) and mixing loss at increasing cascade downstream Mach number (right) as a function of the generalized isentropic pressure-volume exponent $\tilde{\gamma}_{Pv}$. The loss coefficients are normalized by the one of air in ideal gas conditions ($\tilde{\gamma}_{Pv} = 1.4$). Loss is computed assuming $VR_{sh} = 1.2$.

along the span, to take three-dimensional effects into account. The most relevant 3D flow distribution, e.g. free- or controlled-vortex, can be imposed at the impeller outlet section to optimize the stage performance. The numerical framework is programmed in *Python*, and coupled to the thermodynamic libraries of the *REFPROP* software [17].

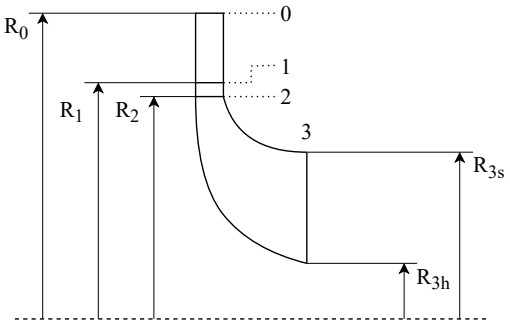

Figure 2.2: Meridional view of a radial-inflow turbine stage with all the relevant dimensions indicated.

A simplified workflow illustrating the design methodology implemented in *TurboSim* is shown in Figure 2.3. The design is performed in two main steps, highlighted in the figure by means of the colored boxes. With reference to the yellow box, the stage is first sized by assuming isentropic and uniform flow along the span; the actual flow quantities at each span-wise location are subsequently calculated by selecting a span-wise flow distribution and by applying a loss model (red box). The whole design process is iterative, with several internal loops highlighted in the figure by the arrow wrapping around each block of the diagram 2.3. Convergence is achieved when the calculated mass flow averaged pressure ratio $\overline{PR}$ equals the user specified value.

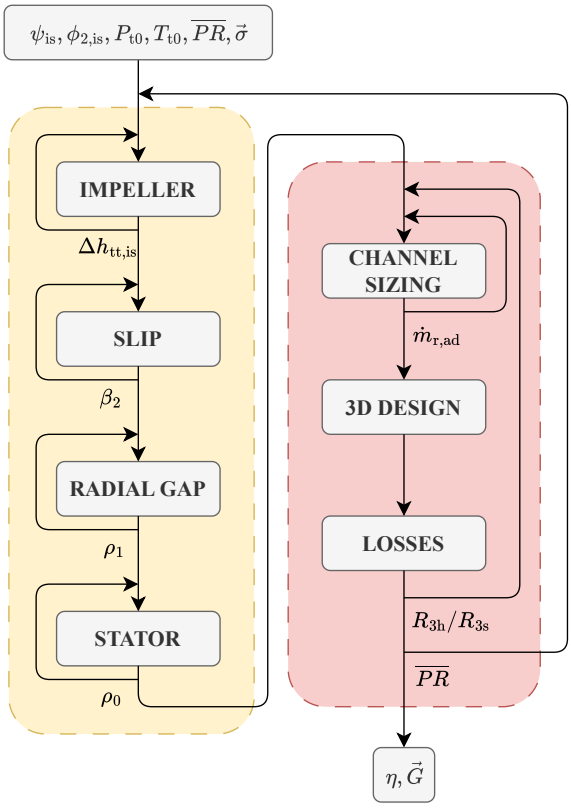

Figure 2.3: Workflow diagram of the turbine preliminary design method.

In the following, the calculation process of the isentropic flow quantities along the machine and the method for loss accounting is described in more detail. Moreover, addi-

tional information on the algorithm used to achieve convergence of the exducer radius ratio R_{3h}/R_{3s} have been provided in Appendix E.

IMPELLER

The impeller is sized according to the classical method based on the work and flow coefficients [18]. Given ψ_{is} and $\phi_{2,is}$ and the stage boundary conditions T_{t0}, P_{t0}, $\overline{PR}(VR, \bar{\gamma}_{Pv})$, the inlet and outlet velocity triangles at mid span-wise section are computed. The tip peripheral velocity is calculated as

$$U_2 = \sqrt{\frac{\Delta h_{tt,is}}{\psi_{is}}}, \tag{2.6}$$

where the isentropic enthalpy drop $\Delta h_{tt,is}$ is defined by the stage boundary conditions. The inlet meridional velocity can be calculated from the flow coefficient $\phi_{2,is}$ and U_2 as

$$V_{m2,is} = \phi_{2,is} \cdot U_2. \tag{2.7}$$

Using the impeller design variables ν, μ and α_3, the outlet velocity triangle is retrieved, and so the outlet work coefficient $\psi_{3,is} = V_{\theta 3,is}/U_3$. The inlet work coefficient $\psi_{2,is}$ is determined by means of the adimensional *Euler* equation for isentropic flow:

$$\psi_{is} = \psi_{2,is} - \nu \cdot \psi_{3,is}, \tag{2.8}$$

$$\psi_{2,is} = \psi_{is} + \nu \cdot \psi_{3,is}. \tag{2.9}$$

Rearranging Equation 2.8 into Equation 2.9 yields the value of $\psi_{2,is}$, from which $V_{\theta 2,is}$ can be finally computed. The above described procedure is straightforward if the total-total pressure or density ratio are specified, because $\Delta h_{tt,is}$ in Equation 2.6 is directly calculated. If the total-static pressure or density ratio are instead specified, the calculation of $\Delta h_{tt,is}$ needed in Equation 2.6 becomes iterative, using the total-static isentropic enthalpy drop $\Delta h_{ts,is}$ as first guess to compute U_2.

The prediction of the optimal impeller incidence angle is based on the method proposed by Chen and Baines [18]. The impeller blade count is computed according to an empirical model [2], see Equation 2.10, rigorously valid only for radial bladed impellers.

$$N = \frac{\pi}{30°}(110° - \alpha_{2,is})\tan(\alpha_{2,is}). \tag{2.10}$$

Given the blade count N and the isentropic tangential velocity $V_{\theta 2,is}$, Equation 2.11 allows one to compute the slip factor σ as

$$\sigma = 1 - \frac{0.63\pi}{N}\sin(\xi)\cos(\beta_{2g}). \tag{2.11}$$

In Equation 2.11, ξ is referred to as the inlet cone angle, namely the angle between the meridional direction and the rotation axis in the meridional plane at the inlet of the impeller. β_{2g} is the blade metal angle at the impeller inlet, initially assumed to be equal to the value of the relative flow angle $\beta_{2,is}$. The slip velocity difference ΔV_θ^*, is defined as in Equation 2.12 and is used to compute the optimal impeller inlet velocity triangle.

$$\Delta V_\theta^* = V_{\theta 2,is} \cdot \left(\frac{1}{\sigma} - 1 \right). \tag{2.12}$$

Given that the blade count N is a function of the impeller inlet absolute flow angle $\alpha_{2,is}$, the slip angle is calculated by iteratively solving Equation 2.10, Equation 2.11, and Equation 2.12. The absolute flow tangential velocity is finally given by

$$V'_{\theta 2} = V_{\theta 2} - \Delta V_\theta^*. \tag{2.13}$$

Note that, as opposed to common design practices for radial-inflow turbines, the design methodology described here can lead to impellers characterized by non-zero blade sweep angles at the inlet. As impellers of supersonic ORC radial turbines operate at temperatures not exceeding 250-300 °C and feature relatively low peripheral speed, thus comparatively low thermo-mechanical stresses, sweep angles up to 45° can be adopted.

RADIAL GAP

The flow quantities at the outlet of the stator vane are determined by assuming that the flow distribution follows a free vortex law in the radial gap. Two further design variables, namely the radial gap span ratio b_2/b_1 and the radial gap radius ratio R_2/R_1 are specified. The conservation of mass, angular momentum and energy (Equations 2.15, 2.14, 2.16) between section 1 and 2 of Figure 2.2 are written as

$$\frac{V_{m1}}{V_{m2}} = \frac{\rho_2}{\rho_1} \frac{R_2}{R_1} \frac{b_2}{b_1}, \tag{2.14}$$

$$\frac{V_{\theta 1}}{V_{\theta 2}} = \frac{R_2}{R_1}, \tag{2.15}$$

$$h_1 = h_{t1} - \frac{{V_1}^2}{2}. \tag{2.16}$$

The system of non-linear equations is solved by iterating on the density ρ_1.

RADIAL STATOR

The flow quantities at the inlet of the radial vane are calculated by specifying the value of the absolute inlet flow angle α_0, the radius ratio R_1/R_0, and the vane span ratio b_1/b_0.

The continuity equation

$$V_{m0} = V_{m1} \frac{\rho_1}{\rho_0} \frac{R_1}{R_0} \frac{b_1}{b_0}, \tag{2.17}$$

and the energy balance

$$h_0 = h_{t0} - \frac{{V_0}^2}{2}, \tag{2.18}$$

are iteratively solved to find the inlet flow velocity and the fluid thermodynamic properties.

2.3.1. CALCULATION OF TURBINE EFFICIENCY

The total-total turbine efficiency is computed according to

$$\eta_{tt} = 1 - T_{1,is} \cdot \sum \Delta s_{st} - T_{3,is} \cdot \sum \Delta s_{imp}, \tag{2.19}$$

where the term $T_{is} \cdot \sum \Delta s$ is the overall efficiency penalty of the blade row due to the various loss mechanisms. The modeling of losses is documented in the following.

2.3.2. LOSS ACCOUNTING

STATOR PASSAGE LOSS

As radial vanes of supersonic RITs are typically constituted by prismatic blades featuring converging-diverging nozzle profiles, secondary flow losses are often negligible with respect to boundary layer losses occurring on the blades and on the endwalls. The model of Meitner & Glassman [19] based on the two-dimensional boundary layer theory was adopted for the computation of blade profile losses

$$\zeta_{2D} = \frac{E(Q) \cdot \frac{\theta}{g}}{\cos \alpha_1 - \frac{t}{g} - H(Q) \cdot \frac{\theta}{g}}, \tag{2.20}$$

as also recommended in Manfredi *et al.* [4].

In Equation 2.20, E is the energy factor and H the shape factor of the boundary layer, calculated as suggested by Meitner & Glassman [19]. The angle α_1 is the stator outlet flow angle. The quantities θ and t are the momentum thickness of the boundary layer and the blade thickness at the trailing edge, normalized by the pitch g. The calculation of the boundary layer factors E and H requires the determination of

$$Q = \frac{\bar{\gamma}_{Pv} - 1}{\bar{\gamma}_{Pv} + 1} \cdot \left(\frac{V_1}{V_{cr}} \right)^2, \tag{2.21}$$

that depends on the *outlet* flow conditions, where V_1 is the stator outlet flow velocity and V_{cr} is the critical velocity corresponding to a chocked flow. Since in Equation 2.21

$\bar{\gamma}_{Pv}$ corresponds to the average value between sections 0 and 1, the calculation of the loss coefficient becomes iterative. The entropy change due to profile loss is therefore obtained from

$$\Delta s_{\text{st,prof}} = s(h_1, P_1) - s_0, \tag{2.22}$$

where $h_1 = h_{\text{t0}} - V_{\text{1,is}} \cdot \sqrt{1-\zeta_{\text{2D}}}$.

Following Denton [16], the entropy generation due to endwall loss is obtained by numerical integration of the right hand side term of

$$\Delta s_{\text{st,ew}} = 2C_{\text{D}} \cdot \frac{\int_{A_{\text{ew}}} \rho V^3 / T \, dA}{\dot{m}}. \tag{2.23}$$

In the equation, ρ, V and T are the free stream flow quantities at the edge of the boundary layer, while the values of the dissipation coefficient C_{D} is assumed to be constant [16] and was listed in Appendix F. For simplicity, a rectangular velocity distribution [16] was assumed to compute the freestream quantities within the bladed channel. Coull [20] compared losses obtained with such a simple distribution against those obtained with a velocity distribution computed with CFD, and found small difference in the loss coefficient.

MIXING LOSS

Losses generated by wake mixing downstream of stator vanes and impeller blades are computed using the method documented in Denton [16], in which the effective base pressure coefficient is computed as

$$C_{P_{\text{b}},eff} = \left(\frac{P_{\text{b}}}{P_{\text{ref}}} - 1 \right) \cdot \frac{2}{\gamma_{Pv} M_{\text{ref}}^2} \cdot \frac{t}{g}. \tag{2.24}$$

Equation 2.24 is a generalization of the base pressure coefficient model to compressible flows and arbitrary working fluids [14]. In the equation, P_{ref} and M_{ref} are the reference pressure and Mach number, namely the total pressure at the inlet and the isentropic Mach number at the outlet of the cascade, while P_{b} is the base pressure, whose value is a function of the cascade total-static pressure ratio and of the critical area ratio, based on cascade experimental data [21]. The entropy change associated to wake mixing losses is eventually expressed as

$$\Delta s_{\text{mx}} = \left(-\frac{C_{P_{\text{b}},eff} \cdot t}{g} + \frac{2\theta}{g} - \left(\frac{\delta^* + t}{g} \right)^2 \right) \cdot \frac{V_{\text{out,is}}^2}{2T_{\text{out,is}}}, \tag{2.25}$$

in which θ and δ^* are the momentum and the displacement thickness of the boundary layer at the trailing edge, calculated considering the scaling parameters in Appendix F which are valid for both the stator vanes and the impeller blades. g is the cascade pitch and t the trailing edge thickness.

SHOCK LOSS

The entropy generation across shock waves formed at the trailing edge of either stator vanes and impeller blades is computed using the model based on first-principles documented in [22] and [7]. The governing equations are the Rankine-Hugoniot (RH) relations for an oblique shock, reported by Equation 2.26 through 2.29.

$$h_B - h_A = \frac{1}{2}(P_B - P_A)(v_B - v_A) \tag{2.26}$$

$$-\frac{P_B - P_A}{v_B - v_A} = (\rho_A V_A \sin\epsilon)^2 \tag{2.27}$$

$$\rho_A \tan\epsilon = \rho_B \tan\epsilon - \delta \tag{2.28}$$

$$V_A \cos\epsilon = V_B \cos\epsilon - \delta, \tag{2.29}$$

where ϵ is the shock angle and δ is the flow deviation past the shock. The flow state upstream of the shock is denoted by A, while state B identifies the downstream conditions. The shock angle depends on the upstream flow conditions through the following relation taken from [23], only valid for weak shock waves where the normal component of the upstream Mach number $M_A \cdot \sin\epsilon$ is slightly larger than 1

$$\epsilon = \arcsin\left(\frac{1}{M_A}\right) + \frac{\Gamma_A}{2}\frac{M_A^2}{M_A^2 - 1}\cdot\delta + \mathcal{O}\left(\delta^2\right). \tag{2.30}$$

The entropy change across the shock is equal to

$$\Delta s_{sh} = s(h_B, P_B) - s(h_A, P_A), \tag{2.31}$$

where h_B and P_B result from solving the RH relations for a nonideal compressible flow. The upstream state P_A and M_A is related to the values of pressure and Mach in section 1, and the correlation is found using the results of CFD simulations of the supersonic flow in radial stators operating in over- and under-expanded conditions [24].

To assess the sensitivity of the shock losses to different pre-shock conditions and shock-wave angle, the entropy generation across an oblique shock wave inclined at 45° has been computed as a function of the pre-shock Mach number M_A and compared to that of a shock-wave whose inclination angle depends on the upstream Mach number in accordance to Equation 2.30. The results are plotted in Figure 2.4. The trend of the shock angle ϵ with the upstream Mach M_A is also displayed on the right hand side y-axis of Figure 2.4. It can be observed that the entropy generation is largely dependent on the value of the inclination angle, and that the use of a fixed shock angle in a ROM for turbomachinery design can lead to a significant overestimation of the associated shock losses.

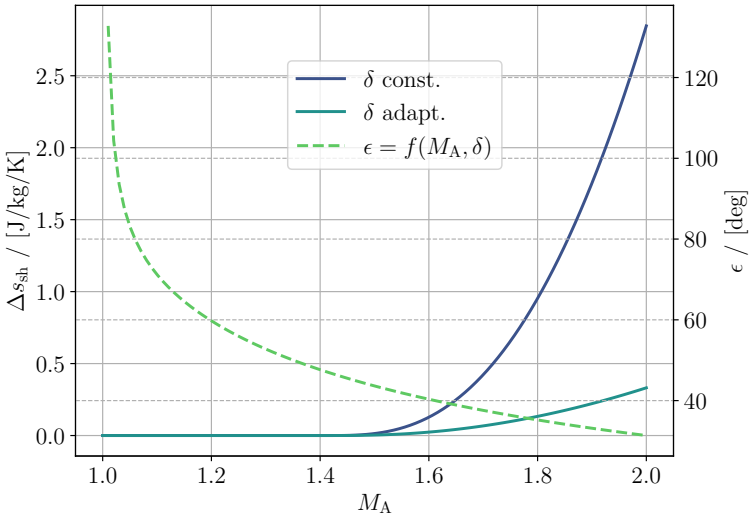

Figure 2.4: On the left y-axis: entropy change obtained by solving the RH governing equations (solid lines) as a function of the pre-shock Mach number M_A assuming i) a constant shock angle $\epsilon = 45°$, and ii) a varying shock angle as a function of M_A (Equation 2.30). On the right y-axis: shock angle ϵ as a function of M_A (dashed line).

The accuracy of the first-principle shock loss model has been verified against results from a two-dimensional CFD simulation. Table 2.1 reports the comparison of the computed entropy change with the two models for a case of supersonic nozzle flow passing through a normal shock, highlighting that the results between the two models are very similar.

Table 2.1: Entropy change across a normal shock in a flow through a planar nozzle calculated with an inviscid 2D CFD model and comparison with the solution of the RH equations. In both cases, the pre-shock conditions are $P_A = 2.93\ bar$ and $M_A = 1.84$ and the fluid is Siloxane MM.

Model	$\Delta s/[kJ/kgK]$	$P_B/[bar]$	M_B
CFD	16.35	9.92	0.552
ROM	16.94	9.79	0.552

RADIAL GAP LOSS

Losses in the radial gap are attributed to viscous friction on the endwalls and the associated entropy generation can be expressed as [9]

$$\Delta s_{\mathrm{rg,ew}} = s(h_2, P_2) - s_1, \tag{2.32}$$

where h_2 can be determined from the energy conservation $h_2 = ht0 - (V_{\theta 2}^2 + V_{\mathrm{m2}}^2)/2$.

$V_{\theta 2}$ can be calculated in accordance to Equation 2.33 as

$$\frac{V_{\theta 1}}{V_{\theta 2}} = \left[\frac{R_2}{R_1} + \frac{2\pi\, C_f \rho_2 V_{\theta 2} (R_1{}^2 - R_1 R_2)}{\dot{m}} \right], \tag{2.33}$$

in which the turbulent friction coefficient C_f is calculated as recommended in Equation 2.34

$$C_f = k\,(1.8 \cdot 10^5 / \mathrm{Re})^{0.2}. \tag{2.34}$$

Equation 2.33 is solved in combination with 2.14 and 2.16 to find the flow state at the outlet of the radial gap. A value $k = 0.0035$ was used, determined by comparison with results of RANS simulations [24] of the flow in radial turbine stages featuring gap ratios $R_1/R_2 \in (1.03, 1.24)$ and operating with siloxane MM as working fluid. Figure 2.5 shows the trend of tangential velocity ratio obtained with the CFD and the reduced order model for two values of k.

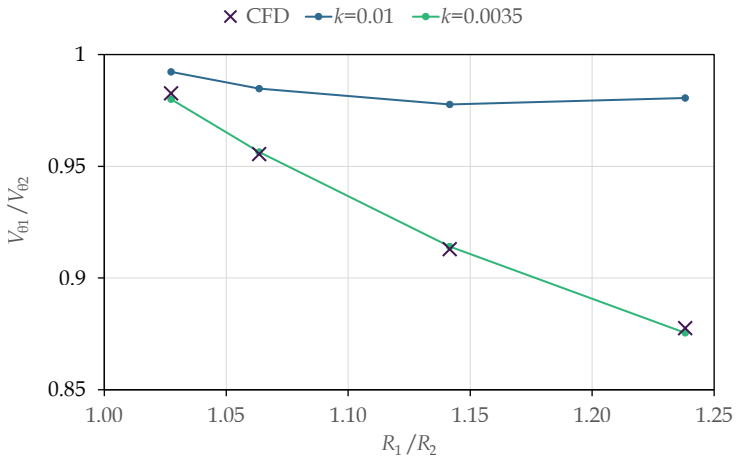

Figure 2.5: Variation of the tangential velocity ratio as given by Equation 2.33 for two values of k (solid lines) and comparison with CFD results (×).

IMPELLER LOSS

Loss sources in the impeller are assumed to be predominantly related to passage and tip leakage flow. Passage flow losses are due to viscous dissipation in the boundary layers, and to mixing of the passage vortex. The semi-empirical model proposed by Baines [5], accounting for viscous, blade loading and secondary flow losses, is used in this work to compute the passage losses. The model, reported in Equation 2.35, has been shown to be more accurate than that of Rodgers, documented in Whitfield & Baines [9], for predicting the efficiency of supersonic ORC RITs by Manfredi *et al.* [4].

$$\Delta h_{\mathrm{pass}} = K_p \left\{ \left(\frac{L_H}{D_H} \right) + 0.68 \left[1 - \left(\frac{\bar{R}_3}{R_2} \right)^2 \right] \frac{\cos \beta_{3g}}{b_3/c} \right\} \cdot \frac{1}{2} (W_2^2 + W_3^2). \tag{2.35}$$

In Equation 2.35, c is the blade chord, z the impeller axial length, L_H the hydraulic length, and D_H.

Losses due to tip leakage flow are computed in accordance to Baines [5]

$$\Delta h_{leak} = \frac{U^3 N}{8\pi}\left(K_x \epsilon_x C_x + K_r \epsilon_r C_r + K_{xr}\sqrt{\epsilon_x \epsilon_r C_x C_r}\right). \tag{2.36}$$

In Equation 2.36, ϵ_x is the axial and ϵ_r the radial tip gap, K_x, K_r and K_{xr} are the discharge coefficients, assumed constant and reported in Appendix F, and C_x and C_r are parameters depending on the impeller configuration, whose definitions are reported in the Appendix D together with those of L_H and D_H. The entropy change across the impeller is finally computed as

$$\Delta s_{imp} = s(h_{3,is} + \Delta h_{pass} + \Delta h_{leak}, P_3) - s_2. \tag{2.37}$$

DIFFUSER LOSS

The losses occurring within the diffuser, assumed to be of conical shape, are computed by resorting to the model proposed by Agromayor *et al.* [25]. The governing equations are formulated as an implicit system of ordinary differential equations that are solved iteratively. The diffuser cant angle, the wall semi-aperture angle and the diffuser area ratio need to be specified, as well as the geometry and the flow state at the exit section of the impeller. Viscous flow losses in the diffuser are computed by specifying the friction factor. In this work this was fixed to 0.1 [25].

2.3.3. MODEL VERIFICATION

In order to verify the accuracy of *TurboSim*, the results of the model have been compared with those obtained from CFD simulations. Two radial-inflow turbine test cases have been considered. The first test case consists of a high-pressure ratio RIT used as gas generator in the T100 turbo-shaft engine, designed and tested by Sundstrand Power Systems [26]. The second test case is the so-called ORCHID turbine, representative of an ultra-high pressure ratio, single stage RIT for experimental research on high temperature ORC systems. The stage has been designed and optimized by means of high-fidelity CFD methods by De Servi *et al.* [6].

CFD SETUP

The three-dimensional geometry of the T100 was constructed based on data from the open literature [27] and its discretization was performed using a commercial software [28]. Unsteady, single-passage, RANS computations were used to predict the turbine performance, using a structured mesh comprising about 3 million cells. The optimal cell count of the stator, impeller, and diffuser was informed from a mesh sensitivity study [29] based on the Richardson extrapolation method [30]. For the ORCHID turbine, a mesh of approximately 4 million cells was used to discretize the computational domain, as suggested in Cappiello *et al.* [24]. In this case, the computational domain only comprised the mesh of the convergent-divergent vane and that of the impeller.

For both test cases, the Ansys® CFX [28] flow solver was employed. The discretization of the advection terms was performed using a central differencing scheme (CDS), ensuring a second order accurate solution. Turbulence closure was obtained through the shear stress transport (SST $k-\omega$) model, and the turbulence equations were discretized using a hybrid scheme [31]. The uRANS equations were marched in time using a 1^{st} order backward Euler scheme and the time transformation method [32] was employed to perform single-passage calculations with uneven pitch ratios, and imposing sliding interfaces between the stationary and the rotating components. The total time of the simulation was set to one impeller passing period, subdivided into 100 time-steps. For each case, the computation was run until a time-periodic flow solution was achieved, by monitoring the value of the Mach number at the exit of the impeller blade passage at three different span-wise locations. The boundary conditions were imposed in terms of total thermodynamic conditions and flow direction at the inlet, and average static pressure at the outlet, see Table 2.2. For the T100, the average static pressure was specified at the diffuser exit section, while for the ORCHID at the impeller outlet section. The shroud wall was treated as a counter-rotating wall moving at the specified rotational speed.

Table 2.2: Boundary conditions and fluid models used in the uRANS simulations. The thermodynamic conditions of the MM fluid have been computed using a look-up table (LUT) method. The LUT has been generated using the multi-parameter equation of state (MEoS) [33] implemented by Huber *et al.* [17].

	T100	ORCHID
Fluid	Air	MM
EoS	Ideal-gas	MEoS
γ	1.4	1.025
P_{t0} / bar	4.13	18.1
T_{t0} / K	477.6	573
Z_{t0}	1.0	0.74
$\bar{\gamma}_{Pv}$	1.4	0.95
P_3 / bar	0.724	0.443
n / rpm	71700	98119

PERFORMANCE COMPARISON

Table 2.3 reports the predictions of the turbine power and total-total efficiency obtained with *TurboSim* and with the CFD. The deviation in the efficiency values is within 1% for both cases. For the T100, the experimentally measured efficiency [26] is also reported. It can be observed that the CFD over-predicts the efficiency by 5%. A possible cause of discrepancy is due to the choice of not modeling the losses associated to the leakage flow from the hub. In fact, the scalloping[1] in the T100 impeller disk results in a hub clearance extending from the leading edge of the impeller blades to a location ≈50% along the blade camberline. Thus, much like it happens at the tip of unshrouded rotor blades, leakage flow occurs at the hub between the blade root and the casing. However, to simplify the generation of the computational mesh, the impeller geometry was modeled in

[1] Disk scalloping is common practice in turbochargers, and it refers to the removal of material from the disk between the leading edge of adjacent blades. This helps reducing the stress on the disk in the region where centrifugal loads are highest.

this work without including the disk scallop. As a result, the leakage flow and associated mixing losses due to the generation of secondary flow structures are not captured in the CFD.

Table 2.3: Turbine performance prediction obtained with the ROM, CFD and experiments. The experimental data are available for the T100 only.

	T100[2]			ORCHID	
Quantity	**ROM**	**CFD**	**Exp.**	**ROM**	**CFD**
$\dot{W}$ / kW	66.3	69.8		10.1	10.2
η_{tt} / %	91.2	92.1	87.1	84.9	85

Further insights on the accuracy of the loss accounting methodology implemented can be gained by performing a loss breakdown analysis. The CFD-based loss breakdown was performed by mass flow averaging the flow quantities at the inlet and outlet of each component in both time and space as

$$\overline{Q} = \frac{\sum_{n}^{N}\left(\left[\sum_{\tau=0}^{10t} q(\tau)\right]^{\text{n}} \cdot \rho^{\text{n}} \cdot V_{\text{m}}^{\text{n}} \cdot A^{\text{n}}\right)}{\dot{m}}, \tag{2.38}$$

where q is a generic time and space dependent thermo-physical quantity, τ is a specific time instant and t corresponds to a passage period, thus $t = 100 \cdot \tau$. The term $\rho^{\text{n}} \cdot V_{\text{m}}^{\text{n}}$ is the mass flux across the n^{th} cell boundary, of area A^{n}.

By applying Equation 2.38 to calculate the space-time averaged isentropic outlet temperature and the entropy change across each component, the efficiency deficit can be calculated as

$$\Delta\eta = \frac{T_{\text{out,is}}\,\Delta s}{\Delta h_{\text{tt,is}}}. \tag{2.39}$$

where $\Delta h_{\text{tt,is}}$ is the isentropic work, also computed averaging the enthalpy using Equation 2.38.

Figure 2.6a and 2.6b show the results of the loss breakdown analysis performed with the two models. The efficiency penalty across the stator and the impeller are displayed, along with the loss associated to the exit kinetic energy. The outcome of the loss breakdown analysis qualitatively shows that *TurboSim* predicts efficiency values close to those of the CFD. Notably, the ROM successfully captures the lower efficiency of the ORCHID turbine, which is characterized by a comparatively much higher pressure ratio. Minor deviations between the two models arise when comparing the share of loss of each turbine component, especially concerning the impeller losses which are overestimated by

[2] Efficiency measured at the exit of the diffuser.

the ROM. In spite of the differences in the results illustrated in the plot, the accuracy of *TurboSim* is deemed adequate for systematic studies aimed at establishing guidelines for the design of *hiTORC-RIT*.

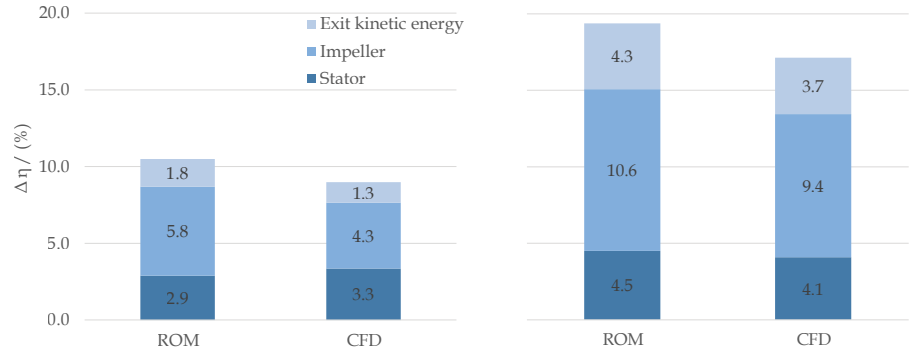

(a) T100 turbine.

(b) ORCHID turbine.

Figure 2.6: Loss breakdown obtained from calculation with *TurboSim* (ROM) and CFD.

2.4. RESULTS

TurboSim is used to generate design maps, namely contours and charts of key performance metrics as function of the most relevant independent variables of Equation 2.3. In particular, the influence of ψ_{is}, $\phi_{2,is}$, $\bar{\gamma}_{Pv}$, VR, and μ on the total-total and total-static stage efficiency is investigated. The size parameter, as defined by Perdichizzi & Lozza [1], was fixed to $SP = 0.025$ m in the study, a value typical of turbines for small-scale high-temperature ORC applications [6, 10]. For size parameters different from that considered, the work of Manfredi *et al.* [10] provides a complete treatment of its impact on efficiency. Constant geometrical scaling parameters and physical coefficients for loss accounting, whose values are listed in Appendix F, were used to perform the design of the RITs. To attain a fixed value of SP for all designs, the mass flow rate was adjusted for each combination of VR, $\bar{\gamma}_{Pv}$, and fluid. The size parameter is defined as

$$SP = \frac{\sqrt{\dot{Q}_{3,is}}}{\Delta h_{tt,is}^{0.25}}, \tag{2.40}$$

where $\dot{Q}_{3,is}$ is the volumetric flow rate at the stage outlet in isentropic conditions, and $\Delta h_{tt,is}$ is the isentropic work. Equation 2.40 can be rearranged considering $VR = \rho_{t0} / \rho_{3,is}$, $\dot{m} = \dot{Q}_{3,is} \cdot \rho_{3,is}$, and $\Delta h_{tt,is} = \psi_{is} \cdot U_2^2$, yielding

$$SP = \frac{\sqrt{\dot{m}\, VR}}{\sqrt{\rho_{t0}} \left(\psi_{is} \cdot U_2^2\right)^{0.25}}. \tag{2.41}$$

This relation was used to compute the mass flow rate $\dot{m}$, given SP, ψ_{is} and VR, and the total thermodynamic quantities at the inlet of the stage.

It should be noted that U_2 depends on the fluid characteristics, notably the speed of sound, according to the relation $U_2 = M_{U_2} \cdot a_2$, where M_{U_2} is the tip peripheral Mach number. Because complex molecule fluids feature comparatively low speed of sound, the peripheral speed and the isentropic work of stages designed for such compounds are lower than for stages operating with fluids made of simple molecules. Consequently, for a given SP, the mass flow rate of stages operating with HMC fluids is inevitably larger. This results in a variation of turbine power in the investigated design space, ranging from tens of kW for turbines operating with HMC fluids in combination with high values of VR and ψ_{is}, up to 550 kW for turbines designed for LMC fluids in combination with low VR and ψ_{is}.

2.4.1. INFLUENCE OF THE WORKING FLUID AND $\bar{\gamma}_{Pv}$ ON STAGE EFFICIENCY

The influence of the working fluid and $\bar{\gamma}_{Pv}$ on total-static efficiency are investigated by varying $VR \in (6, 80)$. Inlet thermodynamic conditions $P_r \in (0.5, 1.4)$ and $T_r \in (0.8, T_{f,max})$ have been considered to obtain $\bar{\gamma}_{Pv}$ values in the range $0.45 - 1.17$. $T_{f,max}$ is the maximum fluid temperature, which is a physical limit corresponding to the thermal stability of the molecule. Figure 2.7 illustrates the total-static efficiency as function of $\bar{\gamma}_{Pv}$. A color plot was used to display the variation of fluid molecular complexity (MC), which was evaluated as the number of active degrees-of-freedom of the molecule at its critical temperature [34]. The working fluids selected to generate the plots belong to the HMC class and are listed in Table 2.4 along with their MC and γ in dilute gas conditions.

The plots show that the efficiency decreases as the value of $\bar{\gamma}_{Pv}$ approaches that of γ, and the decrease is more appreciable for larger values of the volumetric flow ratio. For low values of VR the efficiency of turbines designed for fluids with different MC does not vary, therefore the variation of the fluid molecular complexity and of $\bar{\gamma}_{Pv}$ are not affecting the stage fluid dynamic performance. For intermediate and large values of VR there is a marginal effect of the MC on efficiency: the efficiency value lies within a $\pm 1\%$ uncertainty interval around the arithmetic average, shown with gray bands in Figure 2.7. The impact of the variation of ψ_{is} was furthermore examined for $\phi_{2,is}$ equal to 0.4. Notably, it can be observed that the efficiency increases as ψ_{is} is increased, and the efficiency curves become steeper the larger the load. The reason why the turbine is more efficient when designed at higher ψ_{is} will be clearer in the following. All these results suggest that the impact of $\bar{\gamma}_{Pv}$ on efficiency is more significant at large volumetric flow ratios and loads, as visible in the bottom right plot of Figure 2.7.

To better display the role of $\bar{\gamma}_{Pv}$ to turbine efficiency, the efficiency of turbines computed considering the fluids and the inlet thermodynamic conditions listed in Table 2.5 is further investigated. Three expansions of MM up to $VR = 20$ and starting from the initial conditions listed in Table 2.5 were plotted in the reduced pressure and temperature diagram of Figure 2.10. An LMC fluid in the dilute gas state has been included in the analysis and reported in the same table. Paradigmatic examples of RITs operating with LMC fluids in dilute gas state are turbochargers and gas turbines. Plots of the total-total and total-static efficiency against the work coefficient ψ_{is} are displayed in Figure 2.8 and 2.9.

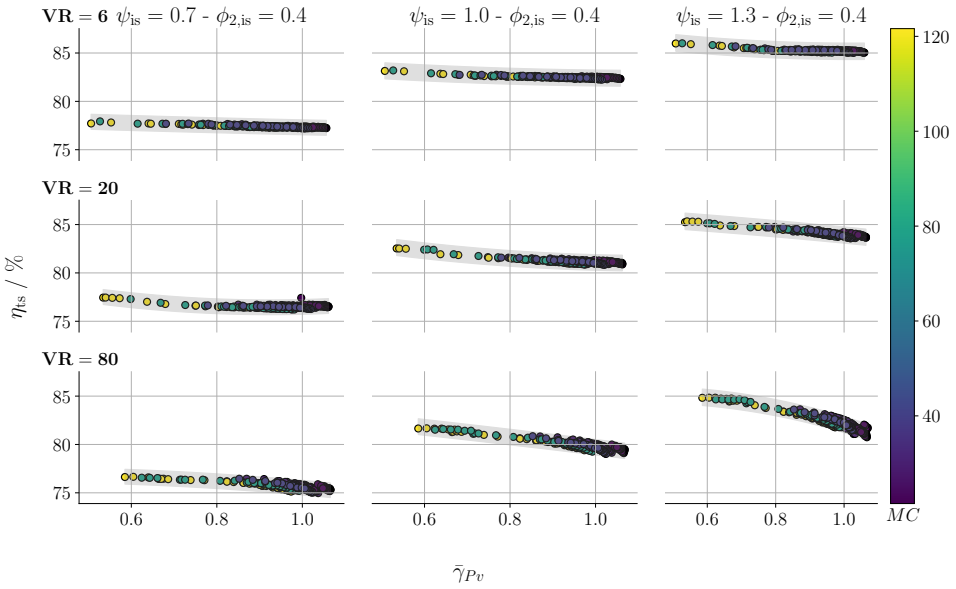

Figure 2.7: Total-static efficiency of RITs as a function of $\bar{\gamma}_{Pv}$ for working fluids of different molecular complexity MC. $SP = 0.025$ m, while $VR = 6$, 20 and 80 from top to bottom. ψ_{is} is equal to 0.7, 1.0 and 1.3 from left to right, and $\phi_{2,is}$ was fixed to 0.4. The gray bands indicate a ±1% uncertainty interval around the arithmetic average.

Table 2.4: Fluids used to generate the data displayed in Figure 2.7 and their main characteristics.

Fluid name	Chemical name	MC	γ
Ethanol	Ethyl alcohol	21.51	1.080
Butane	n-Butane	29.53	1.054
Pentane	-	39.80	1.040
MM	Hexamethyldisiloxane	78.35	1.026
Dodecane	-	121.63	1.018

Figure 2.8 shows the variation of efficiency with three values of VR, and for a fixed $\phi_{2,is}$ of 0.4. Similarly, Figure 2.9 illustrates the impact of $\phi_{2,is}$ on stage efficiency for $VR = 20$. The curves have been obtained by averaging the efficiency predicted at each value of ψ_{is} for siloxane MM and the LMC fluid in the thermodynamic conditions listed in Table 2.5. The colored bands depict the min-max variation around the average, with the turbines designed for expansions characterized by high $\bar{\gamma}_{Pv}$ featuring the lowest efficiency values, in accordance with the results displayed in Figure 2.7. The main conclusion that can be drawn by inspecting the plots is that the value of the optimal work coefficient is weakly dependent on VR, while it is affected by the value of $\phi_{2,is}$.

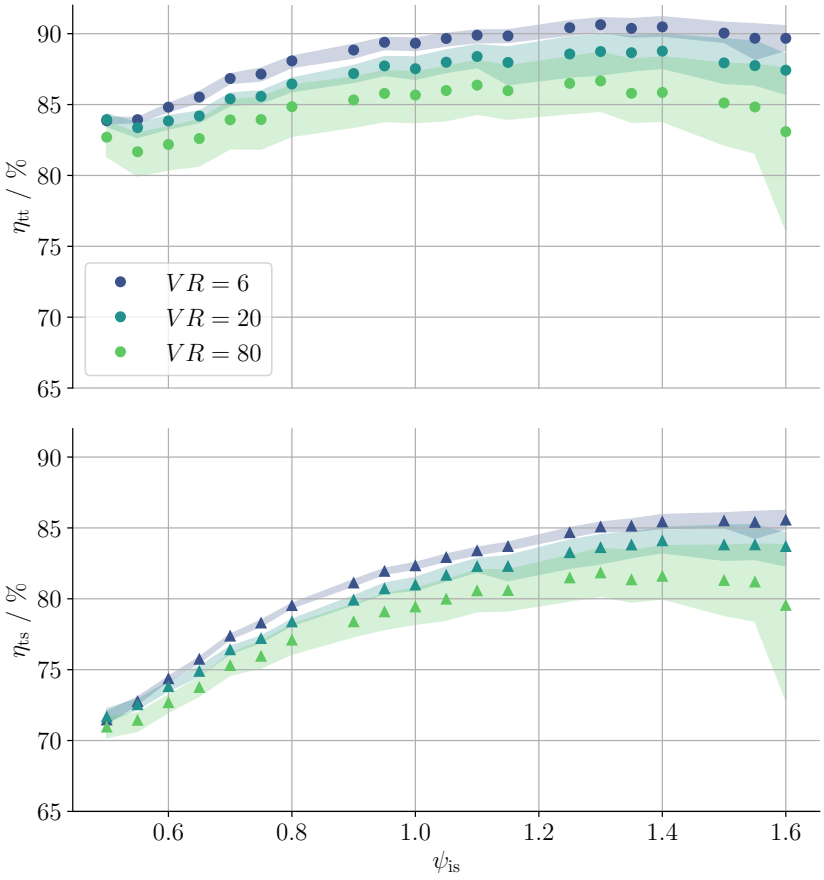

Figure 2.8: Total-total (◯) and total-static (△) efficiency as a function of the load coefficient ψ_{is}, for different values of VR and for a fixed value of the flow coefficient $\phi_{2,\mathrm{is}} = 0.4$. The markers indicate the average value of efficiency among the cases listed in Table 2.5, while the colored bands show the min-max variation of the efficiency for $\tilde{\gamma}_{Pv}$ that varies between 0.78 and 1.15.

Table 2.5: Boundary conditions for the turbine operating with the LMC and the HMC (siloxane MM) fluid. MMi denotes siloxane MM in ideal gas conditions, while MMni1 and MMni2 refer to MM conditions in the nonideal thermodynamic regime.

	MC	$P_{\mathrm{t0,r}}$	$T_{\mathrm{t0,r}}$	Z_{t0}	$\tilde{\gamma}_{Pv}$
LMC	7.0	0.2	4.0	1.0	1.15
MMi	78.35	0.2	1.1	0.95	1.0
MMni1	78.35	1.0	1.1	0.71	0.92
MMni2	78.35	2.0	1.1	0.43	0.78

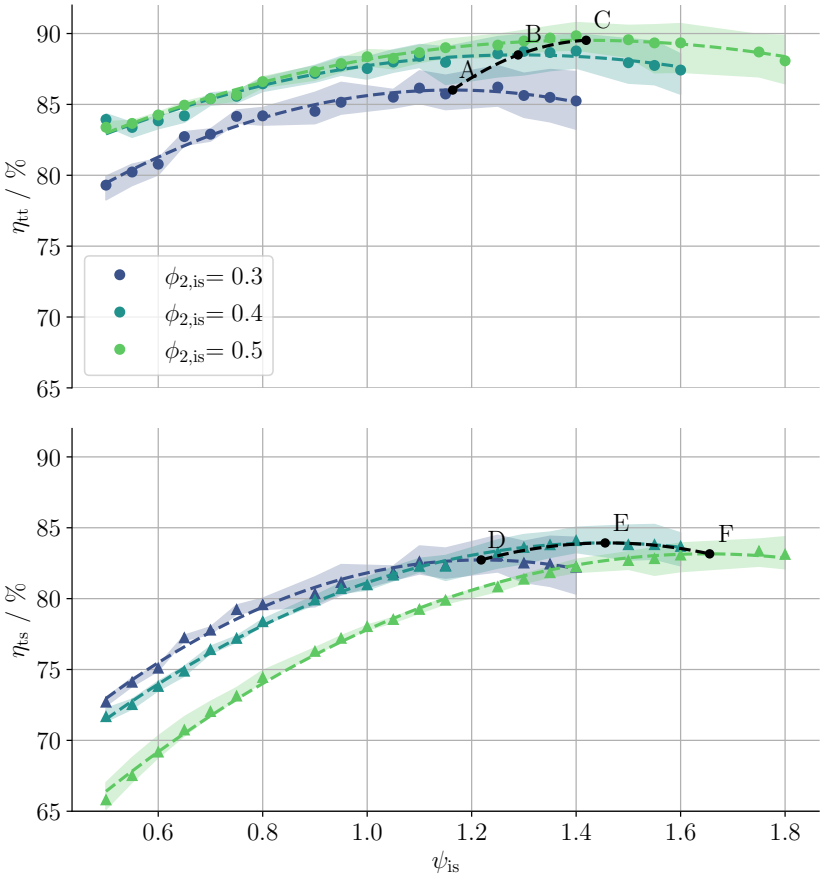

Figure 2.9: Total-total (◯) and total-static (△) efficiency as a function of the load coefficient ψ_{is}, for different values of $\phi_{2,is}$ and for a fixed value of the expansion ratio $VR = 20$. The colored markers indicate the average value of efficiency among the cases listed in Table 2.5, while the colored bands show the min-max variation of the efficiency for $\tilde{\gamma}_{Pv}$ that varies between 0.78 and 1.15. The black dots display the values of the maxima at different values of $\phi_{2,is}$ estimated by fitting the data with a 2nd order polynomial, shown with the dashed line. The black dashed curves are 2nd order polynomials fitting the optimal combinations of ψ_{is} and $\phi_{2,is}$.

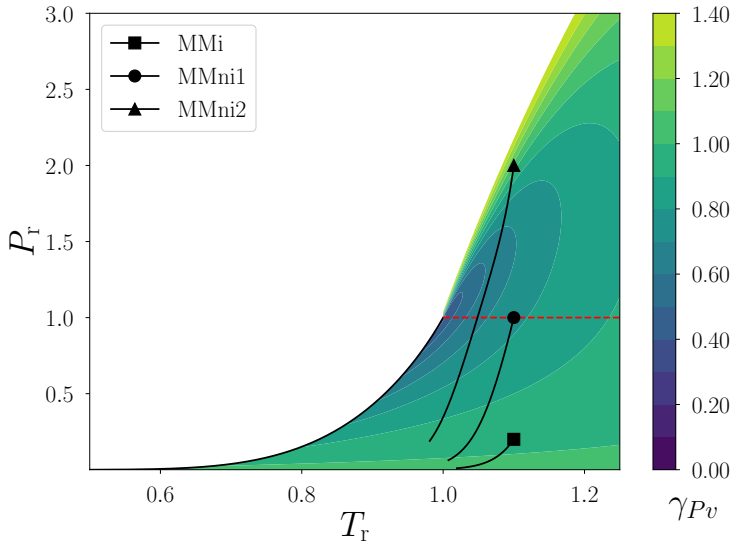

Figure 2.10: Reduced $P-T$ diagram for MM showing γ_{Pv} contours and three paradigmatic expansions at $VR = 20$, and starting from the inlet conditions listed in Table 2.5, namely MMi (□), MMni1 (◯), and MMni2 (△).

2.4.2. LOSS BREAKDOWN ANALYSIS

Insight into the impact of the duty coefficients $\phi_{2,is}$, ψ_{is} on loss mechanisms is gained by examining the design layout of the optimal stages labeled with A, B and C in Figure 2.9, and the corresponding loss breakdown. From theoretical considerations, it can be demonstrated that the degree of reaction r^* decreases for increasing values of $\phi_{2,is} - \psi_{is}$. As r^* decreases, the enthalpy drop across the impeller reduces, along with the density variation. Lower density variation leads to a lower impeller outlet / inlet area ratio A_3/A_2, as illustrated in Figure 2.11. The same figure also reports the values of A_3/A_2 and r^* for each of the three configurations. Moreover, Figure 2.12 shows that both absolute and relative flow angles at the outlet decrease from A to C, ultimately affecting losses and efficiency. Figure 2.13 illustrates the efficiency penalty associated to each of the loss mechanisms occurring in the stages. Because the leakage loss is inversely proportional to $\cos\beta_3$ [16], lower values of the outlet flow angle entail lower tip leakage losses for case C, as confirmed by the analysis. On the contrary, being directly proportional to $\cos\beta_3$, see Equation 2.35, profile losses are lower for case A.

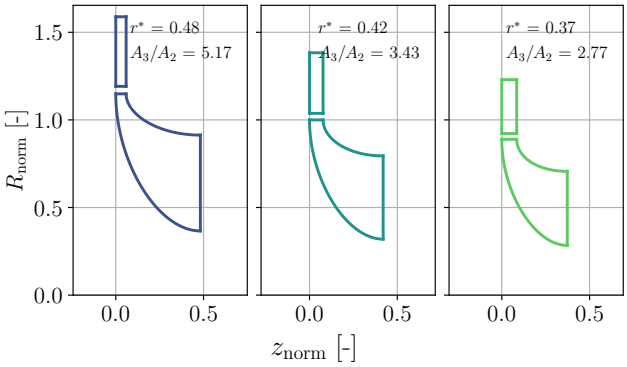

Figure 2.11: Meridional flow path of the optimal designs A, B and C of Figure 2.9. The axial and radial coordinates are non-dimensionalized by the tip radius of case B.

To further clarify the effect of $\bar{\gamma}_{Pv}$ on loss mechanisms, trends of the Mach numbers at the exit of the stator and of the impeller for turbines operating with fluids in the conditions reported in Table 2.5 are shown in Figure 2.14. One can notice that stages characterized by lower values of $\bar{\gamma}_{Pv}$ yield the lowest Mach numbers at the outlet of both components. Lower cascade outlet Mach numbers lead to reduced fluid dynamic losses, as confirmed by the trends of the efficiency penalty $\Delta\eta$ illustrated in Figure 2.15.

Figure 2.16 reports the results of the loss breakdown analysis for the stator and the impeller of two turbines designed for the cases LMC and MMni2, featuring $\psi_{is} = 1.35$, $\phi_{2,is} = 0.4$ and $VR = 20$. The share of mixing losses for both the stator and impeller is very similar between the LMC and MMni2 cases, due to the opposite influence of $\bar{\gamma}_{Pv}$ and Mach number on loss, which could also be inferred by the right hand plot of Figure 2.1. Similar conclusions on mixing losses were drawn by Tosto *et al.* [8], who showed that stages operating with fluid molecules characterized by different complexity, or operating in the nonideal thermodynamic regime, feature comparable values of mixing losses

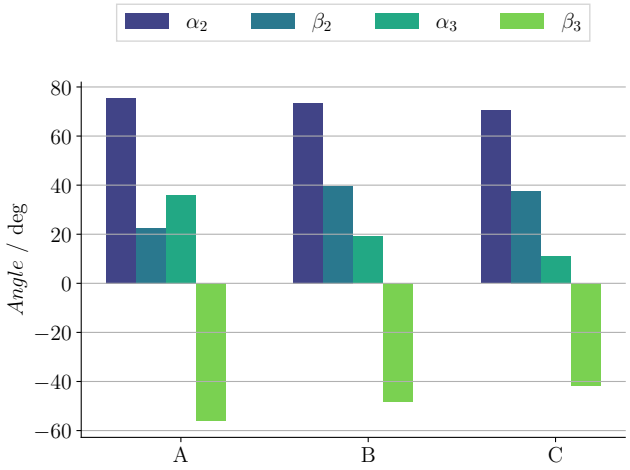

Figure 2.12: Impeller absolute flow angles (α) and relative flow angles (β) for the A, B and C cases.

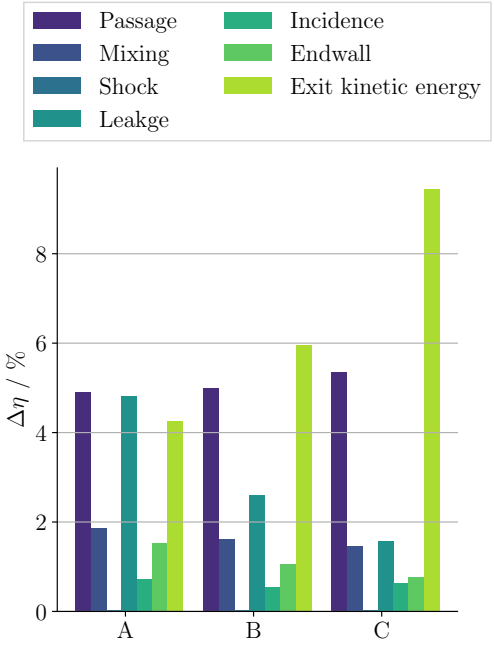

Figure 2.13: Stage (stator + impeller) loss breakdown for optimum designs A, B and C shown in Figure 2.9. The optimal work coefficients are, respectively, 1.15, 1.3 and 1.4. Results obtained for $VR = 20$.

when operating at the same VR. Endwall and profile losses mainly depend on the Mach number and flow angle, and are less relevant for the MMni2 case due to the lower exit Mach numbers.

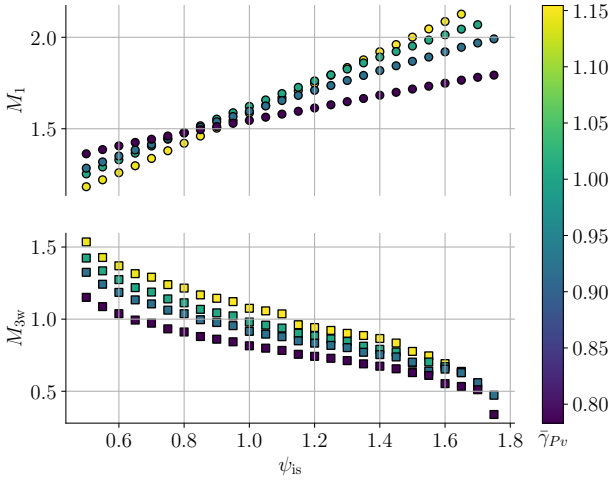

Figure 2.14: Absolute Mach number at the outlet of the stator (◯) and relative Mach number at the outlet of the impeller (□) as a function of the load coefficient ψ_{is}, for the LMC, MMi, MMni1 and MMni2 cases listed in Table 2.5 at fixed $VR = 20$, $SP = 0.025$ m, and $\phi_{2,is} = 0.4$.

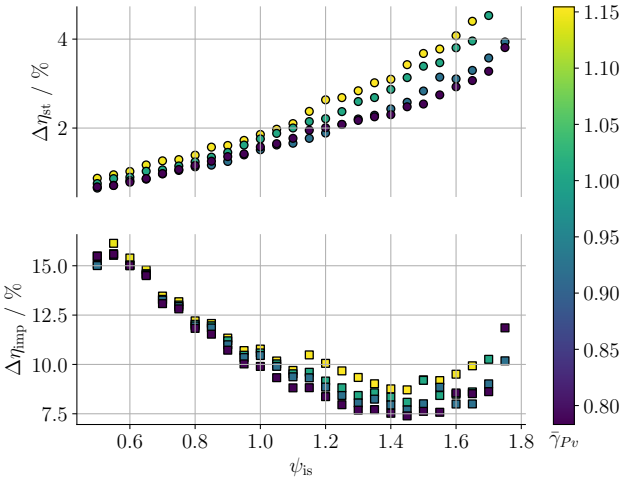

Figure 2.15: Cumulative stator (◯) and impeller (□) loss as a function of the load coefficient ψ_{is}, for the LMC, MMi, MMni1 and MMni2 cases listed in Table 2.5 at fixed $VR = 20$, $SP = 0.025$ m, and $\phi_{2,is} = 0.4$.

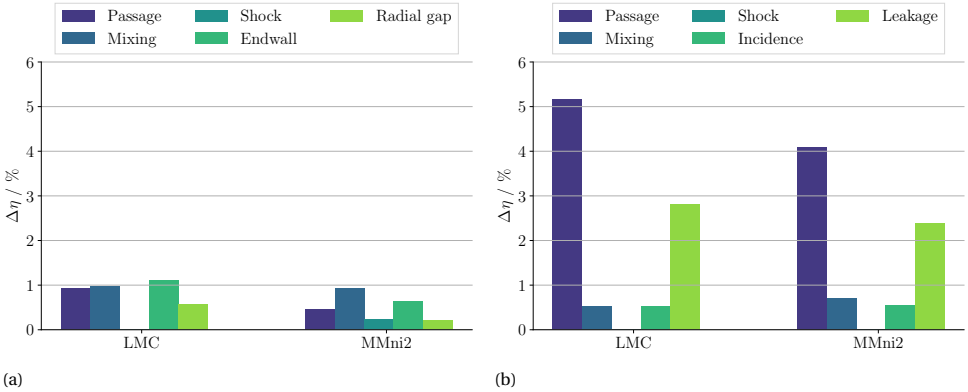

Figure 2.16: Loss breakdown in the stator (a) and the impeller (b) for the LMC and MMni2 cases listed in Table 2.5. $\psi_{is} = 1.35$, $\phi_{2,is} = 0.4$ and $VR = 20$.

2.4.3. INFLUENCE OF THE MERIDIONAL VELOCITY RATIO ON EFFICIENCY

A design parameter which largely affects the turbine layout and whose optimal value for *hiTORC-RIT* is not reported in the literature is the meridional velocity ratio of the impeller, herein denoted with μ. An investigation is therefore carried out to gain insight on its impact on stage efficiency and turbine design. Design maps are computed for $\mu = 1.2, 1.4, 1.6$. In this case, VR was set to the nominal value of the ORCHID turbine, along with the other design parameters listed in Appendix F. The working fluid is siloxane MM, and the stage boundary conditions are those previously listed in Table 2.2. The maps of Figure 2.17a, 2.17b, and 2.17c show the isolines of the total-total efficiency, whereas those of Figure 2.17d, 2.17e, and 2.17f display the contours of the total-static efficiency. The efficiency values reported in the charts indicate that the meridional velocity ratio marginally affects the maximum η_{tt} and η_{ts}, and the only appreciable effect is related to the width and location of the region of optimal designs. Considering the value of η_{tt}, the isoline corresponding to the optimum designs shifts towards lower $\phi_{2,is}$ as μ is increased. The same change occurs to the isoline delimiting the designs featuring the highest η_{ts}. The red markers on the total-total and total-static efficiency maps for $\mu = 1.4$ indicate the design point of the ORCHID turbine and the calculated η_{tt} and η_{ts}.

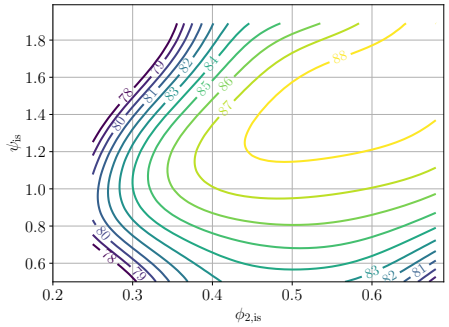

(a) η_{tt} isolines for $\mu = 1.2$.

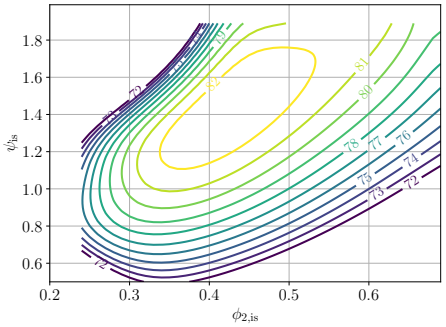

(d) η_{ts} isolines for $\mu = 1.2$.

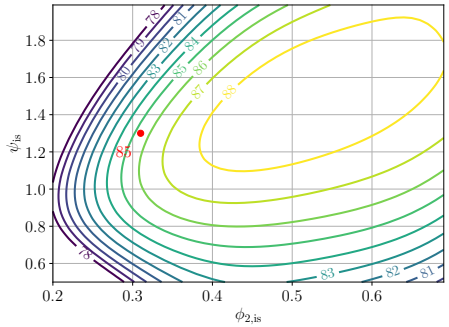

(b) η_{tt} isolines for $\mu = 1.4$.

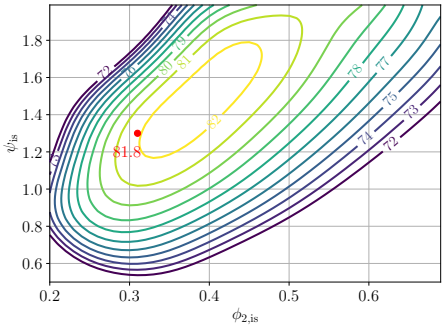

(e) η_{ts} isolines for $\mu = 1.4$.

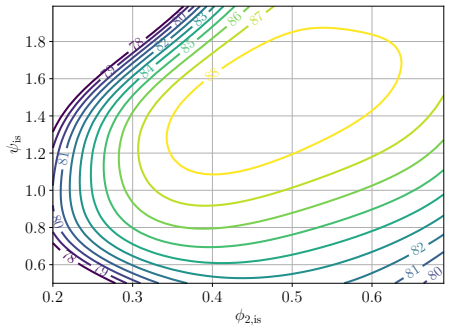

(c) η_{tt} isolines for $\mu = 1.6$.

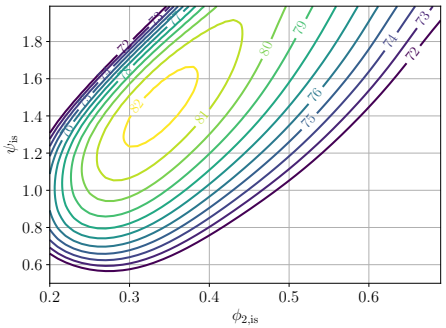

(f) η_{ts} isolines for $\mu = 1.6$.

Figure 2.17: Design maps showing the contours of total-total (a, b, c) and total-static (d, e, f) efficiency of turbines operating at $VR = 49.7$, and for increasing values of μ. The fluid is siloxane MM. The red markers in (b) and (e) highlights the design point and efficiency of the ORCHID turbine.

2.5. DESIGN GUIDELINES

The results used to generate the maps presented in the previous sections are finally converted into design guidelines, namely charts that can be used to quickly size the turbine and compute its efficiency in system-level analysis and optimization. A relevant example in which such a model is exploited is reported in Krempus *et al.* [35].

Figure 2.18 shows the trend of maximum η_{tt} and η_{ts} as a function of $VR \in (3, 80)$ for the four cases listed in Table 2.5. The duty coefficients ϕ_2, ψ corresponding to the maximum efficiency point at each value of VR are displayed in the left hand side graphs, while the corresponding values of the efficiency are shown on the right hand side.

The optimal flow coefficient ϕ_2 value (marked by triangles) remains unchanged above $VR \simeq 10$, represented in the figure using triangular markers. The optimal ϕ_2 value to maximize η_{tt} is $\approx$ 0.52 , while $\phi_2 \approx 0.43$ should be selected to design the turbine for maximum η_{ts}. By comparing the left hand side plots of the Figure 2.18a to 2.18d, one can notice that the optimal ϕ_2 is not affected by change in the value of $\bar{\gamma}_{Pv}$.

On the contrary, the optimal load coefficient ψ (marked by crosses) shows appreciable differences when $\bar{\gamma}_{Pv}$ varies. At low VR, the optimum $\psi \approx 1.3$ for either maximum η_{tt} and η_{ts}, regardless of the value of $\bar{\gamma}_{Pv}$. As VR increases up to values between 10 and 20 depending on $\bar{\gamma}_{Pv}$, ψ increases. This result is in accordance with the findings of Da Lio [36], who also observed that the optimal design load coefficient increases as VR increases from 2.3 to 8.7 for turbines of similar scale and operating with *R245fa* as working fluid. However, as VR is further increased, the value of load coefficient that maximizes η_{tt} decreases to $\psi \approx 1.15$ in Figure 2.18a for the LMC case, and $\psi \approx 1.3$ for the MMi case in Figure 2.18b. For the cases MMni1 and MMni2 of Figure 2.18c and 2.18d, whereby $\bar{\gamma}_{Pv} < 1$, the optimal $\psi \approx 1.35$ and 1.42.

A similar trend occurs with the value of ψ that maximizes η_{ts}, although the change with $\bar{\gamma}_{Pv}$ is less pronounced and ψ varies between 1.3 and 1.45 from Figure 2.18a to 2.18d. The trends shown in Figure 2.18 also highlight that the value of the optimal ψ for maximum η_{tt} is very similar to that guaranteeing maximum η_{ts} when $\bar{\gamma}_{Pv} < 1$.

In summary, when designing RITs operating with fluids in thermodynamic states for which $\bar{\gamma}_{Pv} \geq 1$ and $VR < 10$, as in the case of turbine stages operating with LMC fluids in close to dilute gas conditions, one may choose ψ,$\phi_2 \approx (1.3, 0.52)$ for optimal η_{tt}, and ψ,$\phi_2 \approx (1.3, 0.35)$ for optimal η_{ts}. Conversely, when designing machines for which the fluid states lead to $\bar{\gamma}_{Pv} < 1$ and $VR > 10$, as for turbines of high-temperature ORC power systems, one should select ψ,$\phi_2 \approx (1.43, 0.52)$ for optimal η_{tt}, and ψ,$\phi_2 \approx (1.45, 0.43)$ for optimal η_{ts}.

Considering the values of efficiency, both the optimal η_{tt} and the optimal η_{ts} decrease as VR is increased, as already established by other authors [1, 10, 36]. However, when comparing the efficiency for the four cases displayed in Figure 2.18, the highest values of the efficiency are obtained when $\bar{\gamma}_{Pv} < 1$ for any given VR. Furthermore, the efficiency drop observed at increasing VR values reduces for decreasing values of $\bar{\gamma}_{Pv}$.

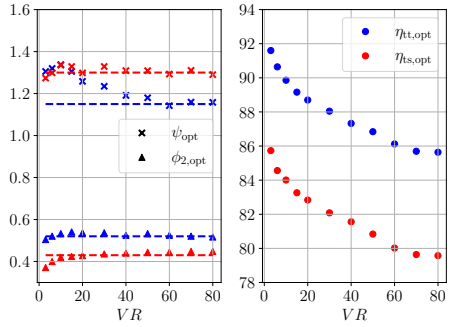

(a) LMC case, $\bar{\gamma}_{Pv} = 1.15$.

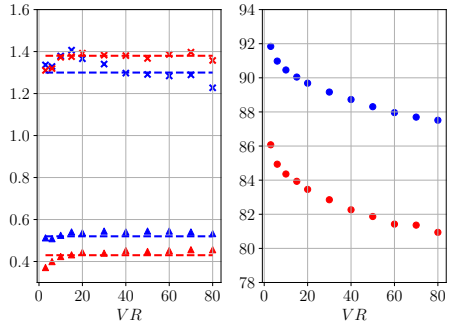

(b) MMi case, $\bar{\gamma}_{Pv} = 1.0$.

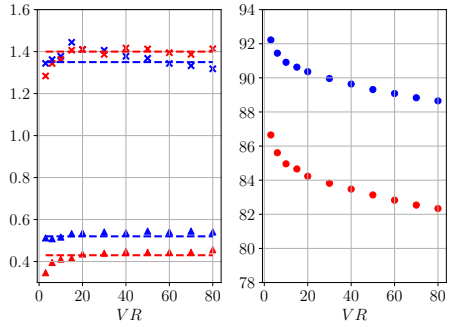

(c) MMni1 case, $\bar{\gamma}_{Pv} = 0.92$.

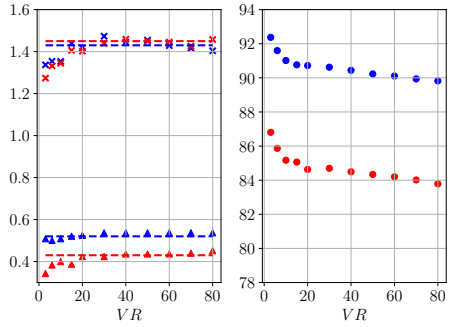

(d) MMni2 case, $\bar{\gamma}_{Pv} = 0.78$.

Figure 2.18: Optimal ψ (×) and ϕ_2 (△) as a function of VR, and corresponding maximum η_{tt} and η_{ts} as a function of VR. The blue markers indicate the duty coefficients that maximize η_{tt} and the red ones those that maximize η_{ts}. The results were obtained for the LMC, MMi, MMni1 and MMni2 cases listed in Table 2.5.

2.6. CONCLUSION & OUTLOOK

Design guidelines for radial-inflow turbines of high-temperature organic Rankine cycle power systems are documented. The influence of the working fluid, nonideal thermodynamic effects, and of the volumetric flow ratio on the choice of optimal design parameters ψ, ϕ_2 and stage efficiency has been investigated. Values up to $VR = 80$ have been considered, while the size parameter was fixed to $SP = 0.025$ m, a value typical of RITs for high-temperature ORC systems up to few hundreds kW power capacity, depending on the working fluid. The guidelines have been derived by analyzing the results obtained with a reduced-order model for turbine design and performance assessment, and based on first principles. The accuracy of the reduced order model has been verified against high fidelity CFD simulations of two test cases representative of a high pressure ratio gas turbine, and a *hiTORC-RIT*. The main outcomes of this study can be summarized as follows:

- The efficiency predicted by the reduced-order model is within 1% the value ob-

tained with uRANS. The model was able to correctly capture the effect of the volumetric flow ratio on the efficiency.

- The optimal value of duty coefficients ψ and ϕ_2 depends on the value of the volumetric flow ratio, and on the value of $\bar{\gamma}_{Pv}$ along the expansion process. RITs for high temperature ORC systems should be designed with ψ,$\phi_2 \approx (1.43, 0.52)$ for optimal η_{tt}, and ψ,$\phi_2 \approx (1.45, 0.43)$ for optimal η_{ts}.
- The values of the optimal duty coefficients derived in this work differ from those that can be inferred from the design maps of Rodgers [37] and Chen & Baines [18]. Therefore, it can be argued that the application of conventional design maps can lead to sub-optimal *hiTORC-RIT* designs.
- Nonideal thermodynamic effects quantified through $\bar{\gamma}_{Pv}$ have an appreciable impact on turbine efficiency only for volumetric flow ratios higher than 10, while their influence is negligible at low values of VR.
- The results documented in this work extend the analysis provided in [1, 10, 36] to volumetric flow ratios beyond 50. From a conceptual standpoint, similar conclusions related to the choice of the optimal load coefficient for *hiTORC-RIT* presented in Da Lio [36] were found.
- The study offers new insights into why *hiTORC-RIT* operating in nonideal thermodynamic conditions can achieve relatively high efficiency, even when designed for very high volumetric flow ratio.

Albeit the investigation is focused on *hiTORC-RIT*, the derived guidelines can be applied to the preliminary design of radial-inflow turbines operating with arbitrary working fluids, at low to very high volumetric flow ratios, and in both ideal and nonideal thermodynamic regime. Future work will be devoted to extend the capability of the reduced-order model to off-design performance assessment, to the development of design guidelines for mixed-flow turbines, and to perform a campaign of experimental validation using the ORCHID facility at the Propulsion and Power laboratory of Delft University of Technology.

BIBLIOGRAPHY

1. Perdichizzi, A. & Lozza, G. *Design Criteria and Efficiency Prediction for Radial Inflow Turbines* in *Proceedings of the ASME Turbo Expo: Power for Land, Sea, and Air* **1** (1987), V001T01A086. doi:10.1115/87-GT-231.
2. Glassman, A. J. *Computer program for design analysis of radial-inflow turbines* Technical report D-8164 (1976).
3. Mounier, V., Olmedo, L. E. & Schiffmann, J. Small scale radial inflow turbine performance and pre-design maps for Organic Rankine Cycles. *Energy* **143,** 1072–1084. doi:10.1016/j.energy.2017.11.002 (2018).
4. Manfredi, M., Alberio, M., Astolfi, M. & Spinelli, A. *A Reduced-Order Model for the Preliminary Design of Small-Scale Radial Inflow Turbines* in *Turbo Expo: Power for Land, Sea, and Air* **4** (2021), V004T06A013. doi:10.1115/gt2021-59444.
5. Baines, N. C. *A meanline prediction method for radial turbine efficiency* Technical report (1998).
6. De Servi, C. M., Burigana, M., Pini, M. & Colonna, P. Design Method and Performance Prediction for Radial-Inflow Turbines of High-Temperature Mini-Organic Rankine Cycle Power Systems. *ASME. J. Eng. Gas Turbines Power* **141,** 091021. doi:10.1115/1.4043973 (2019).
7. Giuffré, A. & Pini, M. Design Guidelines for Axial Turbines Operating With Non-Ideal Compressible Flows. *Journal of Engineering for Gas Turbines and Power* **143,** 011004. doi:10.1115/1.4049137 (2021).
8. Tosto, F., Giuffré, A., Colonna, P. & Pini, M. Flow deviation and critical choking in transonic turbine cascades operating with non-ideal compressible flows. *Journal of the Global Power and Propulsion Society* **6,** 181–199. doi:10.33737/jgpps/151659 (2022).
9. Whitfield, A. & Baines, N. C. *Design of Radial Turbomachines* ISBN: 978-0-470-21667-5 (Longman Scientific & Technical, Harlow, England, 1990).
10. Manfredi, M., Spinelli, A. & Astolfi, M. Definition of a general performance map for single stage radial inflow turbines and analysis of the impact of expander performance on the optimal ORC design in on-board waste heat recovery applications. *Applied Thermal Engineering* **224,** 119390. doi:10.1016/j.applthermaleng.2023.119390 (2023).
11. Kouremenos, D. A. & Kakatsios, X. K. The three isentropic exponents of dry steam. *Forschung im Ingenieurwesen* **51,** 117–122. doi:10.1007/bf02558416 (1985).
12. Guardone, A., Colonna, P., Pini, M. & Spinelli, A. Nonideal Compressible Fluid Dynamics of Dense Vapors and Supercritical Fluids. *Annual Review of Fluid Mechanics* **56,** 241–269. doi:10.1146/annurev-fluid-120720-033342 (2024).

13. Wheeler, A. P. S. & Ong, J. The Role of Dense Gas Dynamics on Organic Rankine Cycle Turbine Performance. *Journal of Engineering for Gas Turbines and Power* **135,** 102603. doi:10.1115/1.4024597 (2013).

14. Baumgärtner, D., Otter, J. J. & Wheeler, A. P. *The effect of isentropic exponent on supersonic turbine wakes* in *International Seminar on Non-Ideal Compressible-Fluid Dynamics for Propulsion & Power* (2020), 153–161. doi:10.1007/978-3-030-69306-0_16.

15. Baumgärtner, D., Otter, J. J. & Wheeler, A. P. S. The Effect of Isentropic Exponent on Transonic Turbine Performance. *Journal of Turbomachinery* **142,** 081007. doi:10.1115/1.4046528 (2020).

16. Denton, J. D. Loss mechanisms in turbomachines. *Journal of Turbomachinery* **115,** 621–656. doi:10.1115/93-gt-435 (1993).

17. Huber, M. L., Lemmon, E. W., Bell, I. & McLinden, M. O. The NIST REFPROP database for highly accurate properties of industrially important fluids. doi:10.1021/acs.iecr.2c01427 (2022).

18. Chen, H. & Baines, N. C. The aerodynamic loading of radial and mixed-flow turbines. *International Journal of Mechanical Sciences* **36,** 63–79. doi:10.1016/0020-7403(94)90007-8 (1994).

19. Meitner, P. L. & Glassman, A. J. *Computer Code for Off-Design Performance Analysis of Radial-lnflow Turbines With Rotor Blade Sweep* Technical report 83-C-4 (1983).

20. Coull, J. D. Endwall Loss in Turbine Cascades. *Journal of Turbomachinery* **139,** 081004. doi:10.1115/1.4035663 (2017).

21. Sieverding, C. H., Stanislas, M. & Snoeck, J. The Base Pressure Problem in Transonic Turbine Cascades. *Journal of Engineering for Power* **102,** 711–718. doi:10.1115/1.3230330 (1980).

22. Vimercati, D., Gori, G. & Guardone, A. Non-ideal oblique shock waves. *Journal of Fluid Mechanics* **847,** 266–285. doi:10.1017/jfm.2018.328 (2018).

23. AMES. *Equations, tables, and charts for compressible flow* Technical report (1953).

24. Cappiello, A., Majer, M., Tuccillo, R. & Pini, M. *On the Influence of Stator-Rotor Radial Gap Size on the Fluid-Dynamic Performance of Mini-ORC Supersonic Turbines* in *Proceedings of the ASME Turbo Expo 2022: Turbomachinery Technical Conference and Exposition* **10B** (2022), V10BT35A015. doi:10.1115/gt2022-83309.

25. Agromayor, R., Müller, B. & Nord, L. O. One-Dimensional Annular Diffuser Model for Preliminary Turbomachinery Design. *International Journal of Turbomachinery, Propulsion and Power* **4,** 31. doi:10.3390/ijtpp4030031 (2019).

26. Jones, A. C. Design and Test of a Small, High Pressure Ratio Radial Turbine. *Journal of Turbomachinery* **118,** 362–370. doi:10.1115/1.2836651 (1996).

27. Sauret, E. *Open Design of High Pressure Ratio Radial-Inflow Turbine for Academic Validation* in *Proceedings of the ASME 2012 International Mechanical Engineering Congress and Exposition* **7** (2012), 3183–3197. doi:10.1115/IMECE2012-88315.

28. Ansys® CFX. Academic Research CFX, Release 22.0.

29. Matabuena, L. S. *Radial Turbine-Diffuser Interaction: Effect of Tip Gap* MA thesis (Delft University of Technology, 2023).

30. Roache, P. J. *Verification and Validation in Computational Science and Engineering* 446. ISBN: 978-0-913478-08-0 (Hermosa Publishers, Albuquerque, NM, 1998).

31. Barth, T. J. & Jespersen, D. C. *The Design and Application of Upwind Schemes on Unstructured Meshes* in *Proceedings of the 27th AIAA Aerospace Sciences Meeting* (American Institute of Aeronautics and Astronautics, Reno, NV, Jan. 1989). doi:10.2514/6.1989-366.

32. Giles, M. B. Calculation of unsteady wake/rotor interaction. *Journal of Propulsion and Power* **4,** 356–362. doi:10.2514/3.23074 (1988).

33. Span, R. & Wagner, W. A New Equation of State for Carbon Dioxide Covering the Fluid Region from the Triple-Point Temperature to 1100 K at Pressures up to 800 MPa. *Journal of Physical and Chemical Reference Data* **25,** 1509–1596. doi:10.1063/1.555991 (1996).

34. Harinck, J., Guardone, A. & Colonna, P. The Influence of Molecular Complexity on Expanding Flows of Ideal and Dense Gases. *Physics of Fluids* **21,** 086101. doi:10.1063/1.3194308 (2009).

35. Krempus, D., Beltrame, F., Majer, M., Servi, C. M. D., Vos, R. & Colonna, P. *ORC Waste Heat Recovery System for the Turboshaft Engines of Turboelectric Aircraft* in *Aerospace Europe Conference 2023* (2023).

36. Da Lio, L. *Preliminary design of organic fluid turbines to predict the efficiency* PhD thesis (University of Padova, 2019).

37. Rodgers, C. *Small High Pressure Ratio Turbines* Technical report TR-1987-01 (Sundstrand Turbomach, San Diego, CA, June 1987).

3

PRELIMINARY DESIGN OF THE ORCHID TURBOGENERATOR: A NOVEL PROTOTYPE FOR EXPERIMENTAL RESEARCH ON RITS FOR HIGH-TEMPERATURE ORC SYSTEMS

Parts of this chapter have been published in:

M. Majer, S. Chatterton, L. Dassi, E. Gheller, P. E. L. M. Pennacchi, P. Colonna, M. Pini, *Mechanical design and rotordynamic analysis of the ORCHID turbine,* Journal of the Global Power and Propulsion Society **8**, 1–22 (2025).

ABSTRACT
The ORCHID turbine is a laboratory single-stage 10 kW high-speed (~100 krpm) radial-inflow turbine for high-temperature / high-efficiency organic Rankine cycle (ORC) systems, designed at the Propulsion and Power laboratory of Delft University of Technology. It will be installed within a test section of the organic Rankine cycle hybrid integrated device (ORCHID) facility, the setup for fundamental and applied studies on ORC technology currently in operation in the same lab. Experimental data from future measurement campaigns will be employed to validate design and performance prediction tools and to develop best practices for operating these unconventional machines, whose most notable features are the ultra-high expansion ratio (> 40), highly supersonic flow in the stator (M > 2), and the large flow deflection within the rotor channels (> 90°). In this chapter, a multi-disciplinary approach for the design of the ORCHID turbine rotor is presented, including the selection of main components such as bearings and seals. Methods to carry out the mechanical assessment of the impeller, and the estimation of the main thermal loads allowing the determination of the cooling requirements, were documented. Furthermore, the rotordynamic assessment and best practices for the numerical evaluation of the rotordynamic characteristics and stability of high-speed ORC turbine rotors are presented. The emphasis is on three main aspects: i) the modeling and quantification of the damping characteristics of a squeeze film damper (SFD) cartridge for the selected turbocharger ball bearings supporting the turbine shaft; ii) the characterization of the stiffness and damping coefficients of a custom designed pocket gas seal, performed using 3D RANS simulations; iii) the analysis of linear elastic rotordynamic simulations using a finite beam element model of the turbine rotor. Results of the rotordynamic simulations show that the rotor would operate in the sub-critical regime with respect to the first bending mode. The influence of model parameters such as the rotor eccentricity and the orbit radius was included in the analysis by conducting a parametric study of the SFD fluid forces. The Campbell diagrams show that shaft bending frequencies are significantly affected by changes in the SFD dynamic response depending on the rotational speed. The influence of the stiffness of rolling bearing elements and of the destabilizing forces due to the impeller and gas seal cross-coupled stiffness was also evaluated. The rigidity of the rolling elements slightly affects the shaft bending mode, while large values of the destabilizing forces cause a rotordynamic instability of the first rigid mode.

3.1. INTRODUCTION

The initial mechanical design of the ORCHID turbine is presented in this chapter. Building upon the fluid dynamic design of the expander stage, the rotor layout was developed, including the selection of essential components such as bearings and seals. Mechanical loads and the thermal power dissipated by the machine were also estimated. The finite element method was applied to evaluate the maximum mechanical stresses in the impeller and the power transferred to the lubricant flow, for which a finite element model of the entire turbine assembly was generated. The chapter ends with the development of a beam element model of the turbine rotor, the modeling of the most relevant rotordynamic coefficients, and the results of rotordynamic analyses of the shaft train.

The ORCHID turbine is a single stage supersonic radial inflow turbo expander whose fluid dynamic design was carried out in the TU Delft Propulsion and Power research group, and is representative of turbines for high-temperature, low-power-capacity ORC systems [1]. The device can generate ≈ 10 kW of mechanical power at the design point and will be tested in the ORCHID setup, a unique closed-loop test rig capable of delivering superheated or supercritical siloxane MM vapor up to 25 bar and 300 °C, and with a maximum mass flow rate of ~1.5 kg s^{-1} [2].

The main design parameters considered by De Servi *et al.* [1] for the sizing of the turbine are reported in Table 3.1 together with the most relevant geometrical constraints.

Table 3.1: Main design variables and geometrical constraints for the design of the ORCHID turbine stage by De Servi *et al.* [1].

Description	**Symbol**	**Value and unit**
Design variables		
Isentropic load coefficient	ψ_{is}	1.3
Isentropic flow coefficient	$\phi_{2,is}$	0.305
Inlet total pressure	P_{t0}	18.1 bar
Inlet total temperature	T_{t0}	300 °C
Outlet static pressure	P_3	0.44 bar
Pressure ratio	PR	40.84
Volumetric flow ratio	VR	49.72
Mass flowrate	$\dot{m}$	132 g s^{-1}
Geometrical constraints		
Minimum shroud clearance	-	0.1 mm
Minimum vanes thickness	-	0.2 mm
Minimum blade thickness at tip	-	0.3 mm

The main characteristics of the stage obtained by the same authors using a preliminary design optimization tool based on meanline flow analysis are listed in Table 3.2. The subscripts refer to the sections along the turbine flow path indicated in the meridional view of Figure 3.1. Section 0 corresponds to the volute inlet section, 0′ and 1 are the inlet and outlet sections of the radial stator vanes, and 2 and 3 indicate the inlet and outlet sections of the radial-axial impeller. The section 4 refers to the outlet of the conical diffuser.

The aerodynamic design of the stator vanes and the impeller blades of the ORCHID turbine was described in previous work, see, e.g., [1]. More recently, the design of the stator vanes was adapted to meet manufacturing constraints, and the resulting fluid dynamic performance was documented in [3]. From the unsteady RANS simulation of the stator-impeller stage, of which more details can be found in Chapter 2, the calculated efficiency resulted in $\eta_{ts} = 80.8$ and $\eta_{tt} = 85.3$.

The volute and diffuser were also designed at this stage, but were not considered in the fluid dynamic analysis. For the volute design, the method of Whitfield & Baines [4] was

Table 3.2: Main geometrical characteristics and calculated performance of the ORCHID turbine stage by De Servi *et al.* [1].

Description	Symbol	Value and unit
Geometrical		
Impeller inlet radius	R_2	25.75 mm
Exducer hub radius	R_{3h}	8.2 mm
Impeller inlet blade height	b_2	2 mm
Exducer blade height	b_3	12.3 mm
Impeller axial length	$L_{ax} \equiv z_3$	10.2 mm
Operation and performance		
Rotational speed	n	98.1 krpm
Power	$\dot{W}$	12 kW
Total-static efficiency	η_{ts}	83 %
Peripheral Mach number at impeller inlet	M_{U_2}	1.8
Impeller inlet relative flow angle	β_2	35.5°
Impeller exit relative flow angle	β_3	−57.6°
Stator outlet absolute flow angle	α_1	78°

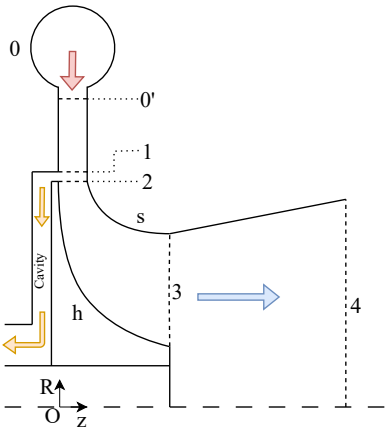

Figure 3.1: Simplified schematic of the ORCHID turbine stage flow path, including the cavity behind the impeller disk. The numbers correspond to the main sections along the streamwise direction of the machine. Solid lines indicate physical boundaries, short-dash lines indicate the leading and trailing edge sections of the stator vanes and impeller blades, and the diffuser outlet boundary. The long-dash line indicates the rotational axis, and the letters "h" and "s" indicate the impeller hub and shroud contours. Finally, the arrows indicate the direction of the flow, and the fill colors illustrate qualitatively the the flow temperature (red = hot, orange = warm, blue = cool).

used to compute geometric characteristics assuming a circular section pipe and a linear distribution of the mass flow along the tangential direction. The flow properties at the inlet of the stator vanes were used as input for the design. The volute inlet diameter obtained measured 40 mm. The diffuser was designed as a conical duct, whose area ratio was fixed by the impeller outlet section (whose diameter is 41 mm) and by the size of the flange through which the turbine test section is connected to the main working fluid loop (whose diameter is 100 mm). The diffuser semi-aperture angle was set to 4.5°, which results in a total length of ≈ 375 mm.

3.2. FLUID DYNAMIC PERFORMANCE ASSESSMENT

The fluid dynamic performance of the stage in the operating envelope of interest was characterized by means of single-passage RANS simulations, using a commercial solver [5]. Figure 3.2 shows the isentropic expansion processes for four different turbine pressure ratios in the reduced temperature-entropy diagram of siloxane MM. The diagram also reports the contours of the compressibility factor Z as an indication of the departure of the thermodynamic behavior of the working fluid from that of an ideal gas. Four values of the turbine inlet total pressure were chosen, corresponding to those of isentropes A, B, C, and D in the figure – respectively 10.9 bar, 14.5 bar, 18.1 bar, and 23.5 bar – and three different values of the rotational speed were considered, namely 80, 98.1, and 120 krpm. Thus, a total of 12 RANS simulations were performed for the combinations of inlet total pressure and rotational speed listed in Table 3.3.

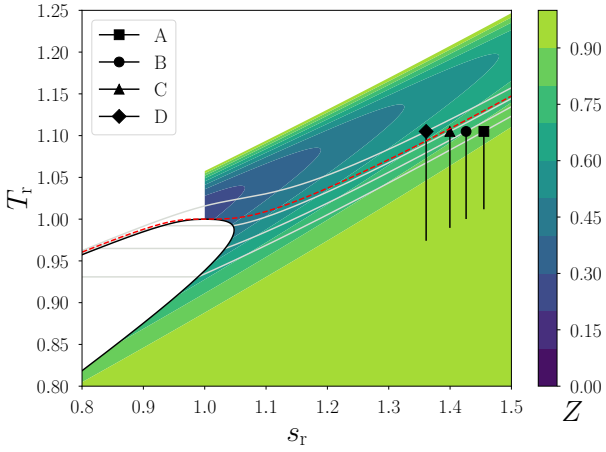

Figure 3.2: Isentropic (or ideal) turbine expansion processes (A, B, C, D) in the reduced temperature-entropy diagram of siloxane MM. The reduced temperature and entropy are defined as $T_r = T/T_{cr}$ and $s_r = s/s_{cr}$, where the subscript cr refers to the vapor liquid critical point. The red dashed line indicates the critical isobar. The outlet static pressure of 0.44 bar is assumed the same for all the expansion processes.

[1] Design point of the expander.

Table 3.3: Operating points selected for the off-design performance assessment of the ORCHID turbine.

		P_{t0} / bar			
		10.9	14.5	18.1	23.5
n / krpm	80	OP1	OP2	OP3	OP4
	98.1	OP5	OP6	OP7[1]	OP8
	120	OP9	OP10	OP11	OP12

CFD SETUP

The computational domain is the same as that adopted in the simulations reported by [3], and used in the work documented in Chapter 2 for the verification of *TurboSim* with uRANS. It includes a 1/12 annular sector stationary domain comprising a convergent-divergent stator vane, and a 1/16 annular sector rotating domain that includes an impeller blade. The interface between the stationary and rotating domains was modeled using a mixing plane to reduce computational cost, and a clearance of 0.2 mm was prescribed between the tip of the impeller blade and the machine shroud. The cavity behind the impeller disk was not modeled. The mesh comprises a total of about 4 million cells, a grid size which was shown to guarantee mesh-independent results. A central difference scheme (CDS) was used to discretize the advection terms to obtain a second-order accurate solution, while the shear stress transport model (SST $k-\omega$) was used for turbulence modeling. The two equations of the turbulence model were discretized using a hybrid scheme as per Barth & Jespersen [6].

CFD RESULTS

Relevant mass flow averaged thermodynamic quantities, such as the static pressure and temperature, were calculated at the stator outlet section and at the impeller inlet section for each operating point in Table 3.3 and plotted in Figure 3.3a and 3.3b as a function of the total inlet pressure P_{t0} and the different rotational speeds.

Moreover, the gross mechanical power of the turbine[2] and the efficiency were calculated as

$$\dot{W} = \dot{m} \cdot (h_{t0} - h_{t3}), \tag{3.1}$$

$$\eta_{tt} = \frac{h_{t0} - h_{t3}}{h_{t0} - h_{t3,is}}, \tag{3.2}$$

$$\eta_{ts} = \frac{h_{t0} - h_{t3}}{h_{t0} - h_{3,is}}, \tag{3.3}$$

where $\dot{W}$ denotes power, $\dot{m}$ the mass flow rate, h the mass flow averaged enthalpy, and η_{tt} and η_{ts} are the total-total and total-static efficiency.

The gross mechanical power $\dot{W}$ is plotted in Figure 3.3c and the efficiency in Figure 3.3d. With reference to the latter, one can notice that both η_{tt} and η_{ts} are highest at the de-

[2] i.e., the mechanical power generated by the impeller blades, without considering windage losses.

sign rotational speed of 98.1 krpm. In particular, η_{ts} peaks at the design inlet pressure of 18.1 bar, while η_{tt} continues to rise as P_{t0} increases. In addition, with the exception of OP9, efficiency remains relatively high in most of the operating range, with $\eta_{tt} > 80\%$ and $\eta_{ts} > 75\%$.

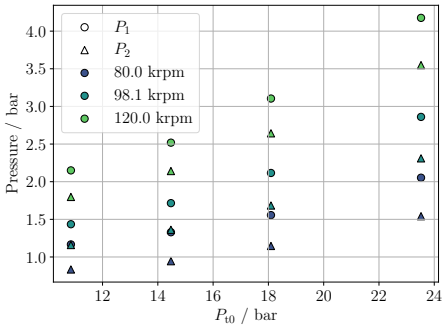

(a) Static pressure at the stator outlet (subscript 1) and at the impeller inlet (subscript 2).

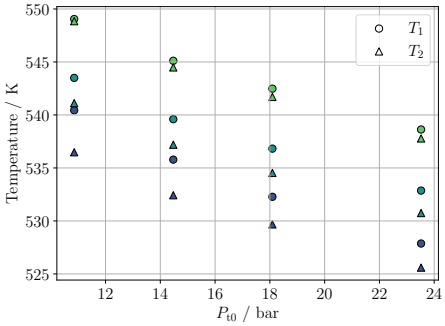

(b) Static temperature at the stator outlet (subscript 1) and at the impeller inlet (subscript 2).

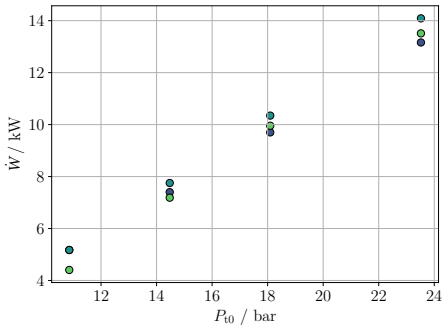

(c) Gross mechanical power.

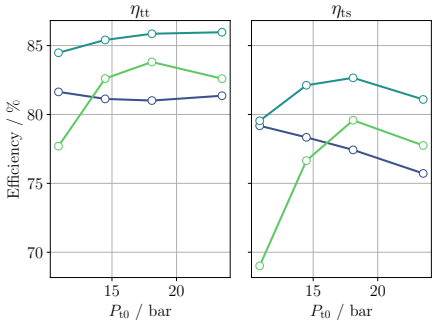

(d) Total-total and total-static efficiency.

Figure 3.3: ORCHID turbine off-design performance results. The line colors in the four figures correspond to the different rotational speeds considered, which were only reported in the legend of Figure 3.3a for brevity. In Figure 3.3a and 3.3b the circular markers indicate stator outlet conditions, whereas the triangular ones indicate the rotor inlet conditions.

The flow fields computed for the operating points labeled OP4, OP7 and OP9 in Table 3.3 have been inspected in detail by plotting the Mach number and the normalized entropy contours on a plane located at midspan, that is, at 50% of the blade height. OP7 corresponds to the design point, while OP4 and OP9 are two operating points at 80 and 120 krpm where the efficiency is lowest.

Figure 3.5 shows the contours of the Mach number at the three operating points. The stator discharge flow is characterized by the presence of expansion and compression waves that create a fish-tail shock pattern at the trailing edge. Considering OP4, the trajectory of the flow exiting the stator vanes deviates towards the radial direction as illustrated in Figure 3.5a by the flow streamlines. This deviation is caused by the stator

underexpansion at OP4 whose expansion ratio is approximately given by $\frac{P_{t0}}{P_1}\Big|_{OP4} \approx 1.3 \cdot \frac{P_{t0}}{P_1}\Big|_{OP7}$. Inspecting the streamlines within the impeller channel in Figure 3.5a, one can notice a large recirculation bubble on the blade suction side. This causes a restriction of the channel, and consequently the flow accelerates to $M_w > 1.5$ at the exducer. At the design point OP7, a smaller recirculation bubble on the suction side of the blades is present, and the relative Mach number remains below ≈ 1.2 at the impeller outlet as displayed in Figure 3.5b. The flow field at OP9 in Figure 3.5c is, instead, very different from those calculated at the previous two operating points. An overexpansion occurs downstream of the stator, given that $\frac{P_{t0}}{P_1}\Big|_{OP9} \approx 0.6 \cdot \frac{P_{t0}}{P_1}\Big|_{OP7}$. Thus, the flow exiting the stator vanes undergoes a partial recompression, which causes the flow going past the trailing edge shocks to deflect in the tangential direction. A detailed description of this type of flow pattern for the same stage geometry evaluated here is documented in [3]. Finally, a large recirculation bubble at the impeller blades pressure side extends from the leading edge up to $\approx 1/3$ of the camberline downstream. This originates due to the flow negative incidence at the impeller inlet, as shown by streamlines in 3.5c.

The normalized entropy contours plotted in Figure 3.6 provide insight on the regions of the domain where most viscous losses occur. The entropy field in Cartesian space s_{xyz} was normalized according to

$$s^*_{xyz} = \frac{s_{xyz} - \min\left(\min s^S_{xyz}, \min s^R_{xyz}\right)}{\max\left(\max s^S_{xyz}, \max s^R_{xyz}\right) - \min\left(\min s^S_{xyz}, \min s^R_{xyz}\right)}, \tag{3.4}$$

where the superscript * denotes the normalized quantity, the subscript $_{xyz}$ refers to the entire spatial domain, and the superscripts S and R denote the stationary and rotating computational domains.

In Figure 3.6a, the region of highest s^* is in correspondence with the recirculation zone on the rotor suction side displayed by means of streamlines in Figure 3.5a. It is clear, by comparing the entropy contours of Figure 3.6a and Figure 3.6b, that the lower efficiency at OP4 can be mainly attributed to the suction side separation and, secondarily, to the higher entropy generation in the exducer. Inspection of s^* in Figure 3.6c reveals a large entropy production region on the pressure side of the blades, in coincidence with the position and extent of the recirculation bubble observed in Figure 3.5c.

The cumulative loss along the expansion process was calculated and plotted in Figure 3.4 for the three cases OP4, OP7, and OP9. Three stage sections are considered, and these correspond to the locations 1, 2, and 3 reported in Figure 3.1.

As previously observed by De Servi *et al.* [1], the total loss across the stator and radial gap, that is, the middle bar in the plot, in OP7 is about half of the total entropy generation throughout the stage. For the OP9 case, this instead represents the majority of the loss. For OP4, impeller losses are the largest contributor to entropy generation, due to suction side flow separation in impeller blade channels and the high Mach number achieved at the component exit section.

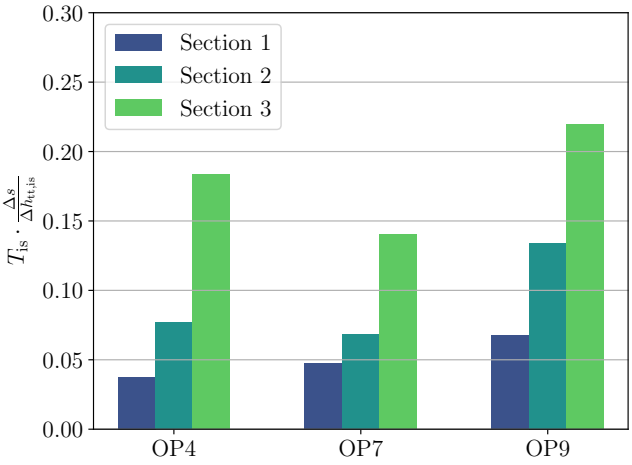

Figure 3.4: Loss accumulated at 1) stator trailing edge, 2) impeller leading edge, and 3) impeller trailing edge. The isentropic static temperature at each section j, i.e., $T_{j,is}$, and the entropy difference (with respect to the reference entropy at the inlet 0' of the stage) Δs_{j-0} were computed by mass flow averaging the quantities at each section of interest.

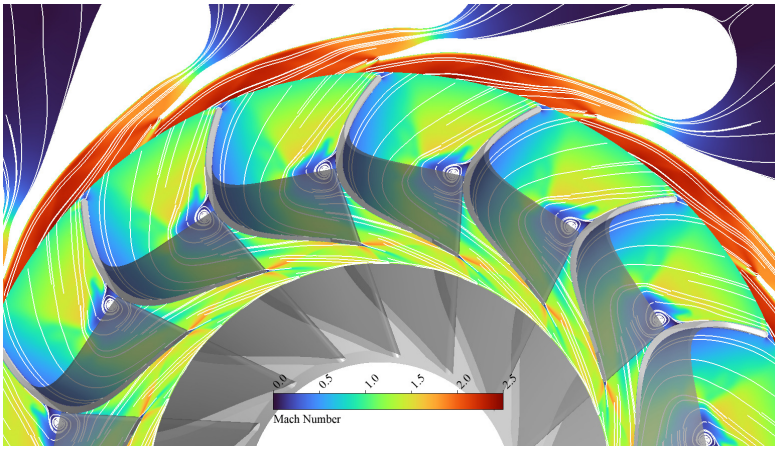

(a) Mach number contours for OP4.

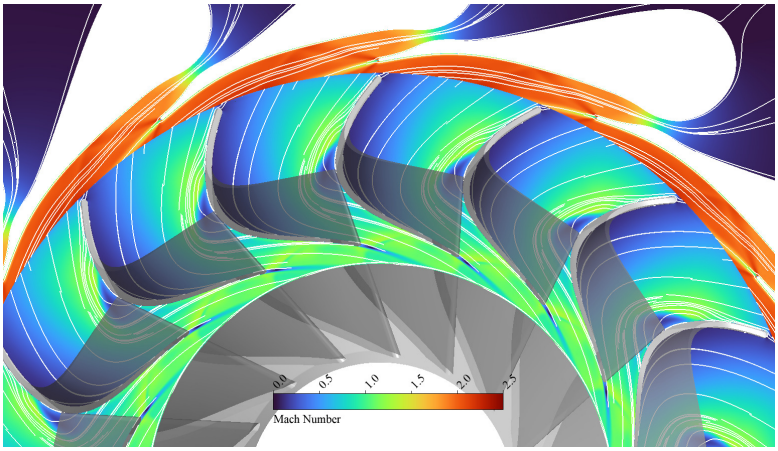

(b) Mach number contours for OP7.

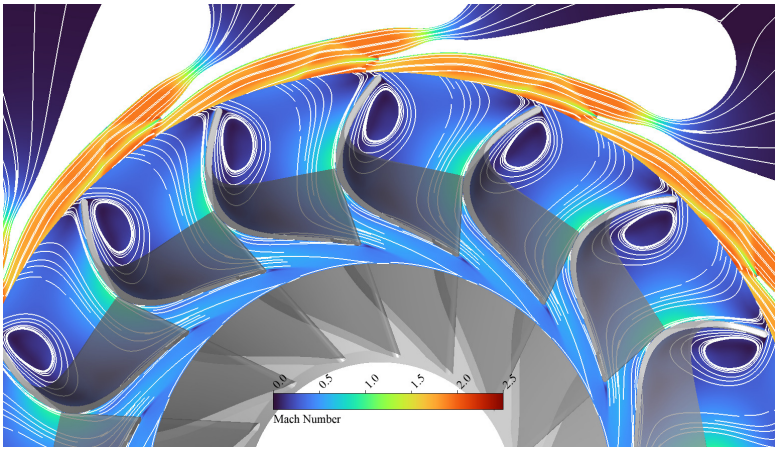

(c) Mach number contours for OP9.

Figure 3.5: Mach number contours at midspan (i.e., 50 % of local blade height) with superimposed flow streamlines (in white) for three operating points of the ORCHID turbine. The plot shows the absolute Mach number in the stationary domain (stator) and the relative Mach number in the rotary domain (impeller).

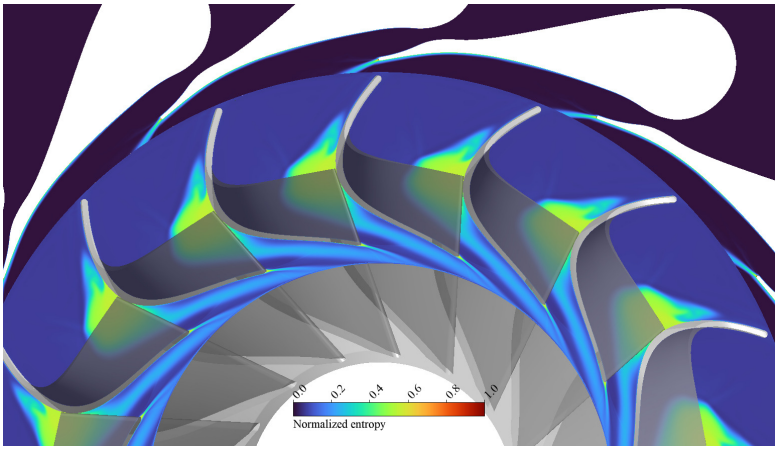

(a) Normalized entropy contours for OP4.

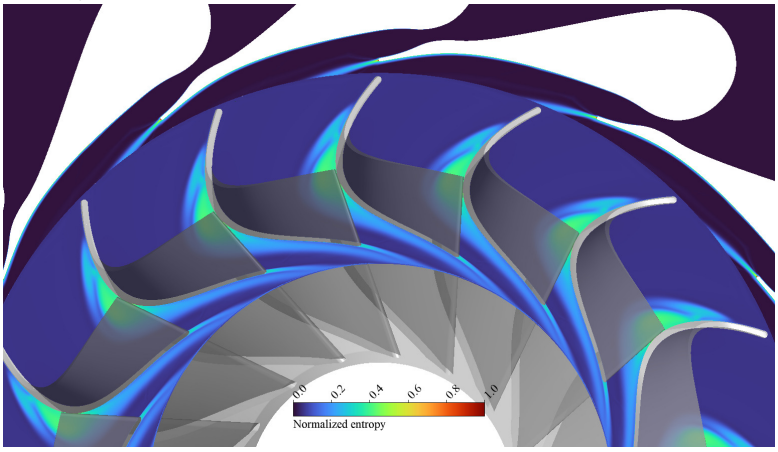

(b) Normalized entropy contours for OP7.

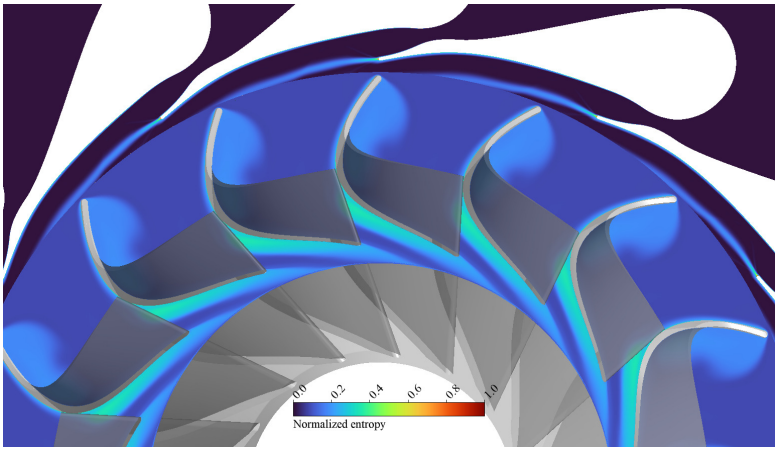

(c) Normalized entropy contours for OP9.

Figure 3.6: Normalized entropy contours at midspan (i.e., 50 % of local blade height) for three operating points of the ORCHID turbine.

3.3. PRELIMINARY MECHANICAL DESIGN

Given the high speed of the turboexpander, the simplest solution to characterize its mechanical power is to connect it via a coupling to a generator that provides brake power. An advantage of such configuration is that the braking system can be cooled simply using compressed air at room temperature, as the mechanical power of the turbine is converted for the large majority into electrical power. Moreover, the high-temperature vapor flow is far away from the generator, as this component and the turbine are separated by the coupling system. The selected generator is a customized version of a 15 kW high-speed electric motor unit – displayed in Figure 3.7 – designed by the Dutch company *Aeronamic* [7], the project partner. This machine was originally developed for a two-stage e-compressor application, and the picture shows the entire package including the two compressor stages on each side of the motor housing. The compressor stages are mounted back-to-back to minimize the residual axial thrust, which is balanced by air bearings supporting the rotor. The modifications required to couple the electric machine to the ORCHID turbine included removing the two compressor wheels and installing a flange on one of the two sides of the machine shaft, to mechanically connect it to the ORCHID turbine via a quill shaft. The electronic control unit (ECU) was also modified to provide active braking torque and maintain the powertrain at the desired rotational speed.

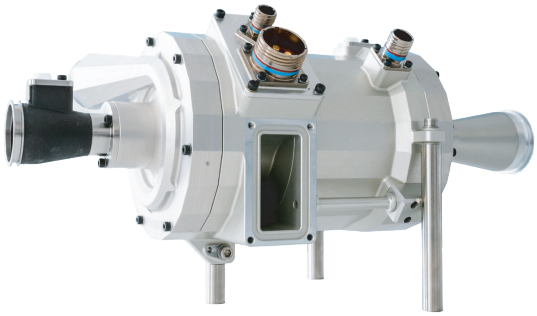

Figure 3.7: Two stage e-compressor CS15. Image courtesy of *Aeronamic* [7].

In addition to the choice of the braking system, the conceptual design of the ORCHID turbine rotor assembly involved three main technical aspects.

1. The choice of the arrangement of the turbine wheel (straddled or overhung impeller).
2. The selection of bearing technology (gas-foil, rolling element – REB – and magnetic).
3. The definition of the sealing arrangement, whose design is closely related to the choice of bearings and rotor configuration.

3.3.1. CONCEPTUAL ROTOR LAYOUT

Figure 3.8a shows the straddled configuration, with the turbine wheel placed within two bearings. Figure 3.8b instead shows an example of an overhung configuration, with the wheel mounted on the right-hand side. Straddled rotors are arguably more robust and lead to smaller shaft deflections, but the bearings on each side of the wheel imply a more complex assembly. Conversely, overhung impellers are less complex, and the assembly is more easily accessible, but the rotordynamics is arguably more challenging. The most notable drawback of overhung impellers is the addition of significant mass and unbalance at a location far from bearing support. This results in lower bending natural frequency of the rotor, which might then fall near or within the operating range of the machine. If this falls within the operating range, the start-up and shut-down of the system will require to cross this frequency, with significant rotor vibrations characterized by large amplitudes that might lead to rubbing and damage to the system. For this reason, overhung impellers are primarily applied in small systems, such as turbochargers, electric compressors, and low power capacity expanders.

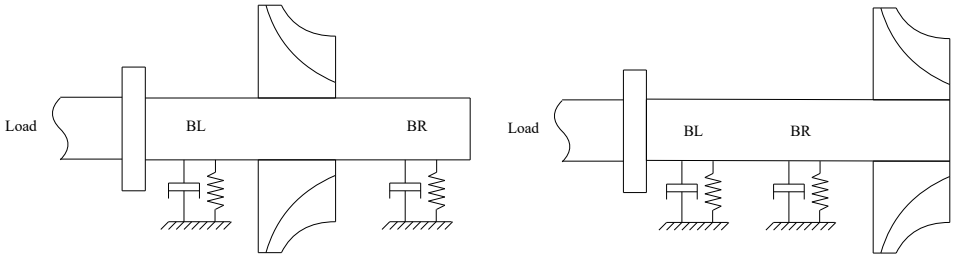

(a) Straddled impeller configuration.

(b) Overhung impeller configuration.

Figure 3.8: Rotorshaft configurations.

Information collected from a few commercial low power capacity ORC turbines, whose design details can be found in the open literature, were used as guidelines to choose the type of architecture.

The radial inflow expander documented in [8] drives a high-speed permanent magnet generator, mounted on the same shaft as shown in Figure 3.9 . The generator can be straddled between magnetic bearings together with the impeller without requiring cooling, because the organic working fluid, that is, R245fa, enters the machine at low temperature and pressure, namely ≈ 80°C and 7 bar. The assembly is made leak-tight by a cast casing that encapsulates the entire powertrain, and the exhaust gas from the radial-axial impeller flows around the generator stator before reaching the outlet port. Two rows of back-up ball bearings are included in the assembly as added support in case of a failure of the magnetic bearings. Sealing of the assembly is made relatively easy with such a layout. However, this is not a suitable choice for high temperature applications, because the generator and bearing might overheat, affecting efficiency and reliability.

The ORC turbogenerator described in [9, 10] expands R245fa and features 132.5 °C inlet temperature and up to ≈ 20 bar inlet pressure. The machine cross section is shown in Figure 3.10. The expander is overhanging from one side of the main housing, which hosts

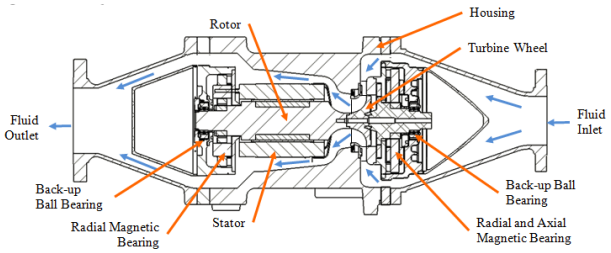

Figure 3.9: Assembly of a 125 kW RIT for low-temperature ORC industrial applications. Image courtesy of Yuksek & Mirmobin [8].

a permanent magnet generator supported by magnetic bearings. This layout allows to separate the hot gas flow from the generator and bearings that can function without cooling.

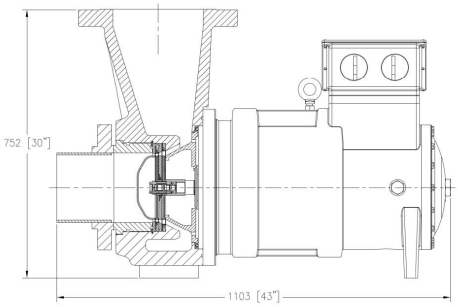

Figure 3.10: Turbogenerator powertrain assembly of a 250 kW AXT for low-temperature ORC industrial applications. Image courtesy of Di Bella [10].

The design of high-temperature ORC turbogenerators is arguably more challenging due to the need for cooling flows in the bearings. The machine of Figure 1.1 expands toluene at 317 °C and ≈ 32 bar. The wheel is overhanging, and the bearings are lubricated using liquid toluene. Also in this case the hot gas flow and the generator are physically separated, despite the fact that the entire assembly is contained in a hermetic casing, which does not require any rotary seals.

The ORC units described above have been summarized in Table 3.4 along with their main characteristics.

3.3.2. BEARINGS

Figure 3.11 displays the main bearing technologies for oil-free high-speed turbomachinery. Herein, a brief and not exhaustive description of these components is given, highlighting the pros and cons of each technology for the specific case of the ORCHID turbine.

Magnetic bearings are shown in Figure 3.11a and are currently adopted in low temperature ORC applications (e.g., [8, 9]). Passive magnetic bearings are characterized by a

Table 3.4: Summary of ORC turbogenerator units and their main characteristics.

	Yuksek & Mirmobin [8]	**Di Bella *et al.* [9]**	**Harinck *et al.* [11]**
$\dot{W}$ / kW	125	250	250
T_{in} / °C	80	132.5	317
P_{in} / bar	7	20	32
Impeller mount	Straddled	Overhung	Overhung
Generator position	Inboard	Outboard	Outboard
Bearings type	Magnetic	Magnetic	Liquid journal bearings

rather simple construction with permanent magnets on both the stator and the rotor, with the poles combined to create repulsive forces that keep the rotor levitating at the center of the journal. The rotor magnet is protected by a sleeve, usually made of carbon fiber, to prevent it from failing under mechanical stress at high rotational speed. Conversely, active bearings make use of a current amplifier to supply the stator coils, which are wrapped around the stator poles, with electric current to control the magnetic field intensity in the rotor electromagnet. The feedback of a proximity sensor is used to keep the rotor centered. Due to the absence of physical contact between the rotating and stationary parts, magnetic bearings are durable and highly efficient. Moreover, they are highly scalable and can be found in diverse power plants. However, thermal degradation of the magnetic properties beyond ≈ 200 °C [12, 13] makes them less attractive for medium- and high-temperature applications. However, successful attempts at experimental magnetic bearings for gas turbine applications operating beyond 500 °C are documented [14, 15], and commercial units have been developed for supercritical CO_2 power systems [16].

Plain gas lubricated bearings (GB) and foil bearings (GFB) are a highly efficient solution for oil-free turbomachinery [17]. They are displayed in Figure 3.11b, where the top image shows the GB and the bottom image the GFB. Both types provide rotor support because of the generation of high pressure when the gas between the rotor and the journal is compressed. GFBs feature a metallic foil coated with a low friction material to support the shaft at its rest position, and provide additional stiffness in operation. Historically, GFBs have found application in low temperature systems, such as air-cycle machines [18]. However, their use has been demonstrated for high temperature applications up to 790 °C in turbochargers [19], and more recently in gas turbine engines [20] reaching 870 °C. One of the main limitations of GB and GFB is the relatively low load carrying capacity, despite the fact that bump-type GFBs of diameter ≈ 20 mm and supporting loads greater than 300 N have been developed and experimentally tested [21]. Furthermore, recent work by de Waart & Pini [22] investigated the impact of working fluid characteristics and nonideal thermodynamic effects on the performance of gas-foil bearings, and found that diminishing values of the bulk modulus when approaching the critical point of the fluid have a detrimental effect on load carrying capacity. Thus, the design and operation of gas and gas-foil bearings for ORC turbogenerators remain critical, and their implementation in a laboratory test rig entails high risks.

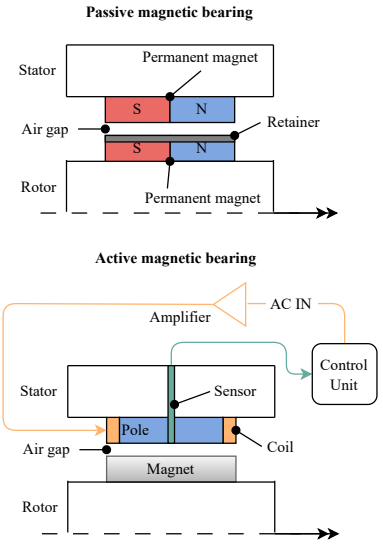

(a) Magnetic bearing schematic. Top: passive permanent magnet bearing with axial poles arrangement. Bottom: active electromagnetic bearing.

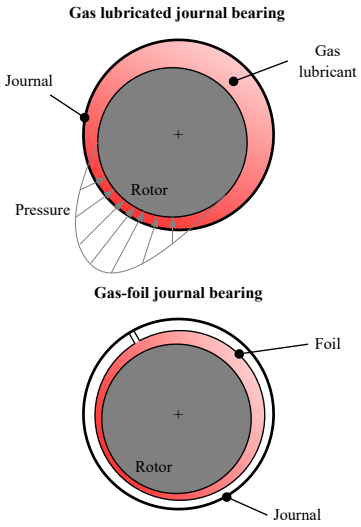

(b) Gas bearings schematic. Top: rigid gas journal bearing. Bottom: gas-foil bearing.

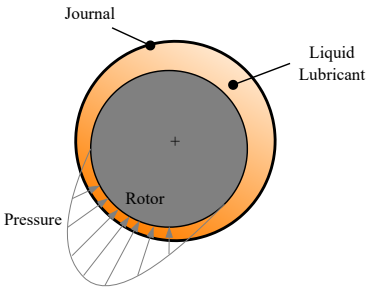

(c) Liquid lubricated journal bearing schematic.

Figure 3.11: Overview of different bearing types. (a) Passive and active magnetic journal bearings, (b) gas lubricated and gas-foil journal bearings, (c) liquid lubricated journal bearing.

In contrast, oil-lubricated journal bearings are widely used and represent the standard technology for small gas turbines and turbochargers [23]. Typically, a mineral oil is used

instead of a gas to form a stiff liquid film which can be sustained up to very high temperatures, as shown in Figure 3.11c. However, contamination of the process fluid due to pressurized oil leaks from the journals can severely impact the performance and integrity of the rig. Leaked oil causes mechanical damage to the rotating components due to erosion, accumulates, and forms sludge that increases the risk of thermal decomposition of the organic fluid in the presence of hot spots in the rig. Therefore, the choice of a proper sealing technology becomes paramount to ensure safe and reliable operation of rotors supported on oil lubricated journal bearings. So-called product lubricated journal bearings (i.e., lubricated by the process fluid in liquid form) eliminate the risks associated with contamination by oil and are a preferable option for ORC machines thanks to simpler sealing. However, like in oil lubricated bearings the liquid pressure in the journals can be very high and thus significant leaks can occur. In turn, these leaks can negatively affect the fluid dynamic performance of the turboexpander, as also documented by [24]. Furthermore, several organic fluids of interest for ORC applications feature low viscosity, which can negatively affect the load capacity of the bearing system and lead to a more challenging design.

Rolling element bearings (REB) provide three main advantages over competing technologies. Firstly, they can withstand substantially higher loads than gas bearings, offering a robust solution for a wide range of operating conditions. Secondly, they require limited lubrication compared to liquid journal bearings, as well as low chamber pressure of the lubricant that prevents significant leakages. Third, thanks to their widespread adoption in a variety of turbomachinery applications, they are available off-the-shelf and can be readily implemented within a new design. Recent trends in the design of turbocharger systems show that REBs can be preferable for compact, mobile systems such as automotive turbochargers [25], providing, even at high speeds, long-term durability with lubrication and mechanical losses comparable to those of noncontact bearings [23].

For these reasons, REB was the preferred option for the ORCHID turbine. In particular, a ceramic ball bearing cartridge was selected[3]. A cross section of the component showing its main dimensions is shown in Figure 3.12, while the main technical specifications are listed in Table 3.5. One distinctive feature of the bearing selected is the presence of a squeeze-film damper (SFD), that is, the external cylindrical surface of the cartridge. The SFD is used to increase the damping of the rotor system by the compressive action of the cartridge on the fluid interposed between the cartridge itself and the casing in which the rotor is installed. The working principle and characterization of the SFD will be further clarified and discussed in the following.

3.3.3. SEALS

In gas turbine engines, labyrinth seals are commonly adopted due to the very high temperature and the high rotation speed. The seal consists of a series of grooves machined either in the rotating part, that is, rotary labyrinth seals, or in the machine shroud, i.e., stationary labyrinth seals. Several types and derivations of the standard labyrinth seal exist, see, e.g., Ludwig [27] and Aslan-zada *et al.* [28] for a more thorough overview. The most important feature of labyrinth seals and their derivatives is the absence of physi-

[3] Product no. AS-1956 distributed by [26].

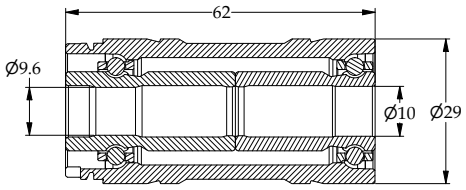

Figure 3.12: Cross-sectional view of the REB cartridge chosen to support the ORCHID turbine rotor. Dimensions are in mm.

Table 3.5: Data of the REB cartridge. Static and dynamic load capacities are intended for a single bearing row.

Material (balls)	Si_3N_4
Material (raceways)	M50 steel
Maximum rotational speed	165 krpm
Lubricant volume flowrate	$0.5 - 1\,L\,min^{-1}$
Static radial load capacity	1889 N
Dynamic radial load capacity	4710 N

cal contact between the sealing surfaces, which makes small amounts of fluid leakage unavoidable. However, leakage can be minimized by reducing the pressure gradient between the two sides of the seal, or by reducing the clearance between stationary and rotating parts, or even by increasing the pressure loss across the seal by means of fluid dynamic optimization [29].

A common strategy adopted for large steam power plants is to use dry gas seals [30], employing an inert gas such as nitrogen as a barrier between the two fluid flows. Therefore, an additional pressurized chamber is added to separate the two main processes. The dry-gas solution combines advantages such as the absence of contact between parts, since the different chambers are separated by labyrinth seals, and the guarantee of a leak-tight assembly, which, however, comes with the drawback of a more complex design, more components, and a more complex control strategy.

As an alternative, rotary shaft lip seals, represented in Figure 3.13, are capable of ensuring almost no oil leak and keeping dust and dirt away from the critical components of the powertrain. These seals have been adopted for decades, especially at low temperature (< 100 °C) and low-medium surface shaft speed (< $20\,m\,s^{-1}$) [31]. Typical applications include, for example, sealing bearings for automotive drive axles or gearboxes, spindle bearings for manufacturing machines, and hydraulic turbines and pumps. More recently, thanks to the development of heat resistant and low friction materials [32], rotary shaft seals are being investigated and adopted in aeronautical applications, for example, in helicopter gearboxes [33]. Compared to contactless seals, these seals lead to a simpler and more compact assembly. The rotational speed and maximum operating temperature of ORC turbines are lower than those of turbochargers; therefore, inexpensive contact seals can be used. Currently, state-of-the-art lip seals can operate at peripheral speeds up to $100\,m\,s^{-1}$ and temperatures in excess of 250 °C.

Seals featuring sealing elements made of polytetrafluoroethylene (PTFE) were considered appropriate for the initial design of the ORCHID turbine, and the suitability of this choice was also confirmed by a manufacturer. Figure 3.13 shows a representation of the lip seal mounted in a stationary housing.

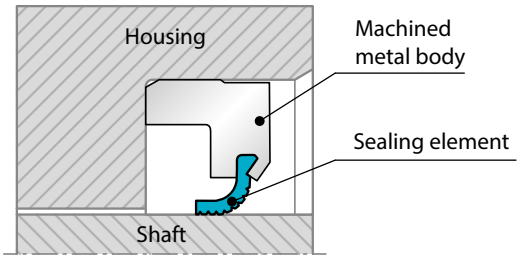

Figure 3.13: Lip seal representation taken from [34].

3.3.4. INITIAL TURBINE LAYOUT

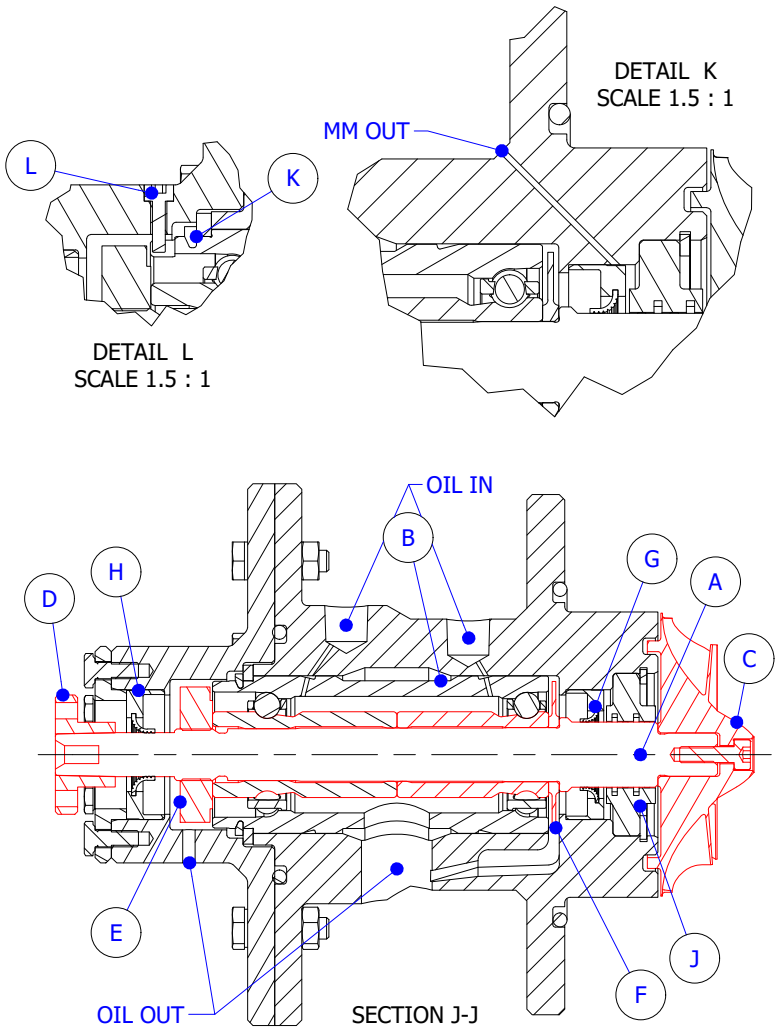

Figure 3.14: ORCHID turbine cross-section, showing the main components and details of the oil delivery system. Red lines indicate the rotating parts. Details K and L are viewed from a cross-section rotated 90° with respect to J-J section. Components: shaft (A); bearings cartridge (B); turbine wheel (C); coupling flange (D); lock-nut (E); stainless steel thin-disk (F); contact lip seal on the impeller side (G); contact lip seal on the coupling side (H); non-contact gas seal (J).

The conceptual layout of the turbine configuration obtained as a result of an iterative design process is shown in Figure 3.14. The rotor includes a shaft (A), a turbocharger cartridge (B), a turbine wheel (C) and a coupling flange (D). A locknut on the left side of the bearing inner raceway (E) is used to regulate the mounted end-play of the rolling ele-

ments by adjusting the preload. The cartridge pushes axially against a thin stainless steel disk (F), whose function is to move the oil outwards and to the main drain bore in the center of the assembly, through a cavity realized in the casing and extending 50° circumferentially (visible to the right of the main drain bore of the oil circuit). Stationary parts include two off-the-shelf contact lip seals to contain the oil within the bearing housing (G on the impeller side or hot side and H on the coupling side) and a non-contact gas seal (J) which was designed in-house.

3.3.5. IMPELLER WHEEL DESIGN

The turbine wheel is a bladed disk (also referred to as "blisk") with 16 blades machined from stock on the front side. A cross-section of the blisk is presented in Figure 3.15, where the main dimensions are also reported.

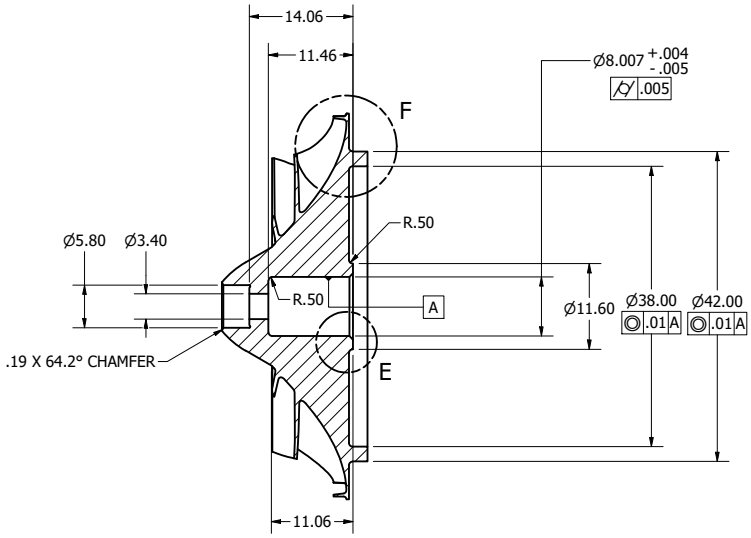

Figure 3.15: Cross-section of the impeller blisk.

A mock-up manufactured in aluminum by the TU Delft manufacturing shop [35] is shown in Figure 3.16a and 3.16b. Aluminum was used to reduce costs and facilitate machining. The realization of the mock-up was done to investigate the feasibility and the attainable accuracy of the specified geometrical features, such as the blade thickness and critical dimensional tolerances. Notice the extra material on the back side of the disk, whose purpose is to facilitate the balancing of the impeller.

The impeller is kept in place by a M3 9.8 steel grade ISO 898-1:2013 [36] bolt, as shown in Figure 3.14. The minimal force required to transfer the maximum torque $M_{\text{turb}} = 1.6$ Nm, generated by the impeller, to the shaft is ≈ 1.6 kN. The calculation assumes the average radius of the contact surface between the impeller disk and the shaft shoulder for the conversion of the force into torque, and a friction coefficient of 0.2 between the contact surfaces of the two parts. The value of the friction coefficient is consistent with the as-

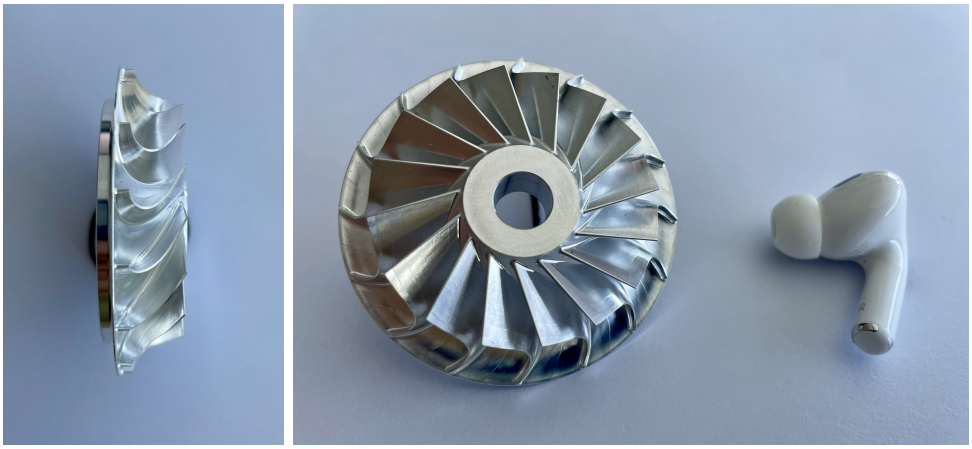

(a) Mock-up impeller viewed from the side.

(b) Mock-up impeller viewed from the front on the left, and Airpod Pro 2 on the right.

Figure 3.16: Impeller side (b) and front (c) view of the manufactured blisk in aluminum (the nose cone was not machined for simplicity).

sumption of a greasy contact interface. Considering a bolt preload of 75 % the material yield strength, which for 9.8 steel is ≈ 650 MPa, and a worst case axial thrust of 600 N, a safety margin to sliding between the two contact surfaces of 16% is obtained, while the bolt safety factor to yield is 1.07.

3.4. STRUCTURAL ANALYSIS OF THE IMPELLER

A mechanical analysis of the initial design of the impeller was performed. The objective was to estimate the component safety factor under the most critical loading conditions and obtain insights on the deformation of the part. The results of the analysis were used to inform the selection of the material and provided useful information for future improvements of the design. First, the most important mechanical loads that act on the impeller were estimated and successively a verification using finite element analysis (FEA) was performed.

3.4.1. ESTIMATION OF THE MECHANICAL LOADS

The gross torque generated by the impeller was calculated from the operating curves reported in section 3.2 and is presented in Figure 3.17. The figure shows the torque values without considering the contribution of the windage losses occurring in the cavity behind the impeller disk, which was not modeled. Therefore, the values reported in Figure 3.17 are conservative. Thus, the maximum torque of ≈ 1.6 N m was considered in the mechanical calculations.

To compute the net axial thrust generated by the impeller one must solve the axial force balance

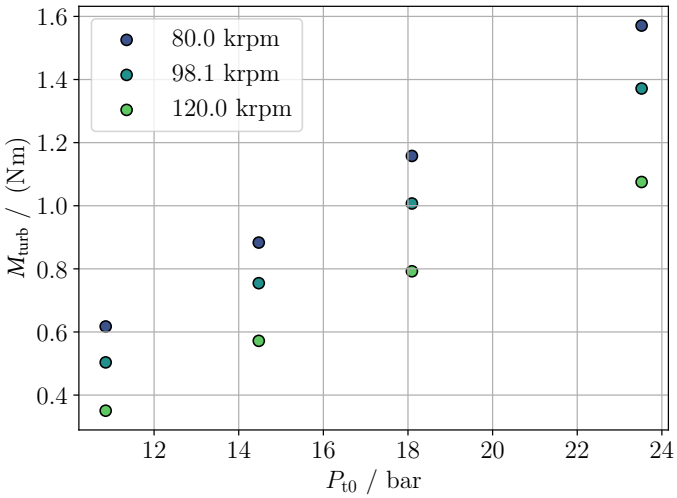

Figure 3.17: ORCHID turbine gross torque at varying inlet pressure and rotational speed.

$$-F_{ax} = F_{bf} - F_{out} - F_{s,z}, \tag{3.5}$$

in which, with reference to the free body diagram of Figure 3.18, F_{out} is the impeller outlet axial momentum, $F_{s,z}$ is the projection in the axial direction of the fluid force on the impeller shroud, and F_{bf} is the force produced by the flow in the cavity behind the impeller disk.

The outlet momentum was computed as

$$F_{out} = P_3 \cdot 2\pi R_{3s}^2 + \dot{m} V_{3m}, \tag{3.6}$$

using mass flow averaged values for P_3 and V_{3m}. The hybrid method of Tiainen *et al.* [37] was used to calculate F_{bf} and $F_{s,z}$. By applying the radial equilibrium between the pressure gradient and the centrifugal force in the cavity, the method yields

$$\begin{aligned} F_{bf} &= P_{amb}\pi R_{sh}^2 + \left(\frac{P_{LS,d} + P_{LS,u}}{2}\right)\pi\left(R_{LS,in}^2 - R_{sh}^2\right) + \int_{R_{sh}}^{R_2} P_{bf} \cdot 2\pi R \, dR, \\ \text{with} \quad P_{bf} &= P_2 \left[\frac{\gamma - 1}{2\gamma P_2}\rho_2 f^2 \omega^2 \left(R^2 - R_2^2\right) + 1\right]^{\frac{\gamma}{\gamma - 1}}, \end{aligned} \tag{3.7}$$

for the backface force, setting $R_{sh} = 12$ mm and using the mass flow averaged values of P_2 and ρ_2, computed from CFD simulations. In the equation, $P_{LS,u}$ and $P_{LS,d}$ are the pressures upstream and downstream of the labyrinth seal. However, the contribution to

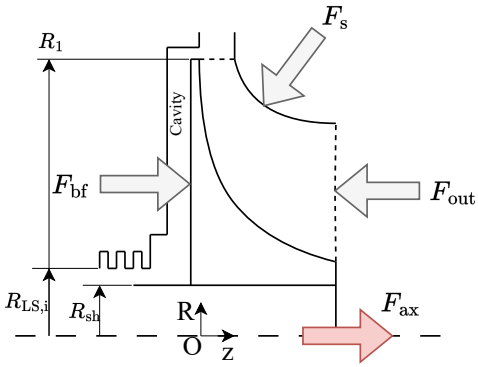

Figure 3.18: Free body diagram reporting the forces that contribute to the impeller net axial thrust F_{ax}. F_{bf} is the force exerted by the flow in the cavity behind the impeller disk on its backface, F_s is the shroud pressure force, and F_{out} is the reaction force to the outlet flow axial momentum. The main dimensions necessary for the computation of F_{bf} are indicated, namely $R_{LS,i}$ the labyrinth seal inner radius, R_{sh} the shaft outer radius, and R_1 the impeller disk outer radius.

the axial thrust of the radial labyrinth seal (i.e., item J in Figure 3.14) is negligible because $R^2_{LS,in} - R^2_{sh}$ is small. Thus, the second term in the definition of F_{bf} in Equation 3.7 was neglected.

The shroud force according to Tiainen *et al.* [37] reads

$$F_{s,z} = \left[0.5 \frac{\bar{\rho}(1-f^2)(2\pi n)^2 (R_2^2 + R_{3s}^2)}{2} + P_3 - \frac{\rho_3 (1-f^2) U_{3s}^2}{2} \right] \cdot \pi (R_2^2 + R_{3s}^2), \tag{3.8}$$

where $\bar{\rho}$ is the average density between the inlet and outlet sections of the impeller, n is the rotational speed in rpm, and U_{3s} the peripheral speed of the impeller outlet at the tip. The quantities P_3 and ρ_3 are obtained by computing the mass flow average of the pressure and density at the outlet section of the impeller from the results of the CFD simulations.

The net axial thrust F_{ax} is displayed in Figure 3.19 against the corrected mass flow rate $\dot{m}_{corr}$ in the 12 operating conditions considered and listed in Table 3.3. $\dot{m}_{corr}$ reads

$$\dot{m}_{corr} = \dot{m} \frac{\sqrt{T_{t0}}}{P_{t0}}. \tag{3.9}$$

The figure also shows the curves obtained by fitting the estimated axial thrust values with an exponential function.

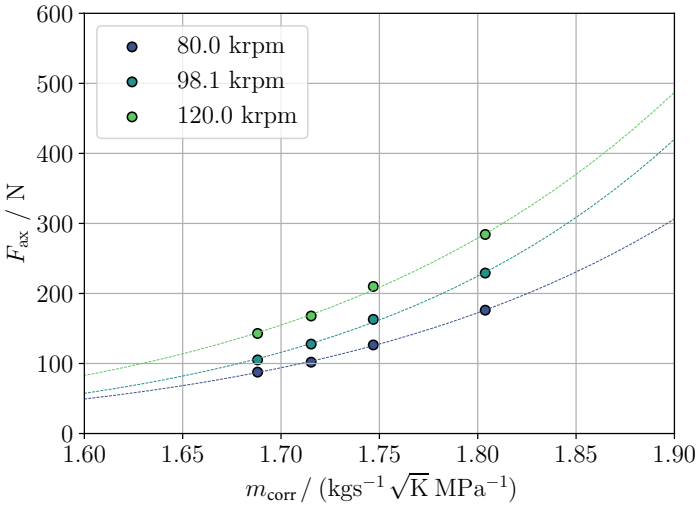

Figure 3.19: Net axial thrust acting on the ORCHID turbine impeller for the operating conditions of Table 3.3. The quantity was plotted against the corrected mass flow rate $\dot{m}_{corr}$, allowing to generalize the fitting to different inlet conditions. The dashed curves represent a numerical fitting of the data.

VERIFICATION OF THE AXIAL THRUST CALCULATION

The computation of the axial thrust performed with the hybrid method documented in Tiainen *et al.* [37] was verified using field quantities from CFD simulations.

The axial component of the shroud pressure load is found by summation of the force in the axial direction for each cell on the shroud surface as

$$F_{s,z} = \sum_{i=1}^{m} P^{i}_{S_s} \cdot \left(A^{i}_{S_s} \times \hat{n}^{i}_{z} \right), \tag{3.10}$$

where m equals the total number of cell faces used to discretize the surface of the shroud S_s, $P^{i}_{S_s}$ is the pressure on a specific cell face i of the area $A^{i}_{S_s}$, and $\hat{n}^{i}_{z}$ is the axial component (i.e., in direction z) of the i^{th} cell face versor.

The force F_{out} on the outlet surface S_3 was calculated as

$$F_{out} = \sum_{i=1}^{q} \left[P^{i}_{S_3} + \rho^{i}_{S_3} \left(V^{i}_{S_3} \times \hat{n}^{i}_{m} \right)^2 \right] \cdot A^{i}_{S_3}, \tag{3.11}$$

where the outlet surface S_3 is discretized by q faces, $P^{i}_{S_3}$, $\rho^{i}_{S_3}$, and $V^{i}_{S_3}$ are the pressure, density, and absolute velocity on a specific cell face i of area $A^{i}_{S_3}$, and $\hat{n}^{i}_{m}$ is the meridional component of the i^{th} cell face normal.

Table 3.6 reports the comparison of the axial thrust components F_{out} – computed by means of Equation 3.6 and 3.11 –, and $F_{s,z}$ – computed using Equation 3.8 and 3.10 – at OP7. The prediction of F_{out} is in good agreement using the two methods, while $F_{s,z}$ is underestimated by 12 % when using Equation 3.8.

	Hybrid method [37]	**CFD**	**Δ**
$\lvert F_{out} \rvert$ / N	68.6	69.1	−0.7 %
$\lvert F_{s,z} \rvert$ / N	81.6	92.7	−12 %
$\lvert F_{bf} \rvert$ / N	304.8	-	
$\lvert F_{ax} \rvert$ / N	154.5	-	

Table 3.6: Absolute value of the force components in the axial force balance at OP7, computed with the hybrid method [37] and with CFD.

3.4.2. FINITE ELEMENTS MECHANICAL ANALYSIS

The safety factor with respect to the yield strength of the material is defined as

$$SF = \frac{\sigma_y}{\sigma_{vM,max}}, \tag{3.12}$$

where $\sigma_{vM,max}$ is the maximum equivalent von Mises (vM) stress and σ_y is the yield strength of the material. Furthermore, the analysis of finite elements allowed the evaluation of the deformation u of the blisk, which is necessary to establish the rubbing margin or contact of the blisk with the housings.

Two different materials were considered, namely a 316L stainless steel alloy grade and a Ti6Al4V - T6 titanium alloy grade (Ti64 herein). The Ti64 is lighter and more elastic than the 316L, has a lower thermal conductivity and thermal expansion coefficient, but is more expensive and difficult to machine. The basic material properties of Ti64 and 316L are listed in Table 3.7.

Table 3.7: Properties of 316L and Ti64 at ambient temperature from Ansys® Mechanical [38] material database.

	316L	**Ti64**	**Units**
Density	7970	4430	$kg\,m^{-3}$
Young's modulus	195	111	GPa
Tensile strength at yield	230	846	MPa
Ultimate tensile strength	521	918	MPa
Linear thermal conductivity	14.2	7.2	$W\,m^{-1}\,K^{-1}$
Coefficient of thermal expansion	16	8.9	$\mu m\,m^{-1}\,K^{-1}$

The analysis was performed using Ansys® Mechanical [38]. The prescribed loads are the pressure acting on the back of the disk, the pressure and impulse forces at the outlet of the impeller, the centrifugal stress at the maximum rotational speed of 120 krpm, and

the pressure distributions on the hub and blade surfaces. A uniform temperature field of 280 °C was prescribed to the blisk, to account for the change in the properties of the material and the thermal expansion at high temperature.

A grid convergence study was conducted using 316L as material and the results are shown in Figure 3.20. Several quantities of interest have been considered to verify the accuracy of the simulation results, and their relative change to a base mesh of ≈ 380k nodes was plotted in Figure 3.20 as a function of the number of nodes. The plots in Figure 3.20a show the relative deviation of the maximum equivalent vM stress and the maximum principal stress, whereas the plots in Figure 3.20b report the relative deviation of the directional deformation in several locations of interest, that is, locations where deformations can lead to interference with stationary parts. The grids were made of tetrahedral elements and the base element size chosen was 1 mm. Surface refinement was applied in regions characterized by the highest stresses, namely the blade root at the pressure side and the fillet at the disk back face. The 1.1M node mesh was selected as the best trade-off between computational time and accuracy for the following analysis of stresses and deformation.

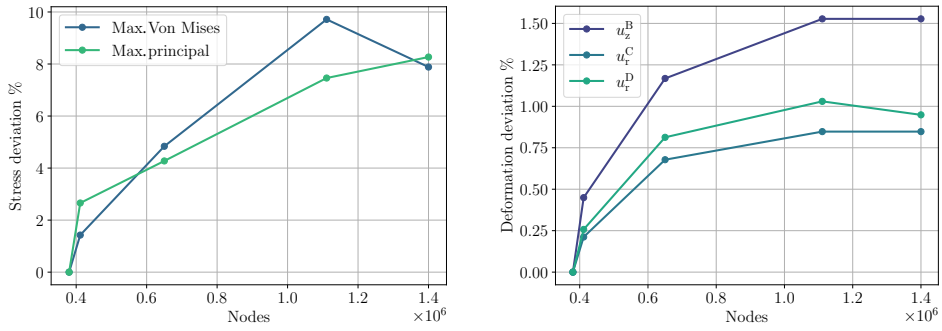

(a) Maximum von Mises equivalent stress and maximum principal stress as a function of the nodes count.

(b) Directional deformation at locations B, C, and D (see Figure 3.21) as a function of the nodes count.

Figure 3.20: Grid independence study for the 316L blisk. a) Plots of the stress, and b) plots of the directional deformations.

Figure 3.21 illustrates the equivalent vM stress contours in the deformed computational domain. The maximum equivalent stress is located at the blade suction side, close to the root fillet. However, the cylindrical section of material protruding from the back face of the blisk is also subject to high loads.

The results of the stress and deformations for the 316L blisk are reported in the first row of Table 3.8. The safety factor to yield is 0.74, which means that the part undergoes permanent deformation under the current loading conditions. Furthermore, the table reports deformations u in the axial and radial directions in some critical locations, which are reported by the arrows in Figure 3.21.

The results obtained with Ti64 as material and using the same 1.1M node mesh and loads are reported in Table 3.8. The value of the maximum equivalent stress leads to a safety

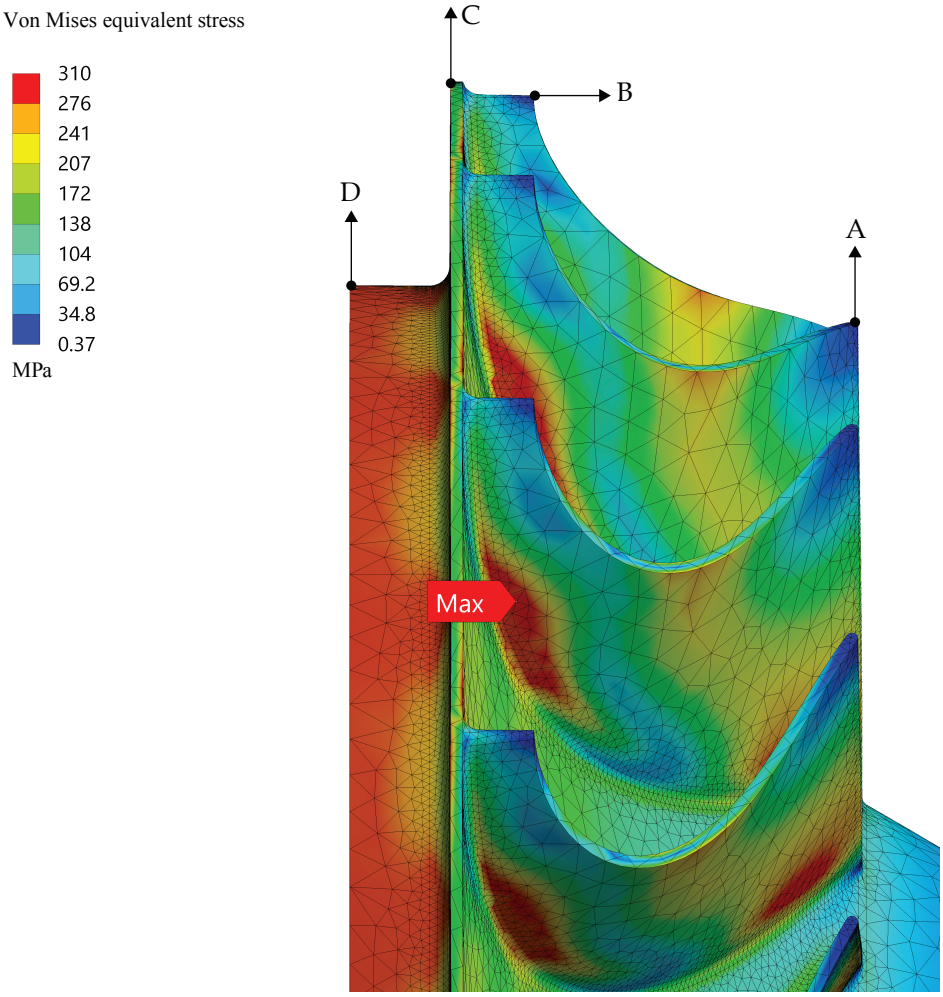

Figure 3.21: Von Mises stress contours for the 316L blisk.

factor of 1.77, thanks to the high strength of Ti64. Radial deformations of the Ti64 blisk are lower due to favorable material properties such as lower density compared to the stainless steel, while the axial deformation resulted very similar for the two materials, as it depends mainly on the stiffness. However, all deformations remained well below 50% of the design impeller clearance with the shrouds, set to 0.2 mm. These results corroborate that titanium alloy is a more suitable material for this application.

However, this choice affects the choice of the bolt material used to hold the impeller in place, which must feature thermal properties similar to those of the blisk. Because the coefficient of thermal expansion of Ti64 is about half that of steel, the use of a steel bolt would inevitably result in a loss of preload on the impeller at high temperature due to

Table 3.8: Results of the finite element simulations on the blisk assuming different materials.

Material	$\sigma_{vM,max}$ / MPa	SF	u_r^A / mm	u_z^B / mm	u_r^C / mm	u_r^D / mm
316L	310	0.74	0.12	0.057	0.14	0.13
Ti64	478.7	1.77	0.072	0.059	0.087	0.088

the different expansion of the two materials. A Ti64 M3 bolt can be used instead of the ISO 898-1:2013 [36] bolt that was initially assumed. The same preload, safety factor, and margin to sliding calculated previously apply in this case, because of the very similar mechanical properties of Ti64 and 9.8 class steel.

3.5. THERMAL ANALYSIS OF THE ASSEMBLY

The thermal analysis documented in this section was conducted to estimate the cooling requirements of the bearing compartment and subsequently the required lubricant flow rate. The thermal load is calculated considering two main sources: the thermal energy generated in the bearings due to friction and the thermal energy transferred by conduction to the bearing compartment from the ORCHID turbine flow path.

3.5.1. ESTIMATION OF THE BEARINGS POWER LOSSES

Friction heating is generated in the bearings by contact of the rolling elements on the raceways. Zander *et al.* [39] has conducted an investigation on the various methods available in the open literature to estimate frictional losses in the bearings. The authors found that the method of [40] is well suited for angular contact ball bearings lubricated with synthetic oils. The other methods considered in the comparison outperformed the accuracy of [40] for most other types of bearings and mineral oils used as lubricants. Nevertheless, these are significantly more complex models that require the estimation of several additional parameters. Consequently, for this preliminary analysis, the simple method from [40] was chosen to calculate the frictional torque in each row of the turbocharger bearings cartridge. This quantity is defined as the sum of two independent contributions.

$$M = M_1 + M_0, \tag{3.13}$$

where M_1 is the load-dependent torque and M_0 is the speed-dependent torque.

The terms in Equation 3.13 are modeled by an empirical relation that reads

$$M = \underbrace{f_1 P_1 d_m}_{M_1} + \underbrace{f_0 d_m^3 \cdot 10^{-7} \cdot \begin{cases} (\nu \cdot n)^{\frac{2}{3}}, & \text{if } \nu \cdot n \geq 2000 \\ 160, & \text{otherwise} \end{cases}}_{M_0}. \tag{3.14}$$

In the equation, f_1 and f_0 are bearing-specific factors dependent on load and speed,

Table 3.9: Coefficients and geometrical parameters used for the calculation of the frictional torque M defined as per Equation 3.14.

		Value	Unit
f_0	Speed factor	$2.145\,\frac{h}{d_\mathrm{m}}^{0.5} + 1.037$	-
f_1	Load factor	$0.001 \cdot (P_0/C_0)^{0.33}$	-
P_0	Decisive load for M_0	$0.6\,F_\mathrm{ax} + 0.5\,F_\mathrm{r}$	N
P_1	Decisive load for M_1	$1.4\,F_\mathrm{ax} - 0.1\,F_\mathrm{r}$	N
C_0	Static load rating	1889	N
h/d_m	Oil bath height ratio	0.9	-
d_m	Mean bearing diameter $\left(d_\mathrm{OR,out} + d_\mathrm{IR,in}\right)/2$	19.5	mm

P_1 is an equivalent load, ν is the kinematic viscosity of the lubricant in $\mathrm{mm^2 s^{-1}}$, n the rotational speed in rpm, and d_m is the mean diameter of the bearing in mm. The power loss due to friction in each bearing row results

$$\dot{Q}_\mathrm{loss} = M \cdot \omega, \tag{3.15}$$

with ω the rotational speed in $\mathrm{rad\,s^{-1}}$.

The values of the coefficients and of the geometrical parameters used to calculate M are listed in Table 3.9. The speed factor f_0 was calculated as a function of the oil bath ratio, that is, the ratio of the oil level height h in the housing over the mean bearing diameter d_m, determined according to [40]. A fully flooded bearing is characterized by $h/d_\mathrm{m} = 1$, while for dry lubrication $h/d_\mathrm{m} = 0$. In this work $h/d_\mathrm{m} = 0.9$ was assumed, considering that the cartridge manufacturer recommended a relatively high lubricant flow rate of $1\,\mathrm{L\,min^{-1}}$, while the empty volume in the bearing housing cavity is only $\approx 0.02\,\mathrm{L}$. As a result, during startup it would take approximately 1.2 s for the bearing housing cavity to be flooded by oil. The viscosity of the lubricant ν was modeled as per the VG32 standard ISO 3448:1992 [41] and varied as a function of the lubricant temperature.

The total loss was calculated by summing the frictional heating in each bearing row. The result is plotted in Figure 3.22, considering a lubricant inlet temperature of 50 °C. The figure shows that the thermal dissipation in the bearings is mainly dependent on the rotational speed. However, high vapor flow rates cause additional losses as a result of the corresponding increase in axial thrust.

Figure 3.23 illustrates the frictional torque for each bearing row, indicated with left (L) and right (R) following the orientation of the bearing cartridge in Figure 3.14. In particular, the axial thrust F_ax produced by the impeller is completely supported by the L row, due to the specific bearing configuration and the direction of the load. At high rotational speed and flow rate, the frictional torque M_1 in the L bearing reaches values comparable in magnitude to M_0. Since the thermal energy generated by M_0 is equal for both rows, this results in a larger amount of power dissipated in row L, as depicted by the white isolines in Figure 3.22, which show that the power dissipation in row L increases relative to row R as both n and $\dot{m}_\mathrm{corr}$ increase.

In Figure 3.22, the circular red marker indicates the ORCHID turbine design point. The triangular and cross markers indicate two off-design conditions. The one marked by △ corresponds to total conditions at the inlet of the turbine equal to 22.5 bar and 300 °C. This corresponds to the highest pressure and temperature at which the machine can be operated. The condition marked by × corresponds instead to 22.5 bar and 255.5 °C at the inlet. At such temperatures, high pressure causes the gas density to increase, leading to a large impeller axial thrust and losses in the bearings.

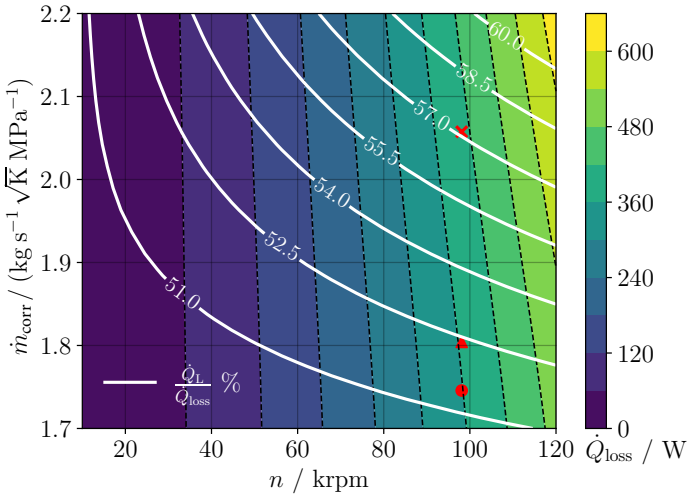

Figure 3.22: Bearing power loss against shaft rotational speed on the horizontal axis, and the corrected mass flow rate on the vertical one. The white isolines indicate the power loss of row L in percentage. The three red markers indicate three operating conditions, specifically the on-design point ○, the highest inlet pressure and temperature point △, and a low temperature and high pressure operating condition ×.

3.5.2. ESTIMATION OF THE COOLING LOAD USING FINITE ELEMENTS ANALYSIS

A finite element model of the preliminary assembly of the ORCHID turbine was developed in Ansys® Mechanical [38]. The geometric domain comprised the turbine housing assembly shown in Figure 3.14 and a circular cross-section flow distributor designed using the method of Whitfield & Baines [4].

Thermal analysis was carried out to estimate the thermal power exchanged between the lubricant and the bearing housing under stationary conditions and consequently to determine the necessary flow rate of the lubricant. Furthermore, the results of this preliminary calculation were used to estimate the size and power rating of a lubricant cooler.

A heat source term was imposed on each bearing, conditions A and B in Figure 3.24, to account for the frictional power loss in the most critical operating condition in Figure 3.22. The surfaces highlighted in red are instead regions where a thermal boundary condition was imposed. The fixed temperature conditions C, D, E, F were taken equal

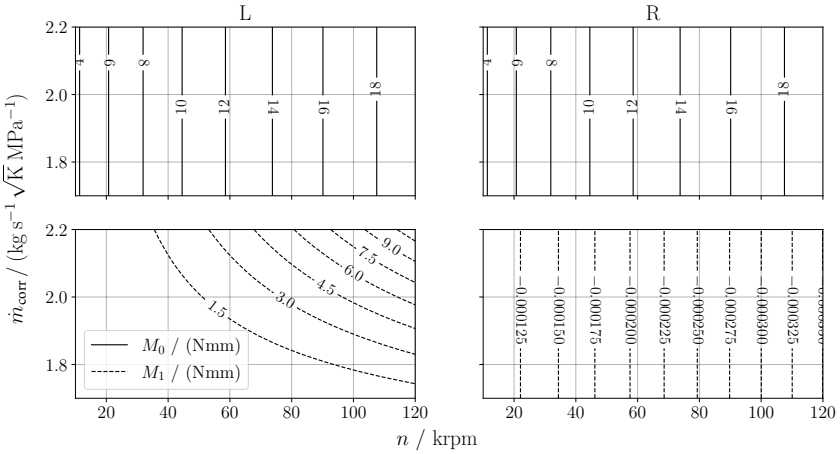

Figure 3.23: Frictional torques for bearing row L, on the left two plots, and R, on the right two plots. The solid lines indicate the speed dependent frictional torque M_0, while the dashed lines depict the load dependent torque M_1.

to the average total temperature of the fluid at those locations, estimated in the CFD simulation assuming adiabatic walls. The temperature on the inner walls of the volute was not calculated directly from the CFD simulations, as the volute fluid domain was not modeled, but it was assumed that its entire inner surface in contact with the high temperature siloxane flow would reach a temperature equal to the total flow inlet temperature, which is deemed reasonable given the low flow velocity in this component. The cavity behind the impeller disk was also not included in the CFD simulations. After the expansion in the stator vanes, fluid flows in the cavity and recovers part of its static temperature. Thus, a temperature of 290 °C was arbitrarily imposed (H and I). Finally, to account for the flow of lubricant in the bearing housing, a temperature condition was imposed on all surfaces in contact with the lubricant. Considering that the bearings are almost fully submerged in lubricant, the presence of cool lubricant in the housing was oversimplified by assuming that all its internal surfaces in contact with lubricant are at a fixed temperature equal to the maximum temperature of the coolant, which is to be maintained ≤ 90 °C (J). The approach documented above is arguably not suited for detailed analysis of the temperature fields in the assembly components, but it was considered satisfactory for a ballpark estimation of the total thermal power transferred from the machine to the lubricant. The quantity was then calculated by integrating the various contributions of heat flux on the surfaces in contact with the lubricant (J) resulting from the FEM simulation over the overall contact area.

Different grids of increasing nodes count were used to assess the impact of the numerical discretization on the results. The grid sensitivity study was repeated twice, once by controlling the spatial discretization of the external housings only, and a second time by increasing the discretization of the bearing cartridge and shaft. The initial coarse mesh of tetrahedral cells has roughly 960k nodes. The results of the grid sensitivity study are

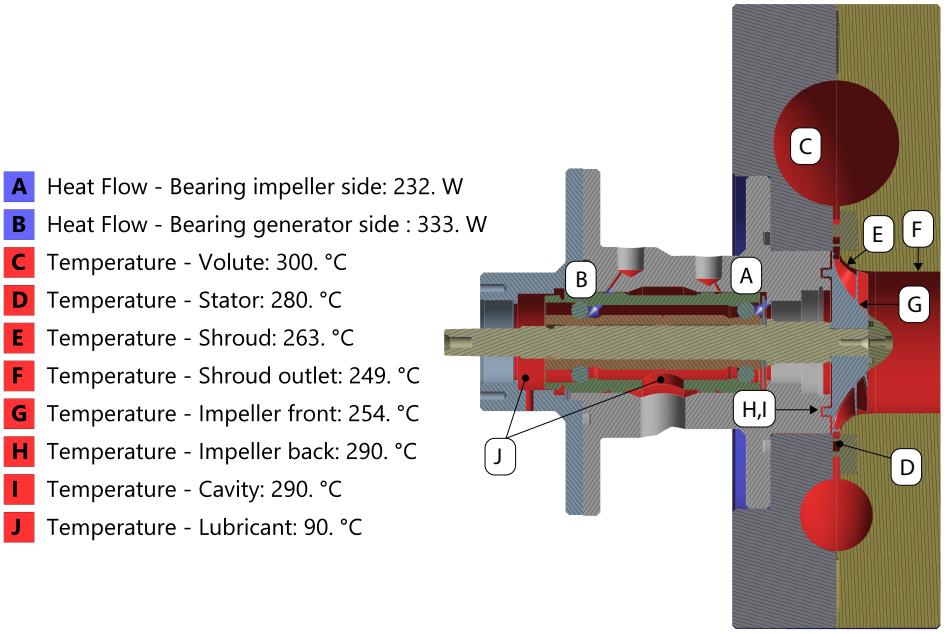

Figure 3.24: Geometrical domain used for the steady-state thermal FEA of the ORCHID turbine.

shown in Figure 3.25, showing the change in predicted thermal load $\dot{Q}_{\text{tot}}$ as a function of the number of nodes. The grid characterized by the highest number of rotor nodes was considered satisfactory for the estimation of the thermal load. The adopted grid is displayed in Figure 3.26.

The heat transferred by conduction to the lubricant from the hot MM flow through the volute, stator vanes and impeller, was obtained by subtracting the bearing frictional heating from the total computed thermal load as

$$\dot{Q}_{\text{cond}} = \dot{Q}_{\text{tot}} - \dot{Q}_{\text{loss}} = 1.22\ \text{kW} - 0.565\ \text{kW} = 0.635\ \text{kW}. \tag{3.16}$$

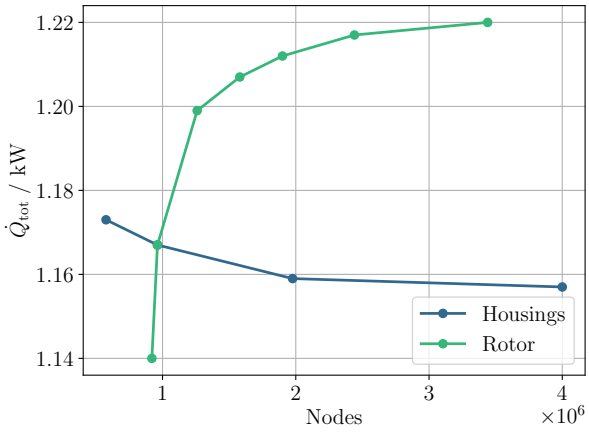

Figure 3.25: Grid sensitivity analysis for the estimation of the ORCHID turbine thermal load to be dumped by the lubricant.

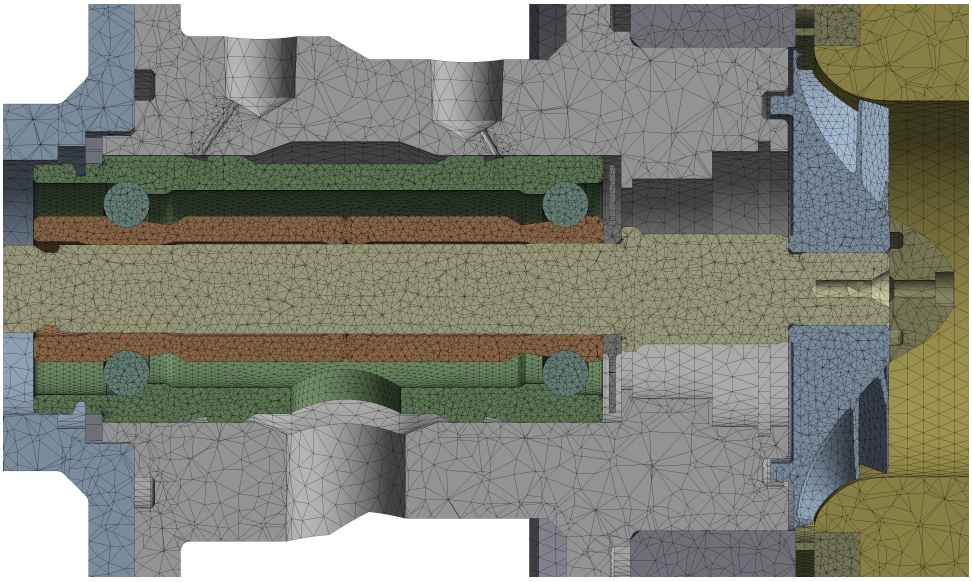

Figure 3.26: Cross sectional view of the tetrahedral mesh used to estimate the thermal load $\dot{Q}_{tot}$.

3.6. ROTORDYNAMIC ANALYSIS

3.6.1. MODELING OF THE ROTORDYNAMIC COEFFICIENTS

The calculation of the so-called rotordynamic coefficients, that is, the stiffness and damping coefficients, is necessary to perform the assessment of the dynamic stability and characteristics of the rotor. External forces acting on the rotor shaft due to the presence of the bearing cartridge SFD, the gas seal, and the turbine impeller have been modeled as stiffness and damping coefficients and used to study the system lateral vibrations. The modeling approach is described in detail in the following.

CHARACTERIZATION OF THE DYNAMIC RESPONSE OF THE SQUEEZE-FILM DAMPER

The main function of the bearing cartridge is to support the powertrain and transfer loads to the structure. The main dimensions of the cartridge are shown in Figure 3.12, while its characteristics are listed in Figure 3.5. A three-dimensional representation of the bearing cartridge is shown in Figure 3.27. The inner ring of the cartridge is fitted to the turbine shaft, while the outer ring has a radial clearance fit of 50 µm with the casing. The outer ring is axially locked in the casing using a snap-ring (item K in detail L of Figure 3.14), while a rectangular slot and pin system (L) is used as a circumferential locking mechanism. The two regions highlighted in red in Figure 3.27 act as squeeze-film-dampers, and they both extend axially by a length of 9 mm. The clearance fit ensures that, as a result of lateral motion of the powertrain, the outer ring squeezes the oil film in the gap, resulting in film pressurization and system damping. The lubricant enters the SFD and is deposited in the supply grooves shown in Figure 3.14 and discharged at the other extremity. Since the bearing cartridge is operated in a full oil bath, air ingestion is neglected in the modeling of the squeeze film damper. As a first approximation, the ambient pressure is assumed at the two axial ends of the SFD.

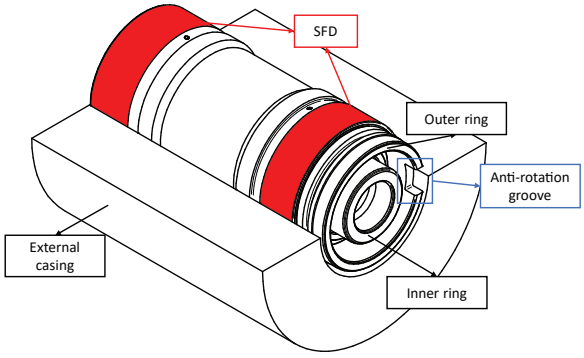

Figure 3.27: Cut-off of the rolling element bearing cartridge.

The Reynolds equation describes the generation of dynamic pressure in the oil film of the SFD. Considering the SFD radial clearance $g = 50\ \mu$m, the synchronous excitation ω at the maximum machine operating speed, and the oil density $\rho = 852.7\ \text{kgm}^{-3}$ and viscosity $\mu = 16.3 \cdot 10^{-3}$ Pa s at 50 °C, it results that the squeeze Reynolds number $Re =$

$\rho\omega g^2\mu^{-1} < 2$ throughout the entire range of considered rotational speeds. Previous studies on the development of dynamic forces in SFD [42, 43] have shown that fluid inertia has a marginal influence on the generation of the pressure field if $Re \leq 10$, and was therefore neglected in this work.

The computer program developed and documented by [44] was modified to model the oil flow squeezing within the SFD. The program performs the numerical integration of the Reynolds equation

$$\frac{\partial}{R\partial\theta}\left(\frac{\beta h^3}{12\mu}\frac{\partial\eta}{R\partial\theta}\right)+\frac{\partial}{\partial z}\left(\frac{\beta h^3}{12\mu}\frac{\partial\eta}{\partial z}\right)=\frac{\partial}{\partial t}\left(\eta-\xi\right)+\rho_c\frac{\partial h}{\partial t}, \tag{3.17}$$

where θ, z and R are the tangential, axial and radial coordinates, h is the thickness of the oil film, P is the oil pressure and β is the bulk modulus of the fluid. η and ξ are a so-called *complementarity pair*, thus variables introduced to linearize the change of fluid properties across phase interfaces. Due to the high operating speed of the turbine and the small radial gap of the SFD, oil cavitation may occur [45]. The motion of the cartridge towards the casing causes the oil-film pressure to rise locally as a result of the squeezing, while on the opposite side of the cartridge the oil-film pressure decreases as the cartridge moves away from the external casing. As a result, the liquid is forced to move circumferentially away from the location of minimum film thickness. Thus, at high pressures the oil flow velocity can be such that its static pressure drops below the saturation pressure and cavitation bubbles form in the film [23]. The application of the linear complementarity problem (LCP) included in Equation 3.17 to model cavitation in SFD has previously been demonstrated by [46]. More details about the method including a derivation of Equation 3.17 can be found in Appendix H.

The powertrain design does not include a centering element for the external ring of the bearing cartridge. Thus, when the machine is not running, the external ring of the bearing cartridge rests on the casing. As the rotational speed increases, the rotor excitation (e.g., residual unbalance forces) drives the outer ring far from the casing and generates the squeeze responsible for the oil pressurization. The ORCHID turbine is designed to operate at constant speed, and once the operating speed is reached, the motion of the outer ring reaches the so-called limit cycle. Full characterization of the limit cycle would require a transient simulation of the start-up. At the level of preliminary analysis, a parametric study of the rotordynamic performance considering circular orbits and a vertical static eccentricity is sufficient. The relation that describes the oil-film thickness distribution over time and space in the tangential direction reads

$$h(\theta,t)=g-(e\cos\omega t+e_s\cos\theta_s)\cos\theta-(e\sin\omega t+e_s\sin\theta_s)\sin\theta, \tag{3.18}$$

where h is a function of the dynamic eccentricity, which in this work has been included using circular orbits of radius e in an orthogonal plane, and of the static eccentricity e_s with phase θ_s.

Equation 3.17 is numerically solved to compute the pressure distribution in the SFD for several shaft positions within a circular orbit. The orbit-based dynamic force coefficients are calculated as suggested by San Andres & Jeung [47]. Figure 3.28 illustrates the circumferential distribution of the pressure evaluated at the SFD midplane, thuse where $z/L_{\mathrm{SFD}} = 0.5$, and for increasing rotational speed, considering a relative orbit radius of $e_{\mathrm{r}} = e/g = 0.25$ and a vibration frequency that is synchronous with the rotational speed of the rotor. As expected, only a fraction of the circumferential extension of the SFD provides a significant reaction force during operation. This is confirmed by the relatively narrow region where the high pressure in the oil film is developed, while the remaining portion of the oil-film undergoes cavitation – i.e., the region where the pressure profiles become a flat line, with a pressure of 1000 Pa. The same figure also shows that increasing rotational speeds have a significant impact on the generation of oil film pressure, highlighted by the increase in magnitude of the pressure peak and by the reduction of the region unaffected by cavitation along the circumferential direction.

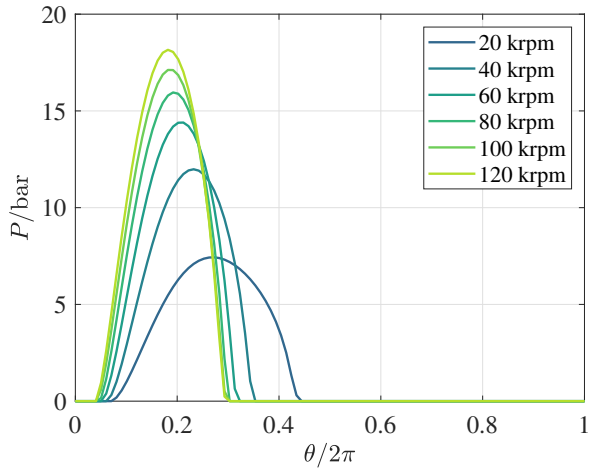

Figure 3.28: SFD pressure profile at midplane for $e_{\mathrm{r}} = 0.25$ calculated with Equation 3.17.

The impact of rotor eccentricity and orbit radius on SFD direct damping and stiffness coefficients is illustrated in Figure 3.29 for the design rotor speed of 100 krpm. The maps on the left of Figure 3.29 depict variations in direct stiffness coefficients, while those on the right show variations in direct damping coefficients. Several SFD orbits were simulated, with a relative static eccentricity ranging from 0 (centered orbit) to 90 % of the available radial clearance in the downward vertical direction. This condition represents a realistic operating scenario, in which the rotor is offset downward due to its weight. The orbit radius ranges from a minimum of 5 % of the radial clearance to a maximum value, which varies linearly with eccentricity. Specifically, the maximum orbit radius reaches 90 % of the radial clearance for a centered orbit and 5 % for an eccentric orbit of 90 %.

Considering the contours on the left of Figure 3.29, one can observe that the SFD generates increasing direct stiffness coefficients as the orbit radius and the eccentricity of the rotor increase. A squeezed oil film affected by partial cavitation generates not only a

damping force, but also a centering force [48]. The oil film thus acts as a centering spring. With reference to the right contours, the damping provided by the SFD increases for small and large orbit radii. This is because despite the fact that the portion of oil film that undergoes cavitation increases with larger orbits, the maximum pressure in the film also increases and compensates for the detrimental effect of cavitation. As expected, static eccentricity has a greater impact on k_{yy} and c_{yy}, as a vertical static eccentricity is considered and the outer ring operates with a reduced clearance in that direction. k_{xx} and c_{xx} are significantly less affected by static eccentricity. For the cases of null static eccentricity, centered circular orbits lead to equal direct force coefficients and thus $c_{xx} = c_{yy}$, and $k_{xx} = k_{yy}$. Finally, since the static eccentricity considered is purely along the vertical direction, the calculated cross-coupled force coefficients are negligible.

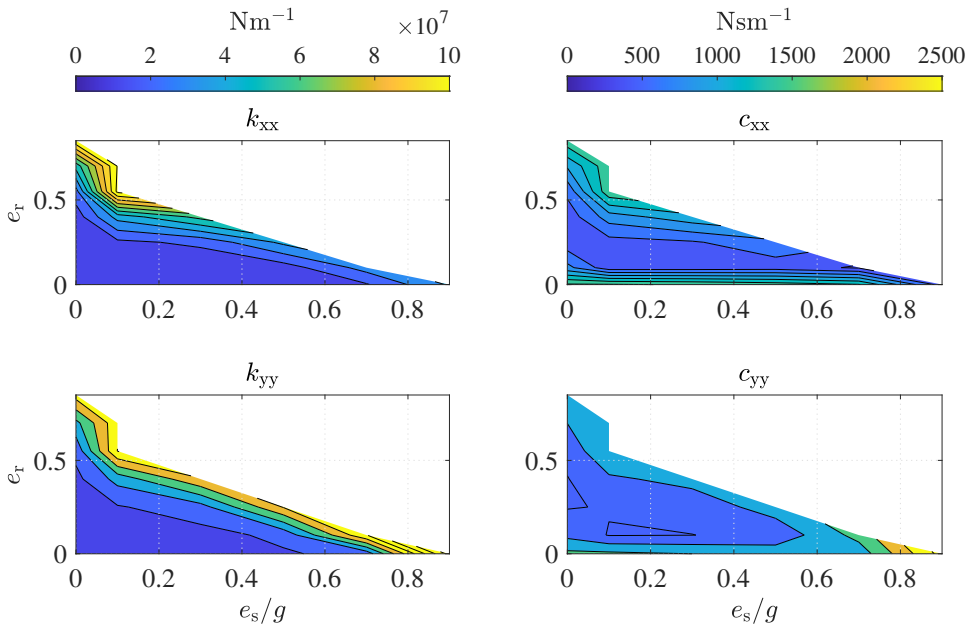

Figure 3.29: SFD stiffness and damping direct coefficients at 100 krpm as a function of the relative rotor eccentricity (e_s/g) and of the relative orbit radius (e_r).

A previous study on oil cavitation in SFD [45] showed that once the so-called *bubbly region* is reached, the oil pressure and thus damping characteristics stabilize even with a further increase in vibration frequency. Moreover, larger SFD vibrations (thus larger orbits) cause larger pressure differences within the oil film [47], causing larger portions of the film to cavitate. The dynamic response of the SFD for synchronous excitation with the rotational speed of the rotor has been analyzed. The evolution of the dynamic coefficients of SFD with rotational speed n is shown in Figure 3.30. The gray bands refer to the variation of coefficients with relative static eccentricities between 0 and 90 %, while the colored bands refer to the variation of rotordynamic coefficients with increasing relative orbit radii for the case of a centered rotor. The mean values as a function of rotor speed used in the rotordynamic analysis are shown in the figure by means of a dashed black

line.

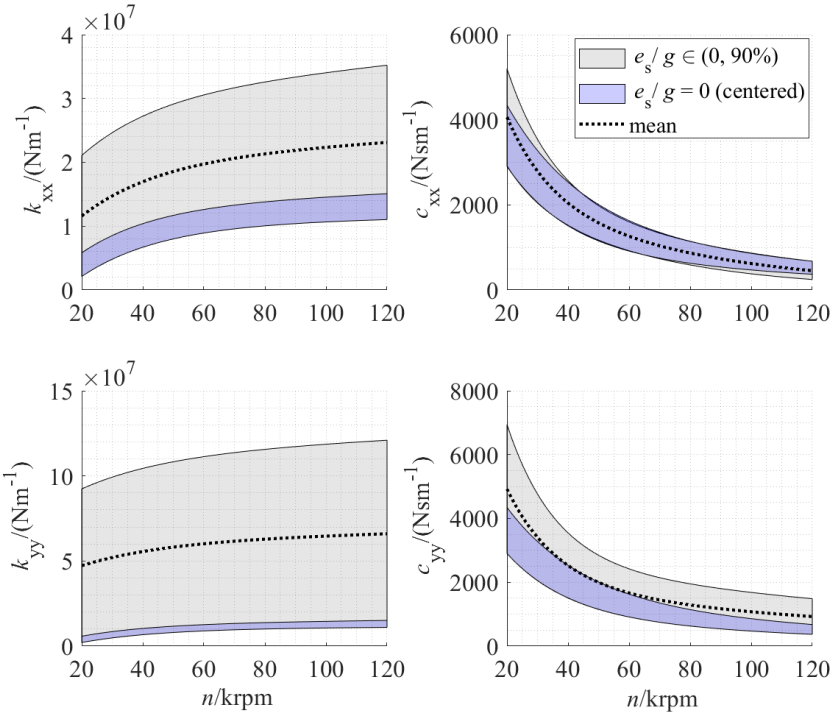

Figure 3.30: SFD dynamic coefficient range for several values of orbit radius and eccentricity. The gray shaded bands are used to account for the variation of coefficients with relative static eccentricities between 0 and 90 %, while the colored bands refer to the variation of rotordynamic coefficients with increasing relative orbit radii between 5 and 85 % assuming a centered rotor. The dashed back lines indicate the average value.

DESIGN AND CHARACTERIZATION OF A POCKET GAS SEAL

The lip seal chosen for this application, that is, G in Figure 3.14, can seal up to 5 bar of pressure differential between the bearing cavity and the outside environment. Inversely, even small pressure gradients could cause gas entrainment in the bearing cavity, with negative consequences for bearing life. Thus, to prevent pressure build-up on the impeller side of the lip seal, a gas seal was introduced between the impeller and the lip seal itself to cause a pressure drop of the pressurized siloxane behind the impeller disk.

The selection of the seal type was made by comparing the rotordynamic coefficients obtained with different types of seals. In particular, for the operating conditions and geometry of the ORCHID rotor, the calculation of the stiffness and damping coefficients was based on the experimental data for labyrinth seals (LS), fully partitioned pocket damper seals (FPDS) and honeycomb seals (HS) provided by Ertas *et al.* [49], normalized following the approach of Childs *et al.* [50]. The calculation requires the shaft rotational speed, the seal type, length, diameter, the radial clearance, and the pressure ratio across the

seal. The pressure ratio across the gas seal of ~ 1.7 was obtained as the ratio between the turbine stator outlet pressure and the maximum allowed pressure on the impeller side of the lip seal to avoid siloxane leakage in the bearing cavity. In this application, since the bearing cavity pressure is assumed to be equal to the ambient pressure, the maximum allowable downstream pressure of the gas seal is also equal to the ambient pressure.

A seal length of 9 mm was chosen, which was selected as a trade-off between a sufficient number of rows of pockets to limit leakage and the manufacturing constraint derived from the minimum material thickness separating the rows of adjacent pockets, while maintaining an acceptable overhang of the impeller wheel. The internal diameter of 12.25 mm of the gas seal was selected to leave enough radial clearance – corresponding to125 µm in the *built* state of the parts – between the outer surface of the shaft and the inner surface of the seal. The value of clearance was informed by a radial stack-up analysis of the components, considering the effect of centrifugal stress, Poisson deformation, thermal expansion, and the contribution of rigid lateral vibrations of the rotor about its barycenter.

The maximum shaft diameter of 12 mm was chosen to keep the shaft surface speed below design conditions, that is, 100 $\mathrm{m\,s^{-1}}$, as prescribed by the presence of the lip seal. The dynamic coefficients computed for three types of seals are reported in Table 3.10. The results of the calculation revealed that the LS provides the lowest effective damping – defined as $c_{\mathrm{eff}} = (c - k/\omega)$, where ω is the shaft angular speed in $\mathrm{rad\,s^{-1}}$ – with the FPDS achieving a damping performance similar to that of the HS.

Table 3.10: Comparison of dynamic coefficients for different seal types. LS: Labyrinth Seal, FPDS: Fully-partitioned Pocket Damper Seal, and HS: Honeycomb Seal.

Seal type	k_{xx} / ($\mathrm{N\,m^{-1}}$)	k_{xy} / ($\mathrm{N\,m^{-1}}$)	c_{xx} / ($\mathrm{N\,s\,m^{-1}}$)	c_{eff} / ($\mathrm{N\,s\,m^{-1}}$)
LS	3154	7884	11	4
FPDS	15768	18922	39	26
HS	20498	16556	23	19

To minimize the destabilizing effects associated with traditional labyrinth seals and to avoid the geometrical complexity of FPDS and HS type seals, a pocket gas seal type (PGS) was designed. The PGS is essentially a labyrinth seal with internal swirl breakers that provide additional damping and dynamic stability, as in FPDS and HS. The component was designed as a single-body, hollow disk made of stainless steel (AISI 316) with four rows of pockets that act as labyrinths. The adjacent rows of pockets were shifted relative to each other to avoid preferential paths for the leaking vapor. The pockets extend 50° along the circumferential direction and 1 mm along the axial one to guarantee the feasibility with additive manufacturing methods.

The geometry of the pocket seal and its relevant dimensions are illustrated in Figure 3.31. Additive manufacturing was chosen as the production process for this component to allow for geometrical freedom and to make the manufacturing cost-effective. Thin walls between adjacent pockets are arguably the most critical component feature from a manufacturing point of view; therefore, their thickness was chosen according to standard de-

sign guidelines for 3D metal parts [51]. Novel printing techniques such as metal binder jetting are effective in manufacturing complex geometries such as the pocket seal, without requiring additional material to support the overhanging regions of the part [52]. However, material finishing with conventional manufacturing techniques will still be required to achieve the tight dimensional tolerance required at the inner diameter of the PGS.

RANS simulations of the flow within the PGS were performed to estimate the leakage mass flow and the dynamic coefficients (i.e., stiffness and damping) under the nominal operating conditions of the rotor. A commercial CFD solver [53] was used for this study, and the computational domain displayed in Figure 3.32 was discretized using a hybrid approach comprising an unstructured mesh body and a structured layer near the walls. The domain was extended at the inlet and outlet of the PGS-shaft clearance gap as shown in the figure to prevent boundary conditions from influencing the flow solution inside the domain. The fluid domain geometry has been simplified to reduce the computational cost of the simulation and because the objective of the analysis is to predict the flow motion within the clearance between the PGS and the shaft. Thermal deformation of the seal geometry due to temperature gradients has been neglected, as a result of the minimal temperature drop of only 3 °C across the seal, which justifies the assumption of isothermal operation of the component. The presence of flow swirl at the inlet of the PGS was also disregarded because a proper characterization of this quantity would require complete modeling of the secondary flow passage behind the impeller disk. The additional modeling and computational efforts are deemed redundant given the low values of the dynamic coefficients of the seal. Moreover, the uncertainty of the PGS rotordynamic coefficients deriving from this simplification has been included in the form of a sensitivity analysis of rotor stability to the magnitude of cross-coupled stiffness terms.

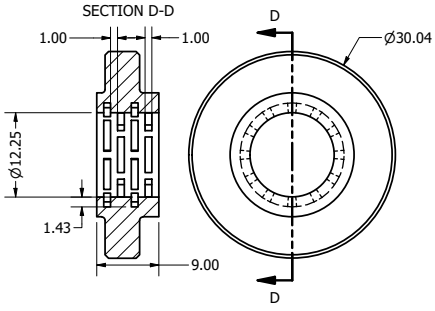

Figure 3.31: Geometry of the PGS showing the main dimensions in mm.

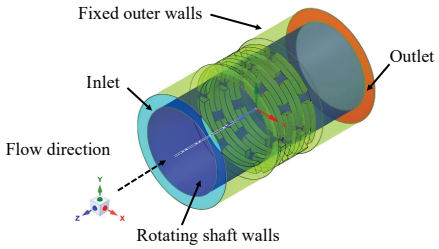

Figure 3.32: Computational domain used for the CFD flow simulations of the PGS. The employed boundary conditions are also indicated. The flow through the geometry of the gap between the shaft outer surface and the PGS inner surface is modeled.

The discretized computational domain comprised 5.1 million cells as a result of a study on mesh independence. Local inflation was added at non-slip walls (i.e., shaft and PGS

surfaces) to properly resolve the boundary layer, while the dimension of the cells was adjusted in the clearance region to maintain a suitable wall distance such that $y^+_{max} < 10$. Total pressure and temperature were imposed at the inlet and static pressure at the outlet, whose values are reported in Table 3.11. The SST k-ω model was used as turbulence closure, and look-up tables generated using a multiparameter equation of state [54] were used to calculate the fluid properties. Flow simulations for shaft rotational speeds varying from 20 krpm to 100 krpm were carried out to investigate the impact of the gas seal on system stability at different speeds. A nominal radial gap was imposed between the inner seal and the outer surface of the shaft of 50 µm, which corresponds to the minimal residual clearance estimated for the parts during operation and also leads to the largest dynamic forces.

Table 3.11: Boundary conditions for gas seal CFD simulations.

	Inlet	**Outlet**
P_t / bar	1.7	-
T_t / K	534	-
P / bar	-	1.0
n / krpm	98.1	

The leakage mass flow rate of siloxane MM computed from CFD was compared with the predictions of an empirical method commonly used in gas turbine engines [27], namely the Egli model of labyrinth seal flows [55]. Figure 3.33 shows the comparison of the mass flow rate through the PGS predicted by the Egli model and by the CFD as a function of radial clearance c. Despite the fact that the Egli model is rigorously valid for labyrinth seal geometries, the mass flow predicted by the two models is in close agreement and varies linearly with the increase in the radial clearance.

For the estimation of the rotordynamic coefficients, the forces in the horizontal and vertical directions acting on the shaft, F_x and F_y, were calculated by integrating the pressure field on the outer surface of the shaft. The direct and cross-term stiffness and damping coefficients were calculated according to their definitions

$$k_{xx} = -\frac{F_x - F_{x_0}}{\Delta x}; \quad k_{xy} = -\frac{F_y - F_{y_0}}{\Delta x}; \quad c_{xx} = -\frac{F_x - F_{x_0}}{\Delta \dot{x}}; \quad c_{xy} = -\frac{F_y - F_{y_0}}{\Delta \dot{x}}, \tag{3.19}$$

where the denominators are the imposed displacements and displacement rates, whose magnitude was determined by means of a convergence study in which their value was varied until stiffness and damping coefficients reached asymptotic values for small-amplitude vibrations. F_{x_0} and F_{y_0} are the fluid dynamic forces with null shaft displacement. Figure 3.34 shows the computed stiffness and damping coefficients at varying rotational speed of the rotor shaft.

At low speeds, direct stiffness coefficients are responsible for most of the PGS stiffness, while the contribution of the cross-coupled stiffness is important only at higher rota-

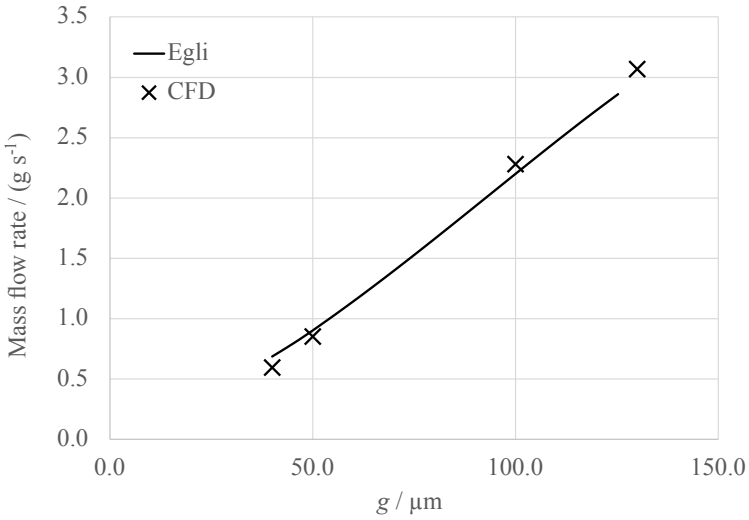

Figure 3.33: Leakage massflow rate through the PGS as a function of the radial clearance. Comparison between CFD results (×) against predictions with the Egli equation (solid line).

tional speeds. According to Ertas *et al.* [49], seals are characterized by opposite cross-coupled stiffness coefficients, which can lead to rotor instability. This is confirmed by the calculations related to the PGS considered. The terms on the secondary diagonal of the stiffness matrix are of opposite sign, although their magnitude is similar, i.e., $|k_{xy}| \approx |k_{yx}|$. The magnitude of the generated damping coefficient is also relevant for evaluating the stabilizing or destabilizing effects on the rotor. However, it is found that the magnitude of all the damping terms is negligible.

The rotordynamic coefficients computed with the CFD model have been compared to those obtained using the empirical correlation by [49] for the honeycomb seal type. Even if the geometry is different, the empirical correlation provides results similar to those obtained with CFD, as reported in Table 3.12. The prediction of cross-coupling stiffness using the two models differs by about 6.9 %. The direct stiffness predicted by the empirical model is approximately 2.6 % higher than the value calculated using CFD. Recently, Delgado *et al.* [56] conducted a similar CFD investigation to characterize the rotordynamic coefficients of a fully partitioned pocket damper seal (FPDS) and found that the direct stiffness terms computed via CFD are overpredicted compared to experimental measurements. This result suggests that CFD can be used to attain conservative values of the stiffness terms related to the PGS.

DETERMINATION OF THE IMPELLER FLUID STRUCTURE INTERACTION FORCES

Fluid structure interaction (FSI) forces in fluid machines are often responsible for rotordynamic instabilities, potentially damaging the components and, in some cases, leading to catastrophic failure of the entire system. Unsteady flows in impeller-shroud clearances due to unsteady pressure fields and rotational eccentricities are responsible for

Table 3.12: Comparison of seal dynamic coefficients calculated with CFD and with a simplified model.

	k_{xx} / (N m^{-1})	k_{xy} / (N m^{-1})	c_{xx} / (N s m^{-1})
CFD	19971	17780	0.012
HS from Table 3.10	20498	16556	23.652
Deviation / [%]	2.64	-6.88	-

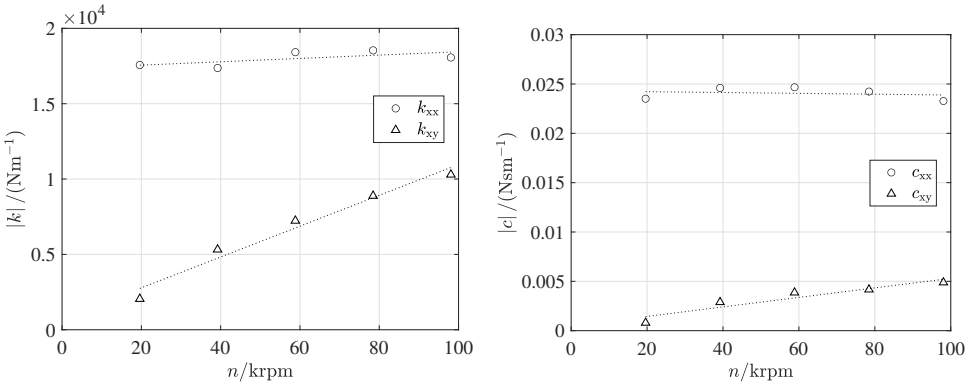

Figure 3.34: Stiffness (left) and damping (right) coefficients computed with CFD simulations. Dotted lines are linear fits used as input for the rotordynamic analysis.

the generation of nonaxisymmetric pressure fields that cause forces perpendicular to the axis of rotation [57]. San Andres [58] performed an extensive review of the different methods to predict the magnitude of destabilizing forces due to this dynamic forcing using semi-empirical methods, such as those of Alford [57] and Wachel [59], and more advanced methods based on CFD [60].

In this study, the destabilizing aerodynamic force coefficient has been predicted according to the Wachel formula [59], i.e., the standard method for radial expander-compressor systems proposed in the API 617:2002 [61]. The model allows one to estimate the stiffness coefficient that contributes to the lateral vibrations of the system.

$$k_{xy}^{FSI} = 9.55 \cdot \frac{\dot{W} \cdot B_c}{D \cdot b \cdot n} \cdot \frac{\rho_{out}}{\rho_{in}}, \tag{3.20}$$

where $\dot{W}$ is the mechanical power in W, D and b are the turbine wheel inlet diameter and inlet blade height in m, n is the angular speed in rpm, and ρ_{in}/ρ_{out} is the density ratio across the impeller. In the API 617 standard, B_c is taken equal to 3. This value is obtained by dividing the molecular weight of a fluid of 30 kg kmol^{-1} by ten, which is representative of light hydrocarbons used in industrial processes.

The destabilizing cross-term was calculated for the different operating points of the turbine, using the fluid density ratio and the stage power determined by means of CFD simulations. Solid lines in Figure 3.35 depict the values of k_{xy} obtained from Equation 3.20

with $B_c = 3$ as function of the inlet total pressure of the stage and at different rotational speeds. The dashed lines were obtained computing k_{xy} according to the same model but with a modified constant B_c – equal to 16.234 considering that the molecular weight of siloxane MM is 162.34 kg kmol^{-1} –, while the dotted lines were obtained using the correlation developed by Moore & Ransom [60] for centrifugal compressors, adapted to radial turbo expanders as suggested by other authors [58, 62]. The values of k_{xy} obtained with the modified Wachel model, i.e., for $B_c = 16.234$, and the Moore & Ransom method are similar in magnitude, although the trends as a function of the stage inlet total pressure and rotational speed are qualitatively different. As highlighted in previous research on this topic [58], a general consensus on the physical phenomena driving aerodynamic instabilities in rotating equipment, and consequently their modeling, is still lacking. Therefore, these estimates can only be used to select the most conservative k_{xy} for preliminary design purposes. Nevertheless, a full characterization of the actual destabilizing effect of the impeller would require at least data obtained with unsteady RANS simulations [62, 63], and preferably experimental verification on a fully instrumented system.

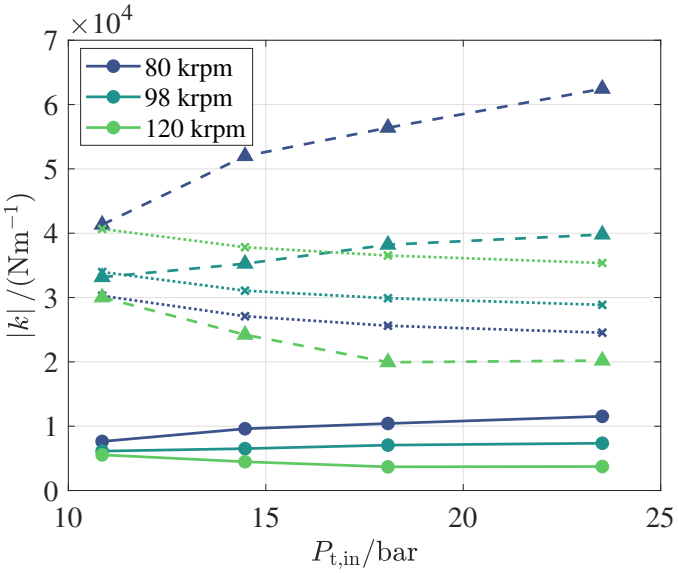

Figure 3.35: Cross-coupled stiffness coefficient k_{xy} (y-axis) computed using the Wachel method of API 617 (solid lines), the modified Wachel formula for siloxane MM (dashed lines) and the numerical correlation of Moore & Ransom (dotted lines) as a function of the stage inlet total pressure (x-axis) for three rotational speeds, namely 80, 98, and 120 krpm.

Consequently, the largest computed value of $\left|k_{xy}^{FSI}\right| = \left|k_{yx}^{FSI}\right| = 6.25 \times 10^4$ N m^{-1} is used in the analysis of lateral vibrations documented below. Notably, these terms of the stiffness matrix are assumed to be of equal magnitude and opposite sign and are thus a source of dynamic instability for the shaft train. Subsequently, a parametric analysis is conducted, as suggested in the API 617 norm, to assess system stability throughout the operating range of the machine.

3.6.2. ANALYSIS OF THE LATERAL VIBRATIONS

The dynamics of the turbine assembly has been investigated by means of a finite element rotordynamic beam model. The model includes the shaft train, the REB cartridge accounting for the SFD characteristics, the pocket gas seal, and the aerodynamic forcing of the turbine wheel. The graphical representation of the resulting rotordynamic model, made of finite beam elements, is schematically shown in Figure 3.36, together with the non-rotating cartridge outer ring. The rotating parts include the coupling hub and flange, the shaft, the bearing lock-nut, the cartridge inner ring, the impeller and the ogive. The presence of a coupling shaft – used to direct drive a high-speed generator attached to the coupling hub D illustrated in Figure 3.14 – has been modeled by adding its mass and inertia as lumped parameters on the second element on the left in Figure 3.36.

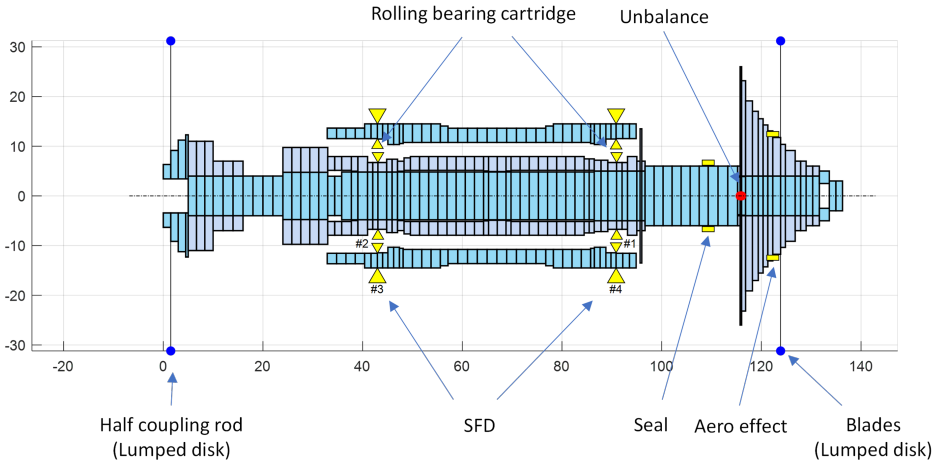

Figure 3.36: Schematic representation of the rotordynamic model showing the mass distribution of the rotor discretized using disks. The locations where the most important rotordynamic coefficients have been applied as lumped parameters are shown by means of yellow arrowheads. These include the REB stiffness, the SFD damping, the PGS stiffness and damping and the impeller FSI stiffness. The residual unbalance computed as per ISO 1940-1:2003 [64] standard is indicated by the red dot, while the coupling disk and the impeller blades lumped masses are indicated by the blue dots. x- and y- axes allow to evaluate the dimensions in mm of the rotor.

The lateral vibrations of the structure are described by the linearized system of equations

$$[M]\,\ddot{\boldsymbol{x}} + ([C] + \Omega\,[G])\,\dot{\boldsymbol{x}} + [K]\,\boldsymbol{x} = \boldsymbol{F}, \tag{3.21}$$

where $[M]$, $[C]$, $[G]$ and $[K]$ are respectively the mass, damping, gyroscopic and the stiffness matrix, while $\boldsymbol{F}$ is a vector representing the synchronous force acting on the center of gravity of the rotor due to the presence of residual unbalance. The unbalance force appears as a result of a relative shift between the rotor center of gravity and the axis of rotation, commonly caused by geometric tolerances and material imperfections.

The dynamics of each bearings row is modeled through linearized coefficients using the classical stiffness and damping matrices

$$[K]^{\mathrm{REB}} = \begin{bmatrix} k_{xx}^{\mathrm{REB}} & 0 \\ 0 & k_{yy}^{\mathrm{REB}} \end{bmatrix}, \quad [C]^{\mathrm{REB}} = \begin{bmatrix} c_{xx}^{\mathrm{REB}} & 0 \\ 0 & c_{xx}^{\mathrm{REB}} \end{bmatrix}.$$

$[K]^{\mathrm{REB}}$ and $[C]^{\mathrm{REB}}$ are diagonal matrices because the stiffness and damping cross-terms are negligible. The values of direct stiffness reported in Table 3.13 were obtained by averaging the stiffness estimated using Hertz contact theory as a function of the radial and axial loads on the bearings, which changed with the rotational speed. A value for the direct damping terms was assumed considering a bearing of similar size with comparable lubrication characteristics.

Table 3.13: Constant direct stiffness and damping coefficients used in the rotordynamics calculation. The stiffness was computed using Hertz contact theory and the value reported is the average throughout the range of rotational speed investigated. It was assumed $k_{yy}^{\mathrm{REB}} = k_{xx}^{\mathrm{REB}}$ and $c_{yy}^{\mathrm{REB}} = c_{xx}^{\mathrm{REB}}$.

Location	k_{xx}^{REB} / (Nm^{-1})	c_{xx}^{REB} / (Nsm^{-1})
Impeller side	$50 \cdot 10^6$	100
coupling side	$12 \cdot 10^6$	100

The effect of the squeeze film damper is considered by introducing a stiffness and a damping matrix with non-null direct terms and null cross-coupled terms $[C]^{\mathrm{SFD}}$ and $[K]^{\mathrm{SFD}}$. Direct terms vary as a function of rotational speed and were evaluated using the Reynolds model (Equation 3.17). Instead, the effect of the gas seal is included by means of a stiffness matrix, namely $[K]^{\mathrm{PGS}}$, with equal direct terms of the same sign and cross-terms with the same magnitude and opposite sign. The aerodynamic forces exerted by the impeller on the machine shroud are considered by introducing the stiffness matrix $[K]^{\mathrm{FSI}}$ with non-zero cross-terms and null direct terms.

$$[C]^{\mathrm{SFD}} = \begin{bmatrix} c_{xx}^{\mathrm{SFD}} & 0 \\ 0 & c_{yy}^{\mathrm{SFD}} \end{bmatrix}, \quad [K]^{\mathrm{SFD}} = \begin{bmatrix} k_{xx}^{\mathrm{SFD}} & 0 \\ 0 & k_{yy}^{\mathrm{SFD}} \end{bmatrix},$$

$$[K]^{\mathrm{PGS}} = \begin{bmatrix} k_{xx}^{\mathrm{PGS}} & k_{xy}^{\mathrm{PGS}} \\ -k_{xy}^{\mathrm{PGS}} & k_{yy}^{\mathrm{PGS}} \end{bmatrix},$$

$$[K]^{\mathrm{FSI}} = \begin{bmatrix} 0 & k_{xy}^{\mathrm{FSI}} \\ -k_{xy}^{\mathrm{FSI}} & 0 \end{bmatrix}.$$

The result of the eigenfrequency analysis as a function of the rotational speed is reported in the Campbell diagram of Figure 3.37. Fundamental and first harmonic critical speeds, hence the excitation frequencies at which the modes damped natural frequencies cross the 1X and the 2X lines in Figure 3.37, have been reported in Table 3.14 along with the corresponding damping ratios (h) in the range of rotor speeds going from 20 krpm up to 120 krpm. The mode shapes at each critical speed are shown in Figure 3.38, where the first 2 mode shapes are mainly rigid modes of the shaft and cartridge relative movement, whereas modes 3 to 7 are also caused by the bending of the shaft.

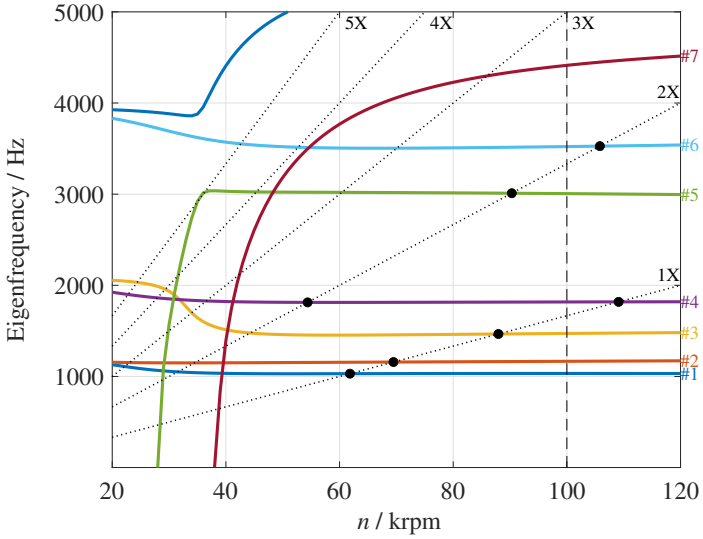

Figure 3.37: Campbell diagram of the ORCHID turbine rotor. The solid lines indicate the damped natural frequencies associated to each vibration mode up to 5000 Hz. Dotted oblique lines represent synchronous and super-synchronous excitation frequencies with respect to the shaft speed. Black dots represent critical speed crossings, occurring if the excitation frequency matches the damped natural frequency of any of the modes. Only intersections involving the 1X and 2X shaft excitations are considered for this preliminary analysis.

The colored bands shown in the Campbell diagram of Figure 3.39 illustrate the range of variation of the eigenfrequency of each vibrating mode for variations of $k_{xx}^{\mathrm{REB}} \in \pm 30\%$ of the nominal value. The eigenfrequency of mode 7 is significantly affected by the bearing stiffness, while that of the other vibrating modes is almost unaltered.

The rotor is composed of many parts stacked together for simplicity of construction. If the shaft vibrates under the action of a bending mode, micro-sliding in the circumferential direction of radially fitted parts can occur. This phenomenon, called *internal damping*, is a possible source of instability if the machine operates largely above the first

Table 3.14: Critical speed and damping ratio of several modes crossing the 1X and 2X shaft excitation frequency.

Mode #	n_{cr} **/ krpm**	h
1 (1X)	61.8	0.060
2 (1X)	69.5	0.032
3 (1X)	88.9	0.096
4 (1X)	109.1	0.030
4 (2X)	54.4	0.052
5 (2X)	90.3	0.067
6 (2X)	105.8	0.045

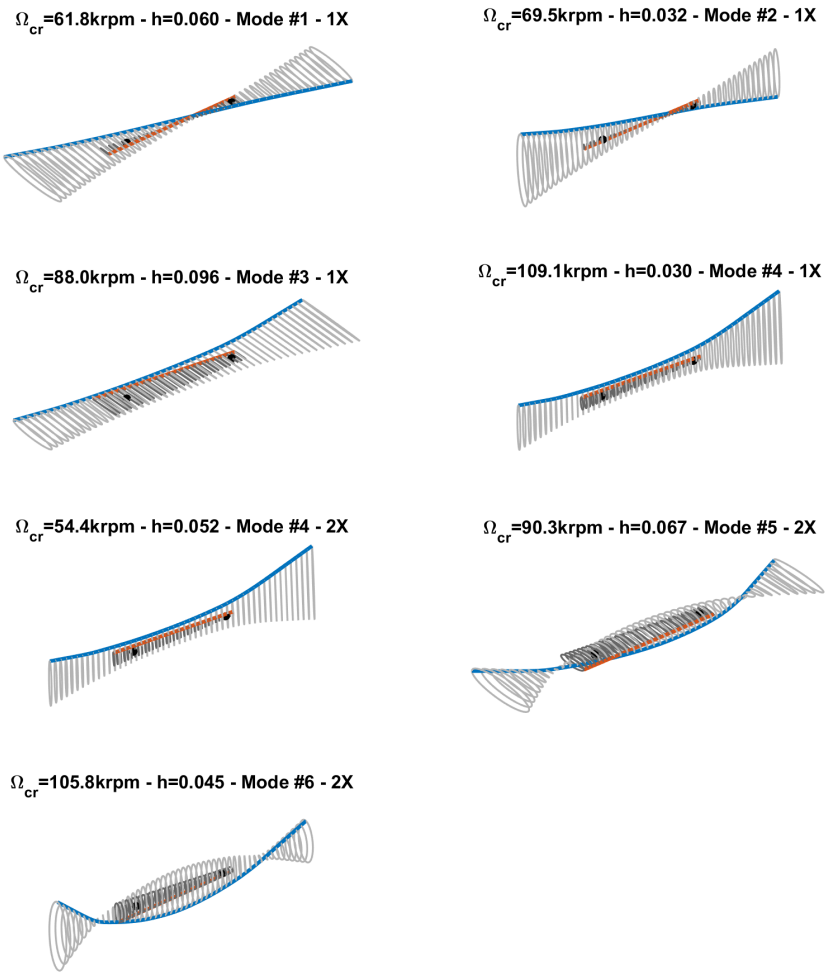

Figure 3.38: Mode shapes at the critical speeds reported in Table 3.14. The solid blue line represents the shaft center line, while the red line indicates the cartridge outer ring center line. Orbits described by the two center lines are represented in grey.

critical bending speed. The current analysis shows that the machine operates in a sub-synchronous regime concerning modes 5 and 6 (first bending modes) at the nominal speed of 100 krpm. As a consequence, internal damping was neglected in this investigation. Super-resonance conditions could only occur for large changes in roller bearing

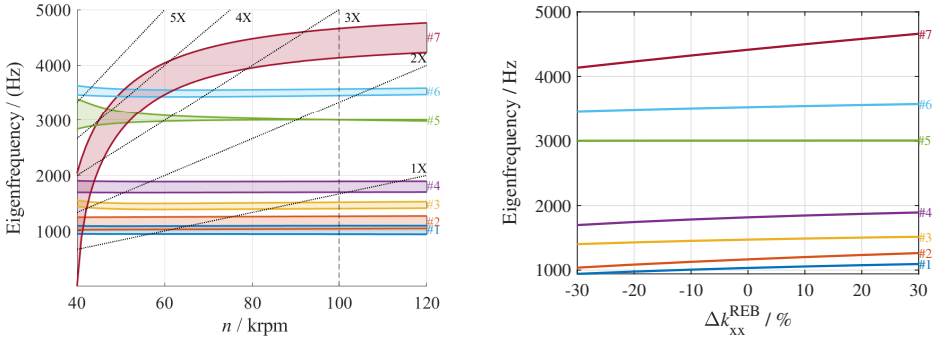

Figure 3.39: On the left, Campbell diagram of the rotor system as a function of shaft speed. The colored bands indicate the impact of a varying bearing stiffness in an interval ±30% of the nominal value given by Hertz contact theory. On the right, system natural frequencies as a function of the bearing stiffness at the nominal speed of 100 krpm.

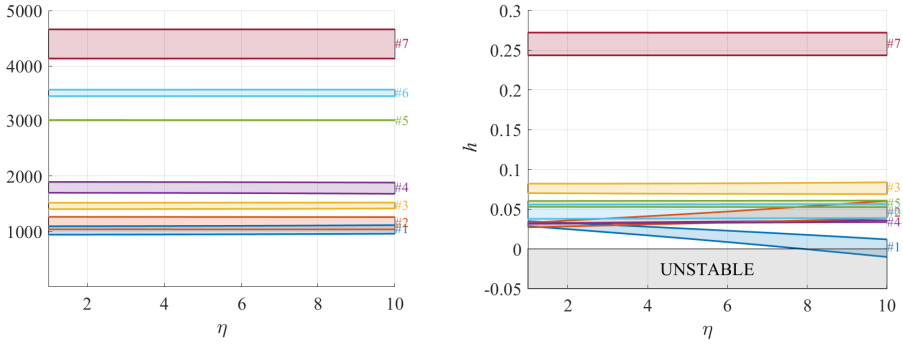

Figure 3.40: System natural frequencies (left) and stability map (right) as a function of the multiplying coefficient η of stiffness cross-terms at $n = 100$ krpm. The colored bands indicate the impact of a varying bearing stiffness in an interval ±30% of the nominal value given by Hertz contact theory.

stiffness, however Figure 3.39 shows that the natural frequencies of these modes are not affected by k_{xx}^{REB}.

The stability of the rotor was investigated by evaluating the damping factor h of each vibrating mode at the nominal rotational speed. The damping factor is defined as $h = -Re(\lambda)/|\lambda|$, where λ is the vector of the eigenvalues of the system described by Equation 3.21. If this is negative, the system is unstable [65]. Following API 617, the stability analysis has been performed by progressively varying the magnitude of the aerodynamic stiffness cross-terms k_{xy}^{FSI} and k_{xy}^{PGS}, by multiplying them by a factor $\eta \in (1,\dots,10)$. The effect of increasing η on the eigenfrequencies of the system is shown in the Campbell diagram to the left of Figure 3.40, while the stability map of the system is shown in the graph to the right, which illustrates the change in the damping factor h associated with each mode. The shaded bands indicate the eigenfrequency variation interval corresponding to variations of $k_{xx}^{REB} \in \pm 30\%$ of the nominal value. The eigenfrequency of each of the

modes is almost unaffected by the change of η. Mode #1 becomes unstable ($h < 0$) for large values of η. However, since mode #1 is a rigid movement between the shaft and the cartridge, the instability is not deemed critical.

3.7. CONCLUSION & OUTLOOK

The methodology for carrying out the preliminary mechanical design of the rotor of a supersonic radial-inflow turbine for a high-temperature, small power capacity ORC system was documented. The chosen rotor concept was determined as a result of a critical assessment considering the advantages and drawbacks of the different configurations, components, and available technologies. To simplify the complexity of the assembly and reduce the cooling requirement of the bearings, the overhung impeller configuration was chosen. Off-the-shelf ball bearings for turbochargers and PTFE rotary shaft seals were selected to keep development time and cost low.

- The off-design performance of the ORCHID turbine was computed using CFD, at increasing rotational speed (80, 98.1, and 120 krpm) and total inlet pressure (10.9, 14.5, 18.1, and 23.5 bar). At the design point, about half of the entire efficiency penalty could be attributed to the losses in the stator vanes and the radial gap, while at high speed and low inlet pressure, i.e., 120 krpm and 10.9 bar, fluid dynamic losses in the stationary components become the major contribution and the impeller operates with negative incidence.

- The axial thrust of the impeller was estimated using the hybrid method proposed by Tiainen *et al.* [37], and a correlation based on data from CFD simulations was derived to express the force F_{ax} as a function of the corrected mass flow rate $\dot{m}_{corr}$. Via the numerical correlation, the highest value of the axial thrust ($\approx$ 600 N) was calculated, corresponding to the operating point featuring maximum inlet total pressure (23.5 bar), minimum inlet total temperature (255 °C), and maximum rotational speed (120 krpm) of the turbine.

- The static structural analysis of the impeller carried out using the finite elements method revealed that titanium alloy Ti6Al4V-T6 is the more suitable material choice. When compared to stainless steel 316L, the former material guarantees a higher safety factor to yield ($\approx$ 1.8) due to its high yield strength, and lower deformation under load ($\approx$ 60-70% that of 316L) thanks to its low density.

- An empirical method [40] to estimate the power loss occurring in ball bearings was implemented, and the thermal energy dissipation was computed at different operating conditions. It was observed that a significant fraction of the total power dissipated by the bearings can be attributed to the axial thrust of the impeller, which was calculated using the numerical correlation discussed above. The maximum power loss in the operating envelope of the machine was 565 W, found in the condition of maximum axial thrust. A thermal analysis of the entire assembly using the finite elements method was conducted to determine the gross thermal power to be transferred to the lubricant, which resulted to be $\approx$ 1.2 kW, using a simplified approach and assuming stationary conditions for the thermal simulation. It results that $\approx$ 635 W of the overall thermal input to the lubricant are due to the

thermal energy by conduction from the turbine casings which are in contact with the hot gas flow.

- The damped rotordynamic response of the rotor when subject to unbalance was finally investigated. The damping coefficients of the cartridge squeeze-film damper were computed numerically throughout the entire operating range of the machine (0-120 krpm), considering a nominal radial clearance of 50 µm with the turbine housing. Results obtained by solving the Reynolds equation for the oil-film complemented by a linearized cavitation model showed that the cartridge acts as a spring, thus introducing additional stiffness which is largely dependent on the dynamic eccentricity and static eccentricity of the rotor. This result suggests that additional effort is required to characterize the rotor transient behavior from start-up to the limit cycle for a more accurate determination of the actual oil-film stiffness, and as a consequence of the natural frequencies of the rotor. Moreover, rotor damping deteriorates at increasing rotational speed due to the increasingly larger portion of oil-film that undergoes cavitation. Thus, the rotor is underdamped in the operating range of interest, which results in poor damping capacity of the damper should resonance at one of the critical speeds occur. These aspects underline the importance of correctly estimating the natural frequencies of the system to ensure safe operation of the machine during testing.

- A pocket gas seal was designed in-house to limit the leakage flow rate of working fluid to the bearings housing. The leakage mass flow rate calculated by means of RANS simulations was found to be in good agreement with values obtained using an empirical method commonly employed for the sealing design of gas turbines. Moreover, the stiffness and damping coefficients of the pocket gas seal were computed using the results of the simulations. These show that the pocket gas seal proposed herein introduces small direct and cross-coupled stiffness relatively to other types of seals, which were included in the rotordynamic analysis to evaluate the impact of the seal on system stability. Conversely, the damping provided by the pocket gas seal is negligible compared to that of the cartridge squeeze-film damper, being about 5 to 6 orders of magnitude lower.

- The lateral vibration analysis of the first 7 mode shapes reveals the presence of rigid modes (1 and 2) and flexible modes (from 3 to 7). A sensitivity analysis was carried out to investigate the impact of modeling assumptions on the results of the rotordynamic analysis. In particular, mode 7 exhibits a large sensitivity to variations of ±30% of the bearings stiffness coefficient, which was computed using the Hertz contact theory. Despite this, no critical speed with the 1X and 2X shaft speed excitation frequencies is observed for this mode within the constant speed range (80-120 krpm) of the rotor. Modes 5 and 6 instead show a weak dependence on the bearing stiffness, but do have critical speeds of 2X shaft speed excitation frequency in the constant speed range.

- Finally, the stability of the rotor was assessed by investigating the change in damping ratio h of each mode shape for increasing values of the cross-coupled stiffness coefficients associated to the impeller-shroud aerodynamic force, which were es-

timated using the Wachel method [59] and of the PGS stiffness coefficients. The analysis highlights that mode 1 becomes unstable only if values of the cross-coupled stiffness coefficients are about one order of magnitude larger than those estimated in this study. Nevertheless, since the computation of the destabilizing stiffness term (especially the impeller-shroud force) is subject to large uncertainty, the analysis presented here is purely indicative of a worst case scenario and further investigations are necessary to properly evaluate its impact on system stability.

Future work will be devoted to the detailed design of the turbine and selection of auxiliary components, and later to the testing of the machine instrumented with embedded sensors. Design reviews of the current turbine concept will be conducted with experts in high-speed turbomachinery design to further improve the design. Furthermore, sensors and instruments for accurate measurement of the efficiency herein estimated with CFD will be selected, as well as for measuring the bearings power loss at different operating conditions. Embedded sensors in the rotor to measure the vibration amplitude at different rotational speeds will help characterize the transient dynamics of the rotor and its limit cycle. Finally, more in-depth numerical investigations using higher-fidelity models, such as full-annulus URANS simulations, are considered useful to obtain further insight about the destabilizing nature of the cross-coupled stiffness coefficients resulting from the impeller secondary flows.

BIBLIOGRAPHY

1. De Servi, C. M., Burigana, M., Pini, M. & Colonna, P. Design Method and Performance Prediction for Radial-Inflow Turbines of High-Temperature Mini-Organic Rankine Cycle Power Systems. *ASME. J. Eng. Gas Turbines Power* **141,** 091021. doi:10.1115/1.4043973 (2019).
2. Head, A. J. *Novel Experiments for the Investigation of Non-Ideal Compressible Fluid Dynamics* PhD thesis (Delft University of Technology, 2021).
3. Cappiello, A., Majer, M., Tuccillo, R. & Pini, M. *On the Influence of Stator-Rotor Radial Gap Size on the Fluid-Dynamic Performance of Mini-ORC Supersonic Turbines* in *Proceedings of the ASME Turbo Expo 2022: Turbomachinery Technical Conference and Exposition* **10B** (2022), V10BT35A015. doi:10.1115/gt2022-83309.
4. Whitfield, A. & Baines, N. C. *Design of Radial Turbomachines* ISBN: 978-0-470-21667-5 (Longman Scientific & Technical, Harlow, England, 1990).
5. Ansys® CFX. Academic Research CFX, Release 22.0.
6. Barth, T. J. & Jespersen, D. C. *The Design and Application of Upwind Schemes on Unstructured Meshes* in *Proceedings of the 27th AIAA Aerospace Sciences Meeting* (American Institute of Aeronautics and Astronautics, Reno, NV, Jan. 1989). doi:10.2514/6.1989-366.
7. *Aeronamic* https://aeronamic.com/.
8. Yuksek, E. L. & Mirmobin, P. Electricity Generation From Large Marine Vessel Engine Jacket Water Heat. *ASME 2015 9th International Conference on Energy Sustainability, ES 2015, collocated with the ASME 2015 Power Conference, the ASME 2015 13th International Conference on Fuel Cell Science, Engineering and Technology, and the ASME 2015 Nuclear Forum* **2.** doi:10.1115/es2015-49226 (2015).
9. Di Bella, F., Cho, J.-K., Kwon, J.-S. & Jeong, H.-g. Development and testing of a 250 kWe ORC system using an integrated axial turbine and high speed generator for 3.7 bar,a condensing steam. *Proceedings of the* 3^{rd} *International Seminar on ORC Power Systems* (2015).
10. Di Bella, F. Gas turbine waste heat recovery using a 20,000 rpm sealless, turbine generator ORC system. *Symposium of the Industrial Application of Gas Turbines Committee* (2015).
11. Harinck, J., Turunen-Saaresti, T., Colonna, P., Rebay, S. & van Buijtenen, J. Computational study of a high-expansion ratio radial organic Rankine cycle turbine stator. *Journal of Engineering for Gas Turbines and Power* **132,** 1565–1636. doi:10.1115/1.3204505 (2010).

12. Swann, M. K., Watkins, J. & Bornstein, K. R. Present Limits Of Operation Of Product Lubricated And Magnetic Bearings In Pumps (1997).

13. Bolotov, A., Novikova, O. & Novikov, V. Temperature properties of passive magnetic bearing. *E3S Web of Conferences* **376,** 01068. doi:10.1051/e3sconf/202337601068 (2023).

14. Kascak, A. F. *High-Temperature Magnetic Bearings Being Developed for Gas Turbine Engines* tech. rep. Technical report 20050177214 (1998).

15. Provenza, A. J., Montague, G. T., Jansen, M. J., Palazzolo, A. B. & Jansen, R. H. High Temperature Characterization of a Radial Magnetic Bearing for Turbomachinery. *Journal of Engineering for Gas Turbines and Power* **127,** 437–444. doi:10.1115/1.1807413 (2005).

16. Shultz, R. & Narayanaswamy, A. *Magnetic Bearings for Supercritical CO2 Turbomachinery* 2018.

17. Gu, L., Guenat, E. & Schiffmann, J. A review of grooved dynamic gas bearings. *Applied Mechanics Reviews* **72** (2020).

18. Agrawal, G. L. *Foil air/gas bearing technology - An overview* in *Proceedings of the ASME Turbo Expo* **1** (American Society of Mechanical Engineers (ASME), 1997). doi:10.1115/97-gt-347.

19. Heshmat, H., Walton, J. F., Corte, C. D. & Valco, M. Oil-Free Turbocharger Demonstration Paves Way to Gas Turbine Engine Applications. *Proceedings of the ASME Turbo Expo: Power for Land, Sea, and Air. Volume 1: Aircraft Engine; Marine; Turbomachinery; Microturbines and Small Turbomachinery.* **1.** doi:10.1115/2000-gt-0620 (2000).

20. Heshmat, H., Walton, J. F. & Nicholson, B. D. Ultra-High Temperature Compliant Foil Bearings: The Journey to 870°C and Application in Gas Turbine Engines — Experiment. *Proceedings of the ASME Turbo Expo: Turbomachinery Technical Conference and Exposition.* **7B.** doi:10.1115/gt2018-75555 (2018).

21. Kim, T. H. & Andrés, L. S. Heavily Loaded Gas Foil Bearings: A Model Anchored to Test Data. *Journal of Engineering for Gas Turbines and Power* **130,** 012504. doi:10.1115/1.2770494 (2008).

22. De Waart, W. & Pini, M. The Role of the Working Fluid and Non-Ideal Thermodynamic Effects on Performance of Gas Lubricated Bearings. *Journal of Engineering for Gas Turbines and Power* **147,** 061015. doi:10.1115/1.4056695 (2024).

23. Nguyen-Schäfer, H. *Rotordynamics of Automotive Turbochargers* doi:10.1007/978-3-642-27518-0 (Springer Berlin, Heidelberg, 2012).

24. Uusitalo, A., Turunen-Saaresti, T., Honkatukia, J. & Dhanasegaran, R. Experimental study of small scale and high expansion ratio ORC for recovering high temperature waste heat. *Energy* **208,** 118321. doi:10.1016/j.energy.2020.118321 (2020).

25. Schweitzer, F. & Adleff, K. Rolling bearings in turbocharger applications. *MTZ worldwide* **67,** 16–19. doi:10.1007/bf03227869 (2006).

26. Minibea Mitsumi automotive turbo bearings, Last accessed Sep 2, 2024. https://nmbtc.com/custom-products/automotive-turbo-bearings/.

27. Ludwig, L. P. Gas path sealing in turbine engines. *Tribology Transactions* **23,** 1–22. doi:10.1080/05698198008982942 (1980).

28. Aslan-zada, F. E., Mammadov, V. A. & Dohnal, F. Brush seals and labyrinth seals in gas turbine applications. *Proceedings of the Institution of Mechanical Engineers, Part A: Journal of Power and Energy* **227,** 216–230 (2013).

29. Hendricks, R. C., Steinetz, B. M. & Braun, M. J. *Turbomachine Sealing and Secondary Flows Part 1—Review of Sealing Performance, Customer, Engine Designer, and Research Issues* 2004. https://ntrs.nasa.gov/api/citations/20040086704/downloads/20040086704.pdf.

30. Forsthoffer, W. E. *Dry Gas Seal Best Practices* in *Forsthoffer's Best Practice Handbook for Rotating Machinery* (Elsevier, 2011), 501–524. doi:10.1016/b978-0-08-096676-2.10009-8.

31. *Rotary shaft seals* Technical datasheet EPS 5350|USA. Parker Hannifin Corp. https://www.parker.com/content/dam/Parker-com/Literature/Engineered-Polymer-Systems/5350.pdf.

32. Johnston, D. E. Design aspects of modern rotary shaft seals. *Proceedings of the Institution of Mechanical Engineers, Part J: Journal of Engineering Tribology* **213,** 203–213. doi:10.1243/1350650991542947 (1999).

33. Shabbir, S., Garvey, S. D., Dakka, S. M. & Rothwell, B. C. An Experimental Study of Contact Temperatures at Sealing Interface against Varying Shaft Surfaces. *Coatings 2021, Vol. 11, Page 156* **11,** 156. doi:10.3390/coatings11020156 (2021).

34. *Turcon Varilip PDR* Technical datasheet. Trelleborg sealing solutions. https://www.trelleborg.com/en/seals/products-and-solutions/rotary-seals-or-shaft-seals/turcon-varilip-pdr.

35. *Dienst Elektronische en Mechanische Ontwikkeling (DEMO) - Delft University of Technology* https://www.tudelft.nl/demo.

36. *Mechanical properties of fasteners made of carbon steel and alloy steel - Part 1: Bolts, screws and studs with specified property classes — Coarse thread and fine pitch thread* ISO 898-1:2013. International Organization for Standardization, 2013.

37. Tiainen, J., Jaatinen-Värri, A., Grönman, A., Sallinen, P., Honkatukia, J. & Hartikainen, T. Validation of the Axial Thrust Estimation Method for Radial Turbomachines. *International Journal of Rotating Machinery* **2021.** doi:10.1155/2021/6669193 (2021).

38. Ansys® Mechanical. Academic Research Mechanical, Release 22.0.

39. Zander, M., Otto, M., Lohner, T. & Stahl, K. Evaluation of friction calculation methods for rolling bearings. *Forschung im Ingenieurwesen/Engineering Research* **87,** 1307–1316. doi:10.1007/s10010-023-00715-1 (2023).

40. *Lubrication of Rolling Bearings* tech. rep. Technical report: TP-176 (). https://www.schaeffler.com/remotemedien/media/_shared_media/08_media_library/01_publications/schaeffler_2/tpi/downloads_8/tpi_176_de_en.pdf.

41. *Industrial liquid lubricants — ISO viscosity classification* ISO 3448:1992. International Organization for Standardization, 1992.

42. San Andres, L. A. & Vance, J. M. Effects of Fluid Inertia on Finite-Length Squeeze-Film Dampers. *ASLE TRANSACTIONS* **30,** 384–393. doi:10.1080/05698198708981771 (1987).

43. Delgado, A. & San Andres, L. A. Model for Improved Prediction of Force Coefficients in Grooved Squeeze-film-dampers and Oil Seal Rings. *ASME J. Tribol.* **132,** 032202. doi:10.1115/1.4001459 (2010).

44. Gheller, E., Chatterton, S., Vania, A. & Pennacchi, P. Squeeze Film Damper Modeling: A Comprehensive Approach. *Machines* **10.** doi:10.3390/machines10090781 (2022).

45. Zeidan, F. Y. & Vance, J. M. Cavitation Regimes in Squeeze-film-dampers and Their Effect on the Pressure Distribution. *Tribology Transactions* **33,** 447–453. doi:10.1080/10402009008981975 (1990).

46. Fan, T. & Behdinan, K. The evaluation of linear complementarity problem method in modeling the fluid cavitation for squeeze film damper with off-centered whirling motion. *Lubricants* **5.** doi:10.3390/lubricants5040046 (2017).

47. San Andres, L. & Jeung, S. H. Orbit-Model Force Coefficients for Fluid Film Bearings: A Step beyond Linearization. *ASME. J. Eng. Gas Turbines Power* **138,** 022502 (2016).

48. Vance, J. *Rotordynamics of Turbomachinery* (John Wiley and Sons, New York, 1998).

49. Ertas, B. H., Delgado, A. & Vannini, G. Rotordynamic Force Coefficients for Three Types of Annular Gas Seals With Inlet Preswirl and High Differential Pressure Ratio. *Journal of Engineering for Gas Turbines and Power* **134,** 042503. doi:10.1115/1.4004537 (2012).

50. Childs, D., Elrod, D. & Hale, K. Annular Honeycomb Seals: Test Results for Leakage and Rotordynamic Coefficients; Comparisons to Labyrinth and Smooth Configurations. *Journal of Tribology* **111,** 293–300. doi:10.1115/1.3261911 (1989).

51. Ewald, A. & Schlattmann, J. Design guidelines for laser metal deposition of lightweight structures. *Journal of Laser Applications* **30,** 032309. doi:10.2351/1.5040612 (2018).

52. Blunk, H. & Seibel, A. Design guidelines for metal binder jetting. *Progress in Additive Manufacturing,* 1–8. doi:10.1007/s40964-023-00475-y (2023).

53. Ansys® Fluent. Academic Research Fluent, Release 21.0.

54. Huber, M. L., Lemmon, E. W., Bell, I. & McLinden, M. O. The NIST REFPROP database for highly accurate properties of industrially important fluids. doi:10.1021/acs.iecr.2c01427 (2022).

55. Egli, A. The Leakage of Steam Through Labyrinth Seals. *Journal of Fluids Engineering* **57,** 115–122. doi:10.1115/1.4019911 (1935).

56. Delgado, A., San Andrés, L., Yang, J. & Thiele, J. *Experimental Force Coefficients for a Fully-Partitioned Pocket Damper Seal and Comparison to Other Two Seal Types* in *Proceedings of the ASME Turbo Expo 2022: Turbomachinery Technical Conference and Exposition* **8A** (2022), V08AT22A020. doi:10.1115/1.4056347.

57. Alford, J. S. Protecting Turbomachinery From Self-Excited Rotor Whirl. *Journal of Engineering for Power* **87,** 333–343. doi:10.1115/1.3678270 (1965).

58. San Andres, L. A Review of Turbine and Compressor Aerodynamic Forces in Turbomachinery. *Lubricants* **11.** doi:10.3390/lubricants11010026 (2023).

59. Wachel, J. & von Nimitz, W. Ensuring the Reliability of Offshore Gas Compression Systems. *Journal of Petroleum Technology* **33,** 2252–2260. doi:10.2118/10591-pa (1981).

60. Moore, J. J., Ransom, D. L. & Viana, F. Rotordynamic Force Prediction of Centrifugal Compressor Impellers Using Computational Fluid Dynamics. *Journal of Engineering for Gas Turbines and Power* **133,** 042504. doi:10.1115/1.2900958 (2010).

61. *Axial and Centrifugal Compressors and Expander-Compressors for Petroleum, Chemical and Gas Industry, 7th ed.* API 617. American Petroleum Institute, 2002.

62. Lerche, A. H., Musgrove, G. O., Moore, J. J., Kulhanek, C. D. & Nordwall, G. *Rotordynamic Force Prediction of an Unshrouded Radial Inflow Turbine Using Computational Fluid Dynamics* in *Proceedings of the ASME Turbo Expo 2013: Turbine Technical Conference and Exposition* **7A** (2013), V07AT29A015. doi:10.1115/gt2013-95137.

63. Pan, Y., Yuan, Q., Huang, G., Gu, J., Li, P. & Zhu, G. Numerical Investigations on the Blade Tip Clearance Excitation Forces in an Unshrouded Turbine. *Applied Sciences 2020, Vol. 10, Page 1532* **10,** 1532. doi:10.3390/app10041532 (2020).

64. *Mechanical vibration — Balance quality requirements for rotors in a constant (rigid) state — Part 1: Specification and verification of balance tolerances* ISO 1940-1. International Organization for Standardization, 2003.

65. Bachschmid, N., Pennacchi, P. & Vania, A. Steam-whirl analysis in a high pressure cylinder of a turbo generator. *Mechanical Systems and Signal Processing* **22,** 121–132. doi:10.1016/j.ymssp.2007.04.005 (2008).

4

DETAILED DESIGN AND REALIZATION OF THE ORCHID TURBINE TEST BED

ABSTRACT
The detailed design and realization of an instrumented rig for testing supersonic radial-inflow turbines for high-temperature ORC power systems are documented. The test bed is integrated within the ORCHID (organic Rankine cycle hybrid integrated device) facility currently in operation at the Propulsion and Power Laboratory (P&P Lab) of the Faculty of Aerospace Engineering at Delft University of Technology. The ultimate goals of the future experimental campaign are the accurate characterization of the fluid-dynamic performance of these unconventional turbines, the validation of guidelines and numerical models for their optimal aerothermal design and performance prediction, and the testing of advanced components such as highly optimized stator and impeller configurations and novel types of diffusers.

4.1. INTRODUCTION

Demonstrating the validity and accuracy of design guidelines and numerical models for high-efficiency radial-inflow turbines for high-temperature ORC power systems, such as those discussed in Chapter 2, requires a state-of-the-art instrumented test bed. The detailed design of the turbine test rig for the ORCHID setup is described in this chapter, and aspects related to its integration within the existing facility are elucidated. The scope of design includes:

1. the definition of the layout of the turbine test bed and its working principle,
2. the detailed design of the turboexpander assembly documented in Chapter 3 and its integration into the turbine test bed,
3. the choice of auxiliary components to ensure safe and reliable operation of the turbogenerator, including the valves for control and emergency shut-down, and the type of lubrication system and its components,
4. the determination of a power conditioning strategy to dissipate the electrical power produced by the turbogenerator, and
5. the selection of process instruments to control and monitor the operation of the setup and to evaluate the fluid dynamic performance of the turboexpander with the highest possible accuracy.

The chapter is organized as follows. First, the ORCHID balance of plant (BoP) is presented, highlighting the strategy to control the process conditions at the inlet and outlet of the turbine test bed. Second, the layout of the turbine test bed is described; the main assumptions, design choices, and its components are discussed. The detailed design of the turbogenerator assembly is extensively reported, outlining the changes and improvements made to the turbine rotor assembly, whose initial design is documented in Chapter 3. Moreover, the integration of the electric generator and the power conditioning strategy selected to dissipate the electric power produced by the powertrain are discussed. Finally, the instrumentation chosen to monitor the test bed during the operation is illustrated. A study aimed at quantifying the uncertainty related to the turbine efficiency measurements is documented by resorting to performance data obtained from CFD simulations.

4.2. THE ORCHID

The design of the ORCHID BoP was carried out and described in detail by Head [1]. Herein the process and instrumentation diagram (P&ID) of the ORCHID is reported in Figure 4.1 for convenience. The control strategy of the ORCHID has been described in Section 5.5.3 of [1]. In summary, the mass flow rate of process fluid at the outlet of the feed pump (zone D1 of Figure 4.1) is used to control the total inlet pressure to the turbine. The inlet total temperature is controlled by regulating the mass flow of thermal oil in the ORCHID evaporator, namely the flow rate passing through the loop highlighted in red in Figure 4.1. This is achieved by controlling the speed of the thermal oil feed pump, not indicated in the figure. The back pressure of the turbine is regulated by adjusting the pressure in the condenser, which can be varied by regulating the water-glycol feed pump speed (zone D6 of Figure 4.1) or the rotational speed of the fans of the air cooler.

Two flanges are available in the ORCHID setup for connecting the turbine test bed to the BoP that are not explicitly indicated in the ORCHID P&ID reported here. The *supply* flange, placed right downstream of the temperature sensor TT005, is of standard size DN80 and is used to route superheated siloxane MM vapour to the ORCHID turbine (zone A4 of Figure 4.1). The *return* flange, located just upstream of the location of the bursting disk BD03 (zone B4), is DN100 and used to dump de-superheated MM back into the ORCHID main loop. The locations of the two flanges are also indicated by the red arrows in Figure 4.2, showing the ORCHID BoP in an isometric plane. The main components of the BoP are numbered and listed in the bill of materials at the bottom left of the figure.

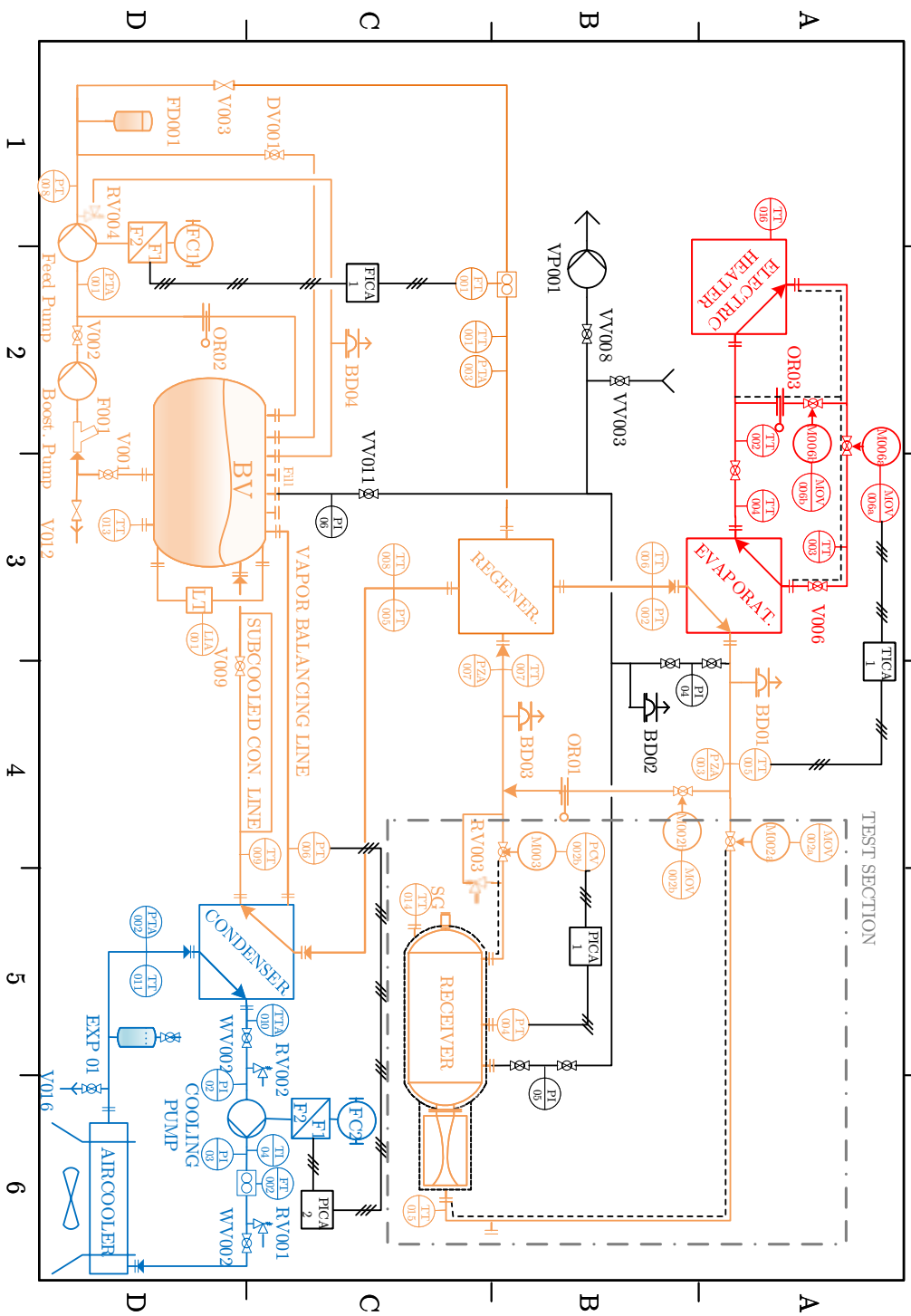

Figure 4.1: P&ID diagram of the ORCHID setup, figure courtesy of [1].

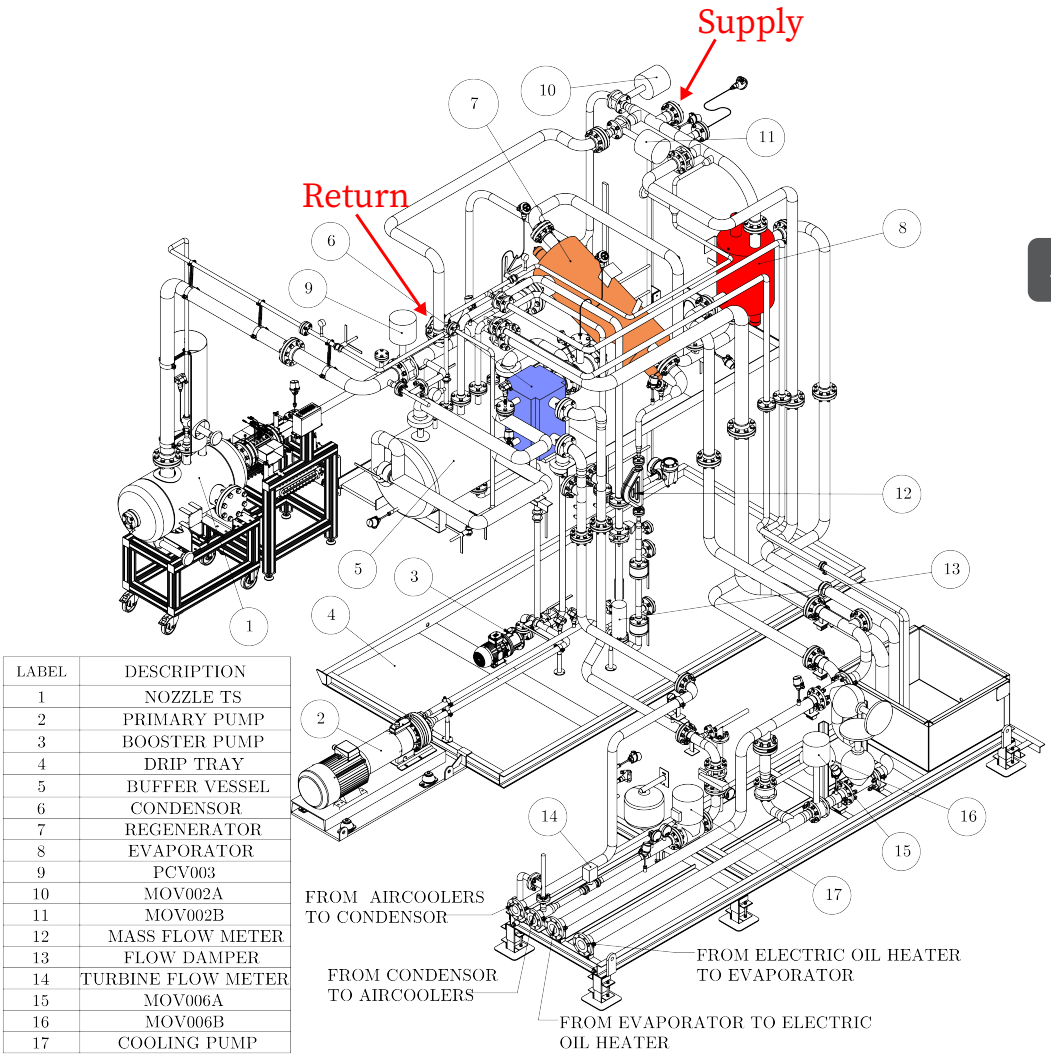

LABEL	DESCRIPTION
1	NOZZLE TS
2	PRIMARY PUMP
3	BOOSTER PUMP
4	DRIP TRAY
5	BUFFER VESSEL
6	CONDENSOR
7	REGENERATOR
8	EVAPORATOR
9	PCV003
10	MOV002A
11	MOV002B
12	MASS FLOW METER
13	FLOW DAMPER
14	TURBINE FLOW METER
15	MOV006A
16	MOV006B
17	COOLING PUMP

Figure 4.2: CAD drawing of the balance of plant of the ORCHID setup, figure courtesy of [1] and adapted for the current use.

4.3. TURBINE TEST BED

4.3.1. DESIGN REQUIREMENTS

Special attention during the design phase of the turbine test bed was devoted to reducing possible risks associated to the turbogenerator operation. Feedback and recommendations received during multiple design reviews with experts of the field provided a guide to improve on the initial design and select the appropriate components. A first of such design reviews held in September 2023 involved colleagues of the *Institue of Turbomachinery and Fluid Dynamics, Hannover Leibniz University* [2], and provided useful inputs and design recommendations for a first iteration of the initial design of the turbine shown in Chapter 3. The second design review was conducted in November 2023 with the support of *Van der Lee Turbo Systems* [3], a Dutch company specialized in design and development of high-speed, high performance, turbomachinery systems. The following elements were considered to design the turbine test bed:

1. The results of the rotordynamic analysis in Section 3.6.2, Figure 3.37, showed that the rotor can operate at speeds close to some of the critical frequencies. However, a margin of at least 10 % from each critical speed should be maintained when operating the setup, to prevent the occurrence of excessive rotordynamic vibrations. The turbine shaft length could be decreased by using a smaller bearings cartridge assembly, which, consequently, allows to increase the critical speeds and the margin.

2. An additional brake, or analogous safety system, should be included to prevent the system from overspeeding in the event of a generator failure.

3. Warm-up of the turbine assembly should be performed before start-up using a tracing system. This is to ensure that components made of different materials reach their "hot" condition before the machine is spun, reducing the risk of rubbing and contact between parts. Furthermore, this prevents vapor from condensing when coming in contact with cold metal.

4. The thickness of the impeller blades should be increased at the root section to increase stiffness. Moreover, the blade count should be changed to avoid having a minimum common denominator with the stator vanes count, to prevent fluid dynamic instabilities.

5. The volute and stator vanes could be machined as a single component to decrease the number of tolerances in the chain, and to reduce the risk of gas leaks by eliminating one gasket from the assembly.

6. The lip seal on the impeller side should be replaced by a piston ring seal because of the risk of thermal degradation of the lip material, which is subject to high temperature and high slip speed. The piston ring seal ensures relatively low leakage flow rate if the pressure difference is kept low, although wear due to sliding contact between metal parts might generate more debris than with the lip seal.

7. Liquid siloxane MM can be used to lubricate the bearing cartridge. This would entail eliminating the risks associated to mutual contamination of the working fluid

and the lubricant, and in turn lead to simpler control strategies during start-up and shut-down. The main disadvantage is that siloxane MM has much lower viscosity than ISO VG oils, leading to increased bearings wear and lower damping.

8. Use of an alternative material other than carbon steel to manufacture the piston rings, which at temperatures ≥ 200 °C might cause thermal degradation of siloxane MM.

4.3.2. TEST BED LAYOUT

The P&ID of the turbine test bed is illustrated in Figure 4.3. The test bed includes three main separate loops, in which the turbine working fluid, i.e., vapor of siloxane MM, is represented by the orange lines, the bearings lubricant fluid by the red lines, and the lubricant cooling fluid, i.e., a water-glycol mixture, is displayed in blue lines. As shown, the turbine process fluid line features a bypass line (LN-103 DN50) which is used to shut-off the turbine, for example in case of a malfunction of one of the components. Liquid siloxane MM is circulated in the lubricant line, following Req. 7. The impact of such a choice on the rotordynamics and power efficiency of the powertrain is further analyzed and documented in Section 4.3.3, where the rolling element bearings cartridge used to support the turbine rotor is presented.

Two process control valves to admit and extract the working fluid to and from the turboexpander test bed are used. These are indicated as V101 and V103 along the MM loop (orange lines) in Figure 4.3. Regulating the opening of V103 can be used to set the turbine back pressure independently of the condensation pressure. Following Req. 2, the process control system is complemented by two emergency shut-off valves, VE102A and VE102B, whose function is to rapidly interrupt the delivery of MM to the turbine in case an alarm is triggered during operation. The supply pipe line is reduced in size from DN80 to DN50, to match the size of valves V101, VE102A, and VE102B recommended by a valve manufacturer for this application [4, 5], and from DN50 to DN40 to match the inlet diameter of the turbine flow distributor, whose optimum value was calculated using the method of Whitfield & Baines [6].

The emergency valves are selected based on the switching time, i.e., the time for the valve positioner to fully open the valve gate starting from the closed position, and vice versa in case of a normally open valve. VE102A is normally fully closed (FC), whereas VE102B is normally fully open (FO) to make sure that siloxane MM is not fed to the turbine unintentionally. Only when the turbine is to be operated, then VE102A is switched to FO position and VE102B to FC.

The required switching time of the valve was determined as the time required to the turbogenerator to reach a maximum speed of 160 krpm, starting from the maximum off-design rotational speed of 120 krpm, assuming that the braking torque goes to zero in case of a fault of the generator. The maximum speed of 160 krpm was advised by the generator manufacturer, based on tests. The only resistant torque which is assumed in this scenario is given by the frictional torque of the rolling element bearings, calculated using Equation 3.13. The drag torque due to the viscous friction in the turbine (resulting

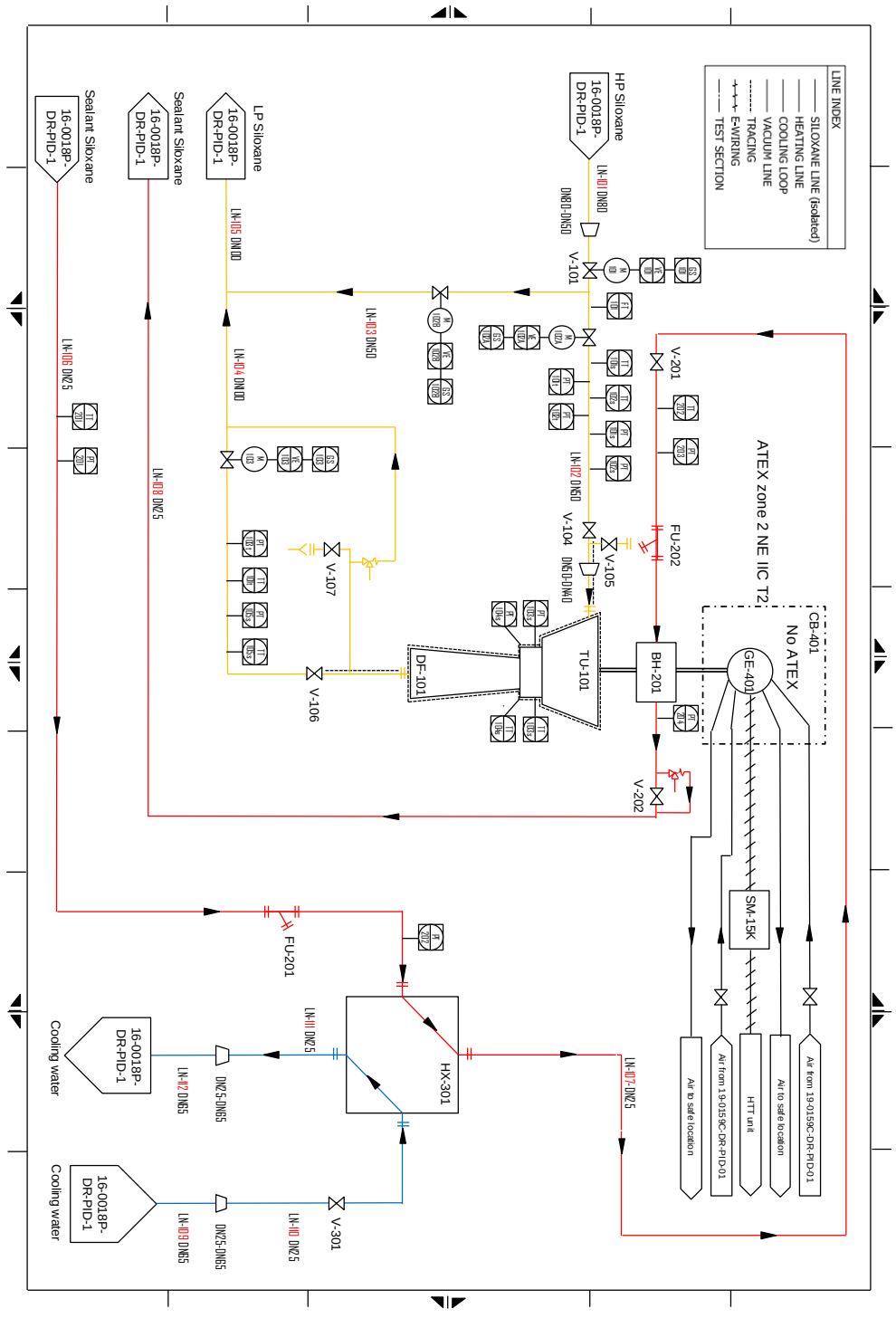

Figure 4.3: P&ID of the ORCHID turbine test bed. The P&ID diagram was realized by Paul Straatman and refashioned by the author of this dissertation for illustrative purposes.

from fluid dynamic losses in the cavity behind the impeller disk) and in the generator (resulting from fluid dynamic losses in the air bearings) is small and was neglected.

The angular acceleration of the powertrain can be calculated starting from the equation of motion of a linear rotary system at steady state

$$M_{\text{turb}} - M = I_z \cdot \dot{\omega}, \tag{4.1}$$

where the turbine torque is M_{turb} = 1600 Nmm, the resistant torque is M = 13.1 Nmm estimated using the model described in Section 3.5.1, and the polar inertia I_z about the rotation axis z is calculated by summation of the inertia of all components in the powertrain. These include the turbine rotor, the coupling shaft with its coupling flange, and the generator rotor. Table 4.1 lists the contribution of each component to the total inertia of the turbine shaft. The rotational acceleration resulting from Equation 4.1 is $\dot{\omega}$ = 136.8 krpm s^{-1}. The switching time of the gate valves VE102A and VE102B should then be smaller than ≈ 0.3 s, considering the maximum allowable velocity increase of 40 krpm.

Table 4.1: Inertia about the rotation axis of the components of the powertrain. The values of the inertia of different components were computed using a CAD modeling software, considering the properties of the materials of each component. The turbine rotor rotor inertia was computed considering an assembly consisting of the impeller, the turbine shaft, the lock nut, the piston rings, and the inner raceway of the bearings. The value of inertia for the generator rotor was provided by the manufacturer.

Component	Material	I_z / kg mm^{-2}
Turbine rotor	See note[1]	11.3
Coupling rod	Al2014-T6	0.036
Coupling hub	Al2014-T6	0.3
Generator flange base	34CrNiMo6	3.1
Generator flange bush	34CrNiMo6	1.4
Generator rotor	-	94.5
Total inertia	-	110.8

Sliding gate valves with piston actuator were selected as they feature a switching time of ≈ 0.2 s according to the manufacturer. The side and front views of the selected valves VE102A and B, including their main dimensions, are illustrated in Figure 4.4. Once VE102A/A are in their normal operating position, V103 is opened first and V101 can then be progressively opened to allow the superheated vapor to reach the turbine. Sliding gate valves for process control featuring a diaphragm actuator were selected for V101 and V103, with switching time of the order of few seconds. Side and front cross-section views of the valve body V101, including its main dimensions, are illustrated in Figure 4.5.

Two additional manual ball valves, i.e., V106 and V104 indicated in Figure 4.3, are necessary to isolate the turbine test bed from the ORCHID BoP to vacuum the power plant and

[1] Impeller: Ti6Al4V; turbine shaft: 17-4PH H900; lock nut: SS316; piston rings: IN718; bearing raceway: X30.

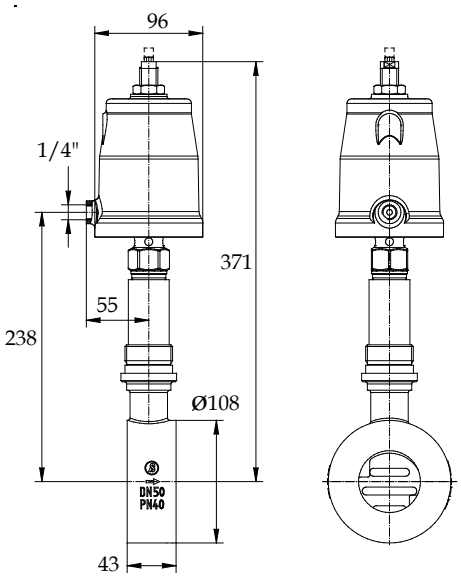

Figure 4.4: Side and front views of the emergency sliding gate valves with piston actuator (VE102A/B) [5], and its main dimensions (for standard pipes DN50). The valve positioner is not shown.

remove the air trapped in the pipes before starting the operation[2]. The air trapped in the turbine test bed is forced out by *blanketing* the piping segment between V104 and V106. Blanketing consists in the injection of a flow of inert gas at sufficiently high pressure to force the trapped air out. For this purpose, N_2 is injected from V105 and V107 is kept open until the pressure in the segment has stabilized. This operation is conducted at a relatively low pressure (between 1.5 and 2 bar of injection pressure) to prevent the turbine from spinning due to the passage of N_2 flow, and prevent damage to the generator bearing journals from low speed operation[3].

A tracing system to pre-heat the pipes and turbine housings prior to operation of the machine has been included following Req. 3, and is indicated in Figure 4.3 by a dashed line, which extends between V104 and V106. The tracing system is turned on after blanketing has terminated to pre-heat the steel pipes and the turbine flow passage to ≈ 160°C over few hours.

As for the lubrication of the bearing housing, liquid MM is bled from a DN25 flange upstream of V012 (zone D3 of Figure 4.1) and, which is placed below the buffer vessel. After lubricating and cooling the bearings, liquid siloxane is returned to the buffer vessel using one of the fill ports shown in zones C2-C3. The lubricant process is indicated in the P&ID of Figure 4.3 by the red lines. A pressure reduction valve (V201) regulates the feed to the

[2] The removal of air trapped in the system is a required safety measure prior to operation of the setup. This prevents the formation of a hazardous mixture between a flammable fluid, i.e., siloxane MM, and an oxidizer that combined with an ignition source at high temperature could trigger a fire.

[3] A rotational speed of ≈ 5 krpm is required for the generator shaft to lift-off from the journal bearings.

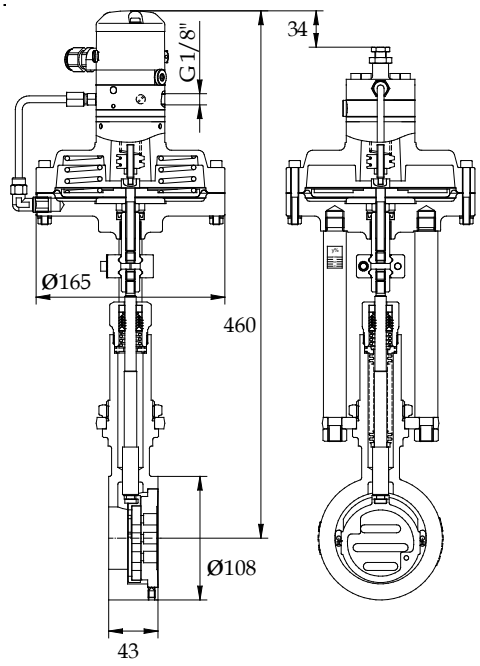

Figure 4.5: Side and front cross-section views of the control sliding gate valve with diaphragm actuator (V101) [4], and its main dimensions (for standard pipes DN50). The valve positioner reported here is different than the intended one. The layout of V103 is identical to the one represented in this figure, however with larger dimensions.

bearing housing (BH201). The valve is placed downstream of a filtering unit[4] (FU201) ensuring that no debris generated upstream can reach V201, the cooler (HX301), and the bearings. At the outlet of the bearing housing a control valve (V202) is used to regulate the housing pressure. A slight overpressure of the lubricant inside the bearings housing between ≈ 5 and 20 kPa is desirable, as it prevents ambient air from being sucked in from the turbine seals. A second identical filtering unit (FU202) is placed just upstream of V202 to prevent dirt and particles generated by the rolling element bearings and the piston seals within BH201 from reaching the valve.

The process indicated in the P&ID by the blue lines is the water-glycol (referred to as *coolant*) cooling loop. Coolant bled from the main ORCHID cooling loop, which is illustrated in Figure 4.1, is fed to HX301 to cool the lubricant to 50 °C before it is injected into the housing. The working principle of the cooler, which is a plate heat exchanger, is represented in Figure 4.6. The two fluid media flow through the clearance between adjacent plates sealed laterally by gaskets. The integrity and performance of these seals limit the operating temperature of the cooler to 225 °C , and the operating pressure to 35 bar. The main specifications and design point characteristics of this component are listed in Table 4.2.

[4] A Y-type 1046 filter by ARI was selected.

Additional information on the auxiliary components selected to operate the ORCHID turbine is reported in Appendix G.

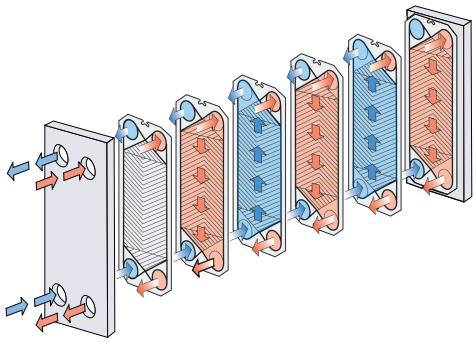

Figure 4.6: Single pass liquid-liquid plate heat exchanger, image courtesy of [7].

Table 4.2: Plate heat exchanger HX301 specifications and design point characteristics provided by the manufacturer [7].

Specifications			
Material	316L		
Power	2 kW		
Heat transfer area	0.1 m^2		
Number of passes	1		
Mean temp. diff.	41.4 °C		
Piping connections	Ext. thread 3/4" ISO 228/1-G		
	Side 1 (Lubricant)	**Side 2 (Coolant)**	**Unit**
Pressure drop	0.582	5.27	kPa
Flow rate	2	5.87	$L min^{-1}$
Inlet temperature	90	30	°C
Outlet temperature	60	35	°C

4.3.3. TURBOGENERATOR LAYOUT

The complete powertrain is depicted in Figure 4.7, and includes the ORCHID turbine, the generator described in Section **??** to brake the turbine, and a coupling shaft in between the two machines to transfer the torque. The figure also partly shows the mechanical supports of the powertrain.

A detail of the coupling mechanism is shown in Figure 4.8, illustrating the different parts used to couple the rotors. The coupling shaft is made of Al2014-T6, has an outer diameter ⌀8 mm, and features two hexagonal shaped ends, as displayed in Figure 4.10. On the left side, the connection with the generator is realized using a tie-shaft strategy, while on the right side the coupling shaft fits in a hexagonal shaped bore machined in the turbine

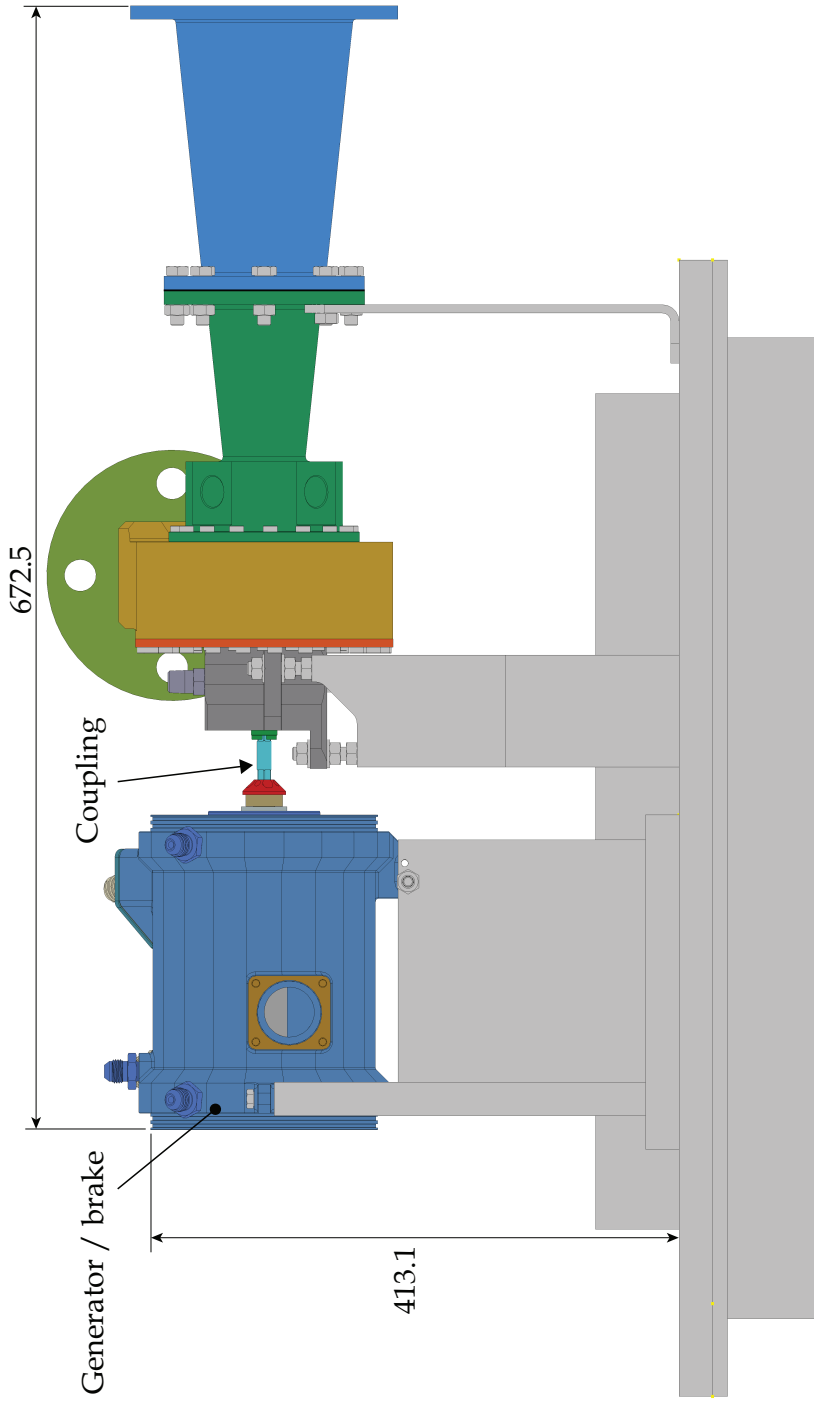

Figure 4.7: ORCHID turbine complete powertrain. The indicated dimensions are in mm.

shaft end. The tie shaft is used to constrain and center a coupling base, see Figure 4.8, to the generator main shaft. The base is then fixed to a coupling flange, shown in Figure 4.9, through a bush and 4x M3 bolts. The other side of the coupling flange is engaged with the coupling shaft through a matching hexagonal cross-section bore. The coupling shaft clearance to the mating pieces was designed to allow a maximum misalignment of 180 µm between the connected shafts. The two shafts are aligned in the vertical and horizontal directions using a combination of tight chains of manufacturing tolerances, set screws for position adjustment, and precision shims as thin as 25 µm for fine tuning. A digital dial with a sensitivity of 0.2 µm is used to reach the desired default position.

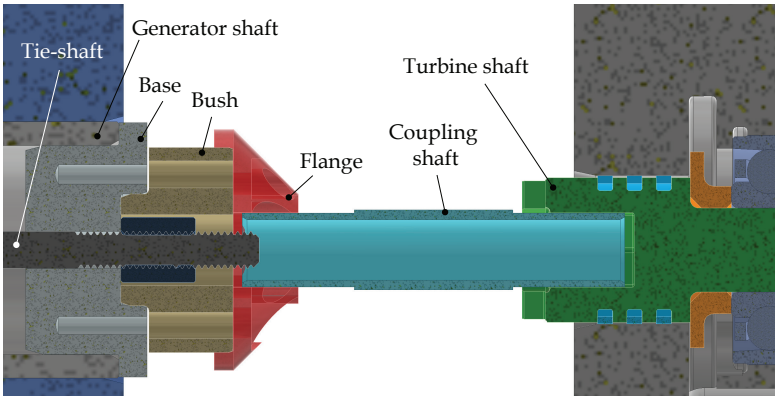

Figure 4.8: Cross-sectional view of the coupling mechanism.

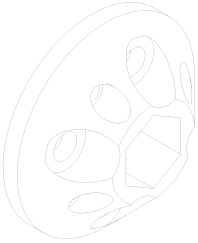

Figure 4.9: Coupling flange.

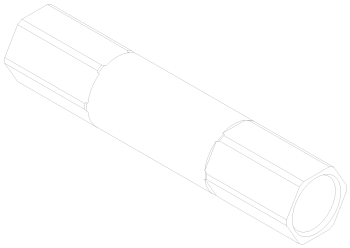

Figure 4.10: Coupling shaft.

DETAILED MECHANICAL DESIGN OF THE TURBOEXPANDER ASSEMBLY

An isometric view of the one-quarter cross section of the turbine assembly is displayed in Figure 4.11. The flow distributor, whose inlet diameter is 40 mm, is made of two pieces. A main body including the stator vanes (3), to which the inlet flange (2) is bolted, and a backplate covering the stator vanes (4). The bearing housing (1) is bolted to the distributor back plate, while the primary diffuser cone (5) is bolted to the distributor main body. For ease of manufacturing, the diffuser is made of two separate parts (5 and 6) joined by bolts. Four G 1/2 B process connections for static temperature and pressure measurements are tapped into the primary diffuser cone at a distance of ≈ 60 mm downstream

the impeller trailing edge section, as shown by the dashed line in the cross-section view of Figure 4.12.

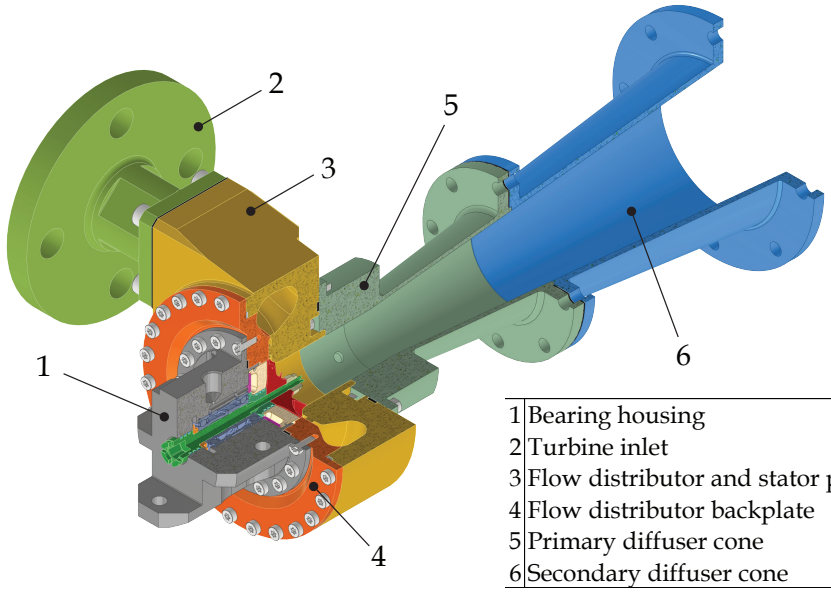

1	Bearing housing
2	Turbine inlet
3	Flow distributor and stator plate
4	Flow distributor backplate
5	Primary diffuser cone
6	Secondary diffuser cone

Figure 4.11: One quarter cross-section of the ORCHID turbine assembly.

All parts are designed and manufactured by *Van der Lee Turbo Systems* [3], with the exception of the design of the stator vanes, impeller blades, and diffuser, whose geometries are supplied by TU Delft.

The shaft bearing system assembly is shown in Figure 4.12 and includes a bearing cartridge (11) mounted on a custom-made stainless steel shaft (9). A piston ring carrier is machined directly in the left end of the shaft. On the opposite side of the shaft, the impeller (7) is locked in place by a nut (14) and pushes axially against a second piston ring carrier (8), which is separate to enable mounting of the assembly. Piston rings (19) are used to limit the leakage of lubricant to the environment, and to seal-off the working fluid from the bearings housing (Req. 6). Following Req. 8, the rings are made of Inconel 718 to prevent possible thermal degradation of the working fluid if coming in contact with carbon steel rings at high temperature, a material that is commonly adopted for these components due to its favorable properties for application involving metal parts operating in sliding contact. The bearing cartridge chosen to support the rotor is shorter and smaller in outer diameter than that used for the initial rotor design shown in Figure 3.14, making the rotor $\approx$ 23 % shorter and $\approx$ 31 % lighter overall (Req. 1). This is expected to increase the natural frequencies of the rotor, which are proportional to the stiffness through the ratio $\omega_0 \propto k \propto 1/L$, where L is the rotor length, and inversely proportional to the mass by recalling that $\omega_0 \propto 1/m$, with m the mass of the rotor.

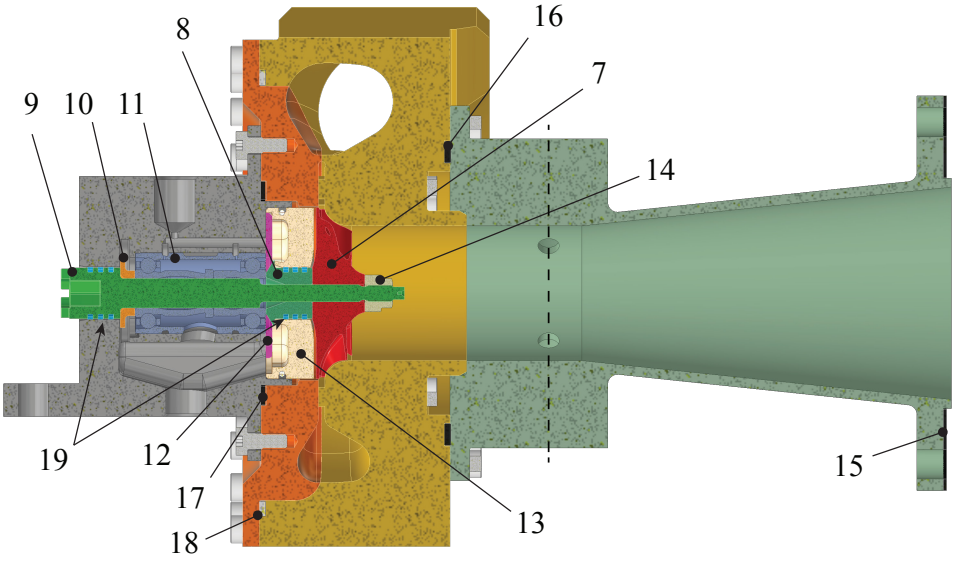

7 Impeller
8 Right piston ring carrier
9 Shaft including left piston ring carrier
10 Bearing cartridge spacer
11 Bearing cartridge
12 Stop plate
13 Impeller seal plate
14 Impeller lock nut
15 Diffuser aft cone gasket
16 Diffuser cone inlet gasket
17 Bearing housing gasket
18 Flow distributor gasket
19 Piston rings

Figure 4.12: Cross-section of the ORCHID turbine rotor assembly.

Bearing cartridge and lubrication

The turbocharger cartridge used is designed by *Van der Lee Turbo Systems* [3], and its cross-section is illustrated in Figure 4.13, also reporting its main dimensions. The main characteristics of the component are listed in Table 4.3. The cartridge is not centered, and therefore the outer raceway rests on the bottom of the housing when the machine is standstill. A spacer (10) is used on the left side to axially center the cartridge in the housing, while a stop plate (12) on the opposite side prevents axial displacement of the rotor by contact with the outer ring of the cartridge. The plate additionally fixes the outer raceway by means of a rectangular protrusion (not shown) which coincides with a slot of similar geometry in the outer raceway. The impeller seal plate (13) fixes the cartridge

stop plate to the bearing housing.

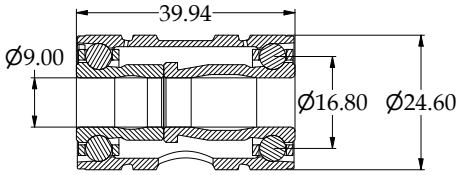

Figure 4.13: Cross-sectional view of the rolling element bearings cartridge by [3]. Dimensions are in mm.

Table 4.3: Data of the rolling element bearings cartridge. Static and dynamic load capacities are intended for a single bearing row.

Material (balls)	Si_3N_4
Material (raceways)	X30 steel
Design rotational speed	130 krpm
Lubricant volume flow rate	1 - 2 L min^{-1}

According to the manufacturer, the cartridge can be lubricated using liquid siloxane MM. Using MM for bearing lubrication provides advantages such as simplified sealing and reduced complexity of the test bed. As discussed, subcooled MM will be bled from the ORCHID buffer vessel and delivered to the bearings cartridge for lubrication and cooling. Compared to standard mineral oils, MM features low viscosity and evaporates at low temperature. Thus, both the lubrication properties and the squeeze-film damper performance are inferior. Figure 4.14 reports the variation of dynamic viscosity as a function of lubricant temperature, for ISO VG32 oil and MM. Inspecting the plot, one can notice that the viscosity of MM is weakly dependent on temperature and approximately one order of magnitude lower than that of the ISO VG32 mineral oil.

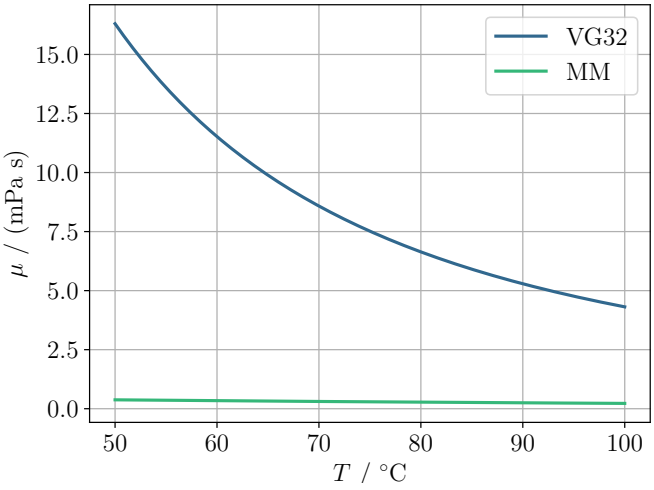

Figure 4.14: Dynamic viscosity of ISO VG32 and Siloxane MM as a function of temperature. The viscosity of MM was obtained via the dedicated REFPROP [8] fluid library.

The thermal and damping performance of the bearing cartridge was assessed considering subcooled pressurized MM as the lubricant, injected into the bearing housing at

50 °C. Considering a siloxane feed rate of 1 L min^{-1} to the bearings, Figure 4.15a illustrates the total power loss in the bearings as a function of the load $\dot{m}_{\text{corr}}$ and speed n, while Figure 4.15b shows the maximum temperature of the siloxane estimated considering that the whole thermal power to be dissipated from the bearing casing, which includes the contribution due to heat transfer from the main working fluid loop estimated as in Section 3.5, is transferred to the lubricant. In particular, the maximum power loss of ≈ 250 W displayed in Figure 4.15a is significantly lower compared to that obtained for the first design iteration of the ORCHID turbine, in which lubrication with mineral oil was assumed, where ≈ 565 W thermal power due to friction in the bearings was obtained. This is due to the lower viscosity of siloxane MM, which reduces the frictional torque on the bearing rows, thus leading to lower dissipation. Inspecting Figure 4.15b one can see that the maximum lubricant temperature obtained at the outlet of the bearings housing is well below the evaporation temperature of siloxane MM, which is ≈ 100°C at ambient pressure.

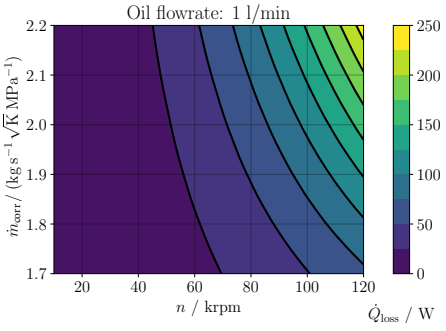

(a) Power loss in the bearings.

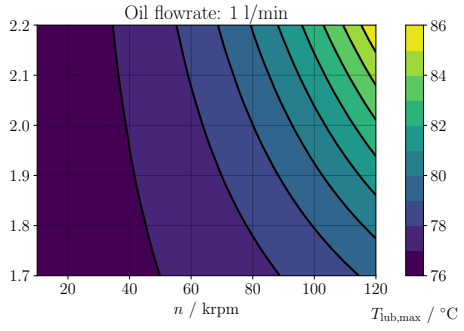

(b) Maximum temperature of siloxane MM at the outlet of the bearing housing.

Figure 4.15: Power loss in the bearings (a) and maximum lubricant temperature at the outlet of the bearing housing (b) considering a lubricant feed rate of 1 L min^{-1}, at an initial temperature of 50 °C.

Figure 4.16 reports a comparison of the direct damping coefficient in the case of oil lubrication (4.16a) and in the current design (4.16b) solution where the lubricant is liquid MM. The damping coefficient is computed using the π-theory [9] analytical formulation for closed-end squeeze-film dampers, which assumes that part of the fluid-film undergoes evaporation and reads

$$c_{xx} = 12\pi\mu L_{\text{SFD}} \left(\frac{OD}{g}\right)^3 \cdot \left[\frac{1}{\left(2+(e_s/g)^2\right)\cdot\sqrt{1-(e_s/g)^2}}\right], \tag{4.2}$$

in which μ is the dynamic viscosity of the lubricant, L_{SFD} is the axial length of the damper, OD is the outer diameter of the cartridge, g is the radial clearance of the squeeze-film damper, and e_s the static eccentricity, assumed to be equal to zero in stationary conditions for both cases. The contours of Figure 4.16 show that the damping capacity is about 5 to 6 times lower when the machine is lubricated with MM.

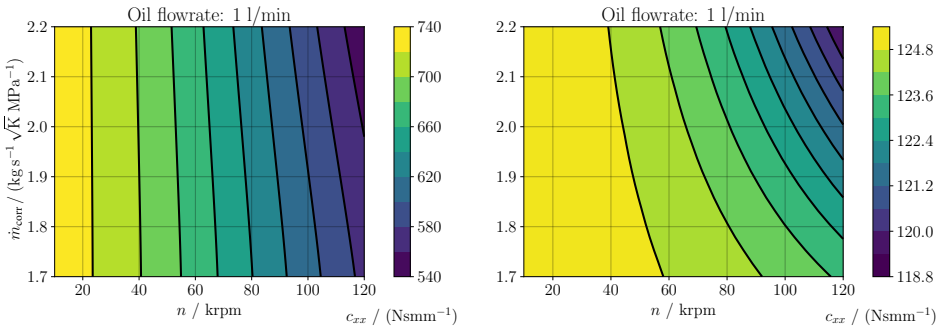

(a) ORCHID turbine initial design using ISO VG32 mineral oil as lubricant. The radial squeeze-film damper clearance is $g = 0.05$ mm, while the other geometrical characteristics are indicated in Figure 3.12.

(b) ORCHID turbine detailed design using liquid MM as lubricant. The radial squeeze-film damper clearance is $g = 0.025$ mm, while the other geometrical characteristics are indicated in Figure 4.13.

Figure 4.16: Direct damping coefficient for centered squeeze-film damper ($e_s = 0$) computed using Equation 4.2. (a) ORCHID turbine initial design with ISO VG 32 oil, and (b) ORCHID detailed design with liquid MM as lubricant. The lubricant feed rates have been fixed equal to 1 L min^{-1}, and an inlet temperature of 50 °C was considered for both cases.

Impeller design

Following the structural analysis performed on the initial design of the impeller disk, few design changes were carried out considering also the recommendations from the manufacturer [3] and the design review with [2].

1. The extra material on the disk back face for balancing purpose was removed to eliminate over-stress in that region of the impeller. Balancing can be performed by removing material from the disk itself in the tip region.

2. The M3 bolt was replaced by an M4 nut that screws onto the threaded end of the shaft. In this way, the impeller design is simplified. A simple cylindrical see-through hole is realized at the inner diameter, thus eliminating the corner stress due to the bolt preload.

3. The impeller disk thickness at the maximum diameter was increased from 0.3 mm to 0.8 mm to reduce the deformation of the disk under load calculated with FEA.

4. The thickness of the blade in the root section was varied as a function of the normalized meridional coordinate, with a maximum thickness $t_{max} = 1.5$ mm at 80 % of the normalized meridional coordinate. This provides additional stiffness to the blade root, decreasing the maximum equivalent stress and the blade deformation. However, the thicknesses of the leading and trailing edge remained unchanged, both varying linearly from 0.6 mm at the hub to 0.3 mm at the tip. The blade tip profile has a constant thickness of 0.3 mm throughout.

5. Finally, the number of impeller blades was reduced from 16 to 13 to prevent the onset of fluid dynamic resonance with the 12 vanes of the stator cascade. This

increases individual blade loading, and in turn the root stress, which, however, is compensated by the adoption of a thicker blade root.

Figure 4.17 shows the comparison of the two blades in the blade-to-blade plane, as well as the thickness distribution in the bottom plot. Table 4.4 lists the maximum stress and deformation at the blade leading edge, on the pressure side flank and at the exducer tip, computed by means of FEA, as well as the turbine efficiency at the design point estimated with CFD for the original impeller design discussed in Chapter 3 and the final one.

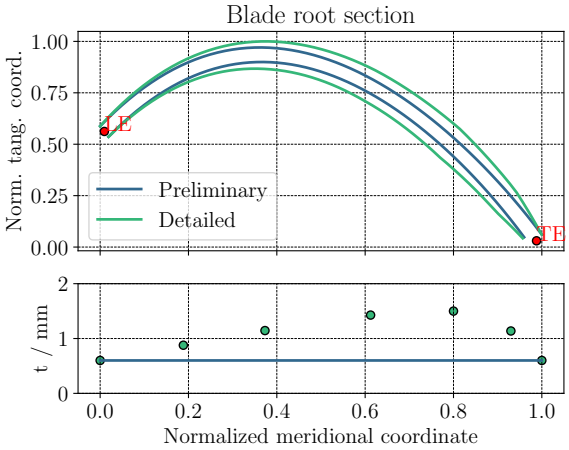

Figure 4.17: Top: plot of the blade root section in the blade-to-blade plane for the initial and the final impeller geometry. Bottom: blade thickness distribution along the meridional direction.

Table 4.4: Results of the FEA of the modified impeller wheel, and of the stator-rotor CFD analysis including the final impeller blade design. The stator model was not changed compared to that of Chapter 3.

	vM stress max / MPa	**Radial deformation / mm**		**Axial deformation / mm**		η_{ts} / %	η_{tt} / %
		Disk tip	Exducer tip	Disk backface	Inducer tip		
Initial	478.73	0.087	0.072		0.059	81.8	85
Final	265.32	0.082	0.056	0.027	0.027	82.2	84.8

A comparison of the equivalent von Mises (vM) stress field for the two impeller designs is shown in Figure 4.18a and Figure 4.18b. For both cases, Ti64 is assumed to be the material. The maximum vM stress in the initial impeller design of 4.18a occurs at the inner diameter, in the corner labeled (A). This occurs as a result of the preload of the bolt, leading to a stress concentration induced by the notch effect due to the presence of a sharp corner. The location indicated by (B) also undergoes high stress because of the overhanging material, which is subject to high centrifugal forces at high speed. The stresses are appreciably lower in 4.18b, thanks to the simplification of the disk geometry and the thicker impeller blades.

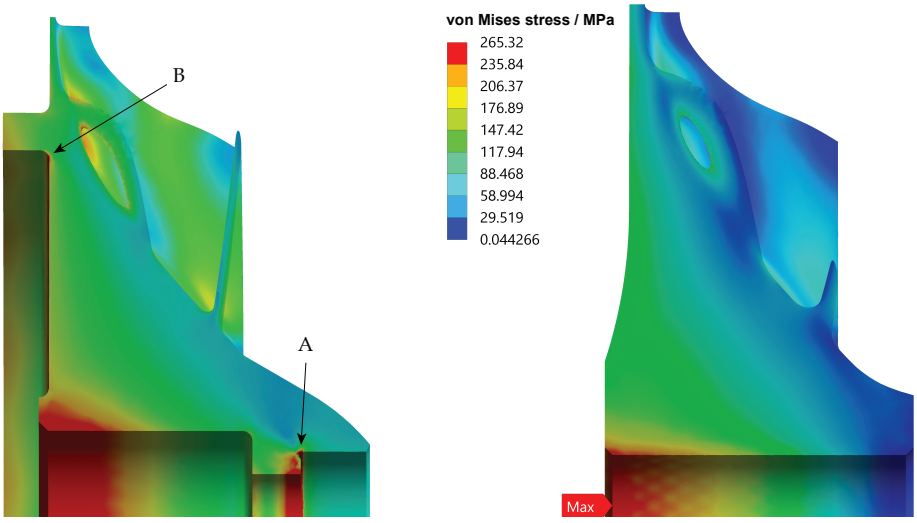

(a) Initial impeller wheel.

(b) Final impeller wheel.

Figure 4.18: Cross-sectional view of the Von-Mises stress contours in the initial impeller wheel design (a) and the final design (b). The contours of (a) were rescaled to the minimum and maximum values of (b), to facilitate the comparison of the stress fields.

4.3.4. ELECTRIC GENERATOR INTEGRATION

BEARING AND COOLING FLOW SUPPLY

The ORCHID turbine CS15 generator [10] is supported on air bearings, which require $13\,g\,s^{-1}$ dry air at 1.6 bar inlet pressure. The electrical components of the machine, that is, the stator windings and the rotor magnet, need a constant cooling flow of $61\,g\,s^{-1}$ dry air to operate. The air available in the APP lab is used for this purpose, and pressure reducing valves indicated by VC401 and VB401 in Figure 4.3 were selected to reduce the air supply pressure from 10 bar. The generator supplier did not consider an active control of the flow rate necessary, so cheap manual valves were selected.

Because the generator and the ECU are not certified according to ATEX [11] directives, they must be surrounded by an inert atmosphere if placed within the ORCHID facility enclosure. This can be achieved by surrounding the generator and the ECU with a sealed box, kept constantly pressurized during the operation of the setup using a flow N_2. In the event of a fire within the ORCHID enclosure, the flame front would not be able to penetrate within this inert zone. However, a better solution is provided by physically placing the generator outside of the ORCHID enclosure so that no nitrogen flow supply is required. This allows simplifying the design and operation of the test bed, at the cost of minor modifications to the ORCHID enclosure itself.

POWER CONDITIONING STRATEGY

The generator provides braking power to the powertrain by generating an electromagnetic field between the stator windings and the rotor magnet. This results in a resistant torque that is actively controlled to maintain a specified set speed. The output power voltage (Vdc) is a linear function of the rotational speed and goes from 0 to 540 Vdc at 110 krpm. The current output depends on the amount of torque necessary to maintain the set speed. The output signal is then transferred through high voltage cables to a DC-AC converter, the SM15K series power box [12] displayed in Figure 4.19. On the right-hand side of the figure, the characteristic curve of the module is shown. The module can automatically convert high voltage signals from a maximum of 1500 Vdc (up to 30 A) into a low voltage AC signal. The signal is also synchronized to the AC frequency of the grid, which is automatically detected by the power box.

A diagram showing the supervisory control and data acquisition (SCADA) system and the electrical wiring of the generator for power conditioning is displayed in Figure 4.20. A high voltage cable transfers electric power (up to 540 Vdc) from the generator ECU to the DC-AC converter SM15K. The SM15K synchronizes the electrical current with that in the main electric circuit of the HTT heater used to provide thermal power to the ORCHID working fluid loop (an isometric view of the heater is reported in Head [1], Fig. 5.9, page 105). The tens of kW produced by the ORCHID turbine and converted in the DC-AC converter module are consumed by the HTT heater 400 kWe resistors (heating rods) and the oil feed pump, which has a rated power of 11 kW [1].

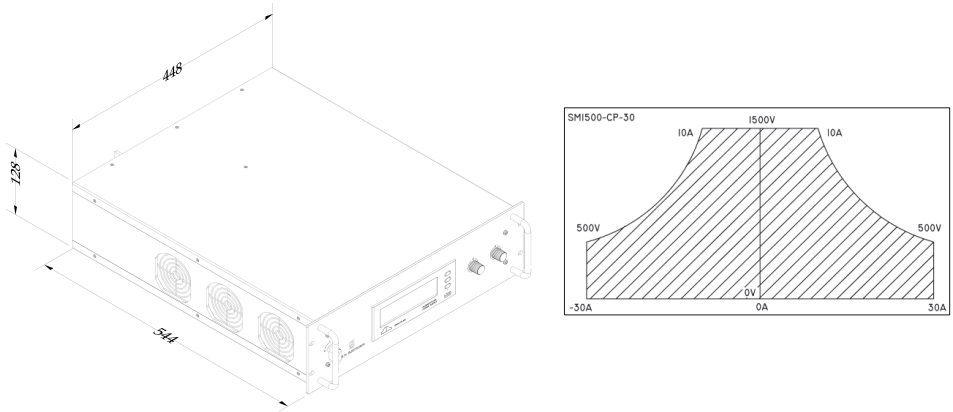

Figure 4.19: View of the DC converter module with main dimensions (mm), and working curve characteristic (Vdc vs. A).

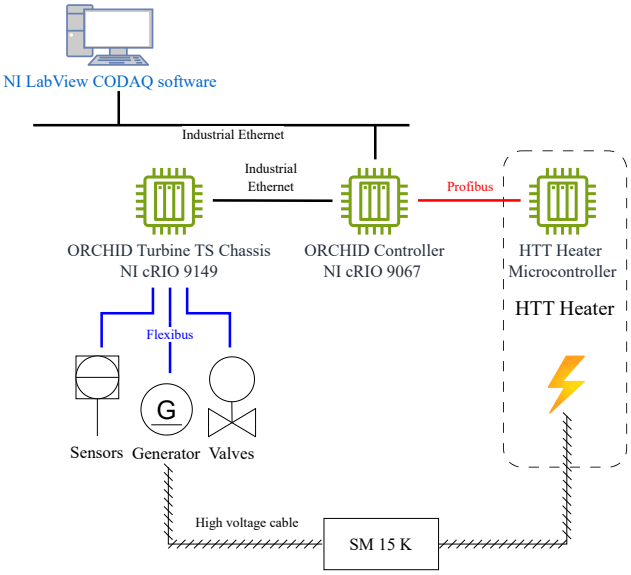

Figure 4.20: Schematic of the SCADA system for control and acquisition. More details about this system can be found in [1], Section 5.5. Compared to the SCADA system of the ORCHID reported in [1], signals directed to and arriving from the turbine test bed are handled by a separate NI cRIO 9149 card. The card communicates with the ORCHID I/O controller via Ethernet cable, whereas the instruments and sensors are interfaced to the NI 9149 card via fieldbus. A high voltage line brings the power converted by the generator to the DC-AC converter (SM15K), which is then routed to the HTT heater.

4.4. INSTRUMENTATION

A total of 20 sensors are used to monitor the process and characterize the flow state. The transmitters are indicated in Figure 4.3 by tags, starting with either P for pressure and T for temperature. If present, a lowercase letter after the three digits indicates the type of quantity measured, being "t" for the total component and "s" for the static one. All sensors are listed in Table 4.5 with their main specifications. The table also reports the measurement accuracy of the instruments.

Table 4.5: List of instruments and their specifications used for control and monitoring of the ORCHID turbine.

Item	Tag	Process	Range	Accuracy	Unit	El. signal	Type signal	Brand/Make
Mass flow meter	FT101	Siloxane	0 - 5588	±0.35%$\dot{m}$	kg/h	4 - 20 mA	AI-C	Krohne/Optimass 6400 C [13]
Total pressure distributor inlet	PT101t	Siloxane	0 - 40	± 0.1 % FS	barg	4 - 20 mA	AI-C	WIKA/UPT-20 & 990.34 [14, 15]
Total pressure distributor inlet	PT102t	Siloxane	0 - 40	± 0.1 % FS	barg	4 - 20 mA	AI-C	WIKA/UPT-20 & 990.34
Static pressure distributor inlet	PT101s	Siloxane	0 - 40	± 0.1 % FS	barg	4 - 20 mA	AI-C	WIKA/UPT-20 & 990.34
Static pressure distributor inlet	PT102s	Siloxane	0 - 40	± 0.1 % FS	barg	4 - 20 mA	AI-C	WIKA/UPT-20 & 990.34
Static pressure diffuser inlet	PT103s	Siloxane	−1 - 5	± 0.1 % FS	barg	4 - 20 mA	AI-C	WIKA/UPT-20 & 990.34
Static pressure diffuser inlet	PT104s	Siloxane	−1 - 5	± 0.1 % FS	barg	4 - 20 mA	AI-C	WIKA/UPT-20 & 990.34
Static pressure diffuser outlet	PT105s	Siloxane	−1 - 5	± 0.1 % FS	barg	4 - 20 mA	AI-C	WIKA/UPT-20 & 990.34
Total pressure diffuser outlet (receiver vessel)	PT103t	Siloxane	−1 - 5	± 0.1 % FS	barg	4 - 20 mA	AI-C	WIKA/UPT-20 & 990.34
Pressure lubricant upstream FU201	PT201	Lubricant	0 - 40	± 0.1 % FS	barg	4 - 20 mA	AI-C	WIKA/UPT-20 & 990.34
Pressure lubricant downstream FU201	PT202	Lubricant	0 - 40	± 0.1 % FS	barg	4 - 20 mA	AI-C	WIKA/UPT-20 & 990.34
Pressure lubricant bearing housing inlet	PT203	Lubricant	−1 - 5	± 0.1 % FS	barg	4 - 20 mA	AI-C	WIKA/UPT-20 & 990.34
Pressure lubricant bearing housing outlet	PT204	Lubricant	−1 - 5	± 0.1 % FS	barg	4 - 20 mA	AI-C	WIKA/UPT-20 & 990.34
Total temperature diffuser outlet	TT101t	Siloxane	0 - 300	Class A [16]	°C	4 - 20 mA	AI-C	WIKA/TR10-C RTD [17]
Static temperature distributor inlet	TT101s	Siloxane	0 - 300	Class A	°C	4 - 20 mA	AI-C	WIKA/TR10-C RTD
Static temperature distributor inlet	TT102s	Siloxane	0 - 300	Class A	°C	4 - 20 mA	AI-C	WIKA/TR10-C RTD
Static temperature diffuser inlet	TT103s	Siloxane	0 - 300	Class A	°C	4 - 20 mA	AI-C	WIKA/TR10-C RTD
Static temperature diffuser inlet	TT104s	Siloxane	0 - 300	Class A	°C	4 - 20 mA	AI-C	WIKA/TR10-C RTD
Static temperature diffuser outlet	TT105s	Siloxane	0 - 300	Class A	°C	4 - 20 mA	AI-C	WIKA/TR10-C RTD
Temperature upstream FU201	TT201	Lubricant	0 - 300	Class A	°C	4 - 20 mA	AI-C	WIKA/TR10-C RTD
Temperature bearing inlet	TT202	Lubricant	0 - 300	Class A	°C	4 - 20 mA	AI-C	WIKA/TR10-C RTD

Starting from the lubrication system, the pressure and temperature are monitored by PT201 and TT201, located upstream of FU201, whereas PT202 reads the downstream pressure of the filter to monitor the pressure drop over time. Two additional sensors, TT202 and PT203, are used downstream of V201 to monitor the inlet temperature and pressure to the bearing housing. At the outlet of this component, the lubricant pressure, which is controlled by regulating the opening of the valve V202, is monitored by the transducer PT204.

Considering the main working fluid loop, several sensors are used to monitor and con-

trol the flow to the turbine. Because the total temperature can be considered conserved along the insulated pipelines of the facility, the total temperature reading of the turbine inlet can be performed relatively far from the turbine inlet, using TT005 in zone A4 of Figure 4.1. The mass flow rate to the turbine is measured with the Coriolis OPTIMASS 6400-C mass flow meter [13]. Total pressure at the inlet of the flow distributor is measured using PT101t/2t, which consists of a pressure transducer mounted on a Pitot tube, and whose signal can be used in a feedback loop with the main pump speed to control the inlet pressure; the static pressure and temperatures are monitored by PT101s/2s, and TT101s/2s, respectively. Downstream of the impeller, sensors PT103s, PT104s and TT103s, TT104s are used to measure the static pressure and temperature. Finally, at the diffuser outlet an additional measurement section allows to monitor the total and static pressure and temperatures with sensors PT103t, TT101t, PT105s and TT105s. PT105s are sent back to the controller which regulates the opening of V103 to reach the set-point back pressure of the diffuser.

To evaluate turboexpander performance, signals from TT005, FT101, PT101t, PT103t, TT101t and PT103s must be continuously monitored and stored in the ORCHID control system data storage for analysis. Using a suitable equation of state, the information provided by TT005 and PT101t allows one to calculate the total enthalpy h_{t0} and entropy s_0 at the turbine inlet section, while the measurements of TT101t and PT103t provide the total enthalpy at the outlet h_{t3}. Through s_0 and the total outlet pressure PT103t, the isentropic total enthalpy $h_{t3,is}$ can also be calculated. Similarly, the static isentropic enthalpy before and after the diffuser $h_{3,is}$ can be obtained from s_0 and PT103s. Finally, the mass flow rate of the process fluid admitted to the turbine is measured by FT101.

4.4.1. UNCERTAINTY QUANTIFICATION

A statistical analysis was carried out to evaluate the impact of uncertainty in the measurement of turbine fluid dynamic performance. The uncertainty associated to a measurement is called total expanded uncertainty and is the combination of uncertainty coming from sensors and data acquisition (DAQ) equipment used to convert current signals from the sensors into a digital output. Assuming that these two sources of uncertainty are statistically independent of each other, the total expanded uncertainty of the measured process variables can be expressed as

$$u_{\text{tot}} = \sqrt{u_{\text{sen}}^2 + u_{\text{A/D}}^2}, \tag{4.3}$$

in which u_{sen} is the sensor uncertainty and $u_{\text{A/D}}$ is the analog-digital (A/D) converter uncertainty.

The accuracy of the pressure sensors corresponds to the measured error per the IEC 61298-2:2008 [18] standard, which includes non-linearity, hysteresis, zero offset and end value deviation. Moreover, according to the manufacturer the sensors are temperature compensated between 10 and 70 °C [14]. Instead, the accuracy of the temperature sensors is in compliance with the Class A tolerance according to the IEC 60751:2002 [16] standard.

In this work, the uncertainty of the instruments was calculated as recommended in the JCGM 100:2008 [19] standard according to a type B evaluation[5], which is to be applied when no direct observations are available for a direct statistical analysis, that is, a type A evaluation. The standard uncertainty is thus defined as

$$u_{\text{sen}} = \frac{a}{k}, \tag{4.4}$$

where a is the half-interval accuracy of the instrument and the denominator k is the coverage factor applied by the manufacturer to define the accuracy of the instruments. The manufacturer datasheet [17] states the coverage factor used to define temperature sensor tolerance classes. In this case, k is equal to 2, corresponding to a standard uncertainty of the 95% confidence interval. When no information is available on the coverage factor applied by the manufacturer to state the accuracy, one can assume a rectangular distribution of the uncertainty using $k = \sqrt{3}$. In this case, all values of pressure within the uncertainty band are equally probable, which can be considered a conservative assumption, since calibrated instruments typically follow normal distributions centered around the mean value. The instrument uncertainties for the measurement of P, T, and $\dot{m}$ chosen for the characterization of the ORCHID turbine efficiency are summarized in Table 4.6.

Table 4.6: Accuracy and standard uncertainty of the instruments in Table 4.5. The temperature T is measured in °C, while the mass flow rate $\dot{m}$ is measured in kg h^{-1}.

Instrument		Accuracy (Expanded uncertainty)	Half-interval accuracy a	Coverage factor k	Standard uncertainty u_{sen}	Symbol
UPT-20	–1 - 5 barg	± 0.005 bar	0.005 bar	$\sqrt{3}$	0.0029 bar	u_{p1}
	0 - 40 barg	± 0.04 bar	0.04 bar	$\sqrt{3}$	0.0231 bar	u_{p2}
TR10-C RTD		± (0.15°C + 0.002 T)	0.15°C + 0.002 T	2	0.075°C + 0.001 T	u_{t}
Optimass 6400 C		± 0.0035 $\dot{m}$	0.0035 $\dot{m}$	$\sqrt{3}$	0.0012 $\dot{m}$	u_{m}

Each sensor transmits a 4 - 20 mA signal to the A/D conversion device, i.e., a 24-bit 16 channels National Instruments card model 9208 (hereon referred to as NI9208), which converts the signal and scales it to the full scale range of the sensor to which it is wired to. This operation is subject to uncertainty. Since the mapping for the current input into the corresponding temperature/pressure/mass flow rate output is essentially a linear operation, the A/D converter characteristic is a straight line with an offset. Therefore, the uncertainty associated to signal conversion is a vector whose entries are a gain (i.e., slope of the characteristic) uncertainty u_{gain}, an offset (i.e., the zero value of the characteristic) uncertainty u_{offset}, plus uncertainties coming from signal noise and non-linearity. Neglecting the contribution of signal noise and non-linearity, one can write the A/D converter standard uncertainty as

$$u_{\text{A/D}} = \sqrt{u_{\text{gain}}^2 + u_{\text{offset}}^2}. \tag{4.5}$$

[5] The definition of type B evaluation of the uncertainty is reported here *ad verbatim* according to [19]: *"Method of evaluation of uncertainty by means other than the statistical analysis of series of observations."*

The uncertainty stated by the supplier of the NI9208 cards is very large for liability reasons [1], namely $u_{\text{gain}} = \pm 0.76\%$ and $u_{\text{offset}} = \pm 0.04\%$ FS. Applying these two uncertainties to the full scale values of temperature, pressure and mass flow rate, we would obtain conversion errors of

$$u_{\text{gain,T}} = \pm \frac{0.76}{100}\, 20\ \text{mA} \cdot \frac{(300-0)\,^{\circ}\text{C}}{(20-4)\ \text{mA}} = \pm 2.85\,^{\circ}\text{C},$$

$$u_{\text{gain,P}} = \pm \frac{0.76}{100}\, 20\ \text{mA} \cdot \frac{(40-0)\ \text{bar}}{(20-4)\ \text{mA}} = \pm 0.38\ \text{bar},$$

$$u_{\text{gain,P}} = \pm \frac{0.76}{100}\, 20\ \text{mA} \cdot \frac{(5-(-1))\ \text{bar}}{(20-4)\ \text{mA}} = \pm 0.057\ \text{bar},$$

$$u_{\text{gain},\dot{m}} = \pm \frac{0.76}{100}\, 20\ \text{mA} \cdot \frac{(5580-420)\ \text{kg h}^{-1}}{(20-4)\ \text{mA}} = \pm 49.02\ \text{kg h}^{-1} = \pm 13.6\ \text{g s}^{-1}.$$

for the gain uncertainty, and

$$u_{\text{offset,T}} = \pm \frac{0.04}{100} \cdot \frac{(300-0)\,^{\circ}\text{C}}{(20-4)\ \text{mA}} = \pm 0.0075\,^{\circ}\text{C},$$

$$u_{\text{offset,P}} = \pm \frac{0.04}{100} \cdot \frac{(40-0)\ \text{bar}}{(20-4)\ \text{mA}} = \pm 0.001\ \text{bar},$$

$$u_{\text{offset,P}} = \pm \frac{0.04}{100} \cdot \frac{(5-(-1))\ \text{bar}}{(20-4)\ \text{mA}} = \pm 0.00015\ \text{bar},$$

$$u_{\text{offset},\dot{m}} = \pm \frac{0.04}{100} \cdot \frac{(5580-420)\ \text{kg h}^{-1}}{(20-4)\ \text{mA}} = \pm 0.129\ \text{kg h}^{-1} = \pm 0.036\ \text{g s}^{-1}.$$

for the offset uncertainty.

To verify the actual performance of the NI9208 A/D converter, the accuracy of two of the three cards installed on the ORCHID setup was assessed by an empirical procedure: the test was conducted by sending a known current signal, specifically 4, 8, 12, 16, and 20 mA signals in succession, and reading the output of the device on screen. By repeating this procedure several times and for different module channels, the slopes and intercepts of different channels were determined and averaged, yielding

NI9208 CARD 1	NI9208 CARD 2
$u_{\text{gain}} = \pm 0.18\%$	$u_{\text{gain}} = \pm 0.04\%$
$u_{\text{offset}} = \pm 0.045\%$ FS	$u_{\text{offset}} = \pm 0.035\%$ FS

The temperatures and pressures at each ORCHID turbine operating point were extracted from CFD simulations (see Section 3.2) and used to determine the total expanded uncertainties of the process variables using Equation 4.3. The inlet total temperature, pressure, and the outlet static pressure are trivial, because they are fixed boundary conditions in the simulations. Conversely, the outlet total temperature and pressure were computed by mass flow averaging the field quantities. The process variables corresponding to the operating points investigated with the CFD simulations and the total expanded uncertainties of the sensors were then used to identify the expected range of measurement of the total pressure and temperature under those operating conditions. The maximum and minimum values of pressure and temperature define four combinations of turbine inlet conditions for which the corresponding entropy and enthalpy were determined by means of the multi-parameter equation of state model [8]. The resulting values of entropy and enthalpy were used to compute the average of these thermodynamic properties and their standard deviations to determine the impact of uncertainty on the measurement of turbine inlet conditions on efficiency and output power. A similar procedure is used to estimate the expected range of variation of the outlet enthalpies used in the definition of turbine efficiency.

The turbine efficiency and power can then be expressed in statistical form as

$$\begin{aligned} \eta_{\text{ts}} &= \frac{A}{B} \pm \left|\frac{A}{B}\right| \sqrt{\left(\frac{\sigma_A}{A}\right)^2 + \left(\frac{\sigma_B}{B}\right)^2 - 2\frac{\sigma_{AB}}{A \cdot B}}, \\ \eta_{\text{tt}} &= \frac{A}{C} \pm \left|\frac{A}{C}\right| \sqrt{\left(\frac{\sigma_A}{A}\right)^2 + \left(\frac{\sigma_C}{C}\right)^2 - 2\frac{\sigma_{AC}}{A \cdot C}}, \end{aligned} \tag{4.6}$$

$$\dot{W} = D \cdot A \pm |D \cdot A| \sqrt{\left(\frac{\sigma_A}{A}\right)^2 + \left(\frac{\sigma_D}{D}\right)^2 + 2\frac{\sigma_{DA}}{D \cdot A}}, \tag{4.7}$$

where $A = h_{\text{t0}} - h_{\text{t3}}$, $B = h_{\text{t0}} - h_{\text{3,is}}$, $C = h_{\text{t0}} - h_{\text{t3,is}}$, and $D = \dot{m}$. σ_{AB}, σ_{AC} and σ_{DA} are co-variances, defined as

$$\begin{aligned} \sigma_{AB} &= \rho_{AB}\, \sigma_A\, \sigma_B, \\ \sigma_{AC} &= \rho_{AC}\, \sigma_A\, \sigma_C, \\ \sigma_{DA} &= \rho_{DA}\, \sigma_D\, \sigma_D, \end{aligned} \tag{4.8}$$

with ρ being the cross-correlation factor, while σ_A, σ_B, and σ_C are the standard deviations of the numerator and the denominator in Equation 4.6 and are calculated as follows:

$$\begin{aligned}\sigma_A &= \sqrt{\sigma_X^2 + \sigma_Y^2 - 2\rho_{XY}\sigma_X\sigma_Y},\\ \sigma_B &= \sqrt{\sigma_X^2 + \sigma_W^2 - 2\rho_{XW}\sigma_X\sigma_W},\\ \sigma_C &= \sqrt{\sigma_X^2 + \sigma_Z^2 - 2\rho_{XZ}\sigma_X\sigma_Z}.\end{aligned} \tag{4.9}$$

In the equations above, for ease of reading, X, Y, W and Z indicates h_{t0}, h_{t3}, $h_{3,is}$, and $h_{t3,is}$, respectively.

The values of X, Y, W and Z can be calculated using an equation of state (f) – in this case, the one proposed by Huber *et al.* [8] and implemented in REFPROP was selected – as

$$\begin{aligned}X &= f\left(P_{t0} \pm u_{tot,p2}, T_{t0} \pm u_{tot,t}\right),\\ Y &= f\left(P_{t3} \pm u_{tot,p1}, T_{t3} \pm u_{tot,t}\right),\\ W &= f\left(P_3 \pm u_{tot,p1}, s_0 \pm u_s\right),\\ Z &= f\left(P_{t3} \pm u_{tot,p1}, s_0 \pm u_s\right),\end{aligned} \tag{4.10}$$

where $u_{tot,p1}$, $u_{tot,p2}$, and $u_{tot,t}$ are the total expanded pressure and temperature uncertainties listed in Table 4.6, while $s_0 = f\left(P_{t0} \pm u_{tot,p2}, T_{t0} \pm u_{tot,t}\right)$ and $u_s = {}^1/_N \cdot \sum_{i=1}^{N} s_{0,i}$, with $N = 4$.

The correlation coefficients tabulated in Table 4.7 were determined applying Pearson's formula to the nominal values of X, Y, W, Z, A, B, C, and D at the 12 operating points of the ORCHID turbine.

Table 4.7: Correlation coefficients used in the uncertainty propagation model. The coefficients were computed with Pearson's formula using data obtained from the off-design CFD simulations of the ORCHID turbine documented in Section 3.2.

Correlation factor	
ρ_{XY}	0.967
ρ_{XW}	0.994
ρ_{XZ}	0.979
ρ_{AB}	0.871
ρ_{AC}	0.954
ρ_{DA}	0.761

The plots of η_{ts} and η_{tt} as a function of the reduced mass flow rate $\dot{m}_{corr}$ and at different rotational speeds are shown in Figure 4.21. In the plots, the dark colored bands indicate the total uncertainty on the efficiency values computed as per Equation 4.3, in which the value of $u_{A/D}$ was computed according to Equation 4.5 and considering the values of the

gain and offset errors of NI9208 CARD 1, which were determined empirically. The lighter bands indicate the total uncertainty computed by assuming the NI9208 performance specified by the manufacturer. The uncertainty specified by the manufacturer is dominated by the gain error. This was confirmed by the empirical tests carried out on 2 acquisition cards of the DAQ system, though the actual gain uncertainty is significantly lower than that reported by the technical data sheet. In contrast, the offset error has a minor contribution to the A/D converter standard uncertainty, and the measured value deviates only slightly from that stated by the constructor. This result suggests that the value for the offset error provided by the manufacturer is a realistic figure for the actual performance of the device. The mechanical power and its uncertainty bands are displayed in Figure 4.22. From the plots, one can observe that the uncertainty bands increase noticeably as $\dot{m}_{\text{corr}}$ increases, given that u_{sen} is directly proportional to the measured mass flow rate.

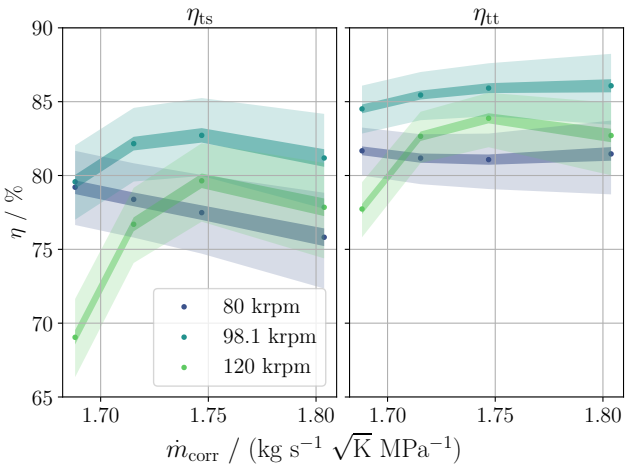

Figure 4.21: ORCHID turbine efficiency as a function of the reduced mass flow rate and at different rotational speeds. The markers are the average values of the efficiency at each operating point. The darker bands indicate the propagated uncertainty calculated assuming the actual uncertainty of the A/D signal conversion for NI9208 card 1. The lighter bands indicate the propagated uncertainty calculated assuming the uncertainty of the A/D signal conversion for NI9208 specified by the manufacturer.

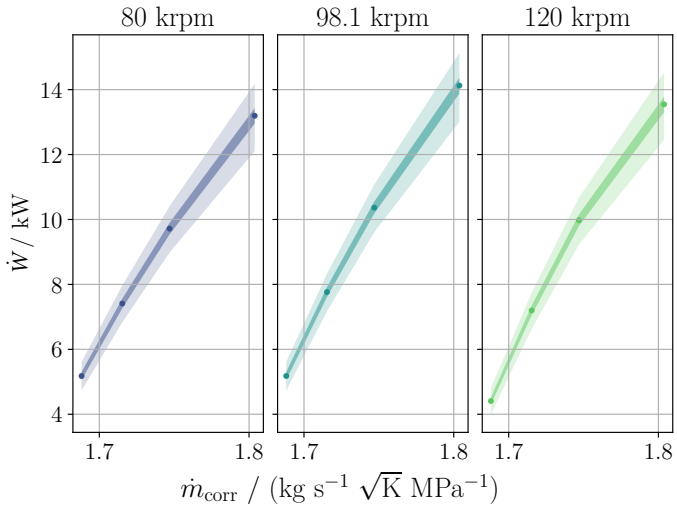

Figure 4.22: ORCHID turbine power as a function of the reduced mass flow rate and at different rotational speeds. The markers are the average values of the efficiency at each operating point. The darker bands indicate the standard uncertainty calculated as per the second term on the right hand side of Equation 4.7. The darker bands indicate the propagated uncertainty calculated assuming the actual uncertainty of the A/D signal conversion for NI9208 card 1, while the lighter bands by assuming the A/D signal conversion uncertainty specified by the manufacturer.

4.5. CONCLUSION & OUTLOOK

The current chapter documents the detailed design of the ORCHID turbine test bed. The design of the turboexpander assembly, which was performed in cooperation with a subcontractor [3], is discussed, and the layout of the entire powertrain, which includes a flexible coupling and a generator to brake the turbine, is presented. A process and instrumentation diagram was defined, and the selected components to operate the turbine were selected and described. The main results can be summarized as follows.

- Three separate process loops are required to operate the turbine, namely:
  - i the working fluid loop which supplies the vapor to the turbine at the desired thermodynamic and flow conditions,
  - ii the lubricant loop which ensures the safe operation of the turbine bearing system, and
  - iii the coolant loop needed to maintain the lubricant temperature below 100 °C.
- The vapor flow of siloxane MM is routed to the turbine from the ORCHID evaporator bypassing the existing ORCHID nozzle test bed. Two electronic sliding gate control valves, actuated via a diaphragm, were chosen to control the delivery and extraction of MM to and from the turbine. Two interlocked sliding gate valves actuated by a piston, which can achieve a switching time of 0.2 s, were chosen to quickly cut the turbine power in case of an emergency. To monitor and control

the process, 8 pressure sensors, 6 temperature sensors, and a mass flow rate sensor were selected based on the range of operation of the turbine test bed and the accuracy of the targeted measurement.

- To lubricate the bearings of the turbine, liquid siloxane MM was preferred over common mineral oils. The main reason motivating this choice is the elimination of risks associated to contamination of the working fluid. The drawbacks of using liquid MM as a lubricant were discussed and regard primarily the operation of the turbine. First, bearing cartridge damping is lower because of the lower viscosity of MM compared to mineral oils; second, ball bearings life is likely to be reduced due to the thinner fluid film created by MM between the rolling elements and the raceways. However, it was estimated that by using MM as a lubricant, mechanical losses due to friction in the bearings significantly reduce, roughly by a factor of 2.5. In turn, this reduces the cooling requirements of the machine and makes it easier to determine the power of the turbine by measuring the electric generator power directly.
- The power generated by the turbine is supplied to the electric heater of the ORCHID setup. A power conditioning system was devised to route the power of the turbogenerator to a power sink module, which can automatically convert up to 15 kW electric power to the required voltage and frequency of the user.
- The uncertainty in the estimation of the turbine performance, that is, efficiency and power, was quantified by computing the propagated uncertainty of the overall measurement chain, including sensor accuracy and A/D conversion errors. The results suggested that the main source of uncertainty is arguably associated with the A/D converter module, while the accuracy of the process sensors has a minor impact on performance prediction. The accuracy of two NI9208 A/D converter modules was evaluated and the results show that the actual performance of these devices is much better than that stated by the manufacturer.

Future work will be devoted to the realization of the setup described herein and to the implementation of a control strategy. Commissioning tests will help characterize the performance of the various components, such as the plate heat exchanger, the valves, the generator, and most importantly the bearings and expander.

BIBLIOGRAPHY

1. Head, A. J. *Novel Experiments for the Investigation of Non-Ideal Compressible Fluid Dynamics* PhD thesis (Delft University of Technology, 2021).
2. *Institue of Turbomachinery and Fluid Dynamics, Hannover Leibniz University* https://www.tfd.uni-hannover.de/en/.
3. *Van der Lee Turbo Systems* https://www.vdlee.com/.
4. *Sliding Gate Valve 8021-GS1* Technical datasheet. Schubert & Salzer. https://controlsystems.schubert-salzer.com/fileadmin/user_upload/ControlSystems/Produkte/Typen/8021_GS1/EN/8021-GS1_-_data_sheet.pdf.
5. *Sliding Gate Valve 8044* Technical datasheet. Schubert & Salzer. https://controlsystems.schubert-salzer.com/fileadmin/user_upload/ControlSystems/Produkte/Typen/8044/EN/8044-GS1_-_data_sheet.pdf.
6. Whitfield, A. & Baines, N. C. *Design of Radial Turbomachines* ISBN: 978-0-470-21667-5 (Longman Scientific & Technical, Harlow, England, 1990).
7. *AlfaNova 14 / HP 14 - Fusion-bonded plate heat exchanger in 100% stainless steel* Technical datasheet. Alfa Laval. https://assets.alfalaval.com/documents/p3837d4b0/alfa-laval-product-leaflet-en-che00045.pdf.
8. Huber, M. L., Lemmon, E. W., Bell, I. & McLinden, M. O. The NIST REFPROP database for highly accurate properties of industrially important fluids. doi:10.1021/acs.iecr.2c01427 (2022).
9. Nguyen-Schäfer, H. *Rotordynamics of Automotive Turbochargers* doi:10.1007/978-3-642-27518-0 (Springer Berlin, Heidelberg, 2012).
10. *15 kW e-compressor: air compressor* Aeronamic (B.V.) https://aeronamic.com/product/15kw-e-compressor-air-compressor/.
11. *Directive - 2014/34 - EN - ATEX directive - EUR-Lex* European Union. https://eur-lex.europa.eu/eli/dir/2014/34/oj.
12. *SM15K - Series 15kW DC Power Supplier* Technical datasheet. Delta Elektronika B.V. https://www.delta-elektronika.nl/sites/default/files/2024-05/SM15K_DTS_V202405.pdf.
13. *Optimass 6000* Technical datasheet no. 4001894105. Khrone. https://cdn.krohne.com/pick2/tagged_docs/TD_OPTIMASS6000_en_210326_4001894105_R05_.pdf.
14. *Process transmitter Model UPT-20, with pressure port Model UPT-21, with flush diaphragm* WIKA data sheet PE 86.05. Wika. https://www.wika.com/media/Datasheets/Pressure/Process-transmitters/ds_pe8605_en_co.pdf.

15. *Diaphragm seal with threaded connection Welded design Model 990.34* WIKA data sheet DS 99.04. Wika. https://www.wika.nl/upload/DS_DS9904_en_co_1167.pdf.

16. *Industrial platinum resistance thermometers and platinum temperature sensors* IEC 60751:2022. International Electrotechnical Commission. https://webstore.iec.ch/en/publication/63753.

17. *Threaded resistance thermometer With protection tube Model TR10-C* WIKA data sheet TE 60.03. Wika. https://www.wika.nl/upload/DS_TE6003_en_co_6992.pdf.

18. *Process measurement and control devices - General methods and procedures for evaluating performance - Part 2: Tests under reference conditions* IEC 61298-2:2008. International Electrotechnical Commission. https://webstore.iec.ch/en/publication/5156.

19. *(GUM 1995 with minor corrections), Evaluation of measurement data — Guide to the expression of uncertainty in measurement.* JGCM 100:2008. International Organization for Standardization. https://www.iso.org/sites/JCGM/GUM-JCGM100.htm.

5

FINAL REMARKS AND OUTLOOK

High efficiency and compactness make radial-inflow turbines (RITs) the ideal expander type for high-temperature ORC systems with low power capacity in thermal energy harvesting applications onboard trucks, ships, and aircraft. Recovery of waste heat from thermal engines is one of the prominent technologies currently investigated to further enhance fuel efficiency and reduce harmful emissions. The design of a high-temperature ORC system for such applications is a challenging problem involving a trade-off between maximizing conversion efficiency and minimizing system weight and volume. In the case of airborne ORC systems, minimizing drag penalties is also critical. Achieving this goal requires solving a complex design optimization problem that integrates the concurrent design of several components, including the aircraft, the primary propulsion system, the ORC heat exchangers, and the ORC turbogenerator. The need for a supersonic turbine often emerges as a result of a large pressure ratio, which is driven by the need to maximize thermodynamic cycle efficiency and by the selection of a molecularly complex fluid to match the heat source temperature profile and minimize exergy losses. Consequently, the expander design is very challenging and estimating its performance is non-trivial, requiring advanced modeling tools to account for nonideal thermodynamic effects in the stator and flow losses caused by shock waves due to the high Mach number at the nozzle outflow.

5.1. ORIGINAL CONTRIBUTIONS

This dissertation documents research work on modeling and design methods for radial-inflow turbines for high-temperature ORC power systems, along with the design of a unique prototype turbine that is about to be installed in the Aerospace Propulsion & Power Laboratory at TU Delft. The objective is to advance current knowledge on the optimal design of these turbines and lay the groundwork for future experimental research by designing a facility to measure their performance, generate empirical models to predict performance under on- and off-design conditions, and provide a test bed for the development of high-speed turboexpanders. The ORCHID turbine setup is also a valuable resource for possibly testing other expanders (different working fluids and operating conditions, as required by other applications), and for studying different powertrain components—such as seals and bearings—and investigating the rotordynamics of oil-free rotors.

The work presented in this dissertation makes two main contributions to the research field of high-temperature ORC turbines:

1. **Formulation of novel preliminary design guidelines for radial-inflow turbines.** A preliminary design code, written in *Python* and named *TurboSim*, was extended to analyze the impact of critical turbine design parameters on losses and efficiency in high temperature ORC radial-inflow turbines. The results were used to formulate design guidelines, providing best practices for selecting stage duty coefficients that maximize expander efficiency. Compared to previous tools, such as the Rodgers [1] and Chen & Baines [2] design maps, the design maps generated with *TurboSim* incorporate additional design parameters, including the volumetric flow ratio (VR) and the average isentropic pressure-volume exponent ($\bar{\gamma}_{Pv}$). Plots of the optimal turbine duty coefficients—namely, the work coefficient (ψ)

and the flow coefficient (ϕ_2)—and the associated turbine efficiency were obtained for VR values ranging from 3 to 80, a typical interval for supersonic RITs of high-temperature ORC systems, and for $\bar{\gamma}_{Pv}$ values between 0.6 and 1.15, accounting therefore for the effects of nonideal thermodynamics on efficiency. Existing methods, such as those of Perdichizzi & Lozza [3] and more recently by Mounier *et al.* [4], Da Lio [5], and Manfredi *et al.* [6], are based on outdated models (e.g., those documented in Ref. [3, 4]), limited to specific fluid families (see, e.g., Ref. [4, 5]), or do not explicitly report values of ϕ_2 and ψ (see, e.g., Ref. [6]), which are essential for preliminary stage design. The best practices documented in this dissertation are not only applicable to high-temperature ORC systems but can also be generalized to any radial-inflow turbine. Their formulation makes them a computationally efficient tool for performance estimation in integrated design and optimization problems.

2. **Design and realization of a test facility for supersonic radial-inflow ORC turbines.**
A detailed design process to select the layout of the *ORCHID turbine* test section, its main components, and the specifications of the assembly and its individual parts was developed and applied. The test section, featuring a supersonic RIT for high-temperature ORC systems of low power capacity (≈ 10 kW), was designed as part of this research and is currently being realized. Once operational, it will enable measurements of the fluid dynamic efficiency of high-pressure ratio RITs, and the assessment of the impact of design choices (e.g., vane count, impeller blade shape, tip clearance) on turbine performance. The results of the experimental campaigns could also provide knowledge applicable to other types of radial turbines and supersonic turbomachinery. Examples are turbines for rocket engines [7–9], expanders to drive fuel cell turbocompressors [10, 11], low-temperature ORC systems for onboard waste heat recovery [12, 13], and geothermal power conversion expanders [14]. Research on oil-free gas bearings and seals is also possible and highly relevant. The powertrain assembly, which couples the turbine to a high-speed electric machine for braking power, will facilitate research and development of next-generation high-speed electric generators—a critical technology for more electric and all-electric aircraft.

5.2. MAIN CONCLUSIONS

Based on the research work carried out and documented in this thesis, the following conclusions can be drawn:

1. The performance of high-temperature ORC radial-inflow turbines can be predicted with sufficient accuracy using preliminary design tools based on state-of-the-art first principle models together with empirical correlations from the scientific literature. One such tools is *TurboSim*. The loss accounting technique discussed in Chapter 2, similar to that employed by Manfredi *et al.* [15] but adapted to include the contribution of dissipation across shock waves, was instrumental to answer the research question:

> A1 *Can TurboSim – a preliminary design tool for radial-inflow turbines – predict the efficiency of high-temperature ORC RITs?*

More specifically, as far as two exemplary test cases are concerned, the value of total-to-static efficiency calculated with *TurboSim* deviates by ±1% from that calculated with unsteady RANS simulations, while the computed mechanical power deviates by ±5%. The test cases are: (i) a high-pressure-ratio gas turbine (i.e., the T100) and (ii) a high-temperature, high-pressure-ratio ORC turbine (i.e., the ORCHID turbine). The method allows to estimate the relative magnitude of the loss in the different components of the turbine, thus it can be used to qualitative assess the influence of different design variables on the losses occurring in the stator vanes, in the radial gap, and in the impeller. From this result, it was also possible to deduce that the ROM correctly estimates the difference in efficiency of 5 percentage points between the two test cases, which can therefore be mainly ascribed to the difference in volumetric flow ratio. These results underline the suitability of *TurboSim*, and more in general of design tools based on a similar modeling framework, for predicting the values and the trends of the integral quantities that are relevant for preliminary design studies.

2. The pioneering work of Giuffré & Pini [16], who first explored the possibility of using VR and $\bar{\gamma}_{Pv}$ as scaling parameters to predict the efficiency of single-stage axial turbines operating with molecularly complex fluids expanding from nonideal thermodynamic conditions, greatly influenced the author of this dissertation. Building on this foundation, the research documented in Chapter 2 focused on the feasibility of applying a similar approach to radial-inflow turbines. The objective was to develop design practices and guidelines for high-temperature ORC RITs by addressing the following research question:

> A2 *Can design guidelines for the selection of optimal duty coefficients, i.e., the work and flow coefficients, be formulated using the modeling framework implemented in TurboSim?*

The results of Chapter 2 elucidate the role of several design parameters with respect to losses and efficiency of supersonic RITs, and further expand the existing knowledge from previous studies by also answering the research question:

> A3 *Which scaling parameters are suitable to account for fluid complexity and nonideal thermodynamic effects on the efficiency?*

Based on these results, the following best practices for the selection of RITs optimal design parameters could be formulated:

(a) For $VR < 10$, ψ=1.3 is a suitable first guess for maximizing both η_{ts} and η_{tt}, independently of $\bar{\gamma}_{Pv}$. As an example, single-stage RITs operating with low molecularly complex fluids at relatively low inlet temperature (e.g., < 300 °C)

and maximum peripheral speed (i.e., $< 450\,\mathrm{m\,s^{-1}}$) can be designed following this indication, because the Mach numbers are bound to be low and thermal and mechanical loads are low, allowing $\psi > 1$. However, with higher temperature and speed, the value of ψ should be set closer to 1 to reduce the inlet blade angle of the impeller, and consequently lower the bending stress at the blade root that is originating from high centrifugal loads acting on non-radial inducers.

(b) For $10 < VR < 40$, the optimal value of ψ changes with VR and $\bar{\gamma}_{Pv}$, and depends on the efficiency of choice, i.e., η_{ts} or η_{tt}. In this case the flow at the outlet of the nozzle is transonic or low-to-mildly supersonic ($M \lesssim 2$), and the value of the ψ should be set on a case-by-case basis using the charts provided in Chapter 2, Figure 2.18.

(c) For $VR > 40$ the optimal value of ψ is insensitive to VR. The graphs of Figure 2.18 allow to select a sufficiently accurate approximation of the optimal value of ψ. The optimal ψ depends both on the relevant efficiency (η_{ts} or η_{tt}), and on the value of $\bar{\gamma}_{Pv}$. As can be inferred by inspecting the four figures 2.18a – 2.18d, the optimum ψ increases as $\bar{\gamma}_{Pv}$ decreases, suggesting that high-temperature ORC RITs – featuring low values of $\bar{\gamma}_{Pv}$ if designed to operate with the inlet thermodynamic state close to the critical point state of the fluid – should be designed with high values of the work coefficient, i.e., a low reaction degree.

(d) For $VR > 20$, $\phi_2 = 0.35$ yields maximum η_{ts}, whereas $\phi_2 = 0.52$ yields maximum η_{tt} at any given VR and $\bar{\gamma}_{Pv}$. Because ϕ_2 is more closely linked to the machine flowrate rather than to the flow velocity, its value does not significantly affect the stage Mach number for values of VR greater than 20. The optimum value of ϕ_2 is therefore a constant for these transonic and supersonic RIT designs.

(e) For $VR < 20$, the optimal value of ϕ_2 should be chosen using the charts provided in Chapter 2, Figure 2.18.

The results displayed in Figure 2.18 provide insights into turbine design as they allow to examine the loss breakdown of two verification cases, namely that of the T100 turbine (Figure 2.6a) and that of the ORCHID turbine (Figure 2.6b). Despite the significant difference in Mach numbers at the stator outlet (T100: $M_1 = 1$, ORCHID: $M_1 = 2$), the main cause of the lower efficiency of the ORCHID turbine are the larger impeller losses and high value of the exit kinetic energy, rather than the supersonic flow at the outlet of the stator vanes, which is often believed to be the primary source of inefficiency of supersonic RITs. The results plotted in Figure 2.18c suggest that the value of the work coefficient of the ORCHID turbine should be higher (≈ 1.4 for $VR \simeq 50$) than the design value of 1.3. This would increase the Mach number at the stator exit, and would lower the value of the Mach number at the impeller exit. Given the three-dimensional shape of the impeller blades and the resulting complex flow field, secondary flows contribute significantly to the overall loss; a heavily loaded impeller affects more negatively the

overall efficiency than a heavily loaded stator. Thus, a more suitable selection of duty coefficients for the design, coupled with a diffuser downstream of the impeller, could mitigate the efficiency loss associated with the high Mach number at the stator outlet, and the high volumetric flow ratio typical of *hiTORC-RIT*s.

3. A comprehensive design methodology was developed to perform the mechanical design of the ORCHID turbine, see Chapter 3. The research conducted allowed to directly address the following fundamental research question:

   B1 *What rotor layout should be adopted for the design of a prototype laboratory turbine intended for experimental research on hiTORC-RIT?*

   The ORCHID turbine was conceived as a standalone assembly mechanically coupled to an off-the-shelf electric generator providing braking torque. This approach offers two key advantages: (i) it reduces the development effort by leveraging readily available electrical generator solutions, and (ii) it enables future updates to the turbine without requiring modifications to the generator. The turbine features a modular design, utilizing standard, cost-effective rolling element bearings to support the rotor. A removable mechanical coupling connects the turbine to the generator, enhancing the adaptability of the setup. The modularity of the design facilitates future investigations, such as those aimed at assessing the effect of different stator vane geometries, flow distributors, or diffusers on flow losses. The overhung impeller design simplifies the access to the turbine wheel, enabling rapid impeller replacement, which is facilitated by easily removable housings. It also reduces manual operations during test campaigns by eliminating the need for full rotor disassembly to ensure a perfect balancing, which can be maintained by compensating the unbalance of the impeller prior to its installation.

4. A finite element model of the ORCHID turbine, also presented in Chapter 3, was developed and used to conduct a rotordynamic analysis under different operating conditions, addressing the research question:

   B2 *What is the rotordynamic response of the rotor supported on oil-lubricated rolling element bearings?*

   Although the scientific literature contains numerous studies on the fluid dynamic design and performance evaluation of ORC RITs, information on their rotordynamic behavior remains scarce. The accurate estimation of the system critical speeds and possible instabilities arising at specific operating conditions, are fundamental information for the development of a control strategy to ensure stable and reliable operation. This research sought to address the overarching question while contributing to the existing knowledge by identifying and modeling key factors influencing the rotordynamic response of the rotor, guided by the following sub-questions:

B2.1 *What rotordynamic coefficients must be included in the mechanical model of the rotor?*

B2.2 *What modeling approaches are available to predict these coefficients, and can they provide accurate predictions of the values at both the design point and off-design conditions?*

Various methods to predict the rotordynamic coefficients of critical components, including the squeeze-film damper, ball bearings, pocket gas seal, and impeller were documented and employed.

- By using the Reynolds equation to model the lubricant-film flow in a squeeze-film damper, it was observed that the damper acts as a centering spring and introduces additional stiffness in the system, which increases in magnitude with increasing rotational speed. Moreover, the damping capacity of the system degrades at high speed due to the increasing fraction of lubricant undergoing cavitation in the squeeze-film damper. Other factors, such as the rotational eccentricity and the vibration orbit radius were found to have a large influence on system stiffness, suggesting that the dynamic response of the rotor is strongly dependent on its geometrical variables and manufacturing tolerances.
- The damping and stiffness coefficients of a pocket gas seal, estimated using RANS simulations, were found to be negligible compared to those of the squeeze-film damper and ball bearings, indicating its minimal impact on rotor vibrations.
- As far as impeller forces are concerned, it was concluded that the different modeling techniques considered in this work, namely empirical methods developed and used for standard industrial practice, do not provide consistent results. Therefore, the effect of impeller forces should be further explored using high-fidelity CFD methods, such as full-annulus unsteady RANS simulations.

The rotordynamic analysis conducted in Chapter 3 was instrumental to answer the research question:

B2.3 *What are the effects of these factors on the damped natural frequencies and the stability of the system?*

Results show that the damped natural frequencies of the system generally increase as the rotational speed increases, due to the presence of a stiff damper, which however causes the rotor to be under-damped in the operating range of interest (80–120 krpm) due to lubricant cavitation at high-speed, which deteriorates the damping capacity.

Several critical speeds were identified in the operating range, underscoring the im-

portance of correctly estimating their value through accurate modeling of the different influencing factors. Operation of the rotor at a critical speed might lead to resonance and large rotor vibrations, with possibly catastrophic consequences. It was also observed that variations in ball bearing stiffness, modeled with the Hertz contact theory and altered within a ±30% range, significantly influenced the critical speeds of the rotor, shifting them by as much as 10 krpm (approximately 10% of the nominal rotor speed), depending on the mode shape.

A stability analysis further revealed that destabilizing forces – namely, the cross-coupled stiffness coefficients of the impeller and pocket gas seal – could lead to rotor instabilities at high loads.

While the Campbell diagrams and stability plots derived in this study are not final, the methodology developed herein provides an essential foundation for further modeling and analysis of the final design of the ORCHID turbine.

5. The challenge of integrating a turbogenerator into a test section for the ORCHID was addressed in Chapter 4, and the findings from this study were crucial in answering the fundamental research question:

> B3 *What technical modifications and auxiliary systems are necessary to integrate the turbine into the ORCHID test section and ensure its proper functionality within the existing experimental facility?*

The layout of the ORCHID turbine test section was obtained as the result of three concurring requirements: (i) the need to supply working fluid to the turbine and return it to the ORCHID, (ii) the need to lubricate the bearings and cool down the lubricant, and (iii) the need to dissipate the electrical power converted by the electric generator braking the turbine.

The selection of the bearings lubricant is arguably one of the most critical aspects, as its characteristics have consequences on lubricant leakage into the working fluid loop, on the rotordynamic response of the system, and on the bearings lifespan. Liquid MM was preferred as the lubricant of rolling element bearings over the more conservative choice of ISO VG 32 oil made for the preliminary analyses reported in Chapter 3. The main advantage is the elimination of possible oil contamination of the working fluid, which can cause the accumulation of hot sludge which could trigger the thermal decomposition of the siloxane. The primary drawback of using liquid MM as lubricant is the fivefold reduction of the system damping compared to that estimated in case the ISO VG 32 oil is the lubricant, which is due to the much lower viscosity of MM. However, the significant reduction in contamination risk far outweighs the additional risks associated with turbine operation. Moreover, this approach is compatible with contactless seals, which offer benefits such as reduced wear, minimized debris formation, and lower drag torque compared to contact seals. Moreover, the updated rotor design featuring a shorter cartridge leads to higher values of the natural frequencies, that were not estimated explicitly in this work, but might eliminate critical speeds from the range of in-

terest in the case at hand. The impact of this design change on the rotordynamic response of the rotor should be investigated in future work.

Another aspect of significant importance to the development of a turbine test rig for experimental research is the selection of process monitoring sensors, along with the quantification of the expanded uncertainty through the measurement chain, i.e., the uncertainty propagating from the sensors to the data acquisition system. The work documented herein provides insights on how to quantify these uncertainties, and on the role of different sources of uncertainty in the measurement chain, and allows to answer one of the secondary research questions that guided the research, that is

> B4 *What sensors and instrumentation are necessary to measure the turbine power and its efficiency, and what is the expected accuracy of these measurements?*

The results presented in Figure 4.21 and Figure 4.22, derived from the CFD simulations discussed in Chapter 3, highlight the importance of accurately quantifying the measurement error associated with all the components of the measurement chain. It is shown that, by characterizing the performance of the analog to digital converter cards used to acquire process variable signals, the uncertainty on the measurement of the turbine efficiency can be reduced from ±2.5 % to approximately ±0.5 %, and of the turbine power from ±1 kW to approximately ±100 W. Sources of uncertainty also include fluid dynamic phenomena occurring near the sensors, such as bow shocks in front of probes inserted in transonic and supersonic flows for the measurement of total pressure and temperature, the boundary layer blockage in high Reynolds number flows, and flow-induced vibrations due to fluid-structure interactions. Moreover, for sensors mounted under a cavity, uncertainties due to flow recirculation in the cavity should be accounted for. Addressing these challenges requires a detailed study of the flow field to mitigate their impact effectively.

5.3. LIMITATIONS AND RECOMMENDATIONS FOR FUTURE WORK

Some limitations of the modeling approach and design presented in this work were identified, and are summarized in the following alongside with recommendations for future work:

- The preliminary design guidelines devised using *TurboSim* allow solely to prescribe the optimal stage duty coefficients to maximize turbine efficiency. As shown, stage efficiency can be predicted independently of the working fluid characteristics, unlike other essential aspects of the expander design, such as its size and weight. However, power density is a fundamental requirement determining the viability of ORC turbogenerators for the recovery of otherwise wasted thermal energy from propulsive engines in general, and more so in case of aircraft propulsion and power systems, whereby the limitations on space and operational empty

mass impose a trade off with conversion efficiency. Including power density in the objective function underlying the preliminary design guidelines can simplify the selection of the optimal working fluid, whose effect on the turbogenerator design can thus be accounted for at the preliminary design stage by means of the size parameter.

- The mechanical integrity of high-speed turbomachinery is significantly affected by static and dynamic loading, which can limit the design space resulting from aero-thermal optimization. Extending the *TurboSim* model to incorporate a preliminary mechanical assessment and a rotordynamic analysis would enhance its capability to identify viable designs. This improvement could be accomplished with tools such as ROSS [17], an open-source rotordynamic analysis software coded in *Python*. Furthermore, several applications, such as turbines for fuel-cell turbochargers, demand expanders that can adapt to varying operating conditions, making performance across the entire operating range fundamental for selecting the optimal RIT configuration. Therefore, future work to include off-design performance in the preliminary design practices documented herein is encouraged.

- The rotordynamic analysis of the ORCHID turbine, which was conducted only for the initial rotor design documented in Chapter 3, should be applied to the final design reported in Chapter 4.

  The following aspects should therefore be addressed in future work:

  – A finite beam-element model of the ORCHID turbine rotor similar to that documented in Chapter 3 should be developed. Using ROSS [17] for modeling and analysis would be beneficial. The ORCHID turbine rotordynamic model could then be released as an open-source test case to the scientific community.

  – The model of the rotor should be complemented by estimates of the aerodynamic forces acting between the impeller blades and the machine shroud under eccentric rotor motion. The values of these forces could be obtained by means of unsteady RANS simulations – in which the geometry of the fluid domain should be generated considering the presence of an eccentric rotor shaft, and model the leakage flow through a varying tip clearance along the circumferential direction – which would support the evaluation of possible rotor instabilities at the operating conditions of interest.

  – Furthermore, the method for the evaluation of the damping coefficient of the squeeze film damper based on the Reynolds equation should be extended to include the properties of the working fluid. This would allow to simulate the operation of the machine in case the working fluid is also used as the lubricant for the shaft bearings and to evaluate the effect of lubricant cavitation on the damping coefficients. As a possible way forward, the Reynolds solver developed by de Waart & Pini [18] to investigate the effect of fluid properties on gas bearings performance could be also employed to compute the damping coefficient in liquid films.

  - Models of the sealing performance and of the rotordynamic characteristics of piston seals should be included to gain insights on their influence on rotor vibrations.

- The characterization of the measurement system presented in this dissertation is not complete and should be complemented with the estimation of additional sources of uncertainty. For example, numerical investigations using high-fidelity CFD tools can be used to evaluate the integration of total temperature and total pressure probes into the assembly, namely their effect on the flow field and on performance measurements.

- Critical aspects of the design of the test section for the ORCHID turbine are still missing and are required prior to the commissioning. A detailed control procedure must be generated, with the objective of ensuring safe operation mainly by avoiding the operation of the turbine at critical speeds. The document describing the control narrative must also include descriptions of the start-up, shut-off, and emergency procedures, considering the different components and their functions, and describing how these work together in the system. Several important items must be identified, such as the failure modes of (part of) the system that might arise during operation, which signals can be used to detect these malfunctions, and what are the corrective actions that must be implemented.

- The design of the ORCHID turbogenerator test bench must be completed. The bench must support all components of the turbogenerator powertrain while facilitating precise alignment of the turbine and generator rotors prior to operation. The use of floating rolling element bearings for the turbine rotor and gas bearings in the generator makes alignment critical to ensure system reliability and robustness. A significant challenge is the accurate prediction of the positions of the turbine and generator rotational axes during operation. This necessitates detailed test preparation, including alignment procedures to determine rotor positions based on their anticipated operational states. To address these requirements, the test bench design must incorporate set screws for fine adjustments, reference pieces for measuring component positions, and shims conveniently placed to achieve optimal alignment.

5.4. OUTLOOK AND FUTURE RESEARCH DIRECTIONS

The *TurboSim* program was developed according to modularity and interface capability principles, to enable its seamless integration with other software tools. In its current development state, it could serve as a foundation for future enhancements, such as the capability of modeling additional powertrain components, including electric machines, pumps, mixed-flow turbines, multistage turbines, and gearboxes. Future developments could focus on incorporating multidisciplinary models, such as those for mechanical stress estimation, thermal analysis, and to account for the presence of other components such as seals and bearings. Moreover, as the pace of development of GPU-accelerated CFD solvers is rapidly increasing and many software industries are investing on it, CFD-based techniques could soon become a viable alternative to traditional loss-accounting

methods in the preliminary design stage, offering significant improvements in accuracy. However, for these methods to be practical for large-scale design exploration and optimization, the computational cost of CFD evaluations must be reduced to just a few tens of seconds per evaluation.

The design and commissioning of the ORCHID turbine experimental setup are ongoing, with several critical tasks yet to be completed. In the long term, the ORCHID turbine will enable the dissemination of open-source data, models, and test cases for verification and validation, but also of best practices and design guidelines for several components and systems of relevance in power and propulsion applications. In a similar fashion to what has been done with other experimental facilities – of which, two notable examples are the High Efficiency Centrifugal Compressor (HECC) in operation at the NASA Glenn Research Center [19] and the transonic compressor of the TU Darmstadt laboratory [20] –, the raw data from experimental measurements, geometrical data from metrological inspection of the parts, and the detailed information on the operating conditions and control of the machine will be consolidated in online repositories to make the ORCHID turbine a first of its kind open test case for verification and validation of numerical models suited for turbomachinery operating with nonideal compressible flows.

In the short term, the following milestones outline the key steps necessary to finalize and commission the facility:

1. **Finalization of the detailed design** of the test bench and piping, including the preparation of safety documentation and certification.
2. **Completion of procurement activities**, with a current focus on the components required for the systems outlined in milestone 1.
3. **Development and implementation of control procedures**, incorporating the results of the rotordynamic assessment of the finalized ORCHID turbine design.
4. **Construction of the experimental setup**, including wiring, installation tests, and validation of component functionality.
5. **Initial commissioning tests**, essential for verifying the system design and ensuring proper operation.

In a first research phase, the facility will be operated to gain operational experience with the turbogenerator and to measure the efficiency of the ORCHID turbine over the operational range. These measurements will provide the first experimental data to validate and verify numerical tools. Future updates may focus on incorporating additional measurement techniques, such as probes for measuring total pressure downstream of the impeller. At a later stage, pressure taps and flush-mounted high-frequency sensors could be introduced to provide deeper insights into the flow field within the passages. However, some of these techniques require additional physical space, which could be achieved by using a larger-scale turbine. This would not only facilitate the integration of instrumentation but also enhance the spatial resolution of the measurements. Concurrently, research efforts will devoted to the study of machine vibration and to the validation of the rotordynamic models, using embedded sensors and accelerometers.

Data from process and vibration sensors could drive the development of advanced monitoring tools and intelligent power generation systems, such as real-time digital twins for health monitoring or virtual machines capable of running numerical models of the expander in real-time during operation. These systems could adapt to sensor feedback, optimizing conversion efficiency and adjusting the turbogenerator operation accounting for component wear and aging. The ORCHID setup and the developed tools will inform through their use the design of efficient power systems for various applications, including those for the heat recovery from aircraft, marine, and ground-vehicle engines. For example, the setup could support research on high-efficiency radial turbines for specific systems, such as expanders for liquid rocket engines – which have recently been investigated as a potential alternative to the common two-stage axial turbine in small-scale rockets by Lioi *et al.* [21] – and which could be studied by utilizing scaling laws to adapt the operating conditions of the ORCHID turbine to the different properties of the gas flow. Similarly, research on radial turbines for large geothermal power plant–e.g., see Ref. [14, 22]–designed for diverse working fluids can be conducted.

The setup capabilities extend beyond the testing of expanders and may include the testing of other critical ORC system components, such as high-speed electric generators, gearboxes, and pumps. An interesting opportunity has been recently discussed, that is, the study of turbopumps for rocket engines, provided that similarity rules can be applied. Thanks to its modular design, the ORCHID setup provides also a platform for advancing flow monitoring and measurement techniques. These techniques support fundamental research on fluid dynamics and the investigation of advanced geometries for flow-path components. Beyond the already operational converging-diverging de Laval nozzle [23], designed primarily for studying dense vapor dynamics and shock-induced flow behavior (see e.g., the recent work on optimal measurements in dense organic vapor [24, 25]), the ORCHID setup could be extended to incorporate linear and annular cascades, enabling more applied research on flow losses downstream of blade rows.

BIBLIOGRAPHY

1. Rodgers, C. *Small High Pressure Ratio Turbines* Technical report TR-1987-01 (Sundstrand Turbomach, San Diego, CA, June 1987).
2. Chen, H. & Baines, N. C. The aerodynamic loading of radial and mixed-flow turbines. *International Journal of Mechanical Sciences* **36,** 63–79. doi:10.1016/0020-7403(94)90007-8 (1994).
3. Perdichizzi, A. & Lozza, G. *Design Criteria and Efficiency Prediction for Radial Inflow Turbines* in *Proceedings of the ASME Turbo Expo: Power for Land, Sea, and Air* **1** (1987), V001T01A086. doi:10.1115/87-GT-231.
4. Mounier, V., Olmedo, L. E. & Schiffmann, J. Small scale radial inflow turbine performance and pre-design maps for Organic Rankine Cycles. *Energy* **143,** 1072–1084. doi:10.1016/j.energy.2017.11.002 (2018).
5. Da Lio, L. *Preliminary design of organic fluid turbines to predict the efficiency* PhD thesis (University of Padova, 2019).
6. Manfredi, M., Spinelli, A. & Astolfi, M. Definition of a general performance map for single stage radial inflow turbines and analysis of the impact of expander performance on the optimal ORC design in on-board waste heat recovery applications. *Applied Thermal Engineering* **224,** 119390. doi:10.1016/j.applthermaleng.2023.119390 (2023).
7. Mack, Y., Haftka, R., Griffin, L., Snellgrove, L., Dorney, D., Huber, F. & Shyy, W. *Radial Turbine Preliminary Aerodynamic Design Optimization for Expander Cycle Liquid Rocket Engine* in *42*nd *AIAA/ASME/SAE/ASEE Joint Propulsion Conference & Exhibit* (2006). doi:10.2514/6.2006-5046.
8. Leto, A. & Bonfiglioli, A. Preliminary Design of a Radial Turbine for Methane Expander Rocket-Engine. *Energy Procedia* **126,** 738–745. doi:10.1016/j.egypro.2017.08.221 (2017).
9. Cancescu, A.-C., Crunteanu, D.-E., Andreescu, A.-M. T. & Danescu, S.-N. Predesign of a Radial Inflow Turbine That Uses Supercritical Methane for a Mid-Scale Thruster for Upper Stage Application. *Aerospace* **11,** 996. doi:10.3390/aerospace11120996 (2024).
10. Fröhlich, P. *Development of an oil-free turbo compressor for mobile fuel cell applications – challenges and results* in *Proceedings of the First FC³ Fuel Cell Conference* (Chemnitz, Germany, Nov. 2019), 123–138. https://www.celeroton.com/en/development-of-an-oil-free-turbo-compressor-for-mobile-fuel-cell-applications-challenges-and-results/.

11. *ZeroAvia ZA600 Compressor* Technical datasheet. ZeroAvia, May 2024. https://zeroavia.com/wp-content/uploads/2024/05/Compressor-Datasheet-7-digital.pdf.

12. Di Bella, F., Cho, J.-K., Kwon, J.-S. & Jeong, H.-g. Development and testing of a 250 kWe ORC system using an integrated axial turbine and high speed generator for 3.7 bar,a condensing steam. *Proceedings of the* 3^{rd} *International Seminar on ORC Power Systems* (2015).

13. Yuksek, E. L. & Mirmobin, P. Electricity Generation From Large Marine Vessel Engine Jacket Water Heat. *ASME 2015 9th International Conference on Energy Sustainability, ES 2015, collocated with the ASME 2015 Power Conference, the ASME 2015 13th International Conference on Fuel Cell Science, Engineering and Technology, and the ASME 2015 Nuclear Forum* **2.** doi:10.1115/es2015-49226 (2015).

14. *Driving expander technology* Information booklet. Atlas Copco Group. https://www.atlascopco.com/content/dam/atlas-copco/compressor-technique/gas-and-process/documents/driving-expander-technology.pdf.

15. Manfredi, M., Alberio, M., Astolfi, M. & Spinelli, A. *A Reduced-Order Model for the Preliminary Design of Small-Scale Radial Inflow Turbines* in *Turbo Expo: Power for Land, Sea, and Air* **4** (2021), V004T06A013. doi:10.1115/gt2021-59444.

16. Giuffré, A. & Pini, M. Design Guidelines for Axial Turbines Operating With Non-Ideal Compressible Flows. *Journal of Engineering for Gas Turbines and Power* **143,** 011004. doi:10.1115/1.4049137 (2021).

17. Timbó, R., Martins, R., Bachmann, G., Rangel, F., Mota, J., Valério, J. & Ritto, T. G. ROSS - Rotordynamic Open Source Software. *Journal of Open Source Software* **5,** 2120. doi:10.21105/joss.02120 (2020).

18. De Waart, W. & Pini, M. The Role of the Working Fluid and Non-Ideal Thermodynamic Effects on Performance of Gas Lubricated Bearings. *Journal of Engineering for Gas Turbines and Power* **147,** 061015. doi:10.1115/1.4056695 (2024).

19. Harrison, H. M. *NASA High Efficiency Centrifugal Compressor Data Archive* Technical report: NASA/TM-20240003692. NASA Glenn Research Center, May 2024. https://ntrs.nasa.gov/citations/20240003692.

20. Klausmann, F., Franke, D., Foret, J. & Schiffer, H.-P. Transonic Compressor Darmstadt — Open Test Case: Introduction of the TUDa Open Test Case. *Journal of the Global Power and Propulsion Society* **6,** 318–329. doi:10.33737/jgpps/156120 (2022).

21. Lioi, A., Cozzi, D., Sambasivam, K. & Corcione, A. D. *Potential of Radial Turbines in Liquid Rocket Engines: A Comparative Study with Classical Axial Turbines* in *Proceedings of the IAF Space Propulsion Symposium* (2024), 1429–1440. doi:10.52202/078371-0156.

22. Valdimarsson, P. *New Development in the ORC Technology* in *Proceedings of Short Course VI on Utilization of Low- and Medium-Enthalpy Geothermal Resources and Financial Aspects of Utilization* (2014).

23. Head, A. J. *Novel Experiments for the Investigation of Non-Ideal Compressible Fluid Dynamics* PhD thesis (Delft University of Technology, 2021).

24. Michelis, T., Head, A. J., Majer, M., Colonna, P. & Servi, C. D. Assessment of particle image velocimetry applied to high speed organic vapor flows. *Exp. in Fluids* **65,** 1–9. doi:10.1007/s00348-024-03822-z. https://link-springer-com.tudelft.idm.oclc.org/article/10.1007/s00348-024-03822-z#citeas (2024).

25. Michelis, T., Head, A. J. & Colonna, P. Estimation of local Mach number in compressible flows of dense organic vapors using Gabor filters and Radon transforms for the post-processing of schlieren images. *Exp. in Fluids* **65,** 1–9. doi:10.1007/s00348-024-03925-7. https://link.springer.com/article/10.1007/s00348-024-03925-7 (2024).

APPENDICES

A. EMISSIONS

Aviation-related emissions comprise CO_2 and non-CO_2 effects on the environment, occurring throughout the entire life-cycle of the aircraft, i.e., design, manufacturing, MRO (maintenance, repair and operation), and end-of-life (decommissioning, disassembly and recycling). When considering the emissions occurring in the operational phase of the aircraft, Lee *et al.* [1] combined estimates from different sources to represent the annual CO_2 emissions of the aviation sector globally, from the 1940 to pre-COVID19 pandemic levels. Between 1970 and 2012, carbon emissions increased in average by $2.2\,\%\,yr^{-1}$, while only in the period going from 2013 to 2018 the annually averaged increase is $5\,\%\,yr^{-1}$, in line with current air passenger travel demand increase [2, 3]. Nevertheless, direct CO_2 emissions are not the only contributor to climate change, and other non-CO_2 emissions such as NOx - leading to cirrus condensation trails formation -, sulfur, soot, and water vapor also contribute to the overall aviation-induced effective radiative forcing (ERF), a measure of the warming impact of different compounds emitted in the atmosphere [4]. The authors of [1] estimated that about one-third of the overall aviation-induced ERF is attributed to direct emission of CO_2 in the atmosphere, while the remaining two-thirds are due to non-CO_2 emissions, despite predictions of the environmental impact for this category of compounds are still affected by large uncertainties. To reach the emission targets set by government legislation [5] and reduce net greenhouse gas emissions of at least 55% by 2030 – in an effort to reach climate neutrality by 2050 – aircraft technology must undergo revolutionary changes. These include new and more efficient engines powered by renewable energy sources, lightweight airframe made with sustainable materials [6, 7], as well as the implementation of a circular life-cycle approach through its integration at the preliminary design stages to reduce the impact of aircraft end-of-life [8, 9].

B. AIRCRAFT ENERGY BALANCE

The aircraft energy balance represented by the Sankey diagram of Figure 1 illustrates the breakdown of the input energy source, i.e. the fuel lower heating value (LHV). Part of the energy input is used for propulsion and onboard power, while a large fraction of it is lost or unused. The lost energy fraction is due to propulsive losses, such as the aircraft drag and thermodynamic losses of the propulsion system. The unused energy is the part of LHV that is stored in the form of heat in the gas flow leaving the engine and dumped in the environment. As shown by the diagram, the exhaust energy fraction is close to 50 % of the LHV.

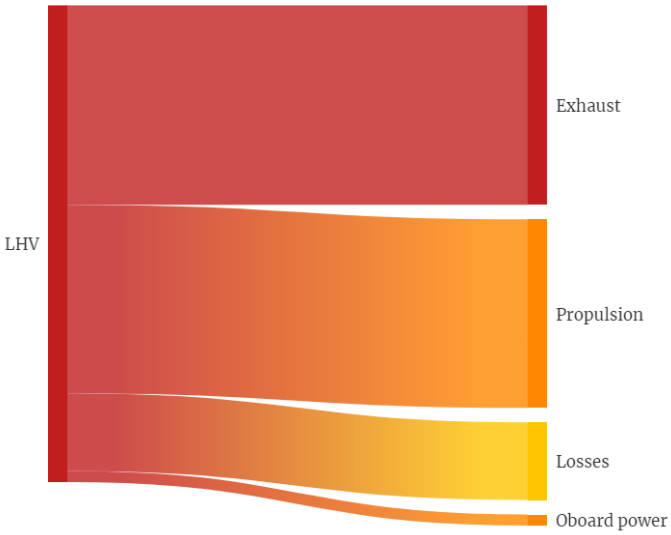

Figure 1: Appendix: Sankey diagram of a modern aircraft showing the breakdown of the input fuel LHV.

C. COMBINED CYCLES

A prime example of residual thermal power recovery is the regenerated gas-turbine (GT) engine, in which compressed air is preheated using thermal energy from the exhaust flow. Because thermal energy is reinserted into the cycle, this engine architecture leads to a larger overall utilization of the fuel LHV. In a combined-cycle gas turbine (CC-GT), the thermal energy of the exhaust gas flow is used to heat a separate fluid media, which is then expanded in a separate turbine to produce additional shaft power. CC-GT's are characterized by high thermodynamic efficiency, with modern industrial applications achieving 10 - 15 % higher efficiencies than their simple GT counterpart [10, 11]. Different configurations of CC power plants can be distinguished depending on the type of bottoming cycle, such as: a) the open- recuperated CC-GT, where ambient air is compressed, heated, expanded in an air turbine, and finally exhausted in the environment, or b) the close-loop recuperated CC-GT, where a fluid media is compressed, heated and expanded cyclically. The close loop cycle can be realized by means of a simple gas cycle, or alternatively by employing a Clausius-Rankine cycle, where water is evaporated up to superheated vapour conditions (i.e., steam), expanded in a steam turbine, and then condensed. Based on the same principle, the organic Rankine cycle (ORC) is arguably the most thermodynamically efficient way to realize a CC-GT engine. In a ORC, the fluid media is an arbitrary (organic) chemical compound. Nevertheless, non-organic fluids can be employed as well, such as synthetic non-flammable fluids and refrigerants. ORC's can yield higher conversion efficiency over the conventional Rankine cycle for relatively small heat sources (i.e., few MW) at an average temperature below 500 °C, a limit dictated by the thermal decomposition temperature of most organic fluids[1].

[1] [12] tested a mixture of pentafluorobenzene and hexafluorobenzene at 468 °C for up to 532 h.

D. COEFFICIENTS OF THE BAINES LOSS MODEL FOR RADIAL-INFLOW TURBINE IMPELLERS

The hydraulic length and diameter used to compute the impeller passage losses as per Equation 2.35 write as

$$L_{\mathrm{H}} = \frac{\pi}{4}\left[\left(z - \frac{b_2}{2}\right) + \left(R_2 - R_{3\mathrm{s}} - \frac{b_3}{2}\right)\right],$$
$$D_{\mathrm{H}} = \frac{1}{2}\left[\left(\frac{2\pi R_2 b_2}{4\pi R_2 + 2Z_{\mathrm{b}} b_2} + \frac{2\pi(R_{3\mathrm{s}}^2 - R_{3\mathrm{h}}^2)}{\pi(R_{3\mathrm{s}} + R_{3\mathrm{h}}) + 2Z_{\mathrm{b}} b_3}\right)\right].$$

The coefficients C_{x} and C_{r} in Equation 2.36 are computed as

$$C_{\mathrm{x}} = \frac{1 - (R_{3\mathrm{s}}/R_2)}{V_{\mathrm{m}2} b_2},$$
$$C_{\mathrm{r}} = \frac{R_{3\mathrm{s}}}{R_2}\frac{z - b_2}{V_{\mathrm{m}3}\bar{R}_3 b_3}.$$

E. STAGE SIZING ROUTINE IN *TurboSim*

A stage sizing routine is implemented in *TurboSim* to determine the inlet and outlet section radii of the impeller and of the stator. With reference to Figure 2, the control parameter for the iterative method is the isentropic exducer radius ratio $R_{3h}/R_{3s}|_i$. The desired $R_{3h}/R_{3s}|_u$ is used to start the iterative calculation process. The program computes the isentropic thermodynamic state and the velocity triangles at each spanwise section and the flow path size is determined by imposing the mass conservation through each section of the machine. The loss accounting is performed based on the flow quantities, thermodynamic fluid properties, and geometry, that are updated at each iteration. The relative velocity at the exit section of the impeller is concurrently verified at each spanwise section to ensure that the obtained solution is physical. The actual exducer radius ratio $R_{3h}/R_{3s}|_r$ is finally calculated, and the convergence is reached once the value of the relative error with respect to the specified exducer radius ratio is lower than a given tolerance.

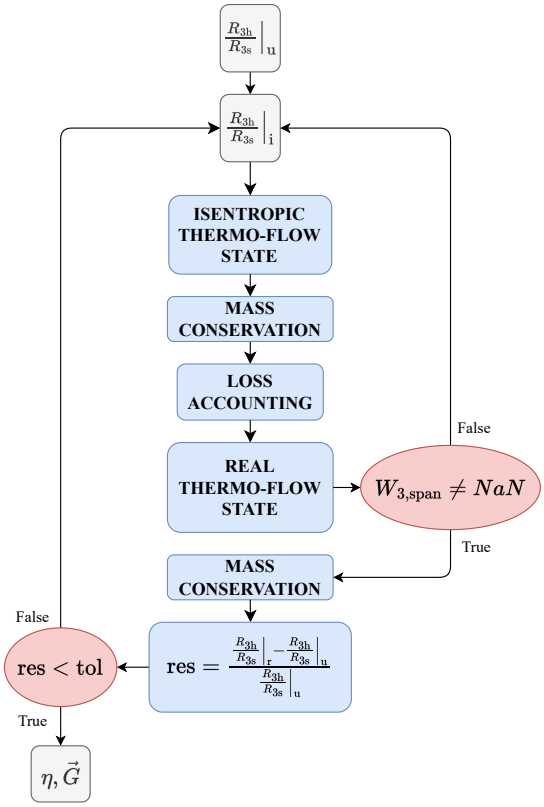

Figure 2: Appendix: Iterative routine implemented in *TurboSim* for sizing a RIT stage.

F. GEOMETRICAL SCALING PARAMETERS USED IN *TurboSim*

The geometrical scaling parameters and physical coefficients used for loss accounting of the turbine designs investigated in Chapter 2 are listed in Table 1.

Table 1: Appendix: Values of the turbine design parameters and loss coefficients used in Chapter 2.

Variable	**Value**	**Variable**	**Value**
α_0	25°	σ_{st}	1.56
α_3	0°	$\left.\frac{t}{g}\right\|_1$	0.015
ξ_2	90°	$\left.\frac{t}{g}\right\|_3$	0.06
ξ_3	0°	$\frac{\epsilon_{\mathrm{x}}}{b_2}$	0.1
$\frac{R_{3\mathrm{h}}}{R_{3\mathrm{s}}}$	0.4	$\frac{\epsilon_{\mathrm{r}}}{b_3}$	0.16
$\frac{R_{3\mathrm{m}}}{R_2}$	0.56	$\frac{V_{\mathrm{m3}}}{V_{\mathrm{m2}}}$	1.25
$\frac{R_2}{R_1}$	0.96	$\frac{\delta^*}{\theta}$	2.0
$\frac{R_1}{R_0}$	0.75	$\frac{\theta}{t_{\mathrm{TE}}}$	0.075
$\frac{b_2}{b_1}$	1.0	C_{D}	0.002
$\frac{b_1}{b_0}$	1.0	K_x	0.4
$\left.\frac{\bar{b}}{\Delta R}\right\|_{\mathrm{st}}$	0.28	K_r	0.75
$\left.\frac{L_{\mathrm{x}}}{\Delta R}\right\|_{\mathrm{imp}}$	0.95	K_{xr}	-0.3

G. ORCHID TURBINE TEST SECTION AUXILIARY COMPONENTS

Table 2: Appendix: List of the auxiliary components selected to operate the ORCHID turbine test section, and related information.

Item	Tag	Process	Make	Model	Standard	Additional info
Inlet valve	V101	Main	Schubert&Salzer	8021 [13] / Positioner type 8049	PN40 / DN 50 / ATEX (positioner)	
Emergency valve turbine line	VE102A	Main	Schubert&Salzer	8044 [14] / Positioner type 8049	PN40 / DN 50 / ATEX (positioner)	Interlock VE102B / default position FO
Emergency valve bypass line	VE102B	Main	Schubert&Salzer	8044 / Positioner type 8049	PN40 / DN 50 / ATEX (positioner)	Interlock VE102A / default position FC
Outlet valve	V103	Main	Schubert&Salzer	8021 / Positioner type 8049	PN40 / DN 100 / ATEX (positioner)	
Inlet valve	V201	Lubricant	Schubert&Salzer	8021 / Positioner type 8049	PN15 / DN25 / ATEX (positioner)	
Outlet valve	V202	Lubricant	Schubert&Salzer	8021 / Positioner type 8049	PN15 / DN25 / ATEX (positioner)	
Cooling loop valve	V301	Coolant	Schubert&Salzer	8021 / Positioner type 8049	PN15 / DN25 / ATEX (positioner)	
Generator cooling valve	VC401	Air	Swagelock	8GU series [15]	DN15	
Generator bearing valve	VB401	Air	Swagelock	4GU series [15]	DN15	
Lube cooler	HX301	Lubricant / Coolant	Alfa Laval	AlfaNova HP14-10H [16]	PN40	
Inlet filter	FU201	Lubricant	ARI	Y-filter type 1046	PN40 / DN25	
Outlet filter	FU202	Lubricant	ARI	Y-filter type 1046	PN40 / DN25	
Generator	GE401	Air	Aeronamic	CS15 [17]		

H. APPLICATION OF THE LINEAR COMPLEMENTARITY PROBLEM TO COMPUTE THE PRESSURE OF CAVITATING LIQUID FLUID-FILMS

The complete Reynolds equation in polar coordinates reads

$$\frac{\partial}{R\partial\theta}\left(\frac{\rho h^3}{12\mu}\frac{\partial P}{R\partial\theta}\right)+\frac{\partial}{\partial z}\left(\frac{\rho h^3}{12\mu}\frac{\partial P}{\partial z}\right)=\frac{\partial}{\partial t}(\rho h)+\frac{\rho h^2}{12\mu}\frac{\partial^2 \rho h}{\partial t^2}, \tag{1}$$

where ρ and μ are the fluid density and dynamic viscosity, and θ, z and R are the tangential, axial and radial coordinates, while h is the fluid-film thickness and P is the fluid pressure.

The relation describing the fluid-film thickness distribution over time and space in the tangential direction reads

$$h(\theta,t)=g-(e\cos\omega t)\cos\theta-(e\sin\omega t)\sin\theta, \tag{2}$$

where e is the radius of the orbit described by the SFD in the plane orthogonal to its axis, and ω is the orbit whirling frequency.

The *linear complementarity problem* (LCP) is introduced herein to linearize the pressure profile across regions of the fluid domain where phase change could occur. The relationship between the fluid density and pressure can be expressed by means of the fluid bulk modulus

$$\beta=\rho\frac{\partial P}{\partial\rho}, \tag{3}$$

which can be assumed constant in a liquid-film flow, apart from the regions where cavitation takes place.

The fluid density ρ in Equation 3 is expressed as

$$\rho=\rho_c e^{\left(\frac{P-P_c}{\beta}\right)}-\xi \qquad \begin{cases}\xi=0, & \text{for the liquid phase}\\ 0<\xi<\rho_c, & \text{in the region undergoing cavitation}\end{cases}, \tag{4}$$

where ρ_c is the fluid density at the cavitation pressure P_c, and ξ is a term that depends on the physical state of the fluid.

Equation 4 can be manipulated to obtain

$$\rho=\rho_c+\eta-\xi, \tag{5}$$

where the newly introduced variable, i.e., η, is defined as

$$\eta = \rho_c \left[e^{\left(\frac{P-P_c}{\beta}\right)} - 1 \right]. \tag{6}$$

By rearranging Equation 6, one can derive the fluid pressure in explicit form as

$$P = P_c + \beta ln\left(1 + \frac{\eta}{\rho_c}\right). \tag{7}$$

The variables η and ξ are a so-called *complementarity pair*, allowing to model the change of fluid properties across phase interfaces linearly.

Plugging Equation 7 into Equation 1 yields the following expression of the Reynolds equation, neglecting the contribution of the fluid inertia, and in which the fluid pressure is determined via the LCP

$$\frac{\partial}{R\partial\theta}\left(\frac{\beta h^3}{12\mu}\frac{\partial\eta}{R\partial\theta}\right) + \frac{\partial}{\partial z}\left(\frac{\beta h^3}{12\mu}\frac{\partial\eta}{\partial z}\right) = \frac{\partial}{\partial t}(\eta - \xi) + \rho_c \frac{\partial h}{\partial t}. \tag{8}$$

BIBLIOGRAPHY

1. Lee, D. S. *et al.* The contribution of global aviation to anthropogenic climate forcing for 2000 to 2018. *Atmospheric Environment* **244,** 117834. doi:10.1016/j.atmosenv.2020.117834 (2021).
2. Overton, J. *The Growth in Greenhouse Gas Emissions from Commercial Aviation Part 1 of a Series on Airlines and Climate Change* Last accessed May 2, 2024. 2019. https://www.eesi.org/papers/view/fact-sheet-the-growth-in-greenhouse-gas-emissions-from-commercial-aviation.
3. ICAO. *Effects of Novel Coronavirus (COVID-19) on Civil Aviation: Economic Impact Analysis - Air Transport Bureau, International Civil Aviation Organization (ICAO), United Nations* Last accessed May 6, 2024. 2022. https://www.icao.int/sustainability/Documents/COVID-19/ICAO%20COVID-19%20Economic%20Impact_2023%2004%2027.pdf.
4. Stocker, T. *et al. Technical Summary. In: Climate Change 2013: The Physical Science Basis. Contribution of Working Group I to the Fifth Assessment Report of the Intergovernmental Panel on Climate Change* tech. rep. (2013). https://www.ipcc.ch/report/ar5/wg1/.
5. *REGULATION (EU) 2021/1119 OF THE EUROPEAN PARLIAMENT AND OF THE COUNCIL of 30 June 2021 establishing the framework for achieving climate neutrality and amending Regulations (EC) No 401/2009 and (EU) 2018/1999 ('European Climate Law')* 2021.
6. Vaidya, U. Thermoplastic composites for aerospace applications. *JEC Composites Magazine* **52,** 41–44. https://link.springer.com/chapter/10.1007/978-3-030-35346-9_4 (2015).
7. Bachmann, J., Hidalgo, C. & Bricout, S. Environmental analysis of innovative sustainable composites with potential use in aviation sector—A life cycle assessment review. *Science China Technological Sciences* **60,** 1301–1317. doi:10.1007/s11431-016-9094-y. https://link.springer.com/article/10.1007/s11431-016-9094-y (2017).
8. Parveez, B., Kittur, M. I., Badruddin, I. A., Kamangar, S., Hussien, M. & Umarfarooq, M. A. Scientific Advancements in Composite Materials for Aircraft Applications: A Review. *Polymers 2022, Vol. 14, Page 5007* **14,** 5007. doi:10.3390/polym14225007. https://www.mdpi.com/2073-4360/14/22/5007/htm%20https://www.mdpi.com/2073-4360/14/22/5007 (2022).

9. Vivalda, P. & Fioriti, M. Stream Life Cycle Assessment Model for Aircraft Preliminary Design. *Aerospace 2024, Vol. 11, Page 113* **11,** 113. doi:10.3390/aerospace11020113. https://www.mdpi.com/2226-4310/11/2/113/htm%20https://www.mdpi.com/2226-4310/11/2/113 (2024).
10. Mom, A. J. Introduction to gas turbines. *Modern Gas Turbine Systems: High Efficiency, Low Emission, Fuel Flexible Power Generation*, 3–20. doi:10.1533/9780857096067.1.3 (2013).
11. Soares, C. *Gas Turbines: A Handbook of Air, Land and Sea Applications* https://books.google.nl/books?id=rTPZp1YCQBkC (Elsevier Science, 2011).
12. Di Nanno, L. R., Di Bella, F. A. & Koplow, M. D. *An RC-1 organic Rankine bottoming cycle for an adiabatic diesel engine* tech. rep. Technical report: 19840024236 (1983).
13. *Sliding Gate Valve 8021-GS1* Technical datasheet. Schubert & Salzer. https://controlsystems.schubert-salzer.com/fileadmin/user_upload/ControlSystems/Produkte/Typen/8021_GS1/EN/8021-GS1_-_data_sheet.pdf.
14. *Sliding Gate Valve 8044* Technical datasheet. Schubert & Salzer. https://controlsystems.schubert-salzer.com/fileadmin/user_upload/ControlSystems/Produkte/Typen/8044/EN/8044-GS1_-_data_sheet.pdf.
15. *General Utility Service Needle Valves* Technical datasheet. Swagelok. https://www.swagelok.com/downloads/webcatalogs/en/ms-02-312.pdf.
16. *AlfaNova 14 / HP 14 - Fusion-bonded plate heat exchanger in 100% stainless steel* Technical datasheet. Alfa Laval. https://assets.alfalaval.com/documents/p3837d4b0/alfa-laval-product-leaflet-en-che00045.pdf.
17. *15 kW e-compressor: air compressor* Aeronamic (B.V.) https://aeronamic.com/product/15kw-e-compressor-air-compressor/.

ACKNOWLEDGEMENTS

Writing this dissertation has been a long and meaningful journey, and I wouldn't have made it here without the support of many incredible people.

First and foremost, I would like to express my gratitude to my supervisors Piero Colonna, Carlo de Servi, and especially Matteo Pini for bringing me onboard and trusting me with this challenging project. It has definitely been a ride to remember—bumpy at times—but one that gave me the opportunity to grow both personally and professionally. My deepest thanks go to Matteo Pini, who over the years patiently mentored me in the art of writing science—a skill seldom mastered, even among seasoned researchers. I came in rough around the edges, and it's thanks to Matteo's feedback and guidance that I eventually refined this skill. I also want to thank my colleague and friend Adam Head. Mate, you are just as responsible for making the ORCHID turbine happen as I am. It wouldn't have been possible without your drive and dedication to this project, which dates back to your own PhD journey. I know how badly you want this to become real—and I feel the same.

Moving on, I'd like to thank my friends and roommates Andrea, Antonio, and Alessandro. A warmhearted thought goes to our evenings of "Turbomachinery Symposium" in the Buitenwatersloot flat, where problem-solving reached a whole new level and velocity triangles filled the room with joy... no, seriously, I mean it. It was fun! Jokes aside, you guys—along with Valentina and Sara—are a very important part of my "Dutch family." Every expat knows how important (and sometimes difficult) it is to find a support system in a new country. The friends you share meals with, celebrate holidays with, turn to when something's off or worth celebrating. You guys rock, and you bring the feeling of home into the room whenever we're all together.

And Gioele... where do I even start? It took us just two months after meeting in the office during the pandemic to hit it off and go on our first surf trip together. The rest is history. Here's to all the surf sessions, evenings in the climbing gym, DIY projects in the most inconvenient places and times, road trips, endless hours in the ocean, cooking in parking lots and improvised campsites, co-living in "caves" disguised as rental apartments. Here's to many more of these awesome moments!

I'd also like to thank my colleagues and friends Dabo, Fabio, Alessio, Lorenzo, Wessel, Evert, and Francesco S. for the teamwork and meaningful interactions that had a significant impact on my journey. I enjoyed working side by side with you and look forward to tackling new challenges together. Special thanks to Alessio—whom I supervised during his Master's thesis project—who later became a fellow PhD. I'm proud of your journey. The passion, energy, and curiosity you bring to your work are inspiring and remind me how much I love being an engineer, even when it doesn't feel enjoyable at all.

I cannot thank enough the colleagues at Politecnico di Milano: Paolo, Steven, Ludovico, and Edoardo. Your contributions to the rotordynamics model and analysis, the interpretation of results, and the guidance you provided for the ORCHID turbine design are invaluable. It's largely thanks to our collaboration that I can now claim to know a thing or two about rotordynamics. Huge thanks also to the colleagues at Van Der Lee Turbo Systems—Jaap, Peter, Chris, and Anne—who helped craft the final design of the ORCHID turbine, which has now been manufactured. I couldn't have met you at a better time. Thank you for putting all your expertise on the table and helping make this dream come true. Thanks to the colleagues of Aeronamic, Onno, Dieter, and Ronald, for the support and the guidance to integrate the electrical generator in the ORCHID turbine test section. Great people and great tech! I'd also like to express my gratitude to Frank from the TU Delft workshop DEMO. Your cooperation, availability, and can-do attitude helped transform my ill-posed ideas and requests into real designs and parts. Your contribution was instrumental in guiding the ORCHID turbine design—and in learning by doing. Finally, I would like to thank Gert-Jan of the TU Delft's High Speed Laboratory, who during countless hours of meetings managed to transfer some of his knowledge on electrical systems to a newbie like me.

A word of appreciation MUST go to all the fellow PhDs who lit up "de Atmosfeer" in the office with jokes and memes. It's always great to refresh your thoughts—especially when you've been stuck on a project for a long time. I'd also like to thank the students I supervised—directly or indirectly—Federico, Luca, Luis, Eray, Rafael, Gianmarco, Diogo, Tota, and Matthias. I enjoyed watching you grow in knowledge and expertise, and I hope I contributed to that, even in a small way. I learned a lot from our interactions, and I thank you for that.

But the biggest thank you goes to my family—Pietro, Stefania, Paolo, Titti, Carolina, and Margherita—for making me who I am today. Thank you for the values, the drive, and for helping shape the man I've become. Most of all, thank you for patiently waiting for me to come home—again and again—over these years. You know how much I need to "do my own thing," and I know how hard it is when months go by without seeing each other. I just want you to know: it's worth it. Every hour of waiting is worth it to see each other again. I couldn't do what I love without your unconditional love, so thank you a thousand times more. And of course, thanks to all my lifelong friends—Stefano, Alessandro, Davide, Riccardo, Emanuele, Marco, Lorenzo, Alessandro, and Francesca. I'm extremely grateful for our friendship, which endures despite the distance. I wish I could be more present. I love you all, and I often find myself thinking about "the good old times" with nostalgia. A big thank you to my "Belgian" family—Matteo, Alessia, Barbara, Giacomo, Federico, and Gustavo. Though we're now scattered across Europe, Brussels will always hold a special place in our hearts.

And finally—but certainly not least—thank you to my partner, Kat. It may sound cliché, but there's no one more deserving of being mentioned in this section than you. You held me together in moments of need, kept the light on when I couldn't, kept me balanced, and gave me solid ground to stand on. I'm forever grateful to you for being by my side and for never stopping believing in me—without which this achievement would never have been possible.

About the Author

Matteo Majer was born on May 16, 1993, in Milan, Italy. Growing up near the Monza Formula 1 circuit, he developed an early passion for motorsports, also inspired by his father's love for motorcycles. This led him to study Mechanical Engineering at Politecnico di Milano, where his interest in engines deepened alongside a fascination with fluid dynamics. He continued with a master's degree, specializing in Turbomachinery and Internal Combustion Engines. Matteo's career took an international turn when he earned a scholarship to complete his master's thesis at the Von Karman Institute for Fluid Dynamics in Belgium. Over nine months, his ambition to specialize in propulsion and powertrain development solidified. After graduating with top honors, he joined Tremec in Zedelgem as a Mechanical Development Engineer, contributing to the launch of the 8-speed dual-clutch transmission for the Corvette C8. His passion for propulsion systems and renewable energy led him to doctoral research at Delft University of Technology, focusing on organic Rankine cycle supersonic turbines for thermal energy harvesting. His work resulted in presentations at major international conferences and two articles in a leading power and propulsion journal. Currently, Matteo is a post-doctoral researcher at the Aerospace Engineering faculty of TU Delft, conducting experimental research on radial turbines and developing design methods for fuel-cell turbocompressors. In his free time, Matteo enjoys surfing in Scheveningen, where he lives with his girlfriend, and climbing at the local gym with friends when the waves are calm.

CURRICULUM VITÆ

16/5/1993 Born in Milan, Italy.

WORK EXPERIENCE

3/2025 – Present *Post doctoral researcher* in turbomachinery
Technische Universiteit Delft, Delft (The Netherlands)

9/2020 – 9/2024 *PhD. Candidate* in turbomachinery for organic Rankine cycle systems
Technische Universiteit Delft, Delft (The Netherlands)

Thesis title: Supersonic organic Rankine cycle radial–inflow turbines for onboard thermal energy harvesting: Preliminary design guidelines and detailed design of a laboratory test rig for experimental validation.

Promotor(s): Prof. dr. ing. P. Colonna
Dr. M. Pini
Dr. C. M. De Servi

2/2019 – 8/2020 *Responsible engineer limited-slip differential* – Mechanical development of dual clutch transmissions
Tremec, Zedelgem (Belgium)

9/2017 – 4/2018 *Intern* on Turbomachinery and Propulsion
Von Karman Institute for Fluid Dynamics, Sint-Genesius-Rode (Belgium)

EDUCATION

9/2016 – 7/2018 Master of Science in Mechanical Engineering – Turbomachinery and Internal Combustion Engines
Politecnico di Milano, Milan (Italy)

Thesis title: Conception and numerical characterization of a passive control strategy for tip clearance loss reduction in unshrouded high-pressure turbine blades

Promotor: Prof. dr. ing. P. Gaetani

9/2012 – 2/2016 Bachelor of Science in Mechanical Engineering
Politecnico di Milano, Milan (Italy)

AWARDS

2017 Scholarship "Thesis abroad program" of 3500€ from Politecnico di Milano

LIST OF PUBLICATIONS

- L. Galieti, **M. Majer**, M. Pini, C. M. de Servi, *On the selection of optimal turbo-expanders for organic Rankine cycle systems*, Applied Thermal Engineering, (2025), *In preparation.*
- **M. Majer**, A. J. Head, C. M. de Servi, P. Colonna, M. Pini, *The ORCHID turbine: a test rig for experimental research on high-temperature supersonic organic Rankine cycle turbines*, Proceeding of the 8th International Seminar on ORC Power Systems, (2025), **Paper ID: 337**, *submitted*.
- **M. Majer**, M. Pini, *Design guidelines for high-pressure ratio supersonic radial-inflow turbines of organic Rankine cycle systems*, Journal of the Global Power and Propulsion Society **8**, 1–28 (2025).
- **M. Majer**, S. Chatterton, L. Dassi, E. Gheller, P. E. L. M. Pennacchi, P. Colonna, M. Pini, *Mechanical design and rotordynamic analysis of the ORCHID turbine*, Journal of the Global Power and Propulsion Society **8**, 1–22 (2025).
- T. Michelis, A. Head, **M. Majer**, P. Colonna, C. M. de Servi, *Assessment of particle image velocimetry applied to high-speed organic vapor flows*, Experiments in Fluids, **65**, 90 (2024).
- D. Krempus, F. Beltrame, **M. Majer**, C. M. de Servi, R. Vos, *ORC Waste Heat Recovery System for the Turboshaft Engines of Turboelectric Aircraft: correction*, (2024).
- D. Krempus, F. Beltrame, **M. Majer**, C. M. de Servi, R. Vos, *ORC Waste Heat Recovery System for the Turboshaft Engines of Turboelectric Aircraft*, Proceedings of the Aerospace Europe Conference 2023 10th EUCASS 9th CEAS, Article EURCASS 2023-658 EUCASS (2023).
- M. Pini, A. Giuffre', A. Cappiello, **M. Majer**, E. Bunschoten, *Data-Driven Regression of Thermodynamic Models in Entropic Form*, Proceedings of the 4th International Seminar on Non-Ideal Compressible Fluid Dynamics for Propulsion and Power, **29**, 22–32 (2023).
- **M. Majer**, S. Chatterton, L. Dassi, A. Secchiaroli, E. Gheller, C. M. de Servi, P. E. L. M. Pennacchi, P. Colonna, M. Pini, *Mechanical Design and Rotor-dynamic Analysis of the ORCHID Turbine*, Proceedings of the 7th International Seminar on ORC Power Systems, **Paper ID: 89**, 1–10 (2023).
- A. Cappiello, **M. Majer**, R. Tuccillo, M. Pini, *On the Influence of Stator-Rotor Radial Gap Size on the Fluid-Dynamic Performance of Mini-ORC Supersonic Turbines*, Proceedings of the ASME Turbo Expo 2022: Turbomachinery Technical Conference and Exposition, **10B**, V10BT35A015 (2022).